KU LEUVEN

ARENBERG DOCTORAL SCHOOL
Faculty of Engineering Science

Inorganic polymers from CaO-FeO-SiO_2 slags

Processing, reaction mechanism and molecular structure

Arne Peys

Supervisor:
Prof. dr. ir. Y. Pontikes
Prof. dr. ir. H. Rahier
(Vrije Universiteit Brussel)
Prof. dr. ir. B. Blanpain

Dissertation presented in partial fulfillment of the requirements for the degree of Doctor in Engineering Science

August 9th, 2018

Inorganic polymers from CaO-FeO-SiO_2 slags

Processing, reaction mechanism and molecular structure

Arne PEYS

Examination committee:
Prof. dr. ir. Y. Willems, chair
Prof. dr. ir. Y. Pontikes, supervisor
Prof. dr. ir. H. Rahier, supervisor
(Vrije Universiteit Brussel)
Prof. dr. ir. B. Blanpain, supervisor
Prof. dr. ir. K. Vanmeensel
Prof. dr. ir. S. Lomov
Prof. dr. ir. C. E. White
(Princeton University)
Prof. dr. A. P. Douvalis
(University of Ioannina)

Dissertation presented in partial fulfillment of the requirements for the degree of Doctor in Engineering Science

August 9th, 2018

© 2018 KU Leuven – Faculty of Engineering Science
Uitgegeven in eigen beheer, Arne Peys, Kasteelpark Arenberg 44, B-3001 Heverlee (Belgium)

Alle rechten voorbehouden. Niets uit deze uitgave mag worden vermenigvuldigd en/of openbaar gemaakt worden door middel van druk, fotokopie, microfilm, elektronisch of op welke andere wijze ook zonder voorafgaande schriftelijke toestemming van de uitgever.

All rights reserved. No part of the publication may be reproduced in any form by print, photoprint, microfilm, electronic or any other means without written permission from the publisher.

ISBN XXX-XX-XXXX-XXX-X

D/XXXX/XXXX/XX

Preface

This thesis would not have been possible without the help of others. This is a sentence which has been overly used in prefaces and so cliché it loses its true meaning. In my case it is necessary to take the sentence literally and interpret it to its full extent as expression of gratitude, as for some people I will mention on this page, the statement is literally true. On the other hand there is also a big bunch of people that made the synthesis process towards this manuscript more enjoyable. Much more enjoyable...

Going against my nature and need for feeling special I follow here the conventional procedure of thanking promotors, colleagues and family in that seemingly fixed order. Even more usual, I will start with my leading promotor Yiannis, who might as well be in the family section of this assemblage of thank yous. Despite the occasional difference in our thinking pattern, I feel we make a great team and I know he will always protect me from the malakas of this world. For this thesis specifically the boost that he brought by bringing me into contact with Alexis and Claire had an incredible impact, not even mentioning the pool of ideas that were thrown at me during the course of this work. Discussing with Hubert is something I always look forward to. We almost always agree and extra insights pop up like a maize seed on a barbecue. This goes together with the kindness that radiates from him like a santa-claus. To Bart I have always looked up, apart from the obvious literal way, also figuratively. A certain sense of authority follows him around like tickbirds on a giraffe. Although uncomfortable in the field of cementitious or inorganic polymer materials the pragmatic impact of his comments has always been significant.

Lukas, brother of the first hour, since we slept together in Hernstein, my life has never been the same. Tobias does not only make the best tzadziki of Bavaria; we share our love for freshly caught fish, ouzo and science. To Pavel, master of JMP software and dancefloors, I say thank you for sitting by my side! Thanks to all the SREMates who helped me, making the work lighter and

more fun. You will see I am changing to general thank yous, because of fear of forgetting someone. People from the best Materials Engineering department of KU Leuven, I thank you for the nice time we have and will spend; my fellow PhD students, post-docs, professors and technicians, who made it possible to work at MTM, who made the numerous events incredibly amazing.

Special thanks go out to Claire and the White boys. After my time in Princeton I was not anymore only a fan of her work, but also of the person. Similarly, Alexis opened the hospitable doors of Ioannina and made the Mössbauer analysis possible. Our trials to build bridges between physics and engineering and the passionate discussions on how to fit the spectra have definitely lead to something beautiful.

Thank you to everyone who has supported me throughout these years, family, friends, girlfriend. You kept the mentally unstable person that I am on the right path and shaped me who I am today. Thank you for sharing the good times and supporting me in the bad times. I'm sorry to the people I've hurt along the way, socially speaking I'm a very stupid person. Luckily, that is compensated by the genius I am in my work, haha!

Dear reader, thank you for your interest! May this text be useful as a reference, an inspiration, or as something to read while doing your business on the toilet. Never mind the bollocks and may the force be with you!

Abstract

Fe-silicate slags, originating from the copper, lead, zinc, nickel, and ferro-nickel industries, are investigated as precursors for a new kind of cementitious material: inorganic polymers. Scientific background is thereby provided to make a case for the valorization of the abundant non-ferrous metallurgy residues that are present in Flanders ($\sim$ 600 ktons/year = 0.1 ton/year.capita) and by extension in Europe and the world. These slags are simplified to the CaO-FeO_x-SiO_2 ternary system to investigate fundamental aspects of the inorganic polymers. The thesis is focused on slags in the compositional range $Ca_xFe_{1-x}Si_yO_{2y+1}$ (x = 0-0.3, y = 0.5-1). Previous studies revealed that similar and higher strengths can be reached in comparison with Portland cement. The processing and properties were found to be comparable to common geopolymers and alkali-activated materials. The work presented in this manuscript sheds light on the chemistry of the reactions and the molecular structure of the reaction product.

Comparing the chemical composition of the Fe-silicate slags with better known precursors for geopolymers and alkali-activated materials, such as metakaolinite and blast furnace slag, the most prominent difference is the abundance of Fe (30-60 wt% FeO). The role of Fe in the slags and inorganic polymers was examined, in the first instance, using ^{57}Fe Mössbauer spectroscopy and X-ray absorption near-edge spectroscopy. These investigations suggested that the final structure of the inorganic polymer contains Fe in the III oxidation state. The coordination number of Fe in the final structure was less clearly defined. Fe^{3+} was present in the silicate network, as determined by pair distribution function analysis, where it was also observed that part of the Fe^{3+} might be clustered. The molecular structure of the inorganic polymer can be adapted by changing the chemical composition of the slag. The alkali silicate solution does not have a profound effect at the nano-scale, although it can be used to influence the microstructure and kinetics.

The addition of time-dependency as a variable enabled a deeper analysis of

the evolution of the molecular structure. No oxidation from Fe^{2+} to Fe^{3+} occurs until the reactions that lead to the setting of the material have started. The formation of the binder then comprises two valences of Fe. Partially, Fe forms part of a silicate structure as Fe^{3+} (probably tetrahedral), with Na^{+} as charge balancer. The Fe^{2+} part of the binder forms trioctahedral layers of $Fe(OH)_2$. These layers are not stacked as in a $Fe(OH)_2$, but show the same in-layer periodicity up to 8.6 Å. They are more accurately referred to, therefore, as trioctahedral 2D clusters. In contact with air these Fe^{2+}-clusters are oxidized, resulting in a complete Fe^{3+} binder. This Fe^{3+} has Mössbauer parameters comparable with the tetrahedra that were formed at initial stages, but pair distribution function analysis suggests that the configuration of the layers partially remains.

As a tool to communicate the potential of residue-based binders to the general public and industry, an online database has begun to be developed. Associated with this, tools are being developed to provide an easier way to calculate mixes or to assess the sustainability of a proposed mix-design. The environmental part of this assessment is based a full life-cycle impact study, which compared the Fe-silicate inorganic polymers to Portland cement based materials. This study showed a potential environmental impact drop of 77% with respect to CEM I cement, making the inorganic polymers from CaO-FeO_x-SiO_2 slags a sustainable alternative for conventional cementitious materials.

Samenvatting

Slakken met een hoog ijzergehalte zoals in de koper, lood, zink, nikkel en ferronikkel industrie zijn onderzocht als grondstof voor een nieuw soort cementachtig materiaal: anorganische polymeren. De wetenschappelijke achtergrond wordt daarbij gegeven om de valorisatie te stimuleren van de overgrote voorraad aan non-ferro slakken die in Vlaanderen en de rest van de wereld te vinden is. De slakken worden in deze thesis chemisch vereenvoudigd tot het ternair CaO-FeO_x-SiO_2 systeem om fundamentele aspecten van de anorganische polymeren beter te kunnen blootleggen. De focus ligt op het samenstellingsdomein $Ca_xFe_{1-x}Si_yO_{2y+1}$ (x = 0-0.3, y = 0.5-1). Studies die v*óó*r deze thesis gedaan werden onthulden het potentieel om gelijkaardige sterktes als Portland cement te bereiken en toonden aan dat de verwerking en eigenschappen veel gelijkenissen vertonen met conventionele geopolymeren en alkalisch geactiveerde materialen. Het werk dat in dit manuscript gepresenteerd wordt geeft een insteek op de chemie achter de reacties en de moleculaire structuur van het reactieproduct.

Als de chemische samenstelling van Fe-silicaat slakken vergeleken wordt met beter gekende precursoren voor geopolymeren of alkalisch geactiveerde materialen zoals metakaoliniet en hoogovenslak, is het meest opvallende verschil het hoge Fe-gehalte (30-60 gew%). De rol van dit element was in eerste instantie onderzocht met ^{57}Fe Mössbauer spectroscopie en Röntgenstralenabsorptie nabijkant spectroscopie, met de determinatie van de oxidatiestaat van Fe in de binder tot gevolg: III. Het coordinaatgetal was (voorlopig) minder goed gedefinieerd. Het Fe^{3+} zit in het silicaatnetwerk, volgens paarverdelingsfunctieanalyse, waaruit ook bleek dat een deel van het Fe geclusterd zou kunnen zijn. De moleculaire structuur van de anorganische polymeren kan aangepast worden door de chemische samenstelling van de precursor te veranderen. De activerende oplossing heeft geen grote invloed op de nanoschaal, maar kan gebruikt worden om de microstructuur en kinetiek te beïnvloeden.

Het toevoegen van tijdsafhankelijkheid liet een diepere analyse van de evolutie

van de moleculaire structuur toe. Het oplossen van het slak gebeurt congruent en zet clusters vrij in de alkalische oplossing. Er gebeurt daarbij geen oxidatie van Fe^{2+} naar Fe^{3+} totdat de reacties beginnen die tot het hard worden van het materiaal leiden. Deze reacties resulteren in een binder met 2 oxidatiestaten van Fe. Gedeeltelijk gaat Fe naar een silicaat structuur als tetrahedrisch Fe^{3+}, met ladingsbalans door Na^{+}. Het Fe^{2+} deel van de binder vormt trioctahedrische lagen van $Fe(OH)_2$. Deze lagen zijn niet gestapeld zoals in $Fe(OH)_2$, maar vertonen dezelfde periodiciteit in de laag tot op 8.6 Å. Als deze Fe^{2+} lagen in contact komen met de lucht, worden ze geoxideerd en wordt het Fe in de binder dus volledig Fe^{3+}. Dit Fe^{3+} heeft dezelfde Mössbauer parameters als de tetrahedra die in het eerste stadium gevormd waren, maar uit paardistributiefunctieanalyse wordt gesuggereerd dat de gelaagde configuratie gedeeltelijk behouden.

De ontwikkeling van een online database was gestart, als hulpmiddel om het grote publiek en bedrijven te overtuigen van het potentieel van op residu gebaseerde bindmaterialen. Verbonden met deze database werden tools ontwikkeld die een eenvoudigere berekening van mengsels bewerkstelligen of een vereenvoudigde beoordeling van de ecologische impact en kost mogelijk maken. Het ecologische aspect van deze berekeningen is gebaseerd op een eigen cradle-to-gate impact studie, die de Fe-rijke anorganische polymeren met Portland cement gebaseerde materialen vergelijkt. Deze studie toonde een mogelijke daling in ecologische impact van 77% met betrekking tot CEM I mortels. De anorganische polymeren uit CaO-FeO_x-SiO_2 slakken zijn dus een duurzaam alternatief voor conventionele cementen.

Contents

Abstract iii

Samenvatting v

Contents vii

List of Figures xi

List of Tables xix

1 Introduction 1

1.1 Cementitious materials and sustainable development 1

1.2 Alkali-activated materials, geopolymers and inorganic polymers 2

1.3 Research aims and outline 3

2 State-of-the-art 7

2.1 Structural and mechanistic insights from related materials: geopolymers and alkali-activated materials 7

2.1.1 Aluminosilicates: metakaolin, class-F fly ash 8

2.1.2 Calcium (alumino)silicates: blast furnace slag 11

2.2 Fe-rich inorganic polymers 12

2.2.1 Overview of resources 13

2.2.2 Inorganic polymers from pyrometallurgical slags 14
2.2.3 Characterization techniques 16
2.3 Formulation of research questions 24

3 Molecular structure of (CaO-)FeO_x-SiO_2 inorganic polymers 27

3.1 The use of ATR-FTIR spectroscopy in the analysis of iron-silicate inorganic polymers 27
3.1.1 Introduction 28
3.1.2 Materials and methods 28
3.1.3 Results and discussion 29
3.1.4 Conclusions 32
3.2 Oxidation state and coordination number of Fe 33
3.2.1 Introduction 34
3.2.2 Materials and Methods 34
3.2.3 Results and discussion 36
3.2.4 Conclusions 40
3.3 Molecular structure of CaO-FeO_x-SiO_2 glassy slags and resultant inorganic polymers 41
3.3.1 Introduction 43
3.3.2 Experimental 45
3.3.3 Results and discussion 47
3.3.4 Conclusions 59
3.4 Tuning the molecular structure by varying the activating solution chemistry 61
3.4.1 Introduction 62
3.4.2 Materials and methods 63
3.4.3 Results and discussion 65
3.4.4 Conclusions 70

4 Mechanism and kinetics of CaO-FeO$_x$-SiO$_2$ binder formation 73

4.1 The start of oxidation of Fe and the formation of a mixed valence binder . . . 73

4.1.1 Introduction . . . 74

4.1.2 Experimental methods and materials . . . 76

4.1.3 Results and discussion . . . 77

4.1.4 Conclusions . . . 87

4.2 Formation mechanism from in-situ X-ray total scattering . . . 89

4.2.1 Introduction . . . 91

4.2.2 Material and methods . . . 93

4.2.3 Results and discussion . . . 93

4.2.4 Conclusions . . . 111

4.3 The origin of oxidation and its influence on the final structure of Fe-rich inorganic polymers . . . 113

4.3.1 Introduction . . . 114

4.3.2 Materials and methods . . . 116

4.3.3 Results . . . 117

4.3.4 Discussion . . . 119

4.3.5 Conclusions . . . 126

5 The internet of Fe-rich inorganic polymers 129

5.1 Software for database collection and support calculations . . . 129

5.1.1 Introduction . . . 130

5.1.2 A brief history . . . 130

5.1.3 Software architecture . . . 132

5.1.4 Instead of conclusions . . . 135

5.2 Simplifying the calculation of the environmental impact . . . 137

5.2.1 Introduction . . . 138

5.2.2 Experimental 140
5.2.3 Life Cycle Assessment 142
5.2.4 Results and Discussion 146
5.2.5 Conclusions 153

6 Highlights 155

6.1 Inorganic polymer structure 155
6.2 Reaction mechanism 155

7 Conclusion 157

A Supplementary data chapter 3.3 161

A.1 X-ray and neutron weighting factors 161
A.2 Calculation of coordination numbers 162
A.3 Scattering functions 164
A.4 Infrared spectroscopy 164
A.5 Long-range PDF data 166
A.6 References 167

B Supplementary data chapter 4.2 169

B.1 X-ray scattering functions 169

C On a lighter note... 173

Bibliography 177

List of Figures

1.1 An overview of alternative cements with geopolymer as part of AAMs [155] 3

2.1 Polyhedral representation of geopolymer structure by Barbosa et al. [9]. The cross in the circle and the star pointing at Si atoms refer to the amount of Al next to the Si, 3 and 2 respectively [9], making it $Q^4(3Al)$ and $Q^4(2Al)$ in Engelhardt notation [40]. Note that not all Al is 4-fold coordinated in the figure, although this should be the case in a pure geopolymer according to Davidovits [27]. 8

2.2 Schematic of the reaction stages in the formation of a geopolymer [154]. 9

2.3 Representation as tobermorite-like structure of C-A-S-H polymer by Provis and Bernal [152]. The triangles represent tetrahedral sites (blue for Si, red for Al), the circles are interlayer species (colors not specified by the authors). 12

2.4 Overview of Fe-rich resources for the synthesis of inorganic polymers. 13

2.5 Fayalite-containing semi-amorphous slag after leaching in NaOH [78]. 15

2.6 Example temperature dependence of a strong and fragile liquid near the glass transition temperature [21]. 15

2.7 Si NMR spectra of silicate glasses including variable amount of Fe_2O_3 [87]. 17

2.8 Energy levels of a nucleus and their change under influence of the electron cloud, explaining the isomer shift and quadrupole split. 20

2.9 Filling of the spin states in high spin Fe^{2+} and Fe^{3+}. 21

2.10 Example Mössbauer spectrum, showing a characteristic combination of doublets. 22

2.11 PDF of alkali-activated blast furnace slag and its carbonated equivalent [122]. 23

3.1 Infrared spectra of the studied precursors with indication of the position of the Si-O stretching band. 30

3.2 The relation between Si-O stretching band position and (Ca+Fe)/Si molar ratio. 31

3.3 Infrared spectra of the fayalite slag (a) [136] and plasmastone (b) [unpublished results] based inorganic polymers. The precursors and the spectrum of a water droplet are added as a reference. . . 31

3.4 Mössbauer spectra of the (a) copper slag and (b-d)resultant inorganic polymers [136] at 300 K. 36

3.5 Mössbauer spectra of the synthetic slags [135] at 300 K. 36

3.6 X-ray absorption spectra of slags and inorganic polymer. 37

3.7 Graphical abstract: The determination of the molecular structure of Fe-rich inorganic polymers by pair distribution function analysis. 42

3.8 Synthesis procedure of the samples. Including (from left to right) melting and quenching the slag, milling slag to powder and mixing the powdered slag with the activating solution to obtain the inorganic polymer samples shown on the right. 46

3.9 X-ray (top) and neutron (bottom) scattering functions of the low and high-Ca slags (stacked plots). 48

3.10 Stacked plot of the X-ray scattering data of the two types of slags with a detector distance of 95 cm. The crystalline phases are indicated. 49

3.11 X-ray (top) and neutron (bottom) PDFs of the low and high-Ca slags. 50

3.12 X-ray and neutron PDFs, showing a zoom of Figure 3.11 over an r range of 2.5 to 3.6 Å. The shoulder of the main metal-metal correlation at approx. 2.95 Å is likely Fe-Fe contributions from edge-sharing ^{V}Fe. 51

3.13 X-ray and neutron PDFs of the low (top) and high-Ca (bottom) slags. 52

3.14 Neutron scattering data of the Fe-rich IPs in reciprocal space before background correction. 53

3.15 X-ray (top) and neutron (bottom) PDFs of the Fe-silicate slags and IP pastes. The plots are stacked and grouped per precursor slag. 54

3.16 Detailed view on the Fe-O correlation in the X-ray (top) and neutron PDFs (bottom) of the IPs and slags. The plots are stacked and grouped per precursor slag. 56

3.17 X-ray (top) and neutron (bottom) PDFs of the slags and IPs, detailed view of the metal-metal correlations. The plots are stacked and grouped per precursor slag. 57

3.18 X-ray and neutron PDFs of the slags and IPs activated with a sodium silicate solution (SiO_2/Na_2O molar ratio 1.6). Top: Low-Ca system, bottom: High-Ca system. 59

3.19 X-ray scattering functions of the IPs. Upper: Low-Ca slag, lower: High-Ca slag 65

3.20 Neutron scattering functions of the IPs. Upper: Low-Ca slag, lower: High-Ca slag 65

3.21 X-ray PDFs of the low-Ca (top) and high-Ca IPs (bottom). . . 66

3.22 Neutron PDFs of the low-Ca (top) and high-Ca IPs (bottom). . 67

3.23 Difference plots of the IPs with respect to the slag. 68

3.24 Detailed view on the metal-metal correlations in the X-ray PDFs of IPs. 68

3.25 Detailed view on the metal-metal correlations in the neutron PDFs of IPs. 69

3.26 Longer range of the X-ray PDFs of IPs. 69

3.27 Longer range of the neutron PDFs of IPs. 70

3.28 X-ray (top) and neutron PDFs (bottom), comparing the IPs from different precursors. 70

4.1 Heat flow in isothermal calorimetry at 20 °C from the first 16 hours after mixing. 78

4.2 Raw ^{57}Fe Mössbauer spectra during the first 28 days of reaction, where the numbers indicate the reaction time after mixing, in minutes (min), hours (h) or days (d). The dashed rectangles indicate the regions where the high velocity parts of the new Fe^{3+} and Fe^{2+} QS doublet contributions of the binder gradually appear. 79

4.3 The ^{57}Fe Mössbauer spectrum of the slag with the three components used in the fitting model shown in different colors. S1 and S2 are Fe^{2+} and S3 is Fe^{3+}. 80

4.4 ^{57}Fe Mössbauer spectra of the IPs recorded at different reaction times: (a) 1 day, (b) 7 days, (c) 28 days. The slag components (S1, S2, S3) are shown as gray filled areas and the binder components (IP1, IP2) as colored lines. 82

4.5 Evolution of the absorption areas of components IP1, IP2 and the sum of absorption areas of components S1, S2 and S3. The insert shows the short term ($\leq$ 24 hours) evolution of the absorption areas of the IP1 and IP2 components. The IP binder components only start forming after 3 hours (0.125 days). 84

4.6 Comparison of the calorimetry measurements with the derivative to time of the sum of absorption areas of the IP components. . 85

4.7 The FTIR spectra during the first 28 days of reaction. The spectra before setting are shown on the left in part a, these thus consider measurements in the liquid state, with the liquid in direct contact with the ATR crystal. The measurements on powdered samples after setting, pressed against the ATR crystal, are shown on the right in part b. 86

4.8 Difference plot of the FTIR spectra after 6 hours compared to 8 minutes, revealing more clearly the changes: (1) transformation of the activating solution, (2) the formation of the binder phase and (3) the dissolution of the slag. 87

4.9 Schematic of the sequence of reaction stages. 87

4.10 Graphical abstract: The formation of trioctahedral 2D clusters, detected by pair distribution function analysis. 90

4.11 X-ray total scattering functions of Na-silicate activated high-Ca IP during the initial 62 hours of reaction. Upper plot: Full total scattering functions. Lower plot: Difference curves obtained by subtracting the initial data set (15 minutes) from those at later times. 94

4.12 X-ray total scattering functions of Na-silicate activated low-Ca IP at 15 minutes, 62 hours and approx. 6 months after mixing. Note that the 6 months sample was cured in a sealed container, then crushed into a powder and loaded into a polyimide capillary before the measurement. 95

4.13 Evolution of the intensity of the small-angle region (maximum S(Q) within a Q range of 0.3-0.4 $Å^{-1}$) in the X-ray total scattering functions. (a) During the initial 15 hours of reaction and (b) up to 80 hours after initial mixing. 96

4.14 X-ray PDFs of the Na-silicate activated low-Ca IP during the initial 62 hours of reaction. Upper plot: Full PDFs and insert showing a zoom of the Fe-O correlation. Lower plot: Difference curves obtained by subtracting the initial data set (15 minutes) from those at later times. 98

4.15 X-ray PDFs of the Na-silicate activated high-Ca IP during the initial 62 hours of reaction. Upper plot: Full PDFs and insert showing a zoom of the Fe-O correlation. Lower plot: Difference curves obtained by subtracting the initial data set (15 minutes) from those at later times. 99

4.16 X-ray PDFs of the K-silicate activated low-Ca IP during the initial 62 hours of reaction. Upper plot: Full PDFs and insert showing a zoom of the Fe-O correlation. Lower plot: Difference curves obtained by subtracting the initial data set (15 minutes) from those at later times. 100

4.17 X-ray PDFs of the K-silicate activated high-Ca IP during the initial 62 hours of reaction. Upper plot: Full PDFs and insert showing a zoom of the Fe-O correlation. Lower plot: Difference curves obtained by subtracting the initial data set (15 minutes) from those at later times. 101

4.18 Long range X-ray PDFs of the Na-silicate activated low-Ca IP during the initial 62 hours of reaction. 102

4.19 Long range X-ray PDFs of the Na-silicate activated high-Ca IP during the initial 62 hours of reaction. 103

4.20 X-ray PDFs of (a) initial (15 minutes) and (b) final (81 hours) sample of the Na-activated low-Ca slag during the in-situ test, compared with ferrosilite ($Fe_2Si_2O_6$), hedenbergite ($CaFeSi_2O_6$), amakinite ($Fe(OH)_2$) and goethite ($FeO(OH)$). 104

4.21 Calculation of the Fe-Fe distances in a trioctahedral Fe^{2+} layer. Fe atoms are located at the corners of the triangles. 104

4.22 Comparison of the X-ray PDFs of the Na-activated low-Ca IP immediately after mixing (15 minutes), after 62 hours of reaction and fully cured/oxidized from chapter 3.3. The insert shows a zoom of the Fe-O correlation. 106

4.23 Comparison between the intensity of the SAS and peak at 5.6 Å in the PDF for the low-Ca (left) and high-Ca (right) system for the same times as presented in Figure 4.22. 107

4.24 Evolution of the intensity of the 5.57 Å correlation in the X-ray PDFs on a (a) linear scale; G, (b) logarithmic y-axis; log time, (c) logarithmic x-axis; log G, (d) reciprocal y-axis; 1/G. 108

4.25 Low r region of the X-ray PDFs for the low-Ca IPs during the first 4 hours. The insert shows a zoom of the nearest neighbor Fe-O correlation. 109

4.26 Evolution of the intensity for the nearest neighbor Fe-O correlation in the low-Ca systems. 110

4.27 Schematic overview of the formation mechanism and different reaction stages of Fe-rich inorganic polymers. 110

4.28 ^{57}Fe Mössbauer spectra of samples cured at room temperature (a) and treated in a furnace (b). 118

4.29 Fitted spectra of samples (a) 1DS, (b) 7DS28 and (c) 7DS800. 119

4.30 Absorption area of Fe^{3+} binder component for samples prepared in inert and atmospheric environments, compared with chapter 4.1. The error on the absorption area is estimated at approximately 3%. 122

4.31 Evolution of the absorption area of the Fe^{2+} (black) and Fe^{3+} (red) components of the binder. After 7 days, part of the samples were milled and exposed to air at room temperature or 200 °C. The error on the absorption area is estimated at approximately 3%.. 122

4.32 Evolution of the Mössbauer parameters of the Fe^{2+} and Fe^{3+} components of the binder. Left: isomer shift; right: quadrupole splitting. 123

4.33 Schematic representation of the configuration of Fe throughout the reactions. The height of the boxes refers to the approximate amount of the configuration in the binder. 124

4.34 Evolution of Fe^{3+} component of the binder with temperature. Left: absorption area; right: Mössbauer parameters. 125

4.35 ATR-FTIR spectra of the samples as function of the temperature. 126

5.1 Home page of 1st SREMat software. 131

5.2 Interface of the Eco-financial analysis tool in the 1st SREMat software. 131

5.3 Overview of the software and its modules. 132

5.4 Example page of residue, showing its origin and chemical composition. 133

5.5 Overview of the ordinary Portland cement system 142

5.6 Overview of sodium silicate activated inorganic polymer system. (Diesel was also used for transport with trucks, but the arrows were not provided to avoid overloading of the figure) 143

5.7 Overview of the biomass activated inorganic polymer system. (Diesel was also used for transport with trucks, but the arrows were not provided to avoid overloading of the figure) 144

5.8 Environmental impact of the different sub-processes, subdivided into midpoint categories. The units are normalized to person equivalents weighted (PEW) to be able to compare the different categories. For the transport, 100 km was considered. A logarithmic scale for the y-axis was needed because of the large differences between the different sub-processes 146

5.9 Sensitivity analysis of selected parameters for single scores of $24H_2O$ (a) and 0.4 A (b) 149

5.10 Influence of the average transport distance on the environmental impact of inorganic polymers and Portland cement mortar . . . 149

5.11 Adapted google maps view of Flanders with indications of cities selected for the analyses and locations of the raw materials suppliers 151

5.12 Future scenario analyses in Mol for 24H_2O comparing the current state of technology with a scenario using wind energy for the production of sodium hydroxide (Wind E). The results are shown relative to OPC 152

5.13 Contribution analysis of hydrothermally produced sodium silicate and sodium hydroxide (*estimation based on Thannimalay et al.[186]). The contributions in sodium hydroxide are normalized to 95% to fit the contribution of sodium hydroxide in sodium silicate. Therefore, the electricity contribution in sodium silicate is directly visualized 153

A.1 X-ray (left) and neutron (right) scattering functions, comparing the slags and inorganic polymers. 165

A.2 Stacked plot of the ATR-FTIR spectra of the IPs. Carbonates are observed at $\sim$ 1400 and 870 cm^{-1}. 166

A.3 Absorbance of the H_2O and CO_2 signal during TGA-FTIR (left) and the result from TGA analysis on the low-Ca IP (right). . . 166

A.4 Long-range PDFs of high-Ca slag and IP. 167

B.1 X-ray total scattering functions of Na-silicate activated low-Ca IP during the initial 62 hours of reaction. 170

B.2 X-ray total scattering functions of Na-silicate activated high-Ca IP during the initial 62 hours of reaction. 170

B.3 X-ray total scattering functions of K-silicate activated low-Ca IP during the initial 62 hours of reaction. 171

B.4 X-ray total scattering functions of K-silicate activated high-Ca IP during the initial 62 hours of reaction. 171

List of Tables

3.1 Chemical compositions of the studied precursor materials in wt%. 29

3.2 Chemical compositions of the studied precursor materials in wt%. 34

3.3 $Fe^{3+}/\sum Fe$ ratios in slags and IPs from [7, 136, 135, 176] (the lower precision of the Mössbauer spectroscopy does not allow to show 2 figures after the comma). 38

3.4 Average coordination numbers in slags and IPs from [136, 135, 176]. Mössbauer spectroscopy shows the average coordination number of the contributions in the slag or the binder phase, XANES considers the binder in combination with undissolved slag. 39

3.5 Chemical composition in mole% of the Fe-rich slags obtained using XRF by Van De Sande et al. [190] (estimated relative error 10%, e.g., 44 ± 4.4 mole%). 45

3.6 Mix-design of the 8 samples. The activating solution chemistry is defined by the alkali atom and molar ratios SiO_2/M_2O and D_2O/M_2O. A constant water/slag mass ratio of 0.28 is maintained, resulting in the reported solution/slag mass ratios. 64

4.1 Chemical composition of precursor slag in wt.%, obtained from XRF (estimated relative error 10%). 76

4.2 Resulting hyperfine parameters values of the components used to fit the ^{57}Fe Mössbauer spectra. IS is the Isomer shift relative to α-Fe at room temperature, (QS) is the central value of the quadrupole splitting, ΔQS is the total Gaussian-type spreading of the quadrupole splitting and AA is the relative absorption area. The half line-width was fixed to $\Gamma/2$=0.14 mm/s to avoid interference with the ΔQS. For component IP1 the QS spreading is asymmetric around the central QS value and is given in the sense ΔQS<QS/ΔQS>QS. Typical errors include ± 0.02 mm/s for IS and QS and ± 5 % for AA. **The table continues on the next page.* 81

4.3 Table 4.2 for samples cured for 7-28 days (splitted from other samples for lay-out purposes). 82

4.4 Chemical composition of precursor slag in wt.% (estimated relative error 10%). 116

4.5 Resultant Mössbauer hyperfine parameters from fitting the spectra of Figure 4.28. IS is the isomer shift with respect to α-Fe at 300 K, QSc is the central value of the quadrupole splitting, B_{hf}c is the central value of the hyperfine magnetic field, Δ QS and Δ B_{hf} are the spreading of the QS and B_{hf} respectively, AA is the relative absorption area of the components. Estimated errors on the parameters are ± 0.02 mm/s for IS and QSc, ± 0.3 T for B_{hf} and ± 5% for AA. The half line-width was kept constant at 0.14 mm/s to avoid interference as this parameter has the same influence on the spectra as Δ QS and Δ B_{hf}. **The table continues on the next page.* 120

4.6 Continuation of Table 4.5: Hyperfine parameters of furnace samples 121

5.1 Investigated mixtures (SiO_2/Na_2O and H_2O/Na_2O only consider the activating solution; solid = ash + slag) 141

5.2 Contributions of the raw materials and transport to the environmental impact (in mPEW/kg, factors I_x in equations 1–3) of the respective raw materials. Considering the sodium silicate solution, dry refers to the fact that the impact is rescaled to the dry content 147

5.3 Compressive strength and environmental impact of the inorganic polymer and Portland cement mortars 148

5.4 Single score environmental impact in % of OPC with an average transport distance of 100 km in four of Flanders' large cities (Ghent, Antwerp, Brussels, Hasselt) and the main raw material suppliers: non-ferrous slag (Beerse, Olen) and sand (Mol) . . . 150

A.1 X-ray weighting factors of possible atomic correlations [1]. The factors are normalized to 100 for easier comparison. 161

A.2 Neutron weighting factors of possible atomic correlations [2]. The factors are normalized to 100 for easier comparison. 162

A.3 Ratio of X-ray weighting factor and neutron weighting factor ($w_{X-ray}/w_{Neutron}$). 162

A.4 Coordination numbers of Fe and Ca in the low-Ca slag calculated from the neutron PDFs. 163

A.5 Coordination numbers of Fe and Ca in the low-Ca slag calculated from the X-ray PDFs. 164

A.6 Coordination numbers of Fe and Ca in the high-Ca slag calculated from the neutron PDFs. 164

A.7 Coordination numbers of Fe and Ca in the high-Ca slag calculated from the X-ray PDFs. 165

Chapter 1

Introduction

1.1 Cementitious materials and sustainable development

Recent evolution in social acceptance of global warming and depletion of resources has rendered the need for research into materials with a better environmental performance obvious. Enacted by the Paris agreement [42], the majority of this world's governments dedicate themselves to supporting the transition to greener technology in an attempt to save our planet. Therein lies the aim of lowering the anthropogenic CO_2 emissions, trying to avoid the increase of global temperatures of more than 2 °C. Simultaneously, a stimulant is put forward by the European Union for pursuing technologies with a lower environmental footprint and more efficient use of resources, embodied for instance by the rise of the European Institute of Innovation and Technology (EIT) and its Knowledge and Innovation Communities (KICs) [1], e.g. Raw Materials.

One of the key materials in this story is concrete or more specifically, the cementitious material that binds it together: ordinary Portland cement (OPC). The production of this greyish white powder that becomes monolithic upon the addition of water contributes about 8% [134] to the total CO_2 emitted by human activities. Despite efforts of the cement industry to increase the efficiency of OPC production [174], decreasing the CO_2 output and processing cost, a large part of the emissions is inherent to the decomposition of limestone during the production and thus unavoidable. For these reasons the research in

alternative cementitious materials is booming.

A wide variety of viable alternatives is found in the research community and specialized companies. Hydraulic material systems with a lower processing temperature are investigated as well as supplementary cementitious materials with latent hydraulic or pozzolanic activity which are blended with OPC [128, 140]. Completely new systems which do not need OPC, but a chemical activator to start the reactions have also recieved considerable attention [140, 155]. The present thesis focuses on the latter. More specifically, the materials under study here are found in literature with the names [155, 159]: alkali-activated materials (AAMs), geopolymers, inorganic polymers (IPs) and low-temperature synthesized aluminosilicate glasses.

1.2 Alkali-activated materials, geopolymers and inorganic polymers

The research community often elaborately discusses the nomenclature to be used in the material system presented in this thesis. Clarification of the different names and those chosen throughout the manuscript has therefore become a necessity, which this section tries to fulfil. The term AAM is interpreted in different ways:. The more general interpretation of the word is a material that needed alkalis to start the reaction of the precursor [155], while others argue that the term is strictly reserved for latent hydraulic precursors to which a small amount of alkalis is added to kick-start hydration reactions [30]. This thesis will use the term in the more general definition of Provis and van Deventer [155].

The term geopolymer is more strictly defined by its coiner, Davidovits [29]. It considers an aluminosilicate polymer network in which the aluminium is tetrahedrally surrounded by oxygen and the silicate species are Q^4 polymerized (Q^x nomenclature by Engelhardt et al. [40]). The synthesis usually involves mixing metakaolin or fly ash with an alkali solution. In literature the term is heavily popularized and has not always been used in the framework of this definition. Depending on the chosen definition of AAMs, geopolymer is thus a subdivision of AAMs, Figure 1.1, or a material co-existing with AAMs.

An inorganic polymer is a 3D connected network (polymer) made of inorganic elements (often Si-O). As such it is a wide family of materials, which partially overlaps with the AAMs. An attempt to avoid the discussion between the AAM and geopolymer using parts of the research community gave birth to the use of the term IP. In literature the term IP is used when a certain precursor is mixed

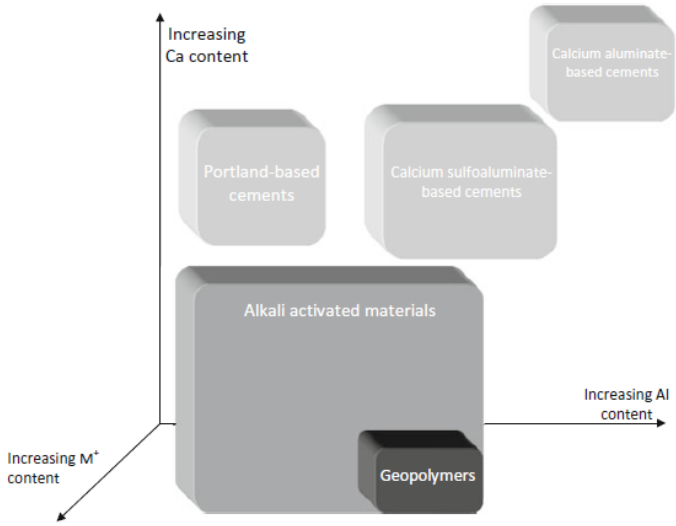

Figure 1.1: An overview of alternative cements with geopolymer as part of AAMs [155]

with alkali silicates or hydroxides to produce a binder, not necessarily matching the definition of a geopolymer. The present thesis considers the product of mixing a CaO-FeO_x-SiO_2 slag and alkali silicates. This therefore fits best in the category of IPs. Figure 1.1 is not convenient for including the IPs, as Ca or Al are not necessary for their synthesis and other elements, like Fe, can play an important role.

1.3 Research aims and outline

This text is meant to give an extra incentive to valorize a currently underutilized material in cementitious systems, slags with a high Fe content. A range of chemistries often used because of their low liquidus temperature is: $Ca_{0-1}Fe_{1-2}Si_{1-2}O_{3-5}$. These slags are produced as by-product in the non-ferrous metallurgical industry and thus rather have the problem of abundance than shortage in industrialized countries, especially in Belgium. These Fe-rich silicates are not widely investigated in the AAM and IP community and therefore contain a certain amount of unknowns with respect to their molecular structure

and reaction mechanism towards the IP. The goal of this thesis is to understand the structure and mechanisms of the system, as it is important for the further development of this new binder system and to tune its physical, chemical and mechanical properties. Only with detailed knowledge on the synthesized reaction products, their full potential can be reached. This can be translated into concrete examples: the designed synthesis of a well-defined arrangement of the Fe-silicate network to achieve an optimal inherent mechanical strength; the design of a precursor that is prone to dissolution in alkaline media and provides the correct stoichiometry for durable binder phases; the estimation of the life-time of the material in a certain environment (e.g. its stability in seawater). Although these examples are not all tackled here, the text aims to contribute to the necessary knowledge to enable or understand these aspects. The following paragraphs explain the content of the chapters incorporating the author's attempt to increase the understanding of CaO-FeO_x-SiO_2 slag-based IPs.

The literature review in chapter 2 provides an overview of the state-of-the-art. Reference materials are discussed (IPs from Fe-poor precursors), with a focus on the aspects investigated in this thesis. The second section of chapter 2 summarizes the knowledge already present on Fe-rich IPs. The goal is to introduce the reader in the world of IPs, starting from the more simple reference materials before going to systems including Fe. The chapter ends with formulating the research questions that are unanswered after the literature review and that will be tackled in the present thesis.

Chapter 3 presents the first set of new data. The research on the molecular structure is bundled. The first section tries to exploit a widely known technique in cement research, Fourier-transform infrared (FTIR) spectroscopy, to obtain structural information on the IP network. The focus on the role of Fe in the network is introduced in section 3.2. The discussion of a combination of co-author works reveals the oxidation state and coordination number of Fe in the final structure of the IP. The chapter concludes in section 3.3 by providing a more detailed picture on the atomic arrangements of the Fe-rich IP by pair distribution function (PDF) analysis.

The factor time is added in chapter 4. The reaction mechanism is investigated. The transition of the Fe speciation from slag to IP is discussed in section 4.1, mostly focussing on results from ^{57}Fe Mössbauer and FTIR spectroscopy. More detail is provided in section 4.2, where the atomic arrangements of all elements during the first 80 hours of reaction are monitored using X-ray PDF analysis. The final section digs deeper into the origin and consequences of the oxidation reactions.

Equivalent to the "Internet of Things", the last results chapter aims to enable the IP/residue valorisation community to virtually synthesize and test their cementitious materials. It is evident that a huge amount of data is needed to support such software. Section 5.1 thus introduces the idea for the software and the associated database creation. The last section, 5.2, contributes to the functionality this software, as a straightforward methodology for analysing the environmental impact of IPs is proposed and used.

Chapter 2

State-of-the-art

The state of the research in inorganic polymers before the start of the presented PhD work is summarized here. Because of the limited literature on Fe-rich IPs, a discussion on the broader material family of AAMs is performed first. The knowledge on this related system is potentially transferable to the material system under study and it can be a useful basis for comparison, as it is more known in the research community. The second section of this chapter focusses on Fe-rich IPs. An overview is provided on the knowledge that was already present at the start of this PhD.

2.1 Structural and mechanistic insights from related materials: geopolymers and alkali-activated materials

In the family of AAMs, there is a clear distinction between materials starting from an aluminosilicate precursor and a calcium silicate precursor [155]. Aluminosilicate precursors, like metakaolin and class-F fly ash, are mixed with sodium/potassium silicate solutions to obtain geopolymers. The variety of chemistries used to activate calcium silicates, like blast furnace slag (BFS), is larger. BFS is usually more reactive and therefore does not need high alkalinities for its activation. Research into the activation with Na_2CO_3, Na_2SO_4 or K equivalents is rising in importance [41, 15, 163] as this lowers the cost and environmental footprint. However, the section below will focus on alkali silicate activated materials to maintain its relevance to the system studied here.

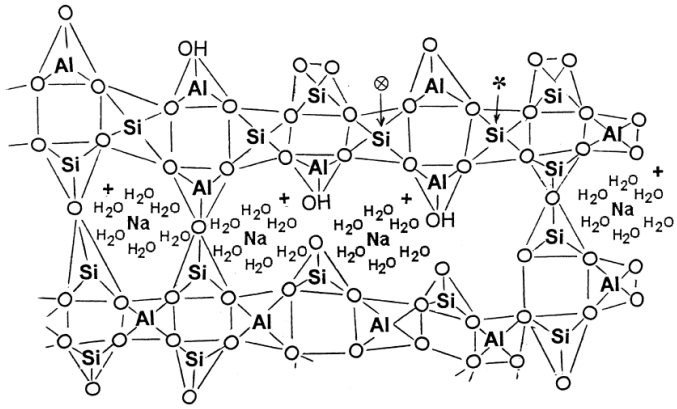

Figure 2.1: Polyhedral representation of geopolymer structure by Barbosa et al. [9]. The cross in the circle and the star pointing at Si atoms refer to the amount of Al next to the Si, 3 and 2 respectively [9], making it $Q^4(3Al)$ and $Q^4(2Al)$ in Engelhardt notation [40]. Note that not all Al is 4-fold coordinated in the figure, although this should be the case in a pure geopolymer according to Davidovits [27].

2.1.1 Aluminosilicates: metakaolin, class-F fly ash

The binder material resulting from aluminosilicate precursors is usually defined as a geopolymer. The molecular structure of this material can be described as a Q^4 polymerized silicate network with aluminum taking place in this network homogeneously distributed in tetrahedral coordination, without Al-O-Al linkages (i.e. Al tetrahedra are always surrounded by Si tetrahedra) [27, 159]. An alkali atom resides in a nano-pore next to the aluminum to provide the charge balance (Al^{3+} surrounded by 4 bridging O^{2-} results in -1). This structure is drawn using a polyhedral representation by Barbosa et al. [9], shown in Figure 2.1. Recent studies provide a more detailed and quantitative view on the structure using pair distribution function (PDF) analyses and theoretical modeling (mainly density functional theory and molecular dynamics). A PDF, derived by Fourier transformation of neutron or synchrotron X-ray scattering, shows the distances between the different atoms in the structure and as such can also confirm the arrangements of the structural units with respect to each other. White et al. [203] performed this for sodium silicate/hydroxide activated samples, confirming the plausability of the structure in Figure 2.1. Bell et al. [11, 12] showed that similar structures are formed when using potassium or caesium-based activators. Like all cementitious systems, the geopolymer has a structurally interesting composition at different length scales. The mesoscale is usually described using the distribution and shape of the pores in the material.

These can be directly observed using Scanning Electron Microscopy (SEM) or Transmission Electron Microscopy (TEM) or can be quantitatively derived from small-angle scattering (X-ray or neutron) or adsorption techniques (nitrogen or mercury) [111, 179, 180, 116]. The classification of mesopore sizes in cements (capillary pores > 10 nm, gel pores < 10 nm) is inconvenient for the description of geopolymers, as the presence of gel pores larger than 10 nm is commonly observed for Na-hydroxide/silicate activated samples. The gel pores are largely controlled by the size of the hydration spheres of alkali atoms, which is approximately 13 and 7 nm for Na and K respectively [180]. These pores have a bottle shape [180] with a hierarchical build up that can be described using a fractal [169, 116].

To obtain the geopolymer structure an aluminosilicate source is mixed with an alkali-silicate solution. This mixture undergoes the stages shown in Figure 2.2. The dissolution of the precursor by alkaline hydrolysis results in the liberation of (alumino)silicate species [154, 161]. These reactions are controlled by the structure of the precursor and the alkalinity of the activating solution. For metakaolinite it is known that the presence of five-fold coordinated Al, ^{V}Al, lies at the origin of its reactivity, as it is a thermodynamically unfavorable component and is therefore easily dissolved in the alkaline solution [29]. The temperature and time of calcination, determining the concentration of this

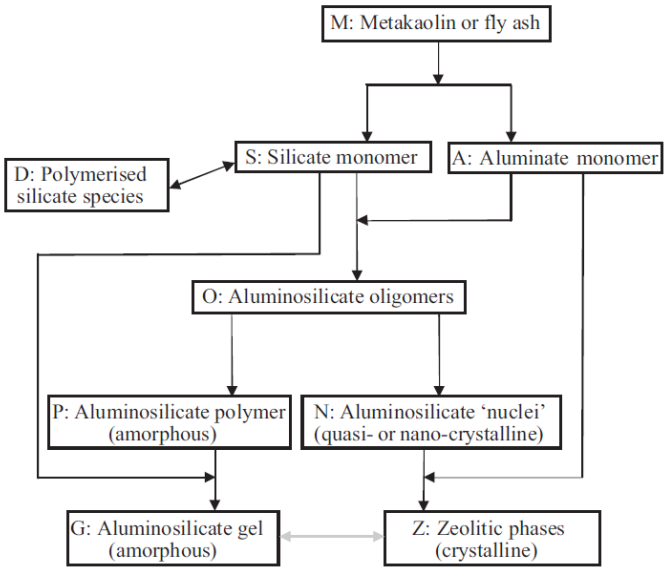

Figure 2.2: Schematic of the reaction stages in the formation of a geopolymer [154].

component, is therefore an important factor determining the reactivity of metakaolin [162, 221, 146]. Additionally, the presence of impurities reduces the amount of reactive metakaolinite and therefore the reactivity of the metakaolin. As the dissolution reactions are due to alkaline hydrolysis, the pH of the activating solution is important. A higher pH results in elevated dissolution kinetics [158, 52]. The kinetics of dissolution were shown to control the overall reaction kinetics when dealing with "larger" particles (for metakaolinite, BET $<$ 12 m^2/g) [157], which is practically always the case. Additionally, the dissolution rate of the alumina from the precursor was seen to control the microstructure of the reaction product [65], with a more homogeneous structure with relatively faster alumina releasing precursors.

The dissolved monomers rearrange themselves and increase in polymerization degree by polycondensation, i.e. by combining 2 silanol (Si-O-H) groups into a Si-O-Si linkage and a water molecule [160, 27, 161, 155]. The polymer network is built up further by these polycondensation reactions striving to the maximum connectivity, 4 [159, 9, 27]. In some cases, when using activating solutions with sodium as alkali and a low SiO_2/Na_2O molar ratio, the precipitation of zeolitic phases is observed instead of the gradual polymerization reactions [27, 154]. Using a combination of density functional theory and coarse-grained Monte Carlo calculations, the mesoscale details of these reactions were also revealed [213]. This is described as the precipitation and growth of clusters. The growth of the clusters follows the same pattern as Ostwald ripening [213]. As discussed in the previous paragraph, the kinetics of the system are largely determined by the dissolution kinetics. Taking control of the polymerization kinetics should thus not be considered if you want to control the overall reaction kinetics.

With metakaolinite as a precursor, the overall reaction can be written as follows [159, 161]:

$$(R_2O)(SiO_2)_s(H_2O)_x + (Al_2O_3)(SiO_2)_2(H_2O)_{0.05} \longrightarrow (R_2O)(Al_2O_3)(SiO_2)_y(H_2O)_z$$

In this reaction, R refers to the alkali atom (Na, K, Cs), s and x indicate the composition of the activating solution which results in the geopolymer with composition indicated with the y and z factors. According to professor Kriven and her research group at Illinois at Urbana-Champaign the stoichiometry is fixed, with y and z equal to 4 and 11 respectively [11, 37, 173]. Other results show a consistently shifting NMR signal when altering the Si/Al ratio (without splitting or broadening, indicating no phase separation [158] and making it more likely that there is a variable Si/Al ratio possible for the geopolymer structure.

Starting from (low-Ca) fly ash as precursor, the basic mechanisms and the molecular structure are the same. Two differences can be observed: (i) fly ash never reaches complete conversion to geopolymer and (ii) the composition and mineralogy of the precursor is more variable, resulting also in more variation on the composition of the geopolymer product. The inability of fly ash to react 100% in the alkaline solution originates from its mineralogy. Apart from the reactive glass phase, crystalline phases are present, which do not readily dissolve in alkalis [127, 93]. The variation in the composition of fly ash is inherently linked with the variation in the feed material used in different incinerators at different locations or different times.

2.1.2 Calcium (alumino)silicates: blast furnace slag

Despite their possible use in blended cements, calcium-aluminosilicate materials are also investigated for the synthesis of inorganic polymers. The reason for this is the potential increased mechanical performance, low CO_2 emissions for production, increased resistance against certain chemical attacks, or just because of the hype of geopolymerization [155]. Research almost exclusively considers slag from the blast furnace in iron production [155], as this is the most abundant and most well-known slag for civil engineers.

The similarity of the molecular structure of the material to common OPC has encouraged the use of cement nomenclature in the research community working on this system. This nomenclature abbreviates the elements in the structure with 1 letter: Ca = C, Si = S, Al = A, Na = N. Hydrated phases are ended with an H. As such, the binding phase of OPC, calcium silicate hydrate is denoted C-S-H. The molecular structure of the calcium-aluminosilicate inorganic polymers is often referred to as a C-A-S-H. The arrangement of the atoms, shown in Figure 2.3, is in short range order more similar to C-S-H than the geopolymer. In fact, the local arrangements (< 8 Å) are almost identical to C-S-H, depending on the Ca/Si ratio [202]. The difference with C-S-H lies in the difference in ordering. Where OPC shows nano-crystallinity, the alkali-activated slag shows only ordering up to 15 Å [202]. The silicate network has a lower degree of polymerization (DOP) with respect to geopolymers, it is rather chain-like ("Dreierketten silicate chains"). Al can substitute Si in the network when Na provides the charge balance to make Al a network former. Ca resides in between the silicate layers, in CaO layers or in the interlayer region, similar to its function in C-S-H or tobermorite, the crystalline equivalent for C-S-H [177, 216]. The alkali atoms reside in the interlayer [152].

The differences in final structure are not extrapolated to the mechanism of

the formation, as this is considered to be similar as that of aluminosilicates. Also here, the dissolution breaks down the precursor structure to the level of (calcium/alumino)silicate species. These silicate species rearrange before the nucleation of a "gel" is observed [153]. This considers the polycondensation of a C-A-S-H network, the structure described in the previous paragraph and Figure 2.3. This network nucleates throughout the pregnant solution [204], this can happen homogeneously [204] or heterogeneously at the surface of nano-particles [214]. The presence of a high amount of magnesium (> 5 wt% [58]) can incite the formation of Layered Double Hydroxide (LDH) phases as secondary reaction product [197, 13, 58]. The similarity of the reaction product with OPC based system renders the surface chemistry the same, making this system more friendly towards conventional admixtures such as superplasticizers [155].

2.2 Fe-rich inorganic polymers

The idea of using Fe-rich materials as a precursor in the synthesis of inorganic polymers developed more recently. The incorporation of these precursors touches a new vast source of raw materials for cementitious binders, as numerous clays, minerals or industrial residues exhibit a Fe content which is not sufficient for steel production, but sufficiently high for Fe to play a role in the behavior as cementitious binder. Earliest trials are reported by Komnitsas et al. [89] (2007), Panias et al. [142, 112] (2007, 2009), Kamseu et al. [82] (2009) and Bell and Kriven [10] (2010). Compressive strengths comparable with OPC have been reported later, 20-90 MPa [108, 92, 78]. As the system has not seen the intensive research of its (calcium-)aluminosilicate counterpart, numerous unknowns are present. The understanding of the basic principles is less detailed and a discussion of the system is still absent in mainstream review literature [152, 151, 103].

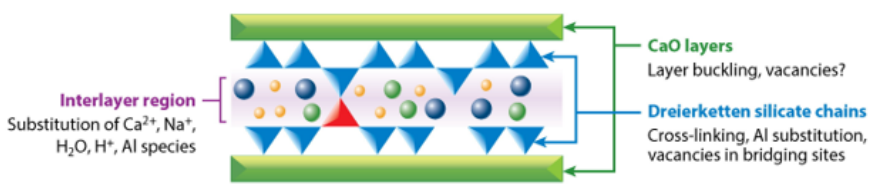

Figure 2.3: Representation as tobermorite-like structure of C-A-S-H polymer by Provis and Bernal [152]. The triangles represent tetrahedral sites (blue for Si, red for Al), the circles are interlayer species (colors not specified by the authors).

2.2.1 Overview of resources

The Fe-rich precursors can originate from different sources, which can be generally classified (Figure 2.4) as soils [132, 100, 85], volcanic ashes [82, 101, 98], waste incinerator ashes [108, 92, 23, 97, 96] and metallurgical residues [150, 78, 139, 89, 90, 81, 2, 94]. The clayey fraction of soils has been investigated extensively for its application in cements, of which kaolin clay is the best example. Some of these clays contain relatively high amounts of Fe, mostly in the form of hematite (Fe_2O_3) or goethite ($FeO(OH)$) [132, 85]. As these clays are always calcined before use in geopolymers, the Fe in the precursor is present as hematite. Its limited solubility in alkaline media leads to the Fe in these clays not participating in the reactions. Metakaolinite is still the phase contributing to geopolymerization and thus these materials follow the same laws as described in section 2.1.1. The presence of Fe however does influence the structure of the kaolinite in the clay. The contact of kaolinite with a Fe^{3+}-rich solution, substitutes Al^{3+} from kaolinite with Fe^{3+}, increasing the disorder of the phase. The required calcination temperature of Fe-rich soils can therefore be decreased (towards 500 °C) [85].

The Fe in volcanic ashes can participate in the dissolution and polymerization reactions [102] delivering other products than aluminosilicate geopolymers [98]. The present Fe-bearing minerals are dependent on the region and can vary from a combination of augite and forsterite [102] to olivines and pyroxenes [104]. The participation of Fe in the reaction is significant, but low, rendering the characterization of newly developed phase and the role of Fe herein complex. On the other hand, significant indications are present to state the oxidation state of the Fe in the final product to be III. A compressive strength of 55 MPa was achieved [101] and a thermal stability up to 800 °C is observed.

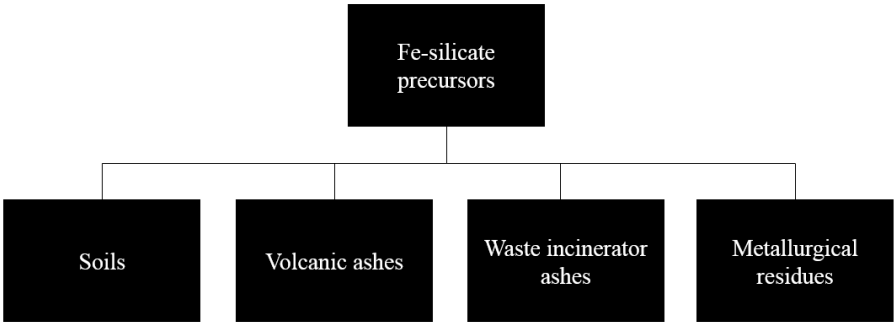

Figure 2.4: Overview of Fe-rich resources for the synthesis of inorganic polymers.

The concept of landfill mining has been introduced throughout Europe, giving rise to a new potential source of Fe-containing precursors: the bottom ashes resulting from the incineration of (household) waste. Depending on the incinerator conditions, the obtained residue can be an ash (conventional burning) or a slag (plasma incineration technology). In the plasma incineration process the organic fraction of the waste is converted to syngas by the high temperatures in the plasma. The inorganic fraction is present as a metal and slag phase. Whereas the ash has not been proven to exhibit good performance in cementitious materials [23, 97, 96], the slag has been successfully applied in inorganic polymers [108, 92]. Being an Fe-rich glass after water quenching, the slag from plasma incineration of household waste is similar to slag from high temperature non-ferrous metallurgy. As such, also non-ferrous slag shows good behavior in inorganic polymers. Slags from Fe-Ni [89, 112, 172], copper [137, 78] and lead [139] production have shown to achieve decent properties after mixing with alkalis. This is not directly the case for hydrometallurgical residues, because their mineralogy is less favorable for dissolution in alkalis. However, these can be treated to increase their reactivity [70] or often they are valorized using an integrated flow sheet from which a more reactive slag will result, e.g. the valorization of Al and Na from bauxite residue, while also delivering a reactive slag for inorganic polymers [71]. The characteristics of a "reactive" slag are discussed in section 2.2.2, discussing in detail inorganic polymers from Fe-rich slags.

2.2.2 Inorganic polymers from pyrometallurgical slags

Of the different Fe-rich precursors, pyrometallurgical slags (or other residues that underwent heat treatments) seem most promising for IP synthesis. More research has therefore been performed on these materials, enabling a more detailed discussion.

Crystalline Fe-silicate phases dissolve slowly in alkaline media. Figure 2.5 shows for instance the remainder of a semi-amorphous slag after leaching in NaOH, where fayalite seems untouched [78]. The amount of amorphous fraction is therefore an important characteristic of the slag [150]. This can be increased by increasing the cooling speed [150], but a comparison of slags cooled similarly, e.g. from [92] and [78], shows that also the chemical composition plays a role in the fraction of amorphous phase due to the glass forming ability of the melt. A silicate melt with a higher viscosity or configurational entropy will show more resistance to crystallization and therefore produce easier a glassy material, i.e. it will need a lower cooling rate for obtaining the same amount of amorphous fraction [126]. Also kinetic effects are important. A general term to describe

the ease of glass formation is the strong-fragile liquids theory [195, 130, 3]. The temperature dependence of the relaxation time (τ) near the glass transition temperature (T_g) of strong glass formers approximate an Arrhenius relation, while longer relaxation times define fragile glass formers [21], as illustrated in Figure 2.6. The fragility of a melt is quantified by the fragility index, m

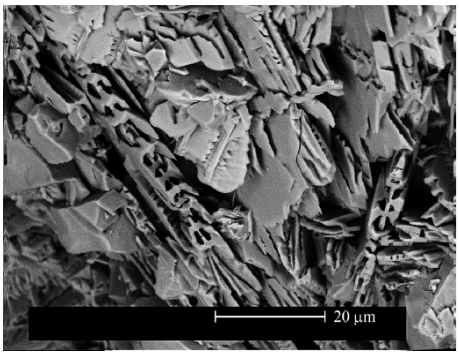

Figure 2.5: Fayalite-containing semi-amorphous slag after leaching in NaOH [78].

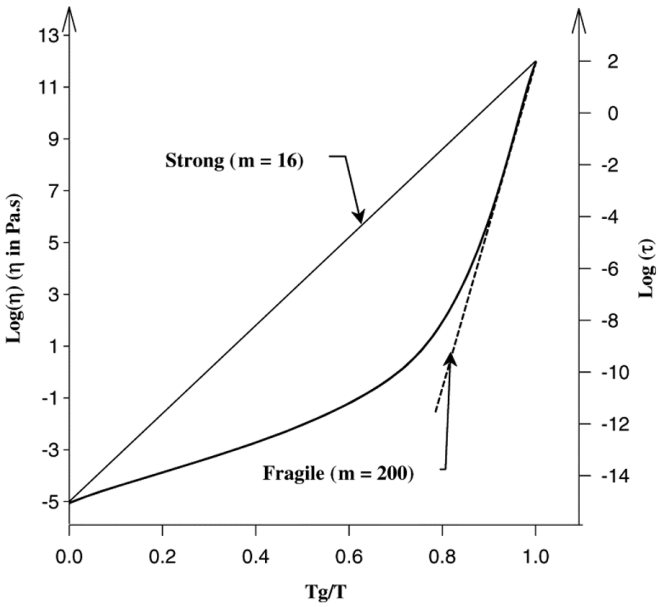

Figure 2.6: Example temperature dependence of a strong and fragile liquid near the glass transition temperature [21].

[21, 130]:

$$m = \frac{dlog_{10}(\tau)}{d(T_g/T)_{T=Tg}}$$

A quantitative relationship between chemical composition and glass formation for Fe-silicate melts/glasses in the compositional range presented in this thesis is not found in literature.

Apart from the glass, also the composition of the activator and the ratio between the activator and the slag are important to control the kinetics and resulting mechanical properties. The latter follows the same general rules as cements. Sufficient liquid should be added to obtain a workable mixture and provide sufficient alkalinity to dissolve the amount of slag needed for making a continuous binder phase [108, 155]. Too much liquid on the other hand causes low compressive strength, high levels of shrinkage, particle settling, bleeding of the activating solution and carbonation of excess sodium [108, 155]. The optimal solution/slag mass ratio for a slag with fineness similar to the work of Machiels et al. without admixtures is 0.45 [108]. In practice, 0.45 is rather an upper limit. In the composition of the activating solution an optimum is observed for achieving reasonable setting kinetics (> 1 hour) and compressive strengths (> 50 MPa). This can be achieved with activators with molar ratios about SiO_2/Na_2O = 1-2 and H_2O/Na_2O = 13-25 (with a high solution/slag mass ratio = 0.58) [137, 92].

The molecular structure and reaction mechanism of inorganic polymers from Fe-rich slags is unclear. The glassy nature of the precursor and reaction products [78, 108] compromises the usefulness of conventional X-ray diffraction. The presence of a high amount of Fe causes the inability of using nuclear magnetic resonance, a technique often used in cement and geopolymer science to gain insight in the aluminosilicate network. Other techniques like ^{57}Fe Mössbauer spectroscopy suggest the presence of Fe^{3+} in the inorganic polymer binder from volcanic ashes, on average in 5-fold coordination or 4-fold with a distorted environment [102]. The results were not definite because of a limited reaction extent and the unusual/uncertain coordination number. The use of (in situ) Fourier transformed infrared spectroscopy did not result in the addition of fundamental information on the reaction mechanism [137, 92].

2.2.3 Characterization techniques

Obtaining fundamental knowledge requires advanced characterization techniques. The selection of the appropriate technique for the posed research question is

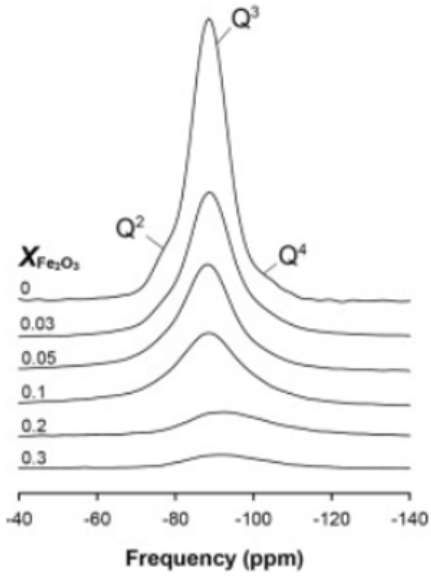

Figure 2.7: Si NMR spectra of silicate glasses including variable amount of Fe_2O_3 [87].

thus an essential aspect in the quest for achieving the goals of chapter 1.3. The main novelty and complexity of the Fe-rich IPs is the high Fe content. In cement or geopolymer science, the small amount of Fe present in fly ash or blast furnace slag is assumed to be inert (Fe is in these materials usually present as hematite). Characterization techniques dedicated to determining the configuration of Fe are thus not common in cement/geopolymer chemistry labs. The most suited technique for determining the short-range order in cementitious materials, nuclear magnetic resonance, cannot be used with high amounts of Fe. Even when trying to determine the configuration of Si or O, the magnetic properties of Fe deteriorates the signal, drastically increasing the uncertainty of the measurement [87]. A Si NMR measurement on glasses with different Fe content is shown in Figure 2.7 (X_{Fe2O3} = mass fraction of Fe).

The first focus is to find characterization techniques that can determine the configuration (oxidation state, coordination number) of Fe in a silicate network. The methods that were identified from literature and will be briefly discussed are: UV-visible spectroscopy, temperature programmed reduction (TPR), electron paramagnetic resonance (EPR) and X-ray absorption near-edge spectroscopy (XANES)/extended X-ray absorption fine-structure (EXAFS). A more detailed

discussion is provided on the techniques that are used throughout this thesis. These are Mössbauer spectroscopy and pair distribution function (PDF) analysis.

UV-visible spectroscopy enables the investigation of the molecular structure, by measuring the absorption of the material in the spectrum of UV and visible wavelengths. Thereby, vibrational natural frequencies of the elemental configurations of the material are detected. Practically, the iron configuration is investigated by this technique, as the energies associated with the outer shell electrons and d-bands are associated with UV-vis frequencies [17, 46, 84]. Oxidation states and coordination numbers of Fe have been investigated by this technique in clays [84], silicate catalysts [17, 46], glassy slags [131] and natural occuring glasses [32].

Quantification of different oxidation states of iron has been done using TPR. In this technique, a reducing H_2 atmosphere is created and sustained, while the sample is heated. Depending on the structure, the reduction of the material occurs at different temperatures. Measuring the H_2 consumption enables the quantification of the Fe^{2+} content [17].

In EPR the unpaired electrons of transition metals can be investigated, because of the separation of their energies in parallel and antiparallel spin states under the influence of a magnetic field. This can be used to study the coordination of radicals or transition metals in a material. Relevant to this thesis, the state of the outer electrons of the iron ion can be investigated [14], which is related to the structure.

With the help of a synchrotron, XANES or EXAFS can be performed. The absorption of X-rays in an energy range near and at the absorption edge of a selected element is measured, for Fe this is for instance approximately 7120 eV. XANES considers the shape of the absorption edge and possible pre-edge features. In case of Fe, a pre-edge peak is present which can be used to determine the oxidation state and coordination number. The oscillating features at energies higher than the absorption edge are exploited in EXAFS. After a normalization and baseline correction the data can be Fourier transformed to render a radial distribution function, i.e. a distribution of elements near the selected element. X-ray absorption techniques have been elaborately used already in Fe-bearing silicate glasses [54, 88, 5, 168], minerals [209] and Fe-doped catalysts [17].

Two techniques that will be elaborately used in the results sections of this thesis are discussed in more detail: ^{57}Fe Mössbauer spectroscopy and Pair Distribution Function (PDF) analysis. A brief illustration of the use of these methods in similar materials is provided. The basic principles are explained,

mainly regarding the physics behind the techniques. Each section will conclude with suggesting how to examine and interpret the data resulting from the respective experiments.

^{57}Fe Mössbauer spectroscopy

^{57}Fe Mössbauer spectroscopy has been extensively used in mineralogy and glass science to probe the configuration of Fe in the network [19, 125, 126, 24]. In glasses, where the use of X-ray diffraction is limited for structural analysis, the knowledge on the environment of the Fe delivers detailed knowledge on the atomic arrangements in the glass network [125, 126]. In crystalline materials which exhibit complex or hard interpretable diffractograms, Mössbauer spectroscopy can also be a useful addition for a detailed analysis of the structure of Fe-bearing minerals [19, 22]. In Fe-containing inorganic polymers, it has been used once before [102]. Every Mössbauer spectroscopy measurement mentioned above was performed on powders, although measurements on frozen liquids are also possible [175, 91, 80]. The first measurements on cementitious pastes before and after hardening will be presented in this thesis in chapter 4.1. The most famous Mössbauer spectrometer is on board of the Mars Rover [22], where the technique is used for characterizing the Fe-rich clays which make up a large part of the red planet's surface.

The following discussion is based on the book of Coey (edited by Long) [24], unless mentioned otherwise.

The ^{57}Fe isotope shows the Mössbauer effect (recoilless absorption/emission) for gamma radiation at 14.41 keV, usually generated by the decay of ^{57}Co, enabling the determination of changes in the core energy levels. Such a transition from the core ground state to an excited energy level is illustrated in Figure 2.8. The energy levels of the nucleus are influenced by its surroundings and this influence are divided in three types: isomer shift, quadrupole splitting and magnetic splitting. The isomer shift is directly related to the electron density in the nucleus. More exact, the isomer shift is quantified with the following equation:

$$\delta = const(\mid \phi_{ns}(0) \mid^2_{std} - \mid \phi_{ns}(0) \mid^2_{abs})\frac{\delta R}{R}$$

Here, δR/R is the relative radius of the exited core with respect to the ground state. For Fe, the exited state has a decreased size, δR/R is negative. The isomer shift thus increases with a decrease of the term $\mid \phi_{ns}(0) \mid^2_{std} - (\mid \phi_{ns}(0) \mid^2_{abs}$. This term consists of the probabilities of having an electron in the core of the atom,

in the absorber, $\mid \phi_{ns}(0) \mid^2_{abs}$, and in a calibration standard, $\mid \phi_{ns}(0) \mid^2_{std}$. The latter is constant for a certain isotope, so the isomer shift is directly linked with the probability of an electron being in the nucleus of the absorber, i.e. of the sample under study. It can be expected from this background that Fe^{2+} and Fe^{3+} show different values for the isomer shift. Going from 2+ to 3+, a d electron is lost. As d electrons do not have a probability of being at the nucleus, there is no direct impact. However, because of the screening effect, the charge of the nucleus is less shielded and attracts the other electrons more, including the s electrons, which have a non-zero probability in the nucleus. The isomer shift is thus lowered, because of the negative δR/R.

When the azimuthal quantum number, l, can have more than 1 value (e.g. 1/2 and 3/2), the energy levels of the excited state of the nucleus can split. This is called the quadrupole splitting. This occurs when the electronic environment of the nucleus is not symmetric. This asymmetry can be caused by the asymmetric filling of the spin states or by an asymmetry of the surrounding species. The former is explained here for the case of high spin Fe^{2+} and Fe^{3+}. The filling of the electrons (Fe^{3+} has 5 d electrons, Fe^{2+} has 6) is shown in Figure 2.9. Symmetry is observed for the high spin Fe^{3+} and as a consequence the electrons will not contribute to the quadrupole splitting. On the contrary, the high spin Fe^{2+} has an asymmetric filling of the spin states. For this reason, high quadrupole splits are observed in Fe^{2+}. The second contribution to the quadrupole splitting results

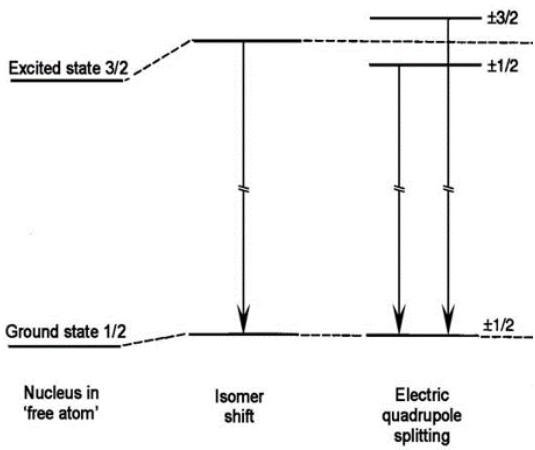

Figure 2.8: Energy levels of a nucleus and their change under influence of the electron cloud, explaining the isomer shift and quadrupole split.

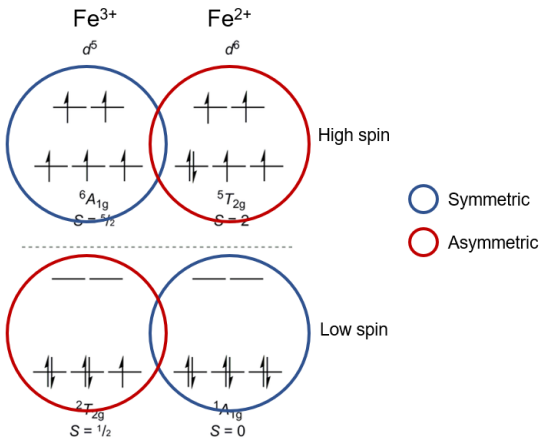

Figure 2.9: Filling of the spin states in high spin Fe^{2+} and Fe^{3+}.

from an asymmetry in the environment of the Fe atom, in the surrounding species. Regular tetrahedra or octahedra are symmetric. When all the surrounding species are the same, this would thus result in zero contribution to the quadrupole splitting. However, when the polyhedra are distorted or the surrounding species are irregular, for instance a combination of bridging or non-bridging oxygen in a silicate network, quadruple splitting is observed.

If the studied sample exhibits (para- or ferro-)magnetic properties, magnetic splitting occurs; this is also known as hyperfine splitting. The degeneracy of the electrons with different magnetic quantum numbers is lifted under the influence of the internal (or an applied external) magnetic field: a sextet is observed in the spectrum.

A Mössbauer spectrum is shown in Figure 2.10. Typical for silicate glasses, a combination of several doublets is shown. The isomer shift and quadrupole splitting of the different contributions can be determined using least square minimization programs, such as IMSG [34], where the fitting of the experimental spectrum can be performed. Apart from the Mössbauer parameters, also the absorption area, the area underneath the fitted spectra, is determined. This area is related to the relative abundance of the species. For glasses at room temperature, this corresponds well to the molar percentage of the species; at 77K, Fe^{3+} contributions are often overestimated with 5% (relative error) or less [125]. A relative error of 5% usually lies within the error margin: also for a combination of Fe^{2+} and Fe^{3+} the absorption area and mole percentage of the

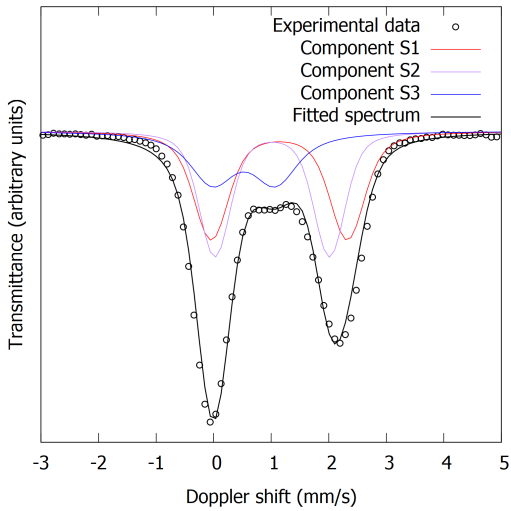

Figure 2.10: Example Mössbauer spectrum, showing a characteristic combination of doublets.

species is approximately equal.

Pair distribution function analysis

The techniques discussed above focus on Fe, but some advanced techniques can study the silicate network incorporating Fe as a whole. Pair distribution function (PDF) analysis, resulting from the Fourier-transformation of X-ray or neutron scattering experiments, can reveal the atomic distances within the sample, thereby revealing essential information on the molecular structure. In cementitious materials this has been used to reveal the structure of (Fe-)silicate glasses [4, 200], C-S-H [117] and alkali-activated materials [11, 202], as well as to reveal details on the formation mechanism of alkali-activated materials [203, 122, 50].

The discussion in the following section is based on Egami and Billinge [39] unless mentioned otherwise.

To enable PDF analysis a function in real space with sufficient resolution and limited rippling is needed. As a consequence, the scattering experiment needs to have a wide momentum transfer (Q) range and limited noise. For the derivation of the PDF from X-ray scattering, theoretically, the Q-range is

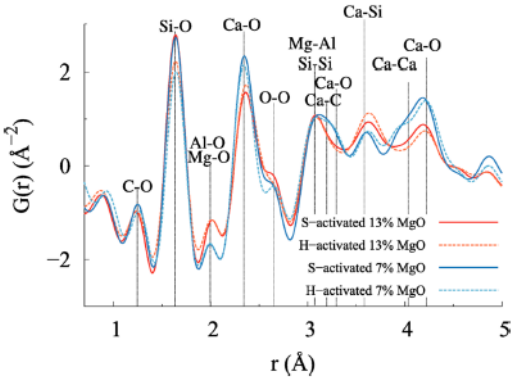

Figure 2.11: PDF of alkali-activated blast furnace slag and its carbonated equivalent [122].

sufficiently large when using a silver radiation source (or heavier), while the noise can be limited by slowing down the scan. Practically however, X-ray PDFs will always be derived from synchrotron radiation sources, as higher quality can be obtained with faster acquisition rates than regular XRD scans (own experiments at Argonne National Lab had a duration of 2-3 minutes), enabling also in-situ measurements. The basic principles for obtaining good quality neutron PDFs are similar, but the equipment is different. Dedicated beamlines at neutron scattering facilities, usually equipped with 3He detectors or recently rather scintillation counters because of the increasing price of 3He, can deliver high quality diffractograms which can be transformed to real space.

An example of a PDF from X-ray scattering is provided in Figure 2.11, on which the atomic distances are mentioned. The indications of the atomic correlations are not automatically received from the experiment. Literature review and knowledge on the chemical composition of the material should provide insight in the potential correlations. Preferentially, the PDF study is combined with theoretical modelling techniques (or calculations from literature), to provide a suggestion of where the correlations should be according to the laws of physics [206]. Usually, the determination of the correlations corresponding to the first neighbors is not complicated, e.g. Si-O, Ca-O on Figure 2.11, but the number of possibilities and therefore complexity rises when going to larger distances (larger r). Additionally, some elements do not have a fixed oxidation state or coordination number, bringing extra variation in the potential distances and therefore extra complexity to the analysis of the PDF. The most abundant example is Fe, which in silicate glasses can be in the Fe^{2+} and Fe^{3+} state, which can have coordination numbers 4-6.

2.3 Formulation of research questions

Fe-rich inorganic polymers seem an interesting engineering material, but their is a lack in fundamental knowledge on the system which is essential for a scientific and technological breakthrough. Chapter 3 and 4 of the present thesis therefore focus on the molecular structure and how this structure is formed. The doors to a wider parametric knowledge are opened by the design of a software (chapter 5), enabling the collection of a database and providing easy daily tools to make the research(er) more efficient.

The specific research questions that are tackled in these chapters are:

Molecular structure (chapter 3)

- What is the connectivity of the silicate network in Fe-rich IP?
- What is the oxidation state and coordination number of Fe in the binder?
- What is the role of Fe in the structure?
- What is the function of minor elements in the binder structure (Ca, Na, K)?
- How can the molecular structure be tweaked?

Mechanism and kinetics (chapter 4)

- Chapter 3 shows that Fe is in the 3+ oxidation state in the IP, whereas in the slag it is Fe^{2+}. When does Fe^{2+} oxidize to Fe^{3+}?
- What are the different reaction stages?
- How does the molecular structure evolve from slag to binder?
- What oxidizes the Fe^{2+} to Fe^{3+}?
- Does the availability of oxygen play a role in the kinetics of binder formation?

Parametric study - internet of IP (chapter 5)

- Can the transition of tonnes of data to the community be simplified - can an equivalent to the *internet of things* be set up for making virtual IP and test their properties?

- How can this new binder material be environmentally assessed in a simple way?

Chapter 3

Molecular structure of (CaO-)FeO_x-SiO_2 inorganic polymers

3.1 The use of ATR-FTIR spectroscopy in the analysis of iron-silicate inorganic polymers

This section is based on the published proceeding paper:
A. Peys, L. Arnout, T. Hertel, R.I. Iacobescu, S. Onisei, L. Kriskova, H. Rahier, B. Blanpain, Y. Pontikes, "The use of ATR-FTIR spectroscopy in the analysis of iron-silicate inorganic polymers", *Proceedings of the 5th International Slag Valorisation Symposium* p385-388, April 2017, Leuven, Belgium.

The text contains slight adjustments compared to the original publication to incorporate new insights.

Contributions of the authors:
The paper considers the collection of infrared spectroscopy data from within the whole research group. The A. Peys performed the analyses and formulated the conclusions. The co-authors provided data and helped in the discussion of the results.

3.1.1 Introduction

Fourier transform infrared (FTIR) spectroscopy has seen intensive use in the structural analysis of silicates. Especially when the material is amorphous/glassy, disabling the applicability of conventional X-ray diffraction, the information gained from FTIR spectroscopy is highly important. FTIR spectroscopy has been crucial for the analysis of silicate glasses [51], cementitious binders [141] and inorganic polymers [155, 165]. The spectra can be coupled to the connectivity of the silicate network, the participation of Al in this network [51, 141] and the formation or transformation of phases can be observed for cements and inorganic polymers [141, 165].

A glass of pure SiO_2 shows only 3 bands in the FTIR spectrum, associated with 3 kinds of vibrations: stretching vibrations ($\pm$ 1100 cm^{-1}) and two modes of bending vibrations, out-of-plane bending ($\pm$ 500 cm^{-1}), commonly referred to as "rocking", and in-plane bending ($\pm$ 800 cm^{-1}), commonly just referred to as "bending" [51]. In aluminosilicate IPs, "geopolymers", the evolution of the spectrum when adding the alkaline activator to metakaolin is mainly seen as a shift of the stretching band to lower wavenumbers [165, 161]. Other features tend to appear, which can be associated to water in the IP system (bands at $\pm$ 3600 cm^{-1} and $\pm$ 1650 cm^{-1}) or the formation of carbonates (bands at $\pm$ 1500 cm^{-1} and $\pm$ 850 cm^{-1}) [76].

The present section provides an overview of the ATR-FTIR spectra of iron-silicate slags and inorganic polymers made therefrom. The considered slags are not applied in cementitious applications today: copper slag [137, 78, 136], plasmastone [92, 7], treated bauxite residue (BR) [70]. The overview aims to expose similarities and differences between particular slags, which can increase the understanding of the spectra and ultimately, the structure of the materials under study.

3.1.2 Materials and methods

Slags from different sources are studied in the present section. Slags from copper production typically include a low amount of CaO ($<$ 5 wt%), making it almost a simple Fe-silicate, and even after water quenching a significant amount of crystalline phases are present ($>$ 15 wt%) [137, 78, 136]. The chemical composition of plasmastone is more complex, with increased contents of CaO and Al2O3 ($\sim$ 20 wt%), resulting in a 100% XRD amorphous material after water quenching [92, 108]. Thermally treated red mud, still containing part of the mineralogical complexity of the bauxite residue, is also included in this

Table 3.1: Chemical compositions of the studied precursor materials in wt%.

Name [reference]	FeO	SiO_2	CaO	Al_2O_3	MgO	Others
Copper slag [136]	52	29	1	6	1	11 (9 ZnO)
Plasmastone [92]	20	34	22	12	3	9 (4 Na_2O)
Treated red mud [70]	43	20	10	17	-	10 (6 TiO_2)
Synthetic 1 [190]	49	32	18	1	-	-
Synthetic 2 [190]	59	31	9	1	-	-
Synthetic 3 [190]	39	45	15	1	-	-
Synthetic 4 [190]	49	43	7	1	-	-
Synthetic 5 [190]	50	37	12	1	-	-

study [70]. As reference materials, synthetic slags with variable composition in the CaO-FeO-SiO2 ternary are melted and quenched. The synthesis procedure was first used in Simon et al. [176] and the same slags as in Van De Sande et al. [190] are used here: five slags with varying FeO/CaO and (FeO+CaO)/SiO_2 molar ratios. Inorganic polymers are made by mixing the finely ground slags with sodium silicate activating solutions. More elaborate discussions on the characterization of the slags and synthesis procedures of the inorganic polymers can be found in their respective references in this paragraph, the chemical compositions are given in Table 3.1.

The slags and IPs were investigated by attenuated total reflectance Fourier-transform infrared (ATR-FTIR) spectroscopy. Spectra from powdered samples were acquired on a Bruker Alpha-P with a diamond crystal, from 4000 cm^{-1} to 380 cm^{-1}, at a resolution of 4 cm^{-1} and with at least 32 scans per measurement; the measurements were supported by Opus software.

3.1.3 Results and discussion

Metakaolin [146] is added to the slags as a reference in Figure 3.1. All samples show the Si-O stretching ($\pm$ 850-1050 cm^{-1}) and rocking bands ($\pm$ 400-500 cm^{-1}). The in-plane bending band ($\pm$ 700-800 cm^{-1}) is not clear for every sample, which is commonly observed for silicates with a high content of network modifying elements [51]. The treated BR shows extra bands around 600-700 cm^{-1}, which are attributed to iron oxide phases in this particular residue [70]. The broadness of the bands in the spectra is in agreement with the amount of amorphous/glassy phase in the residues, which follows the trend plasmastone $\approx$ synthetic Fe-Si-Ca-O $>$ fayalite $>$ treated BR. The sharper features in the spectrum of the fayalitic slag correspond to different vibrational modes of crystalline fayalite [74]. The Si-O stretching band decreases in wavenumber when the Si-O bond is strained or increases in length, e.g. by substitution of Si

in the network (with Al/Fe) [165, 69], or the increase in non-bridging oxygens (NBO) [165, 114]. Because of the latter, slags incorporating more network modifying elements have the band at a lower wavenumber. This is especially clear in the synthetic slags which consist purely of Si and network modifying elements Ca and Fe^{2+}. For these slags, a linear relation is observed between the position of the Si-O stretching band and the (FeO+CaO)/SiO_2 ratio, Figure 3.2. The deviations from the linear relation of the industrial slags are associated with the presence of Al. As discussed above, Al drags the Si-O stretching band towards lower wavenumbers because of the larger bond length of Al-O with respect to Si-O.

After the synthesis of the IPs (synthesis conditions in the referred documents) changes in the spectra involved new features, as well as shifts of bands that were already observed in the slags (Figure 3.3). New bands show the presence of water at $\pm$ 1650 cm^{-1} and $\pm$ 3600 cm^{-1} (the latter not shown in Figure 3.3) and carbonates at $\pm$ 1500 cm^{-1} and $\pm$ 870 cm^{-1}. Another band is observed at $\pm$ 1400 cm^{-1}. As this band is also observed for a sample that was not in contact with air before the measurement (Figure 3.3a, cured in closed container), the formation of a carbonate is unlikely. This band might indicate the presence of hydroxyl groups in the material.

The Si-O stretching band shifts to higher wavenumbers from the slag to the inorganic polymer from approximately 900 cm^{-1} to 950 cm^{-1}. The inorganic polymer structure is too complex to follow this simple relation seen in glasses (as

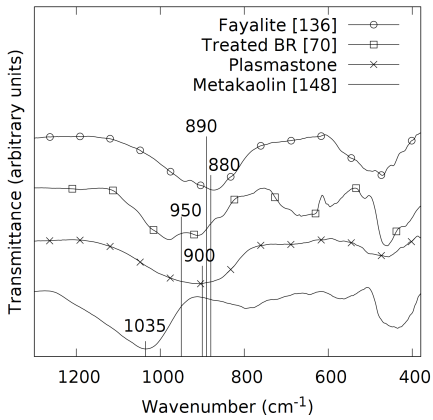

Figure 3.1: Infrared spectra of the studied precursors with indication of the position of the Si-O stretching band.

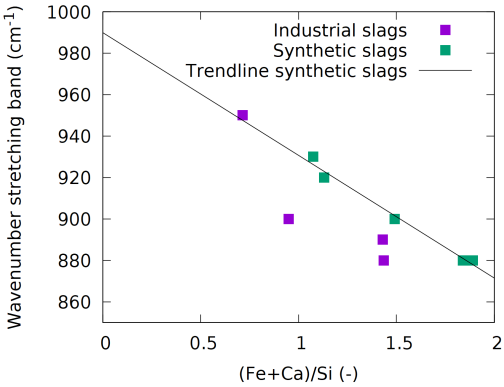

Figure 3.2: The relation between Si-O stretching band position and (Ca+Fe)/Si molar ratio.

will be seen in the continuation of this chapter and the next). The explanation will be found in the papers in chapter 4, and especially section 4.2. The precipitation of trioctahedral 2D clusters of $Fe(OH)_2$ causes an aggregation of the Fe and thus a decrease of the participation of Fe^{2+} as network modifier in the silicate network. The amount of Si-NBO is decreased and Si-O-Si linkages are increased, i.e. the level of connectivity, Q^n of Si increases. Chapter 4.1 will show

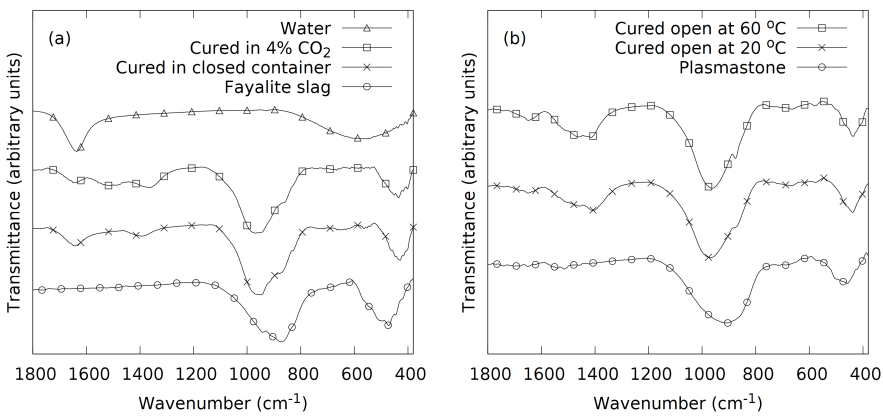

Figure 3.3: Infrared spectra of the fayalite slag (a) [136] and plasmastone (b) [unpublished results] based inorganic polymers. The precursors and the spectrum of a water droplet are added as a reference.

that the rest of the Fe is oxidized to Fe^{3+} and might take place in the silicate framework, charge balanced by Na (or K). The increase of Si-O-Si linkages, together with lowering the amount of network modifiers by incorporating Fe^{3+} in the framework, increases the wavenumber of the Si-O stretching band. From the perspective of pure silica glass, the band is still present at "low" wavenumbers (i.e. < 1200 cm^{-1} of silica glass), because of the Fe^{3+} that is present in the silicate framework, increasing the bond length and mass with respect to Si-O.

Differences in the wavenumber of the Si-O stretching band between different inorganic polymers are observed and can be attributed to three reasons: the extent of dissolution of the slag, the amount of silicate in the activating solution, the chemistry of the precursor. Increasing the amount of dissolution of the slag decreases its contribution in the spectrum. As the Si-O stretching band of the slag is usually at a lower wavenumber than that of the inorganic polymer, the band of the paste shifts towards higher wavenumbers with more dissolution. An increase in silicates in the activating solution can increase the wavenumber by increasing the amount of Si-O-Si linkages (as seen in Onisei et al. [136]). The influence of the slag chemistry on the silicate network and thus FTIR spectrum is less clear, because of the unclear influence of Ca and Al on the configuration of the binder phase.

3.1.4 Conclusions

The derivation of information on the structure of Fe-rich inorganic polymers from Fourier-transform infrared spectroscopy is not straightforward and previous attempts failed to provide a correct explanation of the position of the Si-O stretching band. The knowledge obtained in the following chapters of the present thesis however enables a qualitative reverse engineering of the band. The Si-O stretching band is shifted towards a higher wavenumber with respect to the slag because of (1) the aggregation of Fe^{2+} into layers, increasing Fe-O-Fe and thus Si-O-Si linkages and (2) the incorporation of Fe^{3+} in the silicate framework instead of the former role of Fe^{2+} as network modifier in the slag. The final band position is also controlled by processing parameters, such as the amount of silicates in the activating solution and the chemistry of the precursor slag.

3.2 Oxidation state and coordination number of Fe

This section is a summary of information obtained on the oxidation state and coordination number of Fe in the inorganic polymers and slag precursors in co-authored works.

Information from Mössbauer spectroscopy originates from:
S. Onisei, A. P. Douvalis, A. Malfliet, **A. Peys**, Y. Pontikes (2018), "Inorganic polymers made of fayalite slag: On the microstructure and behavior of Fe", *Journal of the American Ceramic Society* 101 (6), 2245-2257.
S. Onisei, W. Crijns, A. P. Douvalis, C. Siakati, **A. Peys**, Y. Pontikes, "The influence of Ca on the microstructure of Fe-rich slags for use as inorganic polymers", *in preparation.*

The X-ray absorption spectroscopy was measured in the framework of:
S. Simon, G. J. G. Gluth, **A. Peys**, S. Onisei, D. Banerjee, Y. Pontikes (2018), "The fate of iron during the alkali-activation of synthetic (CaO-)FeO_x-SiO_2 slags: An Fe K-edge XANES study", *Journal of the American Ceramic Society* 101 (5), 2107-2118.

Ce titrations were performed and analyzed by L. Arnout:
L. Arnout, **A. Peys**, L. Machiels, P. T. Jones, S. Arnout, E. Nagels, B. Blanpain, Y. Pontikes, "The influence of the iron oxidation state of the precursor in the synthesis of inorganic polymers", *in preparation.*

Contributions of the authors: In all works mentioned, A. Peys was mainly active in the analysis and/or discussion of the more complex experiments which determined the molecular structure of the IP samples.

Table 3.2: Chemical compositions of the studied precursor materials in wt%.

Name [reference]	FeO	SiO_2	CaO	Al_2O_3	MgO	Others
Copper slag [136]	52	29	1	6	1	11 (9 ZnO)
Plasmastone [7]	20	34	22	12	3	9 (4 Na_2O)
Synthetic 1 [176, 135]	72	27	-	1	-	-
Synthetic 2 [176, 135]	62	29	8	1	-	-
Synthetic 3 [176, 135]	48	35	16	1	-	-

3.2.1 Introduction

Research in alternative cementitious materials is booming and in search of new precursors for the synthesis of low-impact construction materials [155, 119]. A vast new pool of resources can be used when the role of Fe in cementitious materials is clarified, such as non-ferrous metallurgy slags, bauxite residue, flotation tailings and volcanic ashes (section 2.2). Several of these precursors have shown to reach promising mechanical properties while their processing conditions do not differ much from conventional precursors for alkali-activation [137, 78, 92, 108, 89, 142, 101]. The role of iron in inorganic polymers from Cameroonian volcanic ashes was studied by Lemougna et al. [102]. A significant proportion of the Fe^{2+} in augite from the ash reacted with the alkali solution to form Fe^{3+} species. The Mössbauer parameters were similar to distorted tetrahedral or five-fold coordinated sites. A limited reaction extent and ambiguous Mössbauer fitting parameters resulted in difficulties to draw straightforward conclusions regarding the role of Fe in the inorganic polymer network.

The precursor slags studied in the present section originate from the copper industry, plasma incineration process or from lab scale synthesis of pure ternary CaO-FeO-SiO_2 slags. The slags and inorganic polymers are investigated using Ce titrations, ^{57}Fe Mössbauer spectroscopy and X-ray absorption near-edge spectroscopy, to reveal details on the oxidation state and coordination number of Fe in the inorganic polymers.

3.2.2 Materials and Methods

The chemical composition of the slags studied in this section is provided in Table 3.2. Details on the synthesis procedure and more thorough characterization can be found in the respective references. Important to note is that although the chemical composition of the slags in Simon et al.[176] and Onisei et al.[135] is the same, they differ in mineralogy and (as will be shown later in this section) average Fe oxidation state. Additionally, the synthesis procedure of the inorganic

polymers was different: mainly, the particle size distribution in Onisei et al.[135] was larger, leading to lower reaction extents.

To perform the Ce titrations the samples were dissolved in a mixture of sulfuric and fluoric acid (4 ml 50 wt% H_2SO_4 + 2 ml 50 wt% HF + 4 ml water). To indicate the oxidation state, ferroine was added (red for Fe^{2+}, pale blue for Fe^{3+}). The dissolved sample with redox indicator was titrated with 0.01 N $Ce(SO_4)_2$. From these titrations, the oxidation state can be determined quantitatively with high accuracy and precision. An absolute error of less than 1 wt% is expected.

^{57}Fe Mössbauer spectra were collected in transmission geometry at 300 and 77 K, using constant acceleration spectrometers equipped with ^{57}Co(Rh) sources kept at room temperature (RT, 300 K), in combination with a liquid N_2 Mössbauer cryostat (Oxford Instruments, Variox 760) for measurements at 77 K. Velocity calibration of the spectrometers was carried out using metallic α-iron at 300 K and the isomer shift (IS) values of the components used to fit the spectra are given relative to this standard. Fitting of the experimental recorded Mössbauer spectra was done using a recently developed least squares minimization program [34]. The oxidation state is quantitative, with an absolute error of approximately 5 wt%. The determination of the coordination number is subject of more interpretation and no number can be assigned to the accuracy.

X-ray absorption spectra of the Fe K-edge were collected at the European Synchrotron Radiation Facility (ESRF; Grenoble, France) on the DUBBLE beamline BM26A. The storage ring operating conditions were 6 GeV electron energy and 150-200 mA electron current. The employed beam size at the sample position was 3 mm x 1 mm. A Si(111) double-crystal monochromator was used for the experiments, which enables a flux of $\sim$ 4x10^{10} photons/s and an energy resolution of DE = 1.87 eV at the Fe K-edge. An iron foil was used to provide an internal energy calibration of the monochromator; the first inflection point of the Fe K-edge was set at 7111.08 eV. The XAS spectra were collected from 150 eV below to 650 eV above the Fe K-edge (6960-7760 eV), with 0.4 eV steps for the edge region (7108-7120 eV). The spectra of all samples were recorded in transmission mode. Normalization of the spectra was done according to the method of Wilke et al. [209] To extract the pre-edge feature in the XANES region, the contribution of the edge jump to the pre-edge was modeled using a second order polynomial function to interpolate the background. The pre-edge feature was fitted with one Gaussian peak, which resulted in normalized height, position (peak centroid), full width at half maximum (FWHM), and integrated area intensity of the peak. The fitting procedure was carried out with the Fityk software.

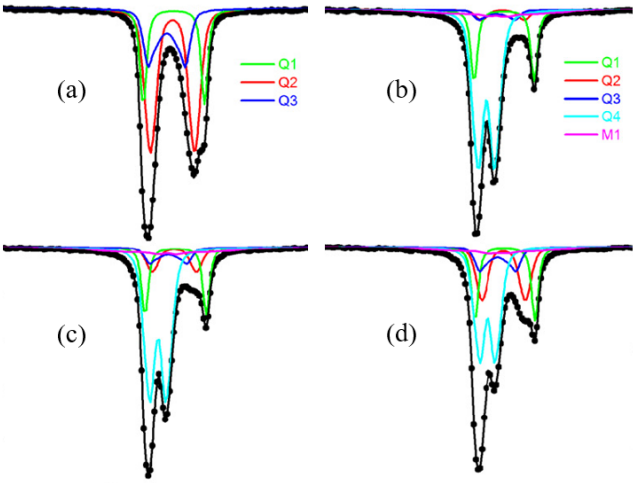

Figure 3.4: Mössbauer spectra of the (a) copper slag and (b-d)resultant inorganic polymers [136] at 300 K.

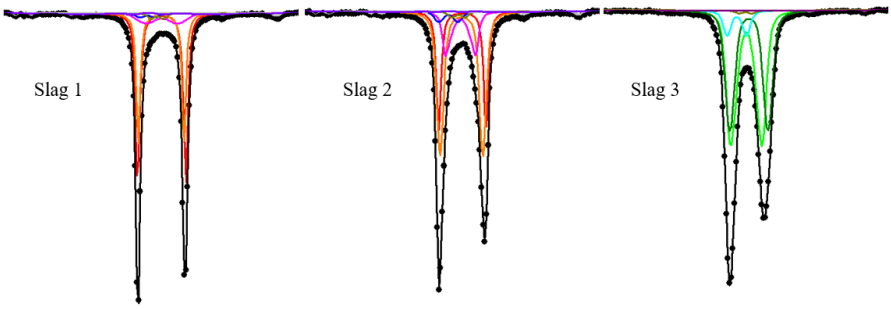

Figure 3.5: Mössbauer spectra of the synthetic slags [135] at 300 K.

3.2.3 Results and discussion

Results

The Ce titrations immediately result in a quantity of Fe^{2+} without a need for interpreting the data. These results are thus immediately transferred to the discussion section. The Mössbauer spectra 300 K are presented in Figure 3.4 and 3.5, including the spectra of the fitted components. The discussion section of this paper uses the relative absorption areas of the Fe^{2+} and Fe^{3+} components

to calculate the $Fe^{3+}/\sum Fe$ ratios of the slags and inorganic polymers. The coordination number is derived from the isomer shift and quadrupole splitting of the fitted components.

A selection of X-ray absorption spectra from Simon et al.[176] are shown in Figure 3.6. The discussion section will use the intensity and position of the pre-edge peak, as described in the methodology section, to calculate the average oxidation state and coordination number.

Discussion: Oxidation state

The oxidation state can be derived quantitatively from titrations, Mössbauer spectroscopy and X-ray absorption near-edge spectroscopy (XANES). The $Fe^{3+}/\sum Fe$ ratio calculated from IPs and their precursors in the different papers is shown in Table 3.3. The main trend is that the $Fe^{3+}/\sum Fe$ ratio is higher for the IP than the slag. Therefore, the IP binder consists of Fe^{3+}, at least partially and in a higher concentration than the slag. In the copper slag samples from Figure 2.8, the only remaining Fe^{2+} states in Figure 2.8b are coming from crystalline Fe-silicate phases, which in the literature study in chapter 2.2 were

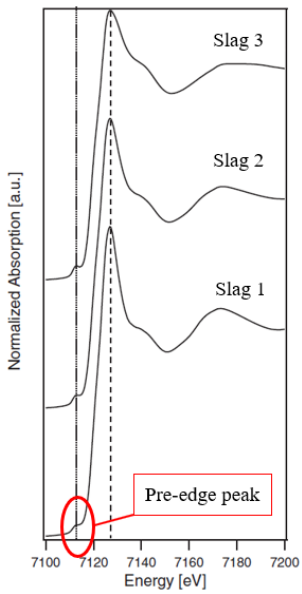

Figure 3.6: X-ray absorption spectra of slags and inorganic polymer.

Table 3.3: $Fe^{3+}/\sum Fe$ ratios in slags and IPs from [7, 136, 135, 176] (the lower precision of the Mössbauer spectroscopy does not allow to show 2 figures after the comma).

Slag name [method]	Slag	IP
Plasmastone [titration]	0.17	0.41
Oxidized plasmastone [titration]	0.72	0.79
Copper slag [Mössbauer]	0.0	0.7
Copper slag [Mössbauer]	0.0	0.6
Copper slag [Mössbauer]	0.0	0.4
Synthetic 1 [Mössbauer]	0.1	0.2
Synthetic 2 [Mössbauer]	0.1	0.2
Synthetic 3 [Mössbauer]	0.1	0.3
Synthetic 1 [XANES]	0.06	0.22
Synthetic 2 [XANES]	0.17	0.61
Synthetic 3 [XANES]	0.28	0.67
Synthetic 3 [XANES]	0.28	0.61
Synthetic 3 [XANES]	0.28	0.72

discussed to react insignificantly in the alkaline solution. As such, the IP binder contains only Fe^{3+}. In other samples, the lower reaction extent causes the presence of remaining amorphous phase from the slag (Figure 2.8b considers IPs synthesized with a highly alkaline solution, molar ratio SiO_2/Na_2O = 0.5). A confirmation that the IP binder contains only Fe^{3+} can be obtained by calculating and comparing the reaction extent (α), from XANES by the equation [176]:

$$\alpha = 1 - \frac{1-(Fe^{3+}/\sum Fe)_{IP}}{1-((Fe^{3+}/\sum Fe)_{slag}}$$

In Mössbauer spectroscopy the extent of reaction is derived directly from the contribution of a newly formed site [136, 135]. For the samples in Table 3.3 the reaction extent thus compromises a range of 40-70%. This extent seems reasonable when comparing with SEM images from similar samples [108, 92, 67]. Therefore, the assumption of the Fe in the binder being completely Fe^{3+} seems also valid from the reaction extent perspective. The reader should know that all samples investigated in the papers relevant to this section were fully cured (> 28 days) and milled (mechanically by a machine). Chapter 4 will provide a more detailed picture of the oxidation state, taking into account changes during the reaction from slag to final milled inorganic polymer. However, for the conditions upheld in the samples in this section, i.e. extensive curing and milling, the Fe in the inorganic polymer binder is observed completely in the Fe^{3+} state.

Table 3.4: Average coordination numbers in slags and IPs from [136, 135, 176]. Mössbauer spectroscopy shows the average coordination number of the contributions in the slag or the binder phase, XANES considers the binder in combination with undissolved slag.

Slag name [method]	Slag	IP paste	IP binder
Copper slag [Mössbauer]	5 + 6	/	4-5
Copper slag [Mössbauer]	5 + 6	/	4-5
Copper slag [Mössbauer]	5 + 6	/	4-5
Synthetic 1 [Mössbauer]	5 + 6	/	4-5
Synthetic 2 [Mössbauer]	5 + 6	/	4-5
Synthetic 3 [Mössbauer]	4 + 5	/	4-5
Synthetic 1 [XANES]	5.5	5.1	/
Synthetic 2 [XANES]	5.4	5.2	/
Synthetic 3 [XANES]	5.0	5.0	/
Synthetic 3 [XANES]	5.0	5.0	/
Synthetic 3 [XANES]	5.0	5.0	/

Discussion: Coordination number

The possibility that Fe has multiple coordination numbers (4, 5, 6), next to the two different oxidation states, is one of the main origins of the complexity of the system. Average coordination numbers of slags and IPs are given in Table 3.4. In Mössbauer spectroscopy, it is possible to derive the coordination number more specifically. A clear distinction between Fe^{2+} and Fe^{3+} sites can be made and as such, the average coordination number of the fully cured and milled binder phase, the new Fe^{3+} state, can be provided. The average coordination number of the slags is dependent on the chemical composition. The presence of more Ca or Si results in a decrease of the average coordination number [176, 135]. This leads to a complicated assessment of the influence of the chemical composition of the slag on its behavior in alkaline media, as changing the composition also influences the configuration of the Fe polyhedra in the slag. A direct relation between the reactivity of a slag and its chemical composition is thus unlikely.

The inorganic polymers always seem to converge to an average coordination number of 5, although slight variations are observed between the different mixtures [176, 136, 135]. Fe^{3+} in 5-fold coordination is not commonly observed, but it is suggested to be present in small quantities in charge balanced Fe-silicate glasses [201, 199]. A combination of 4-fold and 6-fold can also explain the average 5-fold coordination. On the other hand, the interpretation of the coordination number from Mössbauer is not straightforward as the fitting parameters can be influenced by other factors, for instance it can also be only 4-fold if this 4-fold has larger Fe-O distances than what is usually observed. Likewise, the

fitting procedure that was followed for the pre-edge peaks in XANES causes the result to be a combination of slag and IP binder. This might provide a distorted view on the real coordination number of the IP binder, as for most mixes a limited reaction extent causes the slag to be dominant in the IP paste signal, dragging the resulting coordination number towards that of the slag. Chapter 4 will elaborate on the evolution of the coordination numbers that are observed during the synthesis and curing of the inorganic polymers.

3.2.4 Conclusions

The oxidation state of Fe in the inorganic polymer binders that are milled and cured for long periods ($>$ 28 days) is III, independent from the chemical composition of the slag or activating solution. The coordination number of Fe in the inorganic polymer binder is connected to more uncertainty, which chapter 4 should clarify. An average coordination number of 5 was suggested, but the presence of 4-fold coordination or the combination of 4 and 6-fold coordinated species is not disproved.

3.3 Molecular structure of CaO-FeO$_x$-SiO$_2$ glassy slags and resultant inorganic polymers

This section is based on the published paper:
A. Peys, C. E. White, D. Olds, H. Rahier, B. Blanpain, Y. Pontikes, "Molecular structure of CaO-FeO$_x$-SiO$_2$ glassy slags and resultant inorganic polymers", *Journal of the American Ceramic Society*, 10.1111/jace.15880.

Contributions of the authors: A. Peys made the experimental design and synthesis of samples. The analysis of the experiments was performed in discussion with C. E. White. All co-authors contributed in the discussion of the results and formulation of the conclusions.

Abstract

The molecular structures of CaO-FeO$_x$-SiO$_2$ slags and their inorganic polymer counterparts were determined using neutron and X-ray scattering with subsequent pair distribution function (PDF) analysis.The slags were synthesized with approximate molar compositions: 0.17CaO-0.83FeO-SiO$_2$ and 0.33CaO-0.67FeO-SiO$_2$ (referred to as low-Ca and high-Ca, respectively). The PDF data on the slags reasserted the predominantly glassy nature of this iron-rich industrial byproduct. The dominant metal-metal correlation was Fe-Si (3.20-3.25 Å), with smaller contributions from Fe-Ca (3.45-3.50 Å) and Fe-Fe (2.95-3.00 Å). After inorganic polymer synthesis, a rise in the amount of Fe^{3+} was observed via the shift of the Fe-O bond length to shorter distances. This shortening of the Fe-O distance in the binder is also evidenced by the apparent rise of the Fe-Fe correlation at 2.95-3.00 Å, although this feature may also suggest a potential aggregation of FeO$_x$ clusters. In general, the atomic arrangements of the reaction product was shown to be very similar to the precursor structure and the dominance of the Fe-Si correlation suggests the participation of Fe in the silicate network. The binder was shown to be glassy, as no distinct atom-atom correlations were observed beyond 8 Å.

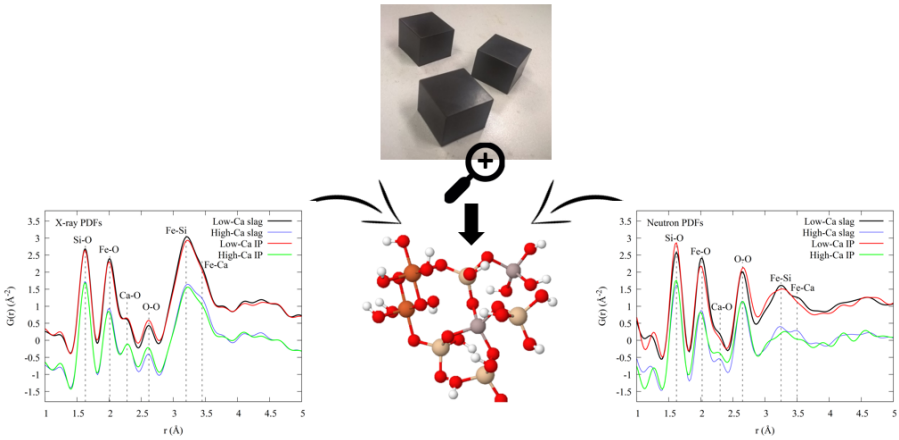

Figure 3.7: Graphical abstract: The determination of the molecular structure of Fe-rich inorganic polymers by pair distribution function analysis.

3.3.1 Introduction

In recent decades, the interest in sustainable development around the world has led to an increased focus on emerging sustainable cementitious materials, as the production of ordinary Portland cement (OPC) contributes extensively to global anthropogenic CO_2 emissions. Alkali-activated materials (AAMs) and inorganic polymers (IPs) are trending as one of these alternatives, considering their lower CO_2 emissions and comparable or better macroscopic properties compared with OPC (e.g., compressive strength, fire resistance) [155, 29]. Although aluminosilicates are popular in state-of-the-art IP materials [151, 124], recently a new kind of IP has been introduced which utilizes Fe-silicates as precursors. These precursors are slags, originating from non-ferrous metallurgy (e.g., copper, tin, lead), which are currently underutilized in the concrete industry. Previous work has shown that these Fe-silicate slags, when used as a precursor in IPs, would result in a large decrease in the environmental impact of mortars with respect to OPC [145].

The mineralogy of Fe-silicate slag has a profound influence on its reactivity for IP synthesis and the properties of synthesized mortars [138], explaining poor mechanical properties in earlier work [89, 10]. More specifically, the reactivity can be boosted drastically by fast cooling (water quenching) of the slag after metal separation, increasing the fraction of the amorphous component [150]. Mortars made using these water quenched slags are seen to have compressive strengths that exceed those of a CEM I mortar [92] (reported up to 250 MPa [unpublished results]). The final Fe-rich IP was seen to contain Fe in the 3+ oxidation state [102], even though most Fe-rich precursors contain Fe^{2+}. Interestingly, recent results have shown that having Fe^{2+} in the precursor slag is actually preferred over Fe^{3+}, leading to faster reaction kinetics and higher compressive strengths [7]. Arnout et al. [7] and Onisei et al. [136] confirmed that the Fe-rich IP binder consists of Fe^{3+} using titrations and Mössbauer spectroscopy, respectively. Furthermore, the use of synchrotron X-ray absorption near-edge spectroscopy (XANES) has given better insight into the neighboring environment of the Fe atom [176], however, the average coordination number of the Fe atoms remains an area of debate in the literature, as Mössbauer results suggest an average number of 4-5 [102, 136], while XANES implies that 5-5.5 is more reasonable [176]. Taking into account both the results from Mössbauer and XANES, an average 5-fold coordinated iron is the most probable. The specific distribution of the 4-, 5- and 6-fold coordinated Fe species that results in this average coordination number is not known from the experiments in the referred papers. The role of a minor amount of calcium in the Fe-silicate slag on the polymerization reaction and subsequent short and intermediate atomic arrangements remains unclear, however, previous research

has shown that calcium seems to strongly influence the strength development in Fe-rich IPs [190].

With the ability to characterize non-crystalline and disordered materials, pair distribution function (PDF) analysis is widely used to characterize AAMs [39, 202, 11, 12, 205, 204, 58] and other cementitious materials [177, 26]. For instance, PDF analysis was used to investigate the difference in the atomic ordering of AAMs from different precursors (slag and metakaolin) and between AAMs and a calcium-alumino-silicate-hydrate (C-A-S-H) structure resulting from the hydration of tricalcium silicate (C3S) and slag [202]. X-ray PDF analysis has also been used to investigate the influence of alkali cations on the molecular structure of metakaolin-based IPs, together with the effect of heating on the structure [11, 12]. The formation mechanisms and kinetics of AAMs have been revealed using in situ PDF experiments, where distinct differences in the atomic rearrangements during dissolution and polymerization were observed. Dissolution and polymerization kinetics could therefore be distinguished, together with the determination of the impact of the precursor on the dissolution kinetics [205, 204]. More recently, an investigation showed that slight structural differences can be traced in materials that initially appear similar [58], and by using a combination of neutron and X-ray experiments, complex materials (i.e., materials with a wide variety of elements) can be analyzed in detail, specifically by exploiting the relative difference in scattering cross sections in the elemental series for neutrons and X-rays [127].

PDF analysis has also been intensively used to investigate short and intermediate range ordering in silicate glasses, often in combination with theoretical modeling. The coordination number can be calculated from the area underneath the M-O partial PDF (for the amount of oxygen surrounding M) taking into account the molar fraction of this element and scattering length of the neutrons/X-rays [144, 143, 86, 83]. Furthermore, information on the coordination state(s) of Fe in Fe-silicate slag and related systems can be obtained from the position of the Fe-O correlation [18, 201, 212]. Interestingly, although 5-fold coordinated iron is rarely found in minerals, it is quite often observed in glasses. This is particularly true for Fe^{2+} found in CaO-FeO-SiO_2 glasses (observed using several spectroscopic techniques and molecular dynamic calculations) [168, 79], but 5-fold Fe has also been observed in charge-balanced $NaFeSi_2O_7$ glasses for a portion of the Fe^{3+} [201, 212]. The latter signifies that Fe^{3+} can act both as a network former (4-fold coordination) and modifier (5-fold coordination), where as a network former it replaces tetrahedral Al^{3+} in a charge-balanced glass structure. This versatility of Fe^{3+} (network former/modifier) may have significant consequences on the molecular structure of Fe-rich IPs.

Table 3.5: Chemical composition in mole% of the Fe-rich slags obtained using XRF by Van De Sande et al. [190] (estimated relative error 10%, e.g., 44 ± 4.4 mole%).

	FeO	SiO_2	CaO	Al_2O_3
Low-Ca	44	46	9	1
High-Ca	34	48	17	1

In this investigation we used neutron and X-ray PDF analysis to study the atomic arrangements in Fe-rich slags, and their IP counterparts. Two slags were synthesized (molar compositions: 0.17CaO-0.83FeO-SiO_2 and 0.33CaO-0.67FeO-SiO_2), and the resulting IP pastes were obtained via mixing with a sodium silicate solution. The nearest-neighbor bonding environments were investigated to obtain information on the oxidation state and coordination number of Fe in the slags and IPs. Furthermore, by analyzing the PDF data between $\sim$ 2.5 and 8 Å, the local structure has been elucidated for the Fe-rich slags, together with the structural rearrangements that occur due to the dissolution and polymerization reactions. By tracking changes to the Fe-Fe, Fe-Si and Fe-Ca correlations upon synthesis, details on the extent of Fe clustering within the IP pastes have been obtained. Hence, by using this combined neutron/X-ray approach new information on the role of Fe in the silicate-based network of Fe-rich IP pastes has been provided.

3.3.2 Experimental

The synthesis procedure and chemical composition of the slag have been previously outlined in the literature [190]. The chemical composition of the two slags is shown in Table 3.5. Briefly, a mixture of powder was heated in an Indutherm TF4000 to 100 °C above the liquidus temperature (respectively 1142 °C and 1099 °C for the low and high-Ca slag) of the aimed composition and the resulting melt was quenched in water. Before quenching, a mixture of CO and CO_2 was bubbled through the melt (40 and 20 L/h, respectively) to obtain the desired 2+ oxidation state for Fe. The mineralogical composition of the solidified material was studied using X-ray diffraction, with which an amorphous content of > 90 wt.% was observed [190]. The slags were subsequently milled using a Fritsch Pulverisette 13 disc mill and a Wiener S attritor mill until a specific fineness of 4000 ± 200 cm^2/g (Blaine method) was reached. In previous work, mortars from both slags reached compressive strengths of 35 MPa after 28 days at room temperature [190].

The (deuterated) alkaline activating solution was made by mixing first NaOH pellets (Sigma-Aldrich, 99 wt.% purity) in liquid D_2O (Sigma-Aldrich, 99.9 wt.% purity). Use of D_2O was necessary to reduce incoherent scattering from H-atoms

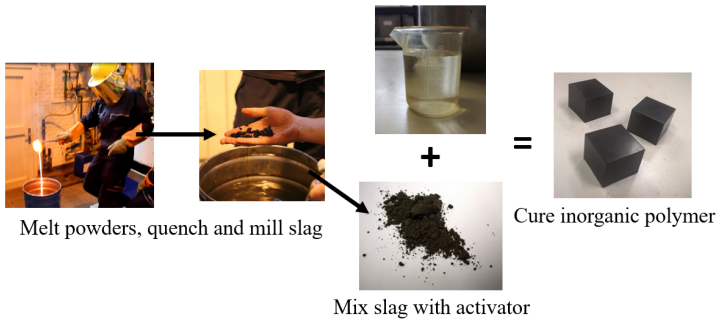

Figure 3.8: Synthesis procedure of the samples. Including (from left to right) melting and quenching the slag, milling slag to powder and mixing the powdered slag with the activating solution to obtain the inorganic polymer samples shown on the right.

during the neutron scattering measurements. Fumed silica (Sigma-Aldrich, 99.8 wt.% purity) was dissolved in this deuterated hydroxide solution (subsequently mixed for 48 hours) to deliver a silicate solution with molar ratios SiO_2/Na_2O = 1.6 and D_2O/Na_2O = 20. IP pastes were created by mixing the slags and solution by hand for 3 minutes in a solution/slag mass ratio of 0.4. The samples were stored in a closed container at 21 ± 1 °C for 61 days. The demolded samples were crushed using a Fritsch Pulverisette 13 disc mill and milled in a Retsch ZM100 centrifugal mill using a 250 µm and 80 µm mesh sieve. The overall synthesis procedure is schematically presented in Figure 3.8.

Attenuated total reflectance-Fourier transform infrared spectroscopy (ATR-FTIR) and thermogravimetric analysis (TGA) coupled with FTIR for the analysis of the off-gas (Perkin Elmer TG-IR GCMS Interface TL 8000) was used on the powdered samples to have a qualitative determination of the content of H_2O, D_2O and carbonates (Perkin Elmer instruments, Frontier MIR with a Frontier UATR diamond/ZnSe attachment, Pyris 1 TGA and a TL8000 transfer line). ATR-FTIR was performed with a resolution of 4 cm^{-1}, 32 scans per measurement and 2 measurements per sample. TGA was performed using a platinum sample pan, a ramp rate of 10 °C/min from 50 °C to 900 °C, and a nitrogen flow of 50 ml/min over the sample. The evolved gas analysis was performed using the TL8000 transfer line attached to the TGA, where the gases flowed through a heated tube to the FTIR module (300 °C). FTIR spectra were measured with a resolution of 8 cm^{-1} and a time between 2 scans of 2.5 seconds. The analyses were performed on the average of 8 scans.

Neutron scattering experiments were performed at Oak Ridge National

Laboratory at the Spallation Neutron Source (SNS) on the Nanoscale Ordered Materials Diffractometer (NOMAD) [129] which has a maximum momentum transfer (Q) of 50 Å^{-1}. Each sample was measured for 1 hour. Standard data reduction protocols were used on NOMAD [129]. Generation of the PDF was carried out using custom python scripts in which contributions to the data from incoherent scattering (often referred to as hydrogen background) were accounted for by firstly fitting the scattering function with a pseudo-Voight function which was subsequently subtracted. The second step consisted of fitting a second order polynomial function at high Q values (6-40 Å^{-1}) to ensure convergence of the scattering function to 1.0. A Q_{min} of 0.9 Å^{-1} and a Q_{max} of 21.5 Å^{-1} were used for the Fourier transform to obtain the PDF with a resolution of 0.02 Å. Complementary X-ray PDFs were obtained from X-ray total scattering experiments at the Advanced Photon Source, Argonne National Laboratory on the 11-ID-B beamline using 60 keV radiation, a sample-detector distance of 180 mm, beam size of 0.2x0.2 mm^2 and a measuring time of 3 minutes per sample. Fit2D was used to integrate the 2-dimensional diffraction data [44], using CeO_2 as the calibrant. Data reduction was performed using PDFgetX2 [156] to obtain the normalized scattering function and the real space PDFs, again using a Q_{min} of 0.9 Å^{-1} and Q_{max} of 21.5 Å^{-1}. For both the neutron and X-ray measurements, the powders were loaded into quartz (for neutron) or polyimide (for X-ray) capillaries of 2 mm and 1 mm inner diameter, respectively.

To plot the various PDF data sets against each other for quantitative analysis, each PDF was normalized systematically based on the function g(r) = G(r) + 4π rρ_0, where ρ_0 is the atomic number density derived from the slope of the PDF over an r range of 0-1.4 Å. The average ρ_0 was obtained from PDFs using three Q_{max} values: 28, 21.5 and 20 Å^{-1}. The Si-O correlation in the g(r) has been fitted with a Gaussian peak. The area of this peak is normalized with respect to the Si content of the material. Figures and atomic distances presented throughout the article are based on the PDFs produced using a Qmax of 21.5 Å^{-1}.

3.3.3 Results and discussion

CaO-FeO$_x$-SiO$_2$ slags

The X-ray and neutron scattering functions of the Fe-silicate slags are shown in Figure 3.9, where it is clear that minor amounts of crystalline phases are present in these samples. Figure 3.10 shows X-ray scattering data with the detector at 95 cm, revealing the crystalline peaks more clearly. The phases present are ferrosilite ($Fe_2Si_2O_6$) [95, 133], hedenbergite ($CaFeSi_2O_6$) [95, 133]

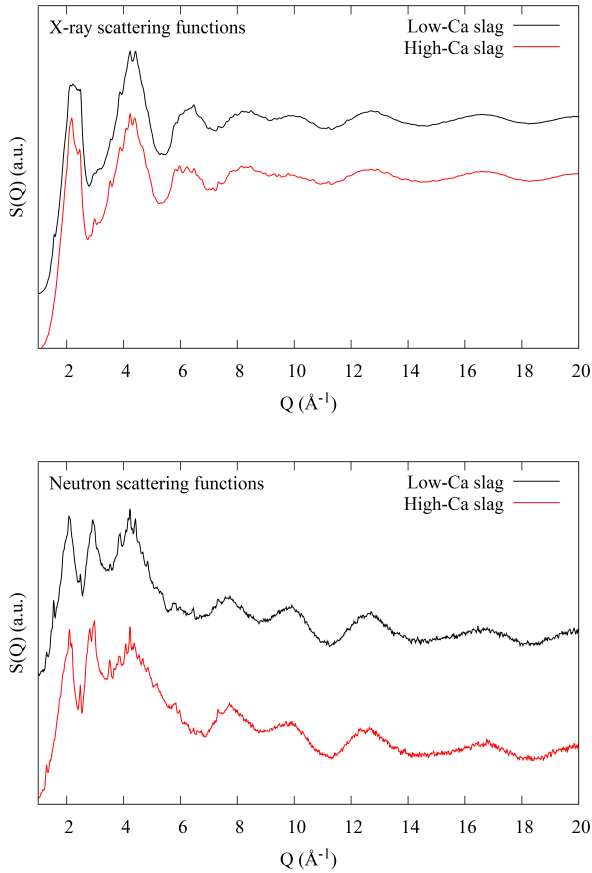

Figure 3.9: X-ray (top) and neutron (bottom) scattering functions of the low and high-Ca slags (stacked plots).

and quartz (SiO_2) [95, 193], the latter only in the low-Ca slag. The ferrosilite and hedenbergite are actually solid solutions in the presented slags. This results in slight shifts of the Q values of the different peaks with respect to X-ray diffraction on an ideal crystal due to the change in lattice parameters accompanying the Fe-Ca substitution or vice versa. The data show that the slags are predominantly glassy in nature, which will also be apparent in the PDFs via the absence of long range order. In comparison with diffraction data of Drewitt et al. [35] and Alderman et al. [4] the glass most closely related to glassy hedenbergite.

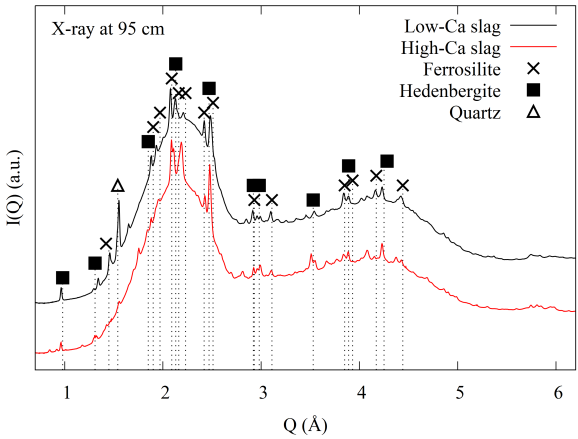

Figure 3.10: Stacked plot of the X-ray scattering data of the two types of slags with a detector distance of 95 cm. The crystalline phases are indicated.

In the X-ray and neutron PDFs shown in Figure 3.11, the Si-O distance is observed at 1.62 Å, which aligns with the values reported in the literature for silicate glasses [198, 211, 126]. The Ca-O correlation is observed as a shoulder or smaller peak at approx. 2.25-2.30 Å [212]. The intensity of this correlation is higher in the high-Ca slag PDF (both X-ray and neutron), since there is twice the amount of Ca in this slag compared with the low-Ca slag.

The Fe-O correlation is present at 2.01 Å in the X-ray and 2.02 Å in the neutron PDFs. The position and shape of this peak is approximately the same for the two slags, implying that the Fe atoms in these samples are similar in terms of oxidation state and coordination number. The intensity of the Fe-O peak is higher for the low-Ca slag, since there is a higher percentage of Fe in this slag (see Experimental section). Theoretically, a confirmation of the presence of different Fe species and determination of their relative quantities would be possible via a deconvolution process using the positions of the species presented by Weigel et al.[201] and Wright et al.[212]. However, these positions are only averages of a continuum of Fe-O distances, as has been observed in the literature [182, 182]. The PDF data can thus not be used to quantitatively determine the distribution of Fe species in the slags, as the exact distance of the present species is unknown. Calculation of the average coordination number from the area under the Fe-O correlation is presented in Appendix A, where the data suggest a coordination number between 4 and 5. However, these results are approximate since a wide range in values can be obtained from the calculation,

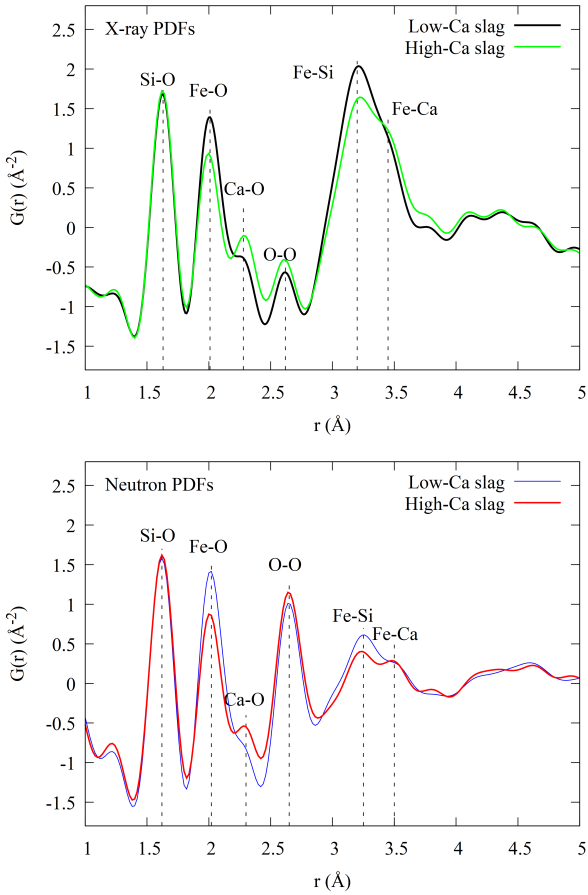

Figure 3.11: X-ray (top) and neutron (bottom) PDFs of the low and high-Ca slags.

as explained further in the appendix. The data in chapter 3.2 using XANES and Mössbauer spectroscopy showed the presence of $^{IV}Fe^{2+}$, $^{V}Fe^{2+}$ and a minor amount of $^{V}Fe^{3+}$ species in a similar slag, which, in comparison with literature [18, 201, 212], is in agreement with the Fe-O peak found in Figure 3.11 at 2.01-2.02 Å.

Looking further at the PDFs in Figure 3.11, the O-O correlation is observed as a peak at 2.62-2.65 Å. The position is common for O-O distances found in SiO_4 tetrahedra. Literature reports the O-O correlation from the FeO_x structural units over a wide range of distances, ranging from 2.85 to 3.1 Å [212, 199],

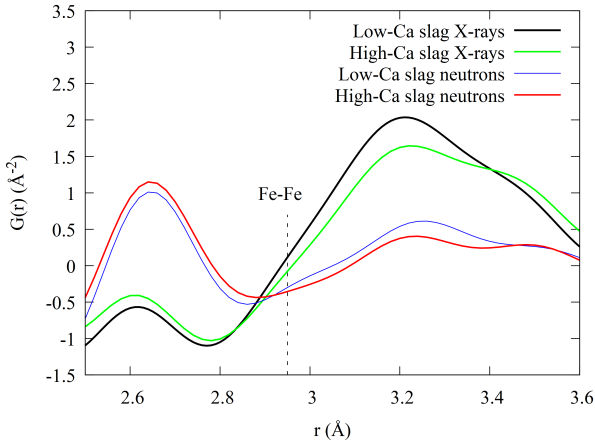

Figure 3.12: X-ray and neutron PDFs, showing a zoom of Figure 3.11 over an r range of 2.5 to 3.6 Å. The shoulder of the main metal-metal correlation at approx. 2.95 Å is likely Fe-Fe contributions from edge-sharing ^{V}Fe.

which is often observed as a shoulder of the main O-O peak at 2.62-2.65 Å. The first metal-metal correlations in Figure 3.11 are observed between 3 and 4 Å. The main peak is centered at 3.20-3.25 Å, which is where Fe-Si correlation is usually observed [168, 199]. The prevalence of this correlation suggests a homogenous distribution of Fe throughout the silicate network of the glass. The shoulder at 3.45-3.50 Å can be attributed to edge-sharing Fe and Ca structural units or two corner-sharing Fe units [168, 199]. However, a large portion of the Fe in these slags exists in 5-fold coordination (^{V}Fe^{2+} and ^{V}Fe^{3+}), and therefore Fe is more likely to share edges [199]. This information, combined with the higher intensity of the 3.45-3.50 Å correlation for the high-Ca slag, indicates that the dominant correlation at this position is probably Fe-Ca. The position of the potential edge-sharing ^{V}Fe structural units would be around [199] or 3.1 Å [168]. Figure 3.12 is a zoomed-in region of the 2.5-3.6 Å region in the slag PDFs, where a shoulder is visible on the lower r portion of the metal-metal correlation (containing Fe-Si and Fe-Ca) for both X-ray and neutron PDFs. The work of Weigel et al. [199] showed that contributions from the O-O shoulder associated with FeO$_x$ structural units are minor compared with the intensity associated with a Fe-Fe correlation. Therefore the shoulder seen at $\sim$ 2.95 Å is attributed to the Fe-Fe correlation, corresponding to edge-sharing ^{V}Fe. In the neutron data, a minor contribution of the O-O correlation associated with the edge-sharing ^{V}Fe remains possible from 2.85 to 3.1 Å, as explained in the previous paragraph. A Si-Si correlation can also be present in this range of r values. However, because of the limited scattering length of Si with respect to

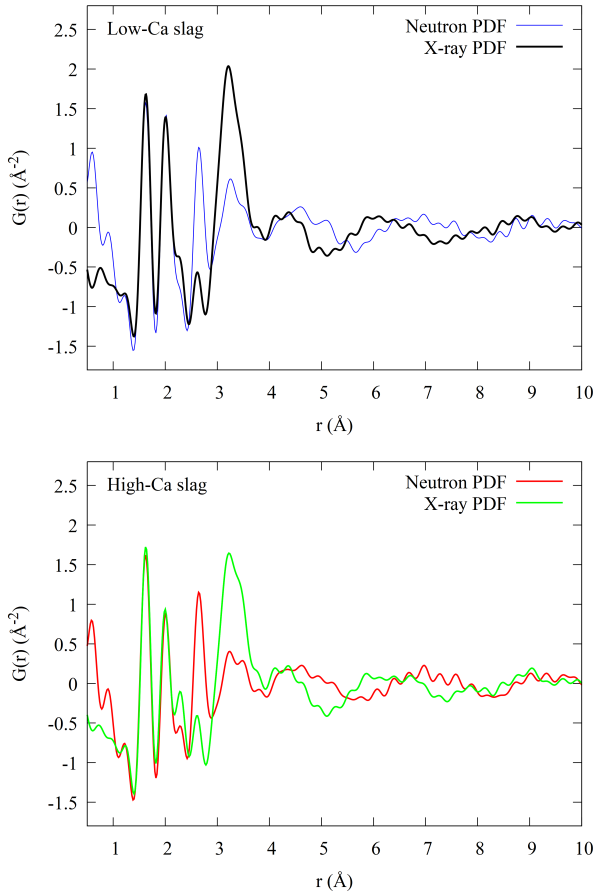

Figure 3.13: X-ray and neutron PDFs of the low (top) and high-Ca (bottom) slags.

Fe or Ca, the contribution of Si-Si is probably minor.

For the interpretation of the longer range (> 4 Å) PDF data in Figure 3.13, a rule of thumb can be used based on the scattering lengths of the different elements (Appendix A, Table A.1-A.2). Where the neutron and X-ray PDFs show similar intensities, those positions mainly consider metal-O correlations. A higher intensity for the neutrons suggests O-O correlations while metal-metal correlations are most probable when the X-ray PDF exceeds the neutron PDF. Thus, metal-O correlations are observed at 4-4.8 Å and 6-7 Å, O-O correlations at about 5 and 7 Å and metal-metal correlations at 5.5-6.5 Å. This information

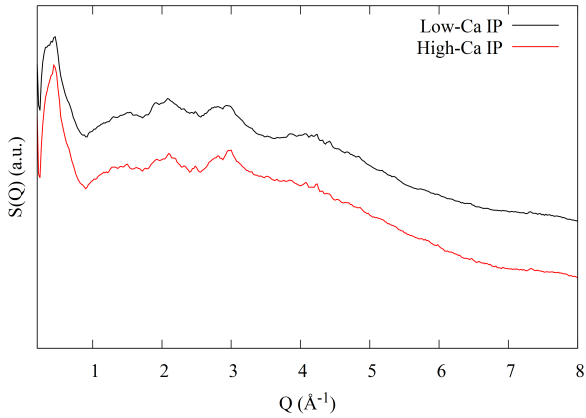

Figure 3.14: Neutron scattering data of the Fe-rich IPs in reciprocal space before background correction.

is in agreement with literature on Fe-containing silicate glasses, where the authors used empirical potential structure refinement (EPSR) modeling or isotopic substitution (i.e., an increase of the ^{57}Fe content), to produce partial PDFs [201, 212, 199]. The r position of the second O-O, the O-O(2), correlation seems to correspond well with that of fused silica or vitreous silica ($\sim$ 5 Å) [211, 207], suggesting a similarity in topological ordering, specifically 2D rings of SiO_4 tetrahedra in the vitreous silica [211, 167] and therefore Si/Fe rings in the slags. A more detailed description of the ring sizes in silicate glasses needs a computational approach [167], as reported by Karalis et al.[83] for a similar Fe-silicate slag.

CaO-(Na_2O-)FeO_x-SiO_2 inorganic polymers

The neutron scattering data of the Fe-rich IPs are shown in Figure 3.14, where the IPs are seen to be predominately amorphous. The minor crystalline components that were observed in the slags (Figure 3.9) are still present in Figure 3.14. As previous work on similar slags and chapter 3.2 showed that the crystalline Fe-silicates do not participate significantly in the reactions [136, 78], this observation was expected. The existence of a "hydrogen background" in Figure 3.14, as seen via the elevated scattering level that decreases at higher Q, originates from incoherent scattering attributed to adsorbed atmospheric water in the cement or the D_2O used in the activating solution (deuterium has a non-negligible incoherent scattering length). Below 1 Å^{-1}, a large broad peak is observed,

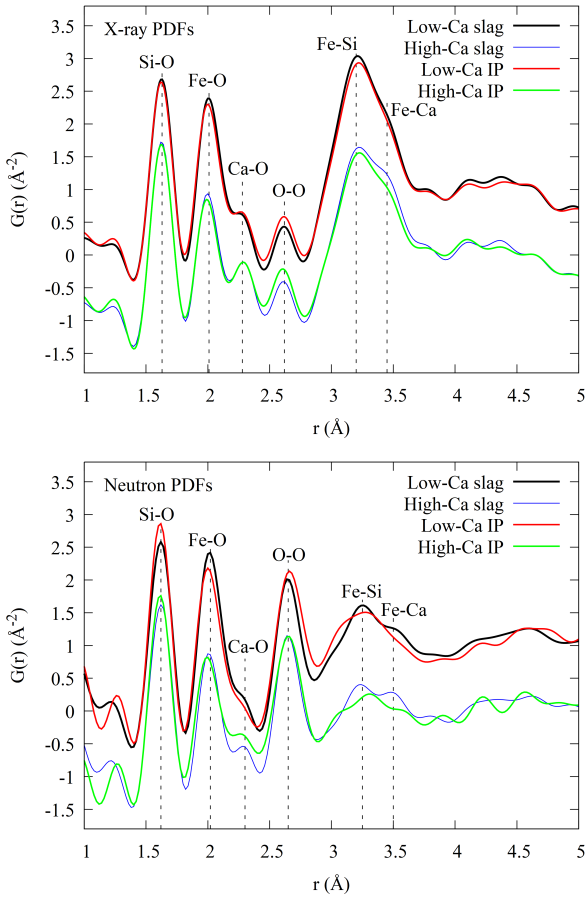

Figure 3.15: X-ray (top) and neutron (bottom) PDFs of the Fe-silicate slags and IP pastes. The plots are stacked and grouped per precursor slag.

which is likely the small-angle scattering from the porous nature of the binder phase, where the small-angle region is cut off at low-Q by the limits in the detector coverage. No additional crystalline components are observed in the IPs compared with those present in the slags, and therefore the binder has a glassy or nano-crystalline structure.

The X-ray and neutron PDFs of the Fe-rich IPs in Figure 3.15 show that the molecular structures of these binders are similar to those of the slags. This is partially due to the presence of unreacted slag residing in the binders, where

approx. 30-60 wt.% of unreacted slag has been observed in similar systems [7, 136, 176]. Based on the activating solutions used in this current study (resulting in a similar Na/Fe), the unreacted portion should be closer to 60 wt.%. However, even when this unreacted component is taken into account, there are significant structural similarities between the binder and the slag. This behavior is in contrast to the structural rearrangements that are seen to occur for IPs of metakaolin or blast furnace slag, as studied using PDF analysis [203, 50]. For metakaolin-based IPs, the formation of the sodium-alumino-silicate-hydrate (N-A-S-H) network is seen via the emergence of distinct correlations between 3.5 and 4.5 Å associated with the formation of 4-membered alumino-silicate rings. In a blast furnace slag-based AAM, the emergence of the C-(N)-A-S-H network is distinctly seen via the increase in the intensity of the Ca-Si correlation at $\sim$ 3.6 Å [117, 122]. In contrast to these AAMs, the Fe-rich IPs only show subtle atomistic changes due to the alkali-activation reaction, which is in agreement with the observed changes seen via Mössbauer spectroscopy, where the parameters, e.g. isomer shift and quadrupole split, of the Fe-species of the slag and IP are related [136].

The influence of the IP synthesis (i.e., alkali-activation) on the local atomic arrangements of Fe-silicate slags is displayed in the PDFs in Figure 3.16, where a slight shift of the Fe-O correlation occurs toward shorter distances, specifically from $\sim$ 2.02 to 2.00 Å. This shift confirms the change in the oxidation state (from Fe^{2+} to Fe^{3+}) for the Fe in slag that undergoes dissolution and incorporation into the binder. The shift to shorter distances and the absence of any significant intensity at approx. 1.85 Å (position of potential $^{IV}Fe^{3+}$ sites), is consistent with the results in chapter 3.2 on fully cured and milled samples, where it was suggested that $^{V}Fe^{3+}$ is the average Fe^{3+} species. As such, the Fe^{3+} at least partially behaves as a network modifier. The absence of $^{IV}Fe^{3+}$ as the most prevalent species in these Fe-rich IPs is in contrast with the literature on $NaFeSi_2O_6$ glasses [201, 199], and also shows an important difference with aluminosilicate metakaolin-based IPs, where the Al^{3+} is always in 4-fold coordination acting as a network former [29, 159].

In Figure 3.15, one of the most apparent changes caused by IP synthesis is the increase in the intensity of the shoulder at 2.95 Å, most clearly observed in the neutron data. As discussed earlier in the context of the slags, a combination of O-O or Fe-Fe correlations can occur at this r-value, with the latter contributing more significantly in this region. Figure 3.17 shows this region in more detail, where a drop in intensity is observed upon IP synthesis for the Fe-Si and especially for the Fe-Ca correlations, as seen in the neutron data. On the other hand, the shoulder at 2.95 Å either increases in intensity (for neutrons) or stays at approximately the same height (for X-rays). The drop in intensity of the

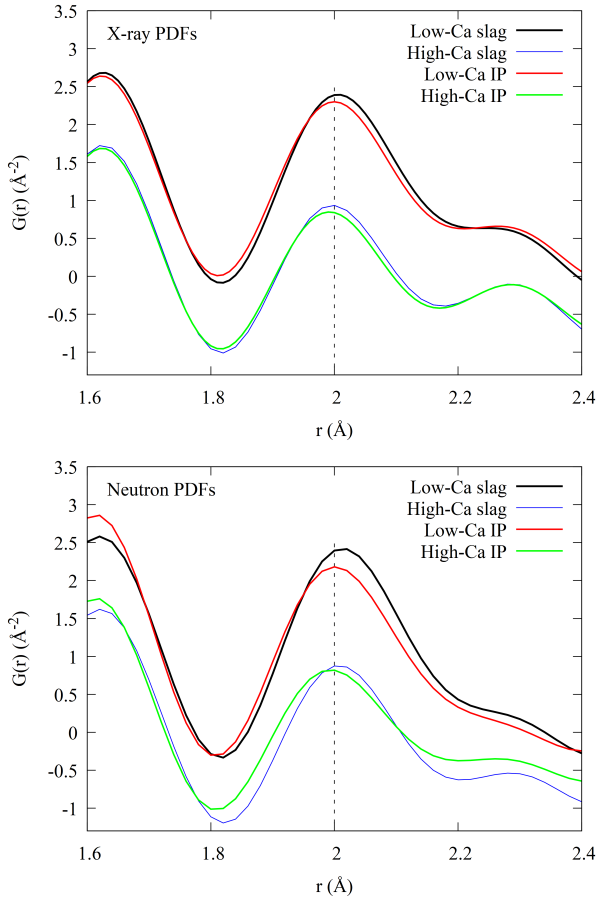

Figure 3.16: Detailed view on the Fe-O correlation in the X-ray (top) and neutron PDFs (bottom) of the IPs and slags. The plots are stacked and grouped per precursor slag.

Fe-Si correlation together with the further emergence of the Fe-Fe correlation, implies that 1) some of the newly emerged Fe^{3+} sites have clustered together, which has also been seen to occur in charge balanced Fe-silicate glasses [201, 199] or 2) the Fe-Fe distance is shortened (by shortening of the Fe-O distance during oxidation), which would have the same effect as the drop in intensity at the distance of Fe-Si and rise at the Fe-Fe position, observed here. Clustering should not be confused with phase separation, as the observed effect occurs at a much smaller length scale (i.e., at the nanoscale). The larger extent of this effect for the low-Ca system can be associated with the higher Fe content of this slag.

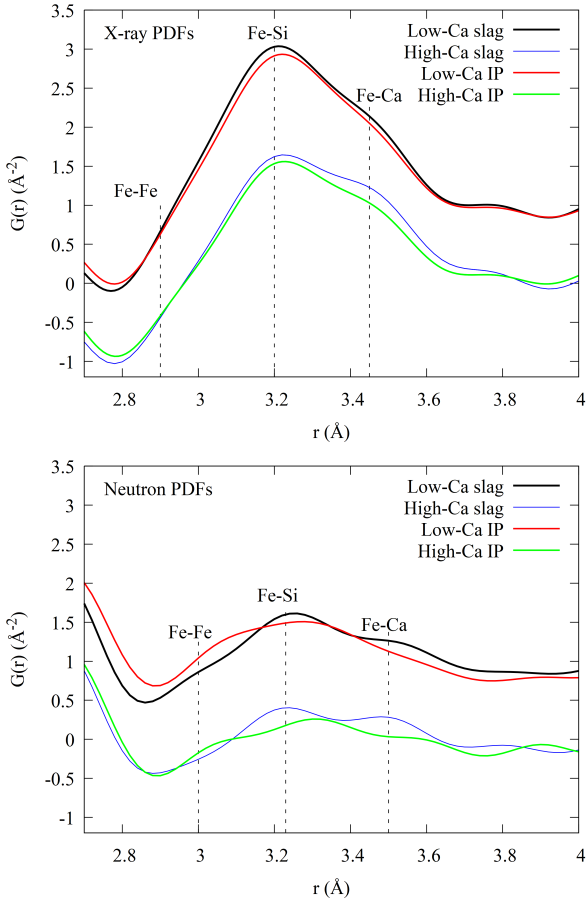

Figure 3.17: X-ray (top) and neutron (bottom) PDFs of the slags and IPs, detailed view of the metal-metal correlations. The plots are stacked and grouped per precursor slag.

Figure 3.17 also shows a rise in the intensity of the Ca-Si correlation for the high-Ca system due to IP synthesis, specifically via a shoulder at 3.6 Å (confirmed using different Q_{max} values during preliminary analysis of the data). Ca and Si in the slag tend to be associated with Fe (as seen via the Fe-Si and Fe-Ca correlations), but after IP synthesis there is a tendency for Ca and Si to form Ca-O-Si linkages. This is in accordance with the drop in Fe-Si and Fe-Ca mentioned above. Whether this is a small percentage of a calcium-silicate-hydrate (C-S-H)-like phase existing in these IPs or a smaller scale segregation is

not clear from the presented experiments. Additionally, the IPs have undergone carbonation (reacted with atmospheric CO_2), as seen in the neutron PDF of the high-Ca IP in Figure 3.15, where a signal at 1.25 Å is observed and is attributed to a C-O correlation from a carbonate phase(s). The presence of carbonates in these IPs has been confirmed using TGA-FTIR (CO2 detected upon heating) and ATR-FTIR (bands at 870 cm^{-1} and $\sim$ 1450 cm^{-1} [95, 77, 63], full spectra in Appendix A, Figure A.4. The absence of peaks in the reciprocal space data that can be associated with calcite or sodium carbonate phases might suggest the formation of an amorphous carbonate. The carbonation of part of the Ca in the IPs can be an additional change in the Ca environment and therefore an additional factor leading to the drop in intensity of the Fe-Ca correlation. Formation of carbonates was most likely caused by CO_2 in the air during hardening or during the simultaneous elevated temperature and exposure to air during milling of the samples [108].

The higher r-range region of the PDF data (4-10 Å) is displayed in Figure 3.18, where changes to the second metal-metal correlations are observed. A decrease in intensity at around 6 Å is seen in the X-ray data, together with an increase at about 5.5 Å. Although attribution of this change to a well-defined correlation is difficult without an accurate structural representation of the material, by considering the strong scattering of Fe compared with the other elements (as can be seen in the weighting factors in the appendix and in the first metal-metal correlation) the changes are likely due to the second Fe-Si, Fe-Ca or Fe-Fe correlations. Furthermore, the shift to lower distances in this region is likely correlated with the observations made for the first metal-metal peaks, where a clustering of the Fe^{3+} sites or lowering of the Fe-Fe distance would induce the observed effect here. An increase in the degree of polymerization of IPs with respect to the slags can provide an additional explanation of this observation. To make a distinction between these possible explanations is hard without a theoretical model which can render partial PDFs (molecular dynamics/density functional theory). With respect to long-range ordering in the samples, it is clear that the correlations are not well-defined beyond 8 Å in Figure 3.18. The absence of any long-range order shows that these binders are truly glassy/amorphous in nature [202], without any features of nano-crystallinity. Appendix A (Figure **??**) shows that the lack of changes extends to 25 Å. The 8 Å is consistent with previous XRD results, where no peaks for the binder were detected [108, 78], as for XRD it is generally assumed that no peaks are observed for structures with order on a smaller scale than 1 nm. Future research should include an investigation of the stability of this glassy phase and if there is a tendency for the structure to evolve towards a (nano-)crystalline phase. Whether this potential structural rearrangement has any consequences for the durability of the Fe-rich IPs is another open research

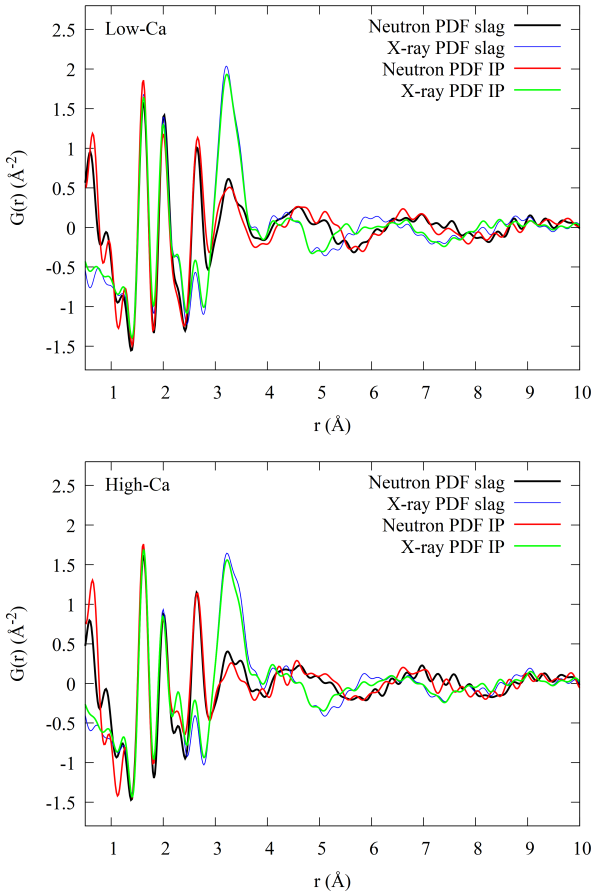

Figure 3.18: X-ray and neutron PDFs of the slags and IPs activated with a sodium silicate solution (SiO_2/Na_2O molar ratio 1.6). Top: Low-Ca system, bottom: High-Ca system.

question.

3.3.4 Conclusions

In this investigation, the local molecular structure of Fe-silicate slags and their inorganic polymer counterparts were investigated using X-ray and neutron total scattering together with thermogravimetric analysis coupled to Fourier transform infrared spectroscopy. By combining neutron and X-ray PDF analysis,

the synthetic Fe-silicate slags were seen to possess a glass structure. Analysis of the Fe-O bond length, centered around 2.02 Å, in conjunction with higher r-range correlations, confirmed the presence of $^{IV}Fe^{2+}$, $^{V}Fe^{2+}$ and $^{V}Fe^{3+}$ species. The metal-metal correlations in the PDF data mostly consisted of Fe-metal (metal = Ca/Si/Fe) correlations, since Fe in these samples exhibited the largest scattering cross-section compared with the other elements for both neutrons and X-rays. Fe-Si (3.20-3.25 Å) was the most prevalent metal-metal correlation, with the Fe-Ca (3.45-3.50 Å) and Fe-Fe (2.9-3.0 Å) correlations positioned on either side. The O-O(2) correlation ($\sim$ 5 Å) aligned well with vitreous silica, suggesting a similar topological ordering consisting of a silicate network with 2D rings. The differences between the slag with low and high-Ca content were merely those associated with exchanging Fe for Ca (decrease of Fe-O and Fe-Si, increase of Ca-O and Fe-Ca).

Inorganic polymer synthesis resulted in the (partial) oxidation of the predominantly Fe^{2+} precursor, observed in the PDFs by the shift of the Fe-O bond length to a shorter distance. The binder phase showed strong structural similarities to its precursor structure. In agreement with chapter 3.2, the presence of Fe^{3+}, on average in 5-fold coordination, is possible in the fully cured and milled samples studied in the present section. Furthermore, the metal-metal correlations showed a slight reconfiguration as a result of the alkali-activation reaction, specifically via a decrease in the nearest-neighbor Fe-Ca and Fe-Si correlations and a rise in Fe-Fe (more pronounced with low-Ca). The emergence of the Fe-Fe correlation is indicative of 1) the clustering of the Fe^{3+}, or 2) the decrease in Fe-Fe distance due to Fe oxidation and associated contraction of the Fe-O bond length. However, Fe-Si is still the most prevalent metal-metal correlation in the IPs and therefore Fe takes part in the silicate network, (at least partially) as a network modifier. This result highlights an important difference with aluminosilicate geopolymers, where Al is always seen to behave as a network former. From the PDF results it was seen that Ca is incorporated into a Ca-Si correlation after synthesis of the IP (observed more clearly for the high-Ca system) although additional Ca may have ended up in some carbonate(s). Lastly, the binder phase did not show significant correlations beyond 8 Å, revealing that IPs synthesized from Fe-silicate glasses are amorphous as opposed to nano-crystalline.

3.4 Tuning the molecular structure by varying the activating solution chemistry

This section includes an unpublished set of data, which will be included in a future publication authored by:
A. Peys, C. E. White, H. Rahier, B. Blanpain, Y. Pontikes

Contributions of the authors: A. Peys made the experimental design and synthesis of samples. The analysis of the experiments was performed in discussion with C. E. White. All co-authors contributed in the discussion of the results and formulation of the conclusions.

Abstract

Inorganic polymers and alkali-activated materials embody a large part of the research on alternative cementitious materials, because of their low environmental impact of production and interesting engineering properties. Having the ability of incorporating Fe-rich residues, e.g. slags from the non-ferrous metal industries, these materials also promote a small increment in the circularization of our economy. This section elaborates on the fundamental insight in inorganic polymers from non-ferrous slag by discussing the atomic correlations of two slags with approximate molar composition 0.17CaO-0.83FeO-SiO_2 and 0.33CaO-0.67FeO-SiO_2. These are activated with alkali silicate solutions with molar ratios SiO_2/M_2O = 1.6-2, H_2O/M_2O = 20 (M = Na or K). The results show that the pair distribution functions of inorganic polymers originating from the same slag, but different activators, show almost identical atomic correlations and seem to be similar to the precursor slag. A comparison between inorganic polymers from the different slags shows much more difference in the PDF curves and it is thus the molecular structure of the slag that controls the reaction products. This leaves room to use the activating solution to tune the microstructure independently of the molecular structure.

3.4.1 Introduction

Fayalite-olivine (CaO-)FeO_x-SiO_2 slags are becoming a more common resource for cementitious materials. Their pozzolanic activity is low, so their valorization is more focused towards alkali-activated materials (AAMs) or inorganic polymers (IPs). The abundance of these slags is guaranteed by their presence as by-product in the production of non-ferrous metals. Currently, the vast majority is not used in applications which provide a significant added value (e.g. blasting grit, aggregates for road construction [59]). A new material in the construction sector incorporating these slags would therefore incite slag valorization, while delivering a lower CO_2 cement. The possible environmental impact reduction was calculated to be up to 77% of a CEMI ordinary Portland cement (OPC) based mortar with equivalent load bearing capacity [145]. Slags from the non-ferrous metals industry most often contain Fe in the 2+ oxidation state [148, 59]. Section 3.2 of this thesis showed that during the reactions towards a solid binder, the oxidation state goes to Fe^{3+} in the final inorganic polymer. Pair distribution functions (PDFs) of this final structure showed that the atomic structure of the alkali-activated slag showed similarity to its precursor, but slight changes were observed like the aforementioned oxidation and potentially an aggregation of the Fe species [147].

The activating solution shows in AAMs and IPs an influence on the structure of the resulting binder. According to Duxson et al. [38] and Onisei et al. [136] the microstructure can be tuned by varying the SiO_2/Na_2O ratio in the silicate solution, going from globular for low ratios to more smooth for higher. The water content of the mixtures in these references was not constant, so the variation of the microstructure cannot definitely be assigned to the SiO_2/Na_2O ratio, but it is surely related to the composition of the activating solution. This effect is also shown in the pore structure, where the average pore size decreases with the addition of silicates [16]. The latter has a significant effect on the permeability of the binder, which is an important aspect for the resistance to ingress related durability issues [16]. The choice of alkali atom also has an effect on the structure (and therefore also properties) of AAMs, especially with regards to the pore structure, as the size of the pores is commonly related to the size of the hydration sphere of the alkali atom [180]. The difference in formation of the molecular structure of sodium silicate and sodium hydroxide activated samples was revealed by PDF analyses [204, 208]. The structure of metakaolin-based inorganic polymers was investigated with different alkali atoms [11, 12]. In Fe-silicate minerals and glasses the alkali atom has an additional effect. There, it influences the short range ordering of Fe, commonly observed as a change in the ^{57}Fe Mössbauer parameters [73].

The present section repeats the methodology of pair distribution function analysis used in previous section (chapter 3.3) on a wider range of samples to investigate the influence of the activating solution chemistry on the atomic structure of CaO-FeO_x-SiO_2 IPs. The effect of the alkali atom (M = Na or K) and the SiO_2/M_2O molar ratio (1.6 and 2.0) on neutron and X-ray PDFs is investigated, thereby aiming to reveal changes in the short range ordering, e.g. Fe coordination, and intermediate range ordering, e.g. extent of Fe aggregation.

3.4.2 Materials and methods

The two precursors in the present section are the same as in section 3.3, having an approximate chemical composition of 0.83FeO-0.17CaO-SiO_2 (low-Ca slag) and 0.67FeO-0.33CaO-SiO_2 (high-Ca slag). These were activated with 4 different activating solutions, resulting in the 8 mixtures in Table 3.6. The samples used deuterated solutions to minimize the hydrogen background in the neutron scattering data whilst obtaining structural information on D_2O/OD in the binder. After mixing, the samples were contained in a closed bottle for 61 days at 21 ± 1 °C. Afterwards, they were milled and loaded in 2 mm inner diameter quartz glass capillaries (neutron scattering) and 1 mm polyimide capillaries (X-ray scattering).

Table 3.6: Mix-design of the 8 samples. The activating solution chemistry is defined by the alkali atom and molar ratios SiO_2/M_2O and D_2O/M_2O. A constant water/slag mass ratio of 0.28 is maintained, resulting in the reported solution/slag mass ratios.

Sample	Slag	Alkali M	SiO_2/M_2O	D_2O/M_2O	Solution/slag
Low-Ca, Na 1.6	Low-Ca	Na	1.6	20	0.41
Low-Ca, Na 2.0	Low-Ca	Na	2.0	20	0.43
High-Ca, Na 1.6	High-Ca	Na	1.6	20	0.41
High-Ca, Na 2.0	High-Ca	Na	2.0	20	0.41
Low-Ca, K 1.6	Low-Ca	K	1.6	20	0.43
Low-Ca, K 2.0	Low-Ca	K	2.0	20	0.45
High-Ca, K 1.6	High-Ca	K	1.6	20	0.43
High-Ca, K 2.0	High-Ca	K	2.0	20	0.45

The experimental setup was similar to chapter 3.3. The Spallation Neutron Source's (SNS) Nanoscale Ordered Materials Diffractometer (NOMAD) at Oak Ridge National Laboratory (ORNL) was used for neutron scattering, providing a range up to to 50 Å^{-1} [129]. The measurements, performed for 1 hour, were normalized with respect to a vanadium rod. An empty capillary was measured for performing background subtractions. As some H_2O still remained in the sample, coming from impurities of the D_2O, the hydroxide pellets or adsorbed water after powdering the samples, the hydrogen background was corrected by the subsequent subtraction of a Lorentzian (fitted in the range 1-50 Å^{-1}) and 2nd order polynomial (fitted in the range 6-40 Å^{-1}) function. The latter resulted in better convergence of the scattering function to 1. For the Fourier transformation, the scattering function was used starting from 0.9 Å^{-1}, to avoid the influence of small angle scattering. For the termination value, Q_{max}, 21.5 Å^{-1} was selected. X-ray scattering was performed at the Advanced Photon Source of Argonne National Laboratory, at beamline 11-ID-B with 60 keV and a distance from sample to detector of 180 mm. The measurements lasted for 3 minutes per scan with a beam size of 0.2x0.2 mm. The 2D diffraction data were analyzed and converted to 1D using PDFfit2D [44]. Subsequent data reduction with PDFgetX2 [156] enabled the calculation of the scattering function and the Fourier transformation to the PDFs. For the latter, the same Q_{min} and Q_{max} was used as for the neutron data: 0.9 and 21.5 Å^{-1}.

A normalization of the PDFs was performed by comparing their chemical composition (by XRF from [147, 190]) with the area of the Si-O correlation. To calculate this area, the g(r) was calculated by the formula: $g(r) = G(r) + 4\pi r\rho_0$, where ρ_0 is the atomic number density which can be derived from the slope of the PDF curves (at 0-1.4 Å). The average slope of the PDFs transformed with 3 different Q_{max} values was used (20, 21.5 and 28). The Si-O correlation was fitted with a Gaussian curve and the area of the Gaussian was normalized with

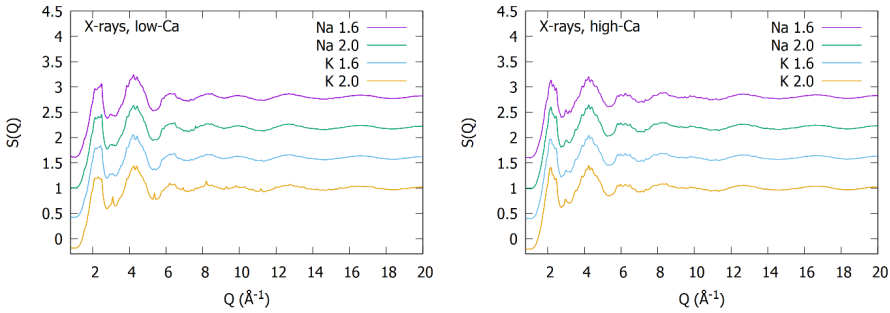

Figure 3.19: X-ray scattering functions of the IPs. Upper: Low-Ca slag, lower: High-Ca slag

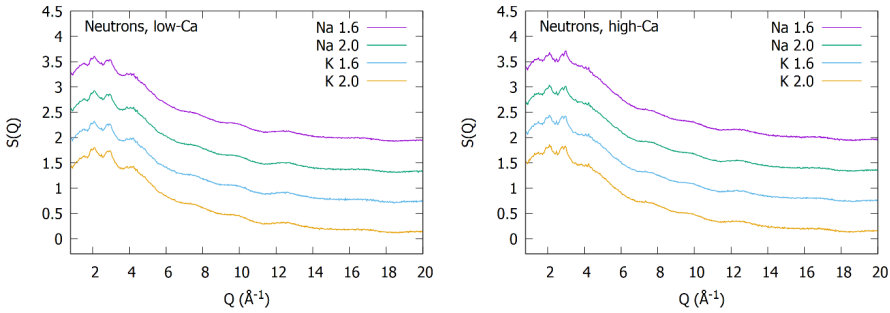

Figure 3.20: Neutron scattering functions of the IPs. Upper: Low-Ca slag, lower: High-Ca slag

respect to the molar fraction of Si derived from XRF.

3.4.3 Results and discussion

Reciprocal space: Scattering functions

The data in reciprocal space are shown for the X-ray and neutron scattering in Figure 3.19 and 3.20, respectively. Only a minor content of crystalline phases is observed, indicated by sharp peaks in the scattering function. Identification of the corresponding crystalline phases was performed by converting Q to equivalent 2θ angles for $Cu_{K\alpha}$ radiation, after which it can be compared to X-ray diffraction databases. This way, the same minor phases as in the slag were

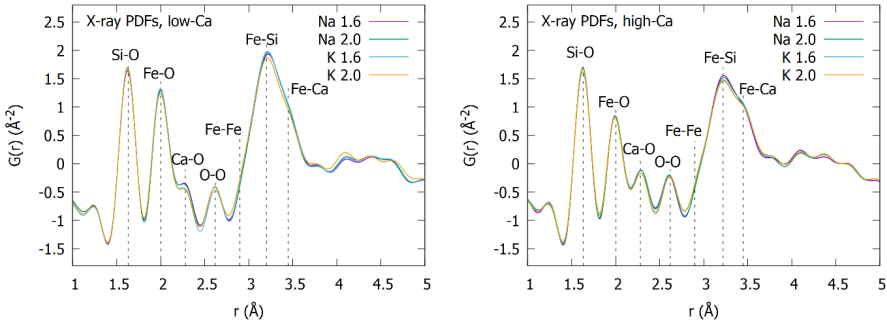

Figure 3.21: X-ray PDFs of the low-Ca (top) and high-Ca IPs (bottom).

detected: ferrosilite, hedenbergite and quartz [147]. The scattering functions of the 8 samples show great similarity. For one precursor, they look identical, apart from the X-ray scattering function of the Low-Ca K 2.0 sample, where an elevated amount of the ferrosilite crystalline phase is observed. This can be attributed to inhomogeneities in the sample. As the beam size of 0.2 x 0.2 mm is not orders of magnitude larger than the particle size of the larger fraction of the slag (particles up to 0.05 mm are probably present), this can affect the measurement. Probably, a bigger grain of the slag was present at the position of the beam, providing an overestimation of the amount of slag that was really present in the sample. The scattering functions of the IPs which use different slags as precursor show slight differences, which are mostly revealed in the shape of the first peak of the X-ray scattering functions ($\sim$ 2 Å^{-1}).

Real space: Pair distribution functions

The transformation to real space provides a more intuitive picture, as in Figure 3.21-3.28 the peaks can be correlated with atomic distances. The X-ray PDFs in Figure 3.21 seem quite similar, however, differences are present, which will be explained below in the text and visually aided by zooms on specific areas of the PDF. The neutron PDFs in Figure 3.22 show larger differences. These are also better revealed using zoomed sections and are discussed later. All samples clearly show the first neighboring atoms, Si-O (1.62 Å), Fe-O (2.00 Å) and Ca-O (2.25-2.30 Å). The O-O correlation presents itself at 2.62-2.65 Å. The next-to-nearest neighbor of Fe is most probably Si, Ca or another Fe, revealed by the dominant Fe-Si (3.20-3.25 Å), Fe-Ca (3.45-3.50 Å) and Fe-Fe (2.9-3.0 Å) correlations. These positions are all similar to section 3.3. The Ca-O correlation is located at 2.3 Å [35, 204], where also the Na-O distance should approximately be in the sodium silicate activated samples [199, 203]. However,

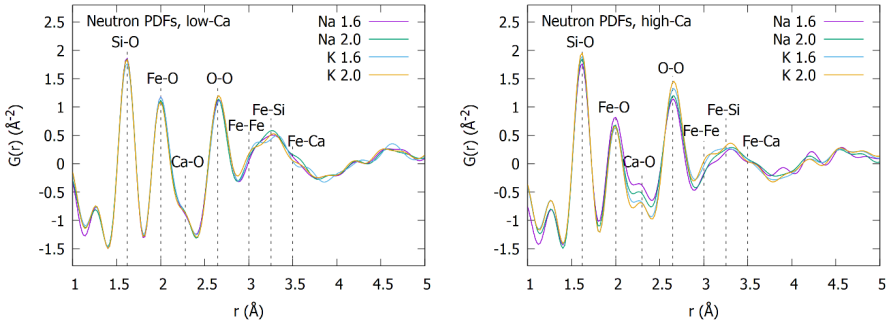

Figure 3.22: Neutron PDFs of the low-Ca (top) and high-Ca IPs (bottom).

by comparison of the Na and K samples in Figure 3.21 and 3.22 or the slags in [147], the (probably broad) contribution of Na-O seems only minor. The K-O correlation is present around 3 Å [11], which can be slightly distinguished by comparing Na and K samples in Figure 3.22.

A wider range of values is possible for the Fe-O distance (1.85-2.14 Å), as this is dependent on the oxidation state and coordination number of Fe [201, 212, 4] (see also section 3.3). Section 3.2 and 4.1 show the presence of a combination of ${}^{IV}Fe^{2+}$, ${}^{V}Fe^{2+}$ and ${}^{V}Fe^{3+}$ or ${}^{IV}Fe^{3+}$ in similar precursors and fully cured samples. The combination of these states is in good correspondence with the observed distance, 2.00 Å, when compared to literature values [199, 212, 83, 4]. This combination of oxidation-coordination states was verified in chapter 3.3 for the slags. A more elaborate analysis of the changes during the reactions towards inorganic polymers will be revealed in chapter 4. The Fe-O correlation is at the same position for all activating solution. The activating solution does not seem to play a role in determining the coordination number or oxidation state of Fe in the final binder, but this might be attributed to competing effects, e.g. less residual slag (would result in more shift towards shorter distance).

The difference of the curves of the PDFs with respect to the slags studied in chapter 3.3 is investigated in more detail in Figure 3.23 by subtracting the slag curves from the inorganic polymers. A decrease just before and increase just after 2 Å represents the shift of the Fe-O correlation to lower distances and indicates the oxidation of the Fe from 2+ to 3+ [147, 136, 176]. An increase around 2.3 Å indicates the rise of a Na-O correlation, therefore this is only observed in the Na 1.6 and Na 2.0 samples. Likewise the increase at 3 Å can be attributed to the K-O correlation in the K 1.6 and 2.0 samples. Around the same position a difference in the Na activated samples is also observed with

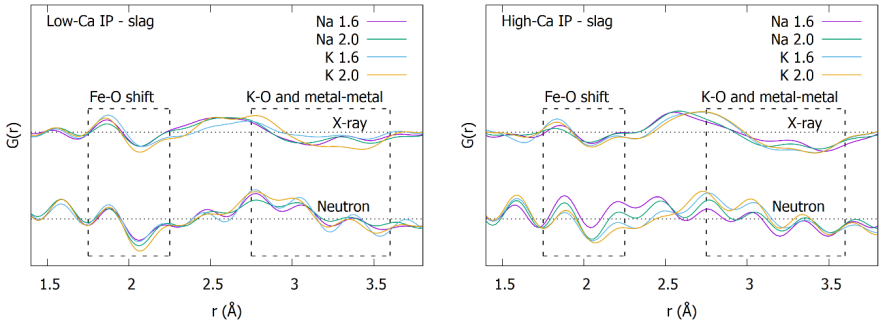

Figure 3.23: Difference plots of the IPs with respect to the slag.

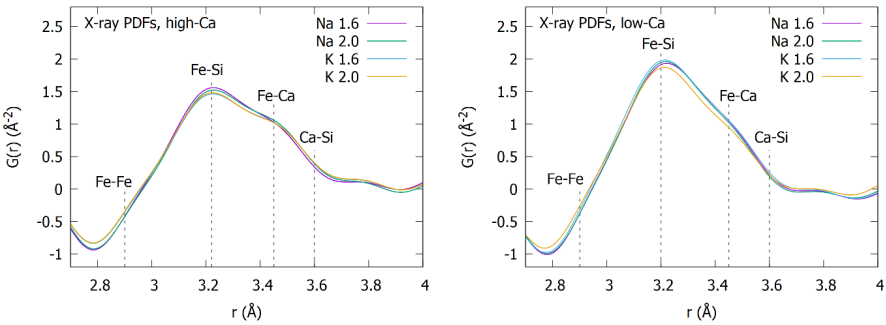

Figure 3.24: Detailed view on the metal-metal correlations in the X-ray PDFs of IPs.

respect to the slag and the changes can thus not be solely attributed to the K-O correlation. A contribution from the metal-metal correlations is expected. The decrease of the Fe-O distance due to the oxidation to Fe^{3+} results in a lowering of the Fe-X distance (X = Fe, Si, Ca) [199, 147]. In the high-Ca slag, the lowering of the intensity around 3.4-3.5 Å (the Fe-Ca correlation) might indicate the segregation of Fe and Ca.

A zoom on the metal-metal correlations is presented in Figure 3.24 for the X-ray data and in Figure 3.25 for the neutron data. The potassium samples in the high-Ca system show a consistent increase at the position of the Fe-Fe correlation, because of the contribution of the K-O correlation. A small shoulder at 3.6 Å is visible (especially in the high-Ca IP neutron data). At this position the Ca-Si correlation is observed in C-A-S-H or C-S-H networks [117, 122]. Together with the lowering of the intensity of the Fe-Ca correlation this can

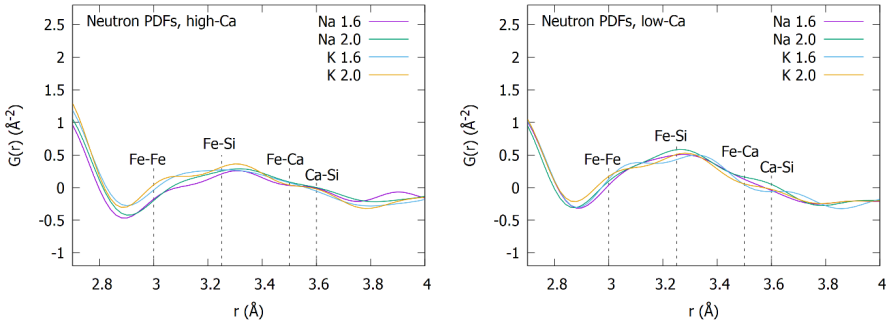

Figure 3.25: Detailed view on the metal-metal correlations in the neutron PDFs of IPs.

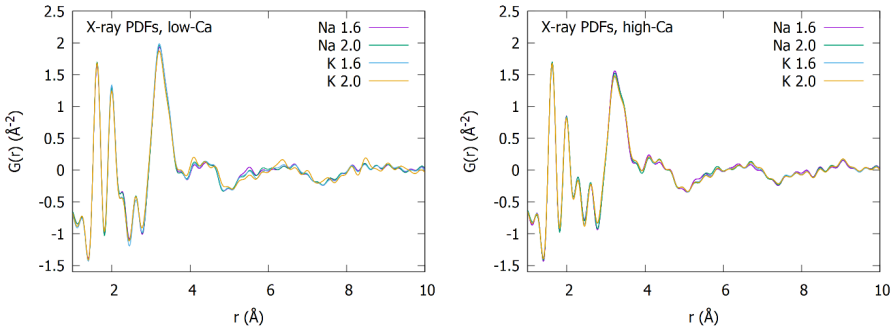

Figure 3.26: Longer range of the X-ray PDFs of IPs.

thus indicate the presence of a Ca-rich phase. The signal is very small and there is no other clear data supporting this suggestion, future work should provide more clarity on this aspect.

At higher distances, Figure 3.26 and 3.27, the differences are very limited. The intermediate range order or network topology is not changed by changing the activating solution. The absence of drastic differences in the figures above poses the question whether the structure of the alkali-activated Fe-rich slags can be adapted by the processing conditions. Comparing different precursors in Figure 3.28, it is clear that the atomic structure of the Fe-rich AAMs is largely determined by its precursor slag structure. The slag structure is therefore the most important parameter for adapting the structure and stability of the formed phases and thus will likely influence the mechanical performance and durability of the AAM. However, the effect of the microstructure and its permeability is

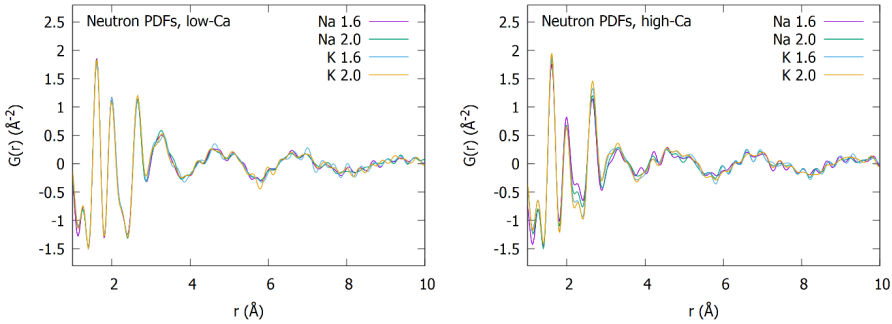

Figure 3.27: Longer range of the neutron PDFs of IPs.

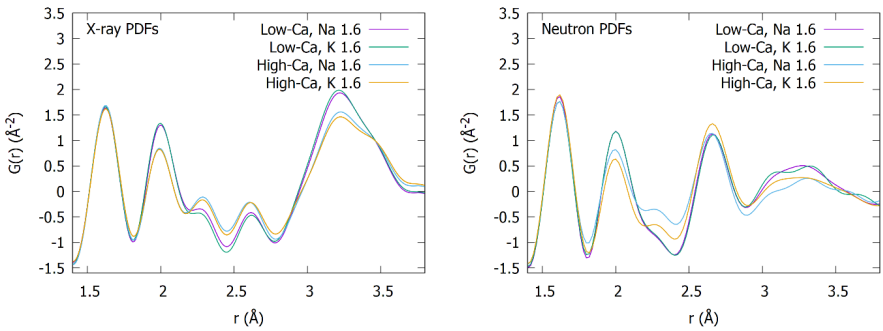

Figure 3.28: X-ray (top) and neutron PDFs (bottom), comparing the IPs from different precursors.

studied here, which is known to have a very strong effect on these properties. Hence, it is envisioned that the activating solution can independently be used to design the micro- and pore structure [38, 180, 16, 136, 66] or to tune the kinetics [92, 137, 66], without changing the fundamentals of the material.

3.4.4 Conclusions

Inorganic polymers were made from two glassy slags with chemical composition in moles: 0.17CaO-0.83FeO-SiO_2 and 0.33CaO-0.67FeO-SiO_2. Sodium and potassium silicate solutions with molar ratios SiO_2/M_2O of 1.6 and 2 and H_2O/M_2O of 20 (M = Na or K) were used as activator. Inorganic polymers resulting from the same slag showed similar pair distribution functions to each other and to the precursor slag and are thus expected to have similar molecular

structures, despite the use of different activating solutions. To have a significant effect on the molecular structure, the slag composition should be considered, as in the pair distribution functions from the two slags the differences are more extensive in comparison with the differences between samples using different activators and the same slag.

Chapter 4

Mechanism and kinetics of CaO-FeO$_x$-SiO$_2$ binder formation

4.1 The start of oxidation of Fe and the formation of a mixed valence binder

This section is based on the submitted paper: A. Peys, A. P. Douvalis, V. Hallet, H. Rahier, B. Blanpain, Y. Pontikes, "Inorganic polymers from CaO-FeO$_x$-SiO$_2$ slag: the start of oxidation of Fe and the formation of a mixed valence binder".

Contributions of the authors: In this paper, A. Peys made the experimental design and synthesis of samples. The Mössbauer experiments at the University of Ioannina were performed together with A. P. Douvalis. The analysis of the experiments was performed in discussion with A. P. Douvalis. All co-authors contributed to the discussion of the results and the formulation of the research questions.

Abstract

Belonging to the family of alternative cementitious materials, inorganic polymers are rising in importance because of the drive to decrease CO_2 emissions of concrete production. A synthetic Fe-rich slag resembling industrial copper or lead slags, was mixed with a sodium silicate activating solution. ^{57}Fe Mössbauer spectra analyses indicate that the oxidation reactions are taking place simultaneously with the polymerization reactions. The slag contains Fe^{2+} states and a small amount of Fe^{3+}. During polymerization a new octahedral Fe^{2+} state is formed, while oxidation is manifested through the appearance of an additional Fe^{3+} state. The reactions continue after setting, lowering the relative contributions of the slag in the Mössbauer and FTIR spectra of the samples. The Na^+/Fe^{3+} molar ratio after 28 days is approximately 1, suggesting the participation of tetrahedral Fe^{3+} in the silicate framework, charge balanced by Na^+.

4.1.1 Introduction

In search for alternative cementitious materials, geopolymers [29] and alkali activated materials (AAM) [155] have received wide attention. More recently, a push for circularization of the economy encouraged metallurgical companies to find alternatives for their residues. In light of this, research in inorganic polymers (IPs) is expanding to ferrosilicate precursors, for instance slags from the non-ferrous metal industries. It was shown that these residues can be increased in reactivity by rapid cooling [150] or hot stage slag engineering [190], while the IPs thereof obtain mechanical properties comparable to geopolymers, i.e. compressive strengths reaching up to 80 MPa [92]. They have shown to be environmentally important, reducing environmental impacts down to 17% of that of ordinary Portland cement (OPC) [145].

Despite these interesting properties and because of the novelty of the understanding that ferrosilicate precursors can be used in alkali-activation, fundamental knowledge on the chemistry of the system and the structural rearrangements during formation is scarce. Using isothermal calorimetry it was shown that, chemically, iron-rich inorganic polymers seem to follow a 2 stage reaction pattern: dissolution and polymerization [92, 137]. As such, they are comparable to their aluminosilicate counterparts, where calorimetric techniques are often used to distinguish these two reaction stages [218, 161] or to compare the reactivity of different formulations [93, 99, 146]. More thorough analysis of calorimetry results also enables the calculation of the reaction enthalpy and subsequent determination of the stoichiometry of the chemical system [158] or

the determination of the rate limiting step in the formation [157]. In terms of the evolution of the molecular structure, in-situ Fourier transform infrared (FTIR) spectroscopy is probably the most used technique, mainly because of its accessibility. Although success is seen for aluminosilicates [166, 65], in-situ FTIR by itself did not show the evolution of the structure sufficiently clearly [137] and the exact reaction mechanism therefore remains unclear. However, the results in chapter 3.1 have increased the understanding of the infrared spectrum of ferrosilicate precursors and their alkali-activated products. The main interesting feature in the spectra is the Si-O stretching band. The position of this band in the precursors varies between 950 and 850 cm^{-1}, depending on the amount of network modifiers per silicon atom in the silicate phases of the slag. This band shifts to approximately 950 cm^{-1} after alkali-activation. This was attributed to a higher degree of polymerization, because of the (at least partial) incorporation of the Fe^{3+} species in the network (chapter 3.2 and 3.3).

The aforementioned oxidation was experimentally observed using ^{57}Fe Mössbauer spectroscopy by Lemougna et al. [102] and in chapter 3.2. In these works the success in providing information for the oxidation state of iron (Fe^{3+}) in the IP binder, did not expanded to the level of the exact description of the coordination of iron. Chapter 3.2 suggested 4- or 5-fold coordination. Similarly, the X-ray absorption spectroscopy (XAS) measurements in chapter 3.2 confirm the oxidation state of the binder phase and suggest an average coordination number of 5. An important characteristic referred to the formation of the binder is that the evolution over time of the oxidation reaction is unknown. Mössbauer spectroscopy measurements can be performed on solutions after freezing in liquid nitrogen temperatures [175, 33]. As this practically decelerates the reaction kinetics towards negligible speeds, it enables their ex-situ study [91, 80]. In-situ kinetic studies have also been performed using synchrotron radiation techniques, e.g. X-ray/neutron total scattering on the alkali-activation of metakaolin [205, 203] and blast furnace slag [204, 50]. With these techniques, the short and intermediate range ordering can be investigated in great detail. The results of these studies are often interpreted with the help of theoretical modeling techniques [206, 213], which increases the understanding of the molecular structure or formation mechanism to a great extent.

In the present section, a combination of ^{57}Fe Mössbauer spectroscopy and attenuated total reflectance Fourier transform infrared (ATR-FTIR) spectroscopy is performed ex-situ up to 28 days after mixing to provide details on the mechanism of formation of the inorganic polymer structure. ^{57}Mössbauer spectroscopy probes the evolution of the iron oxidation state as well as coordination changes. More details on the development of the silicate network are pursued with ATR-FTIR spectroscopy. Isothermal calorimetry

measurements form a base of comparison for the kinetics, by collating the time when the changes in Mössbauer and ATR-FTIR spectroscopy appear with the observed heat flow. The observations from these experimental techniques are combined to suggest the timing of oxidation reactions and to provide information on potential intermediate stages of the material, formed between the initial slag and the final IPs studied in chapter 3. As such, a step is taken in unraveling the mechanism of formation of iron-rich IPs.

4.1.2 Experimental methods and materials

The precursor slag with chemical composition given in Table 4.1 was water quenched from the melt to maximize the amount of glassy phase in the precursor. The precursor hereby replicates a composition often used in non-

Table 4.1: Chemical composition of precursor slag in wt.%, obtained from XRF (estimated relative error 10%).

FeO	SiO_2	CaO	Al_2O_3	MgO
47	34	12	5	2

ferrous metallurgy, but including only the major elements FeO, SiO_2, CaO and Al_2O_3 (a minor content of MgO was detected due to impurities in the raw materials). Milling was performed to reach a specific surface of 4000 $\pm$ 200 cm^2/g measured by the Blaine method. The chemical composition was measured standard-less with wavelength dispersive X-ray fluorescence (XRF) on a Philips PW 2400. The glassy phase in the precursor was quantified by X-ray diffraction (XRD) after mixing with 10 wt.% of internal zincite standard in a McCrone mill. A Bruker D2-Phaser with $Cu_{K\alpha}$ radiation was used for these measurements with 30 kV-10 mA, a slit size of 0.6 mm and an anti-scatter slit of 1 mm. With these settings, no crystalline peaks could be observed apart from those of zincite; the amount of glassy phase is estimated to be $>$ 97 wt.%. The IP mixture consisted of the above described precursor and a sodium silicate solution with molar ratios SiO_2/Na_2O of 1.6 and H_2O/Na_2O of 20. The solution/slag mass ratio was 0.45.

Isothermal calorimetry was performed using a TAM Air at 20 °C. A sample with 4 g of slag was mixed for 90 seconds and transferred into the microcalorimeter. Data is presented from 53.5 minutes of stabilization in the machine (+ 26.5 minutes preparation). The first dissolution heat is not monitored as this information was not needed for the present study. ATR-FTIR spectroscopy was performed on a Bruker Alpha-P, which uses a diamond ATR crystal. A resolution of 4 cm^{-1} was selected and a measurement considered 32 scans.

Before setting, for measurements after 6 hours or less, a drop was measured without applying pressure on the paste in the ATR-cell. Because the powder is not pressed against the crystal, a relatively higher intensity will come from the solution, where the changes are anticipated to be the most interesting. For later reaction stages (> 6 hours), the reported spectrum is the average of 2 measurements on powdered samples (these were pressed against the crystal). ^{57}Fe Mössbauer spectroscopy measurements were performed to investigate the evolution of the state and environment of the Fe atoms during reaction. Gamma rays were emitted from a source using the decay of ^{57}Co in Rh matrix kept at room temperature. The samples were measured in transmission geometry on a constant acceleration spectrometer at 77 K. The reported isomer shift (IS) values are given relative to α-Fe at room temperature. The IMSG software [34] was used for the fitting of the spectra. Before setting, the samples were prepared by adding a drop of paste in the holder and freezing this in liquid nitrogen to solidify the material and stop the reactions. At later stages of the reaction after hardening, the materials were powdered and pressed in the sample holder before freezing and loading into the spectrometer. The effectiveness of this freezing to stop the reactions was tested by measuring a sample that reacted for 3 hours and for 3 hours + 14 days in liquid nitrogen. These two measurements resulted in spectra with no experimental difference and led to the conclusions that: i) the reactions are halting after freezing the samples at 77 K and ii) the samples do not change through the duration of the measurement, which has a typical length of 24 h. For both the ATR-FTIR and ^{57}Fe Mössbauer spectroscopy measurements, the samples were held in a closed bottle at 21 ± 1 °C prior to the experiment-specific sample preparation procedure mentioned above.

4.1.3 Results and discussion

Isothermal calorimetry measures the heat flow, proportional to the reaction rate, coming from the reactions in the sample. It can thereby provide the time-frame in which the different reaction stages occur. The heat flow, Figure 4.1, shows the exotherm which in geopolymers is often used to indicate the timing of the polymerization reactions [161]. The maximum heat flow in Figure 4.1 is observed around 4 hours, which was also approximately the time of setting; the main part of these polymerization reactions seems to occur between 3 and 24 hours after mixing. It should be mentioned that chapter 3.2 showed that in the Fe-rich IPs the Fe^{2+} in the presented slag is oxidized to Fe^{3+} during and/or after the synthesis. A contribution from this reaction is not distinguished here or in previous studies [92, 137]. The oxidation most probably occurs simultaneously with the dissolution or polymerization, or occurs on a longer time-scale and it is not noticed as a separate phenomenon in the calorimetry measurements.

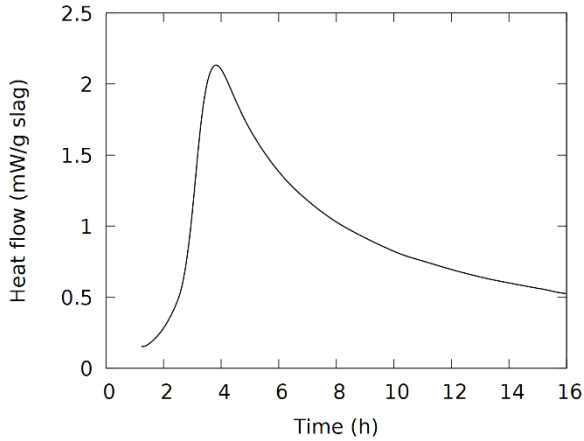

Figure 4.1: Heat flow in isothermal calorimetry at 20 °C from the first 16 hours after mixing.

The kinetics of the oxidation of iron are elucidated with ^{57}Mössbauer spectroscopy. Figure 4.2 presents the raw spectra of the slag and IPs with curing times up to 28 days. There it can be seen that the slag spectrum is dominated by contributions with IS values of $\sim$ 1 mm/s and quadrupole splitting (QS) values of $\sim$ 2.5 mm/s [62, 24], however the asymmetry of the lower and higher velocity resonant line intensities suggests that there must be at least two Fe^{2+} contributions that should have different characteristics, and in particular different QS values. Moreover, a minor peak at $\sim$ 1.0 mm/s suggests the presence of an additional minor Fe^{3+} state. Thus the lowest number of components that could fit the slag spectrum was three, two different Fe^{2+} (S1 and S2) and one Fe^{3+} (S3). The fitting result using this model, in which all three components were allowed a Gaussian-type symmetric spreading of their QS values (Δ QS) to simulate the observed broadening of the absorption resonant lines, is given in Figure 4.3 and the Mössbauer hyperfine parameters are presented in Table 4.2. The IS and QS values of S1 and S2 correspond to high spin (S=2) Fe^{2+} in oxides or silicates [62, 24], while the corresponding values for the minor S3 lie at the upper limit of high spin (S=5/2) Fe^{3+} ions found in such compounds [62, 24]. This result shows that the particular slag contains a majority of Fe^{2+} combined with a minority of Fe^{3+} species.

Moving to the IP sample spectra, a more detailed observation of Figure 4.2 (insert dashed rectangles) reveals the appearance and increase of the intensity of one additional absorption contribution at $\sim$ 0.75 mm/s and a second at $\sim$ 2.50 mm/s as the reaction time increases. These are evidences for the appearance of

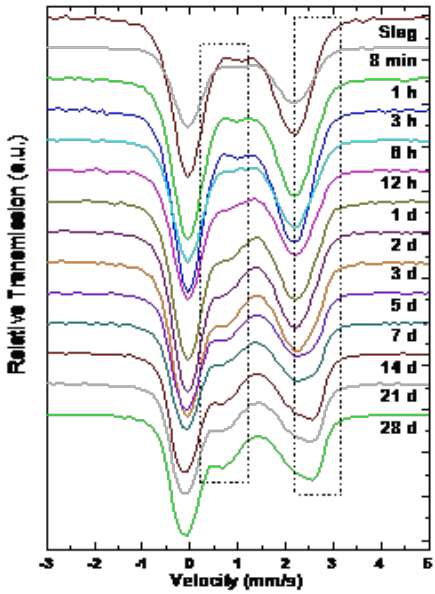

Figure 4.2: Raw ^{57}Fe Mössbauer spectra during the first 28 days of reaction, where the numbers indicate the reaction time after mixing, in minutes (min), hours (h) or days (d). The dashed rectangles indicate the regions where the high velocity parts of the new Fe^{3+} and Fe^{2+} QS doublet contributions of the binder gradually appear.

two additional components, one of Fe^{3+} and one of Fe^{2+} character respectively, during the reaction of the slag with the activating solution. Consequently, the fitting of the IPs spectra could be performed by keeping the 3 contributions of the slag (S1, S2, S3) and adding one new Fe^{2+} (IP1) and one new Fe^{3+} (IP2) contribution to the fitting model, which represent the iron ions in the binder part of the newly formed IP. The parameters of the slag components were fixed to the values resulting from fitting the slag spectrum, the intensities and absorption areas (AAs) of components S1 and S3 were made dependent on the major S2 component to result in the same ratio of AAs as in the slag and only the intensity of component S2 was left to vary in the fits. As such, the IP spectra are fitted with a combination of the slag spectrum and the new Fe^{2+} and Fe^{3+} components. This model embeds the idea that the part of the

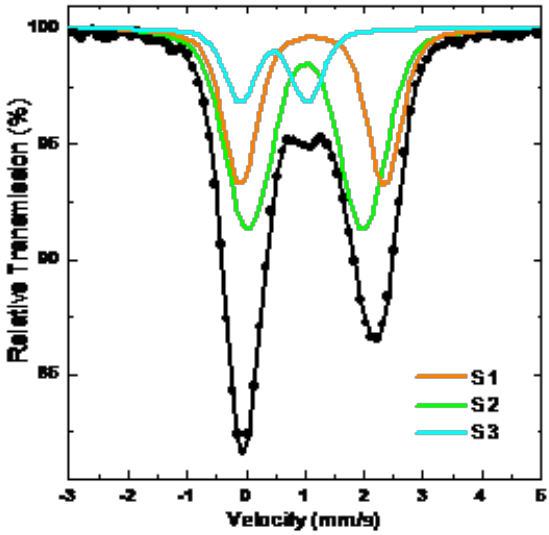

Figure 4.3: The ^{57}Fe Mössbauer spectrum of the slag with the three components used in the fitting model shown in different colors. S1 and S2 are Fe^{2+} and S3 is Fe^{3+}.

slag that has not reacted with the activating solution to form the binder phase of the IP, is thought to be conserved in the form it had before the start of the reactions. Both IP1 and IP2 components were allowed ΔQS, however the asymmetry observed in the shape of the region of the spectra at around $\sim$ 2.50 mm/s, where the high velocity part of the additional Fe^{2+} doublet mostly contributes, led us to include an asymmetric ΔQS around the central QS values for component IP1. We have applied this model to the IP spectra with reaction times equal or longer than 6 h, as for the frozen solutions with reaction times shorter than 6 h the spectra are essentially the same as the slag spectrum within the experimental tolerance limits and according to their fitting results. The model described above gave excellent fitting results, some examples of which are shown in Figure 4.4.

The Mössbauer parameters of the two Fe^{2+} sites in the slag, S1 and S2, show similarities with the slag components in chapter 3.2. However, the composition of the slag there was found to be close to fayalite, while the IS and QS values here are close to those obtained for pyroxenes towards the ferrosilite composition, in which two sites with varying QS values are observed [62, 24]. The small amount

Table 4.2: Resulting hyperfine parameters values of the components used to fit the ^{57}Fe Mössbauer spectra. IS is the Isomer shift relative to α-Fe at room temperature, (QS) is the central value of the quadrupole splitting, ΔQS is the total Gaussian-type spreading of the quadrupole splitting and AA is the relative absorption area. The half line-width was fixed to $\Gamma/2$=0.14 mm/s to avoid interference with the ΔQS. For component IP1 the QS spreading is asymmetric around the central QS value and is given in the sense ΔQS<QS/ΔQS>QS. Typical errors include ± 0.02 mm/s for IS and QS and ± 5 % for AA. **The table continues on the next page.*

Time (days)	IS (mm/s)	QS (mm/s)	Δ QS (mm/s)	AA (%)	Component
0	1.23	2.43	0.44	32	S1
	1.12	1.94	0.65	54	S2
	0.58	1.12	0.38	14	S3
0.25	1.23	2.43	0.44	29	S1
	1.12	1.94	0.65	49	S2
	0.58	1.12	0.38	13	S3
	1.29	2.44	0.27/0.24	7	IP1
	0.48	0.72	0.16	2	IP2
0.5	1.23	2.43	0.44	27	S1
	1.12	1.94	0.65	44	S2
	0.58	1.12	0.38	11	S3
	1.29	2.56	0.28/0.20	11	IP1
	0.48	0.73	0.29	7	IP2
1	1.23	2.43	0.44	24	S1
	1.12	1.94	0.65	40	S2
	0.58	1.12	0.38	10	S3
	1.29	2.56	0.37/0.21	13	IP1
	0.48	0.81	0.38	13	IP2
2	1.23	2.43	0.44	23	S1
	1.12	1.94	0.65	39	S2
	0.58	1.12	0.38	10	S3
	1.29	2.51	0.43/0.22	14	IP1
	0.47	0.81	0.33	14	IP2
3	1.23	2.43	0.44	22	S1
	1.12	1.94	0.65	36	S2
	0.58	1.12	0.38	9	S3
	1.28	2.80	0.35/0.21	15	IP1
	0.49	0.79	0.34	18	IP2
5	1.23	2.43	0.44	20	S1
	1.12	1.94	0.65	33	S2
	0.58	1.12	0.38	9	S3
	1.28	2.86	0.33/0.10	20	IP1
	0.48	0.78	0.32	18	IP2

of Ca in the system brings the chemistry closer to a hedenbergite mineral The spread in the QS values for both components is quite large, showing that this is representing the glassy phase observed with XRD. Component S3 shows relatively large IS and QS values as well as a large ΔQS, it is thus another component in the glassy phase of the slag. Based on the absorption areas, the

Table 4.3: Table 4.2 for samples cured for 7-28 days (splitted from other samples for lay-out purposes).

Time (days)	IS (mm/s)	QS (mm/s)	Δ QS (mm/s)	AA (%)	Component
7	1.23	2.43	0.44	20	S1
	1.12	1.94	0.65	33	S2
	0.58	1.12	0.38	9	S3
	1.29	2.85	0.31/0.09	21	IP1
	0.46	0.77	0.35	17	IP2
14	1.23	2.43	0.44	17	S1
	1.12	1.94	0.65	28	S2
	0.58	1.12	0.38	7	S3
	1.28	2.90	0.30/0.07	28	IP1
	0.46	0.77	0.34	20	IP2
21	1.23	2.43	0.44	17	S1
	1.12	1.94	0.65	28	S2
	0.58	1.12	0.38	7	S3
	1.28	2.90	0.28/0.07	25	IP1
	0.46	0.78	0.35	23	IP2
28	1.23	2.43	0.44	16	S1
	1.12	1.94	0.65	27	S2
	0.58	1.12	0.38	7	S3
	1.28	2.90	0.28/0.07	27	IP1
	0.47	0.78	0.36	23	IP2

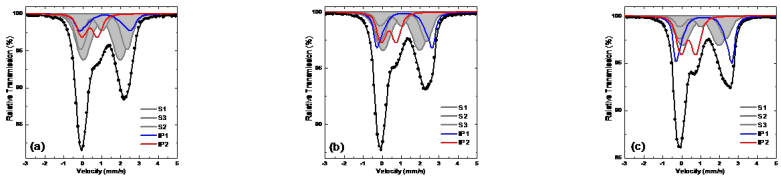

Figure 4.4: ^{57}Fe Mössbauer spectra of the IPs recorded at different reaction times: (a) 1 day, (b) 7 days, (c) 28 days. The slag components (S1, S2, S3) are shown as gray filled areas and the binder components (IP1, IP2) as colored lines.

$Fe^{3+}/\Sigma Fe$ ratio of the slag was 0.14.

The Fe^{3+} in the IP binder (component IP2) shows almost constant Mössbauer parameters throughout the reaction. The IS and QS values are similar as in the Fe^{3+} component of the binder in the samples of chapter 3.2 and thus suggest that an average of 5 fold or 4 fold coordination with rather high Fe-O distances is present. The low QS with respect to other glasses [125] shows, for this high spin Fe^{3+}, that the IP binder contains a higher symmetry of the ligands, i.e. a higher similarity of the species connected to Fe^{3+} or more symmetrically distributed around it [62, 24]. This might be an indication of the participation

of these Fe^{3+} ions in the silicate network as network formers, charged balanced by Na^{+}, as the network forming character would mean (for the example of a tetrahedron) that Fe^{3+} is surrounded by 4 bridging oxygen atoms, instead of 3 bridging and 1 non-bridging. The new Fe^{2+} site, component IP1, has not been observed in chapter 3.2, although similar Fe^{3+} sites as component IP2 have been found. This Fe^{2+} state thus seems to have been oxidized in later reaction stages or after milling these samples to a powder. Component IP1 shows larger IS and QS values than the Fe^{2+} components of the slag (S1 and S2), while its central QS values are increasing with reaction time, suggesting the presence of distorted, asymmetric octahedra, comparable with fayalite minerals [136, 24, 194], Fe-rich smectites [22], micas [47] or Fe(II) hydroxides [56]. The spread in QS for this component is asymmetric, being smaller for the higher and larger for the smaller than the central QS values. In addition the spreading for the higher than the central QS values is reduced considerably for the longer reaction times (> 3 days). The newly formed structure containing Fe^{2+}, can therefore be considered on the one side as being more ordered in environment of the Fe ion compared to the states in the slag, because of increased regularity in the angles and distances inside the FeO_6 octahedra. This is the part represented by the higher values in the QS spreading of the IP1 component. The declination in this part of the QS spreading with reaction time, indicates an increase in ordering of the FeO_6 octahedra during the development of this part of the binder. On the other hand the maintenance of a larger spreading for the lower than the central QS values, although also decreasing with reaction time, suggests that the newly formed structure containing Fe^{2+} is not unique in abundance, but could be composed of several cluster-type assemblies with different morphologies or interconnections.

The evolution of the absorption areas of the new contributions are illustrated in 4.5. Changes in the Mössbauer spectra do not happen immediately upon dissolution. This is not because of an insignificant extent of dissolution: The immediate start of the dissolution reactions was validated by measuring the concentration of the ions with induced coupled plasma optical emission spectroscopy [150]. No rearrangement of the Fe environment occurs, there is no oxidation or coordination change. The first changes are observed from 6 hours on, meaning reactions have started between 3 and 6 hours. This corresponds to the time where according to calorimetry the polymerization reactions start. The Fe^{2+} and Fe^{3+} IP components both emerge at this time stage. The largest increase in absorption area of the new components is observed in the first 24 hours, an observation which is analogous to the heat evolution. This similarity to the calorimetry is stressed in Figure 4.6, where the derivative of the sum of absorption areas of the new Fe sites with time is plotted. The heat flow should thus partially be attributed to oxidation (also exothermic as the polymerization). After the first 24 hours, the new contributions keep increasing in area, although

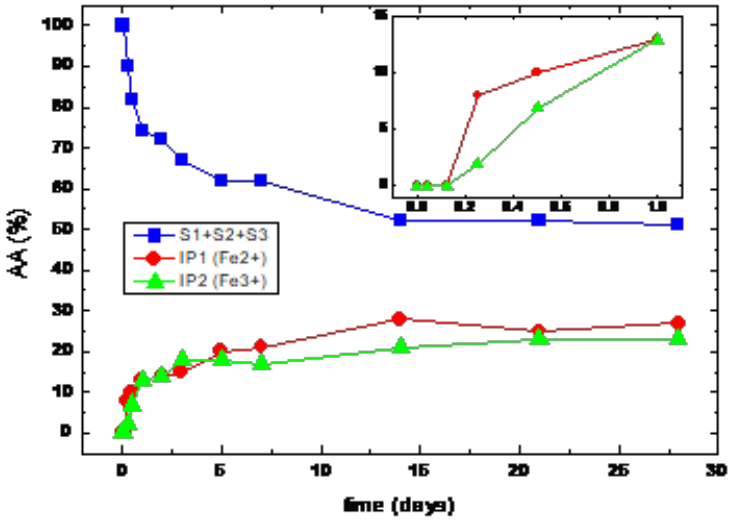

Figure 4.5: Evolution of the absorption areas of components IP1, IP2 and the sum of absorption areas of components S1, S2 and S3. The insert shows the short term ($\leq$ 24 hours) evolution of the absorption areas of the IP1 and IP2 components. The IP binder components only start forming after 3 hours (0.125 days).

at a slower rate. After 28 days, an AA of 27% is observed for the new Fe^{2+} state and 23% for the Fe^{3+}. At this point it is interesting to check the Na/Fe^{3+} ratio to confirm the possibility of having Fe^{3+} in the silicate network of the binder, like Al^{3+} in geopolymers. This ratio is $\sim$ 1 for the mixture presented here, making it possible that Na provides the charge balance for Fe^{3+}. The molar ratio Si/Fe^{3+} provides information on the environment of Si in the network. This ratio is $\sim$ 3; the dominant silicate species (using Engelhardt notation [40]) are thus Q^4(1Fe) and Q^4(2Fe).

The same time stages and samples are investigated with ATR-FTIR, Figure 4.7. The spectra are focused on the Si-O stretching band (700-1200 cm^{-1}). The "initial" spectrum, obtained after 8 minutes, shows two main features. The shoulder at 850 cm^{-1} is associated with the precursor slag, as can be derived from the dotted line representing the spectrum of the slag. The band at 984 cm^{-1} corresponds to the sodium silicate activating solution. The dissolution of the slag is reflected by the decrease in intensity of the shoulder around

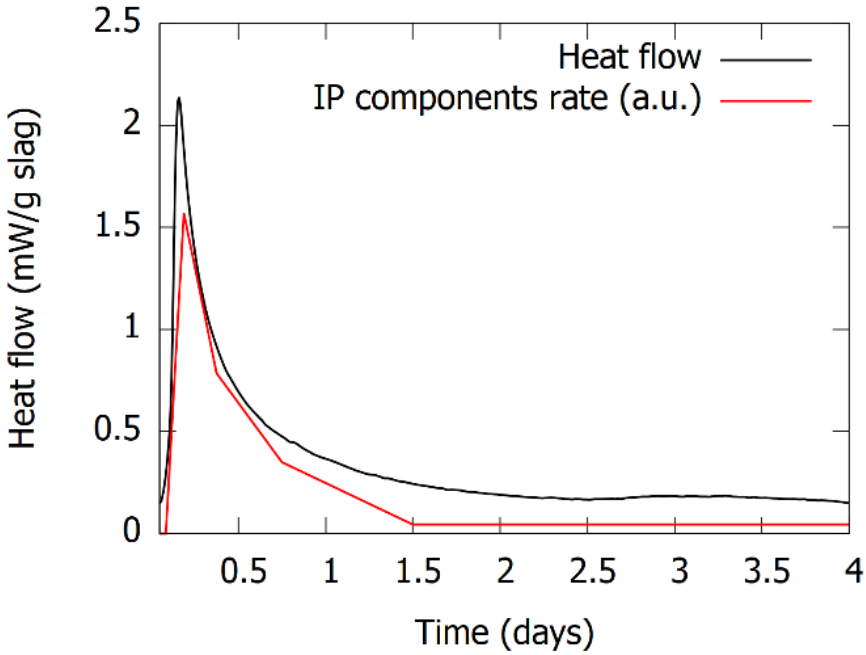

Figure 4.6: Comparison of the calorimetry measurements with the derivative to time of the sum of absorption areas of the IP components.

850 cm^{-1}. This is not only observed in the initial stages (Figure 4.7a), but extends to days after mixing (Figure 4.7b). The formation of the IP network is seen in the FTIR as the growth of a shoulder around 918 cm^{-1} and the shift of the band that was previously at 984 cm^{-1} (Figure 4.7a, notice the transition from 3 to 6 hours). Simultaneously, the shoulder at approximately 1100 cm^{-1} disappears, indicating the consumption of the highly connected silicate species from the activating solution. The difference plot in Figure 4.8 shows the changes between the starting point and the spectrum after 6 hours more clearly. The emergence of the shoulder at 918 cm^{-1} and the shift of the band at 984 cm^{-1} can both be linked with the emergence of a new band around 950 cm^{-1}. These transitions are associated with the observation from Mössbauer spectroscopy: the incorporation of Fe^{3+} in the silicate network (see the calculations in previous paragraph suggesting the presence of Q^4(1Fe) and Q^4(2Fe) Si) and thus the change from Si-O-Si linkages in the activating solution towards Si-O-Fe linkages in the IP binder results in a lower wavenumber of the Si-O stretching band in the IPs with respect to the activating solution. The position of the maximum of the Si-O stretching band after 28 days is

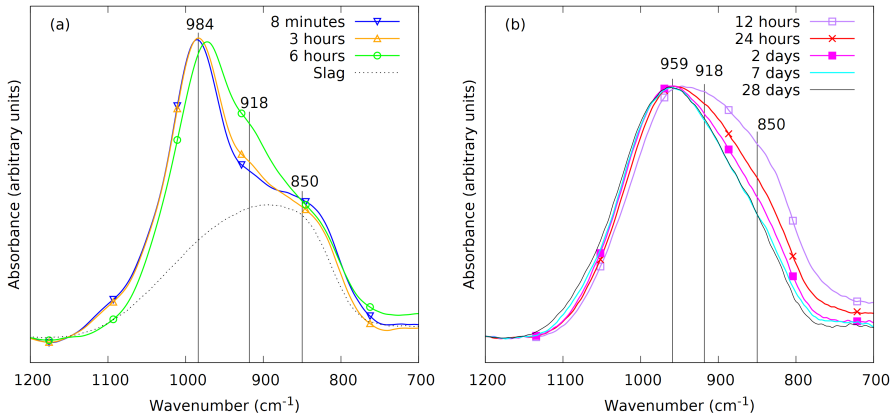

Figure 4.7: The FTIR spectra during the first 28 days of reaction. The spectra before setting are shown on the left in part a, these thus consider measurements in the liquid state, with the liquid in direct contact with the ATR crystal. The measurements on powdered samples after setting, pressed against the ATR crystal, are shown on the right in part b.

observed at 959 cm^{-1}, which is similar to what is observed for Si-O-Al linkages in aluminosilicate IPs (950-1000 cm^{-1}) [161, 166] and in chapter 3.1 where it was suggested that Fe has a similar impact on the band. In general, this shift of the stretching band to lower wavenumbers is due to the widening of the Si-O-T distance, compared to Si-O-Si, and is observed in a wide variety of materials [69].

Using the information from the above experiments it is now possible to suggest a reaction scheme for the Fe-rich IPs. A schematic representation of the reactions is shown in Figure 4.9. After dissolution, Fe-silicate species are present in the pregnant activating solution. The concentration of these species rises until polymerization takes place into the partially oxidized binder, which consists of tetrahedral Fe^{3+} and octahedral Fe^{2+} of which at least one should be present in the silicate framework. For the mixture studied in the present paper the starting time of polymerization-oxidation should be between 3 and 6 hours at 20 °C. The dissolution of the slag and polymerization and oxidation is ongoing until at least 28 days after mixing, however, it is very likely that the time-scale for finalizing the reactions is longer than the 28 days presented here. A comparison with chapter 3.2, where the contribution of the Fe^{3+} binder component was much larger and no Fe^{2+} binder component was observed, shows that a more complete oxidation happens in later stages of the reaction or during intensive milling.

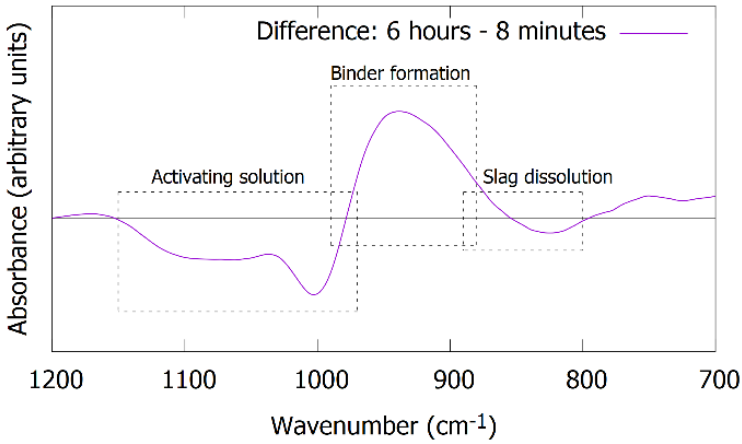

Figure 4.8: Difference plot of the FTIR spectra after 6 hours compared to 8 minutes, revealing more clearly the changes: (1) transformation of the activating solution, (2) the formation of the binder phase and (3) the dissolution of the slag.

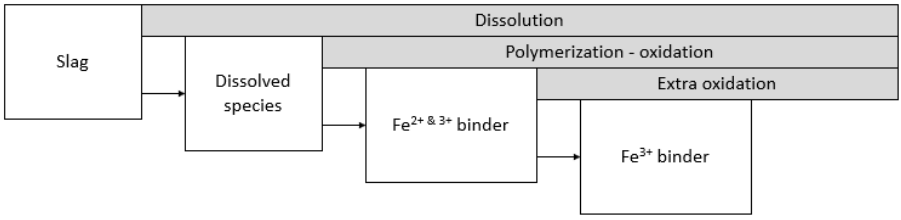

Figure 4.9: Schematic of the sequence of reaction stages.

The next sections (chapter 4.2 and 4.3) will study in detail the transition from the 28 days study presented here, revealing a combination of ${}^{IV}Fe^{3+}$ and ${}^{VI}Fe^{2+}$ in the binder, towards the fully oxidized structure observed in chapter 3.

4.1.4 Conclusions

The evolution of the molecular structure during synthesis of Fe-rich slag based IPs has been monitored with ${}^{57}Fe$ Mössbauer spectroscopy and infrared spectroscopy. Fe-rich slags mainly consist of Fe^{2+} (approximately 85% in

Mössbauer spectrum), whereas an IP binder was shown to contain both Fe^{2+} and Fe^{3+}. The first appearance of a new Fe^{3+} band in Mössbauer spectroscopy occurs after 6 hours of reaction at 20 °C and the main oxidation happened during the first 24 hours. It is suggested that this Fe^{3+} is situated in tetrahedral coordination in the silicate framework. At the same time, a novel octahedral Fe^{2+} component is found to form in the binder phase with Mössbauer parameters that combine a time-evolving structure trending towards fayalite or clay minerals, which approximately follows the same kinetics of formation as the Fe^{3+} state. This result is in line with the onset of the polymerization exotherm in calorimetry, between 3 and 6 hours, and the fact that the largest part of the heat from the reactions evolved in the first 24 hours. ATR-FTIR spectroscopy showed the incorporation of Fe in the silicate network. The dissolution, polymerization and especially oxidation reactions proceed beyond the investigated 28 days, at which a total 50% absorption area of the binder phase in the Mössbauer spectrum combines a 27% of iron ions as Fe^{2+} and 23% of iron ions as Fe^{3+}, compared to 86% Fe^{2+} and 14% Fe^{3+} in the precursor slag. This results in a Na/Fe^{3+} ratio of approximately 1 in the binder phase, revealing an important similarity with geopolymers where a Na/Al^{3+} ratio of 1 is observed. The Fe^{2+} binder state was not observed previously, whereas the Fe^{3+} binder state always had a higher absorption area in previous work. This is probably associated with oxidation at later stages or/and with the milling procedures performed in previous work which increase the surface of the material exposed to air and consequently to oxidation.

4.2 Formation mechanism from in-situ X-ray total scattering

This section is based on the submitted paper:
A. Peys, C. E. White, H. Rahier, B. Blanpain, Y. Pontikes, "CaO-FeO_x-SiO_2 inorganic polymers: Formation mechanism from in-situ X-ray total scattering".

Contributions of the authors: In this paper, A. Peys made the experimental design, synthesis of samples and the experiment at Argonne National Laboratory. The analysis of the experiments was performed in discussion with C. E. White. All co-authors contributed in the discussion and conclusions.

Abstract

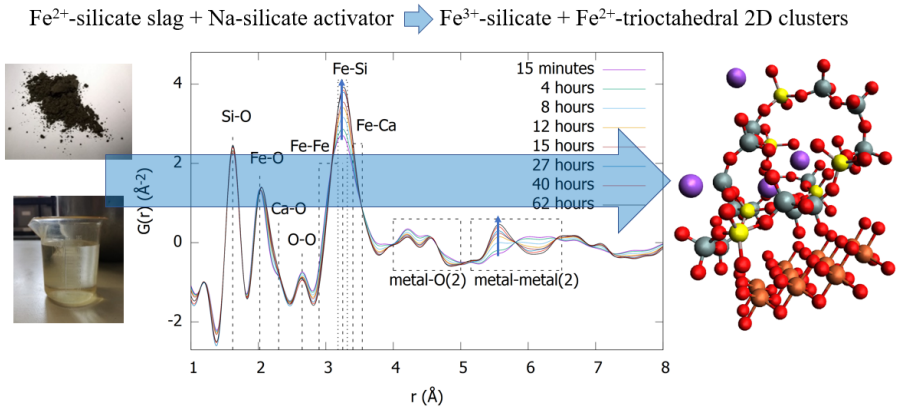

Figure 4.10: Graphical abstract: The formation of trioctahedral 2D clusters, detected by pair distribution function analysis.

The pursuit of low-CO_2 technologies has led to a surge in research on alternative cementitious materials for concrete-based construction applications, including inorganic polymers that are synthesized via alkaline activation of silicate precursors. Such alternatives have significant CO_2 savings compared with ordinary Portland cement-based concrete, and therefore have the potential to substantially reduce the 5-9% of global anthropogenic CO_2 emissions associated with Portland cement production. In recent years inorganic polymers have expanded to encompass Fe-rich precursors in addition to the more commonly employed aluminosilicate precursors such as metakaolin and class F fly ash. The formation mechanism of inorganic polymers from two Fe-rich synthetic slags has been assessed for two distinct activating solutions, specifically Na and K-silicate solutions. By employing in-situ X-ray total scattering and subsequent pair distribution function analysis the evolution of the local atom-atom correlations have been tracked, revealing that the formation mechanism involves three reaction stages. Initially the slag dissolves, resulting in iron silicate clusters in solution. The second reaction stage involves the formation of a binder phase, initially with Fe in both Fe^{2+} and Fe^{3+} oxidation states. The Fe^{2+} state is present in the form of trioctahedral layers, similar to those in $Fe(OH)_2$ or certain clays, while the Fe^{3+} is likely located in the polymerized silicate network. During the third reaction stage, the Fe^{2+} species are seen to transition to the Fe^{3+} state whilst the layered structure partially transforms, as seen via changes to the small-angle intensity in the reciprocal-space data.

4.2.1 Introduction

Determination of the formation mechanism of the binders in cement-based materials is key for understanding their early-age chemical and physical properties and associated long-term performance. Over the last couple of decades, there has been increasing interest in the use of novel alternative cements to decrease the environmental footprint associated with Portland cement production [128, 140, 119]. With the Portland cement industrial sector accounting for 5-9% of global anthropogenic CO_2 emissions due to $\sim$ 4 Gt of production, there is an overwhelming need to enhance the use of sustainable alternatives [119, 171]. Alkali-activated materials (AAMs) and inorganic polymers (IPs) are popular alternative cements [128, 140, 155] synthesized by mixing a solid silicate with a source of alkali, such as sodium/potassium hydroxides or silicates. The formation mechanism of IPs synthesized using an aluminosilicate precursor is quite well-known where two types of chemical reactions take place, dissolution (alkaline hydrolysis) and polymerization (polycondensation) [159, 161, 27]. The polymerization reactions can be further divided in 'gelation', 'reorganization' and 'polymerization and hardening' according to the state of the aluminosilicate network [36, 213].

Prior to discussing Fe-rich residues and their behavior in IP systems, the reaction mechanism of the more commonly studied aluminosilicate residues is elaborated. During dissolution of the aluminosilicate precursor, aluminosilicate and silicate oligomeric species are liberated from the solid [154], where the rate of aluminate release from the precursor has been shown to affect the homogeneity of the microstructure of the resulting binder [65]. The overall rate of dissolution is largely controlled by the precursor molecular/ionic structure [52, 150], the alkalinity of the activating solution [52, 158, 137] and the particle size of the precursor [157]. Once species are released into solution, they undergo polycondensation reactions to form larger aluminosilicate oligomers/nanoprecipitates according to the solution concentration and pH [154, 203, 204, 213]. An aluminosilicate three-dimensional network is created once the solution is supersaturated with respect to the aluminosilicate species, where aluminates are in tetrahedral configuration (charge balanced by the alkali, typically Na/K) [27, 159, 166]. Furthermore, for metakaolin-based IPs the topology of the aluminosilicate network has been seen to consist of four-membered rings [203]. Growth of the aluminosilicate network has been studied using coarse-grained Monte Carlo simulations, where for both metakaolin- and fly ash-based IPs the growth process depends on the activator chemistry. For hydroxide-activated IPs the network emerges via growth of many aluminosilicate particles that ultimately coalesce to form the three-dimensional network, whereas for silicate-activated systems growth is seen to follow an Oswald ripening-type

process, where after aluminosilicate particles have been established in the system the larger particles grow at the expense of the smaller one through dissolution/re-precipitation [213, 208]. During this later stage of reaction, hardening occurs together with an increase in the connectivity of the aluminosilicate network [154, 153]. Subtle longer-term changes to the network have been observed, specifically a slight increase in atomic ordering [205].

There are numerous industrial residues that contain large quantities of Fe. It is only within the last decade that their use in IPs has beeninvestigated where literature report varying mechanical performance and a water insoluble silicate-based binder [89, 139, 92, 81, 78]. These results are promising, if one also considers the lower environmental footprint of these binders. Compared to Portland cement-based systems, the environmental impact single score, i.e. aggregation of all midpoint categories, of IPs synthesized using Fe-rich residues is lower by as much as 77% while CO_2 emissions are reduced by up to 83%. [145]. From a formation mechanism viewpoint, these Fe-rich IPs follow a similar reaction sequence to aluminosilicate IPs, where dissolution is followed by an exothermic peak around the time of setting associated with polycondensation [137, 92]. However, during this process Fe changes oxidation state from II to III [102] (see also chapter 3.2), which, according to ex-situ ^{57}Fe Mössbauer spectroscopy in the previous section (chapter 4.1), is seen to occur in parallel with the polymerization reaction. The Fe^{3+}-based reaction product has an average coordination number of 4-5 (chapter 3.2) and possesses according to chapter 3.3 atomic correlations that are similar to the precursor slag.

This investigation elaborates on the knowledge obtained in these previous works, by providing details on the molecular structure and its evolution over time, beyond the oxidation state and coordination number of Fe. The study in this section uses in-situ high-energy X-ray total scattering to elucidate the atomic evolution of Fe-rich IPs during the early stages of reaction and to unravel the formation mechanism of the binder. This has been achieved by tracking the evolution of the total scattering data and pair distribution function (PDF) during the initial 80 hours reaction, where the speciation of the intermediate reaction products in solution has been identified together with the atomic arrangements of any metastable phases. The kinetics of individual reaction types have been studied via tracking of specific atom-atom correlations in the PDF data and the small-angle region in the reciprocal-space data. Finally, the impact of precursor composition (Fe/Ca molar ratio) and alkali metal in the activating solution (Na/K) on the formation mechanism and resulting atomic structure of the IP binder have been determined.

4.2.2 Material and methods

Two Fe-rich slags have been investigated, a "low-Ca" and a "high-Ca" slag as outlined in chapter 3.3, having approximate molar compositions of 0.83FeO-SiO_2-0.17CaO and 0.67FeO-SiO_2-0.33CaO, respectively. The activators were a sodium silicate solution (molar ratios $SiO_2/Na_2O = 1.6$ and $H_2O/Na_2O = 20$) and a potassium silicate solution (molar ratios $SiO_2/K_2O = 1.6$ and $H_2O/K_2O = 20$). These solutions were made by first dissolving the hydroxide (Sigma-Aldrich, 97.0 (NaOH) and 85 wt.% (KOH) purity) in distilled water followed by mixing with fumed silica (Sigma-Aldrich, 99.8 wt% purity). The silica-rich solutions were allowed to equilibrate for 48 hours. Pastes consisting of the activating solution and Fe-rich slag were mixed for 10 seconds by hand followed by 1 minute with a Fisher Scientific Vortex mixer, maintaining a water/slag mass ratio of 0.28 (solution/slag mass ratio was 0.40 for Na, 0.43 for K-silicate solution). For each X-ray scattering sample, the paste was loaded via suction into a 1 mm diameter polyimide capillary and both ends were sealed using modeling clay.

X-ray scattering experiments were performed at the Advanced Photon Source, Argonne National Laboratory, on beamline 11-ID-B using a monochromatic X-ray energy of 58.66 keV. In-situ scans were acquired for each sample every 10 minutes, starting at 15 minutes after mixing and ending after 15 hours. After these in-situ scans, the same samples were re-measured at 27, 40, 62 and 81 hours. A scan time of 2 minutes per sample was used along with a sample-detector distance of 180 mm. The 2D diffraction data were integrated using GSASII (intensity calibrated with respect to CeO_2). Calculation of the scattering function (S(Q)) and the Fourier transform to obtain the PDF (G(r)) in real space were performed using PDFgetX2 [156], with a Q_{min} of 0.9 $Å^{-1}$ and Q_{max} of 20 $Å^{-1}$. Simulated PDFs of the crystalline phases have been generated using PDFgui [44].

4.2.3 Results and discussion

Evolution in reciprocal space

An example scattering function is provided in Figure 4.11, showing the data for the Na-activated high-Ca IP at different stages of the reaction. The most pronounced change as a function of reaction time is the intensity increase at 0.3-0.4 $Å^{-1}$. This is the high-Q region of the small-angle scattering (SAS) intensity, which is cut off by the beam stop for the current X-ray total scattering setup to avoid oversaturation of the detector. Therefore, the maximum intensity cannot be directly related to the nanoscale morphology of the material, but instead

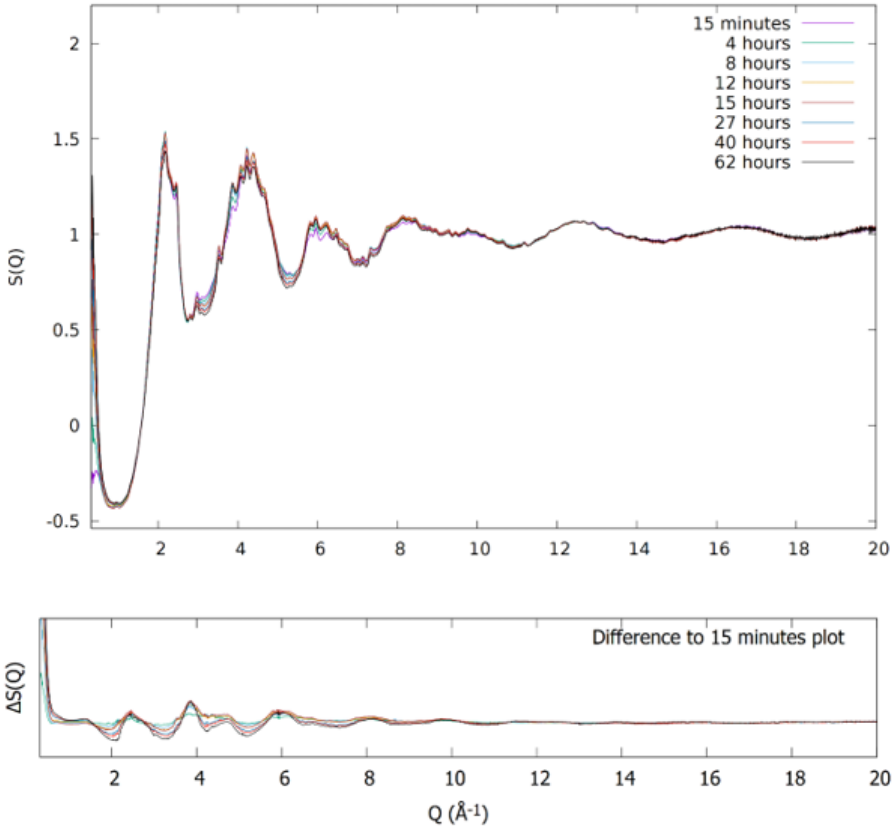

Figure 4.11: X-ray total scattering functions of Na-silicate activated high-Ca IP during the initial 62 hours of reaction. Upper plot: Full total scattering functions. Lower plot: Difference curves obtained by subtracting the initial data set (15 minutes) from those at later times.

will a combination of scattering from the material and contributions from the experimental setup. However, by examining SAS data from the literature for AAMs [179, 116, 210], the intensity at 0.3-0.4 Å^{-1} can be used to qualitatively analyze the formation of pores or a layered structure in the paste as it evolves. Although previous studies on metakaolin-based IPs have shown that this SAS region is attributed to pores in the paste [179], a layered structure cannot be discounted at this stage of the investigation since calcium-silicate-hydrate-type gels typical of Portland cements and Ca-rich AAMs/IPs can give rise to a basal peak in reciprocal space positioned between $\sim 0.35 \leq Q \leq 0.8$ [178].

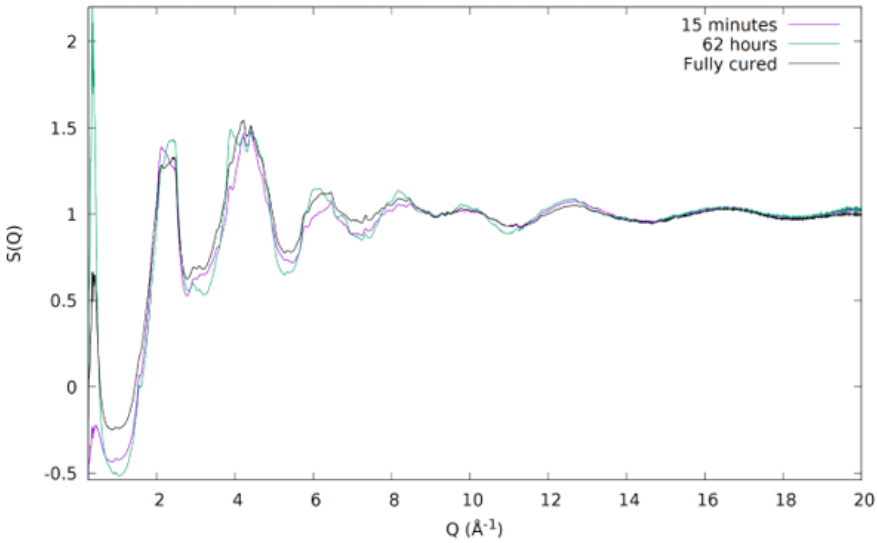

Figure 4.12: X-ray total scattering functions of Na-silicate activated low-Ca IP at 15 minutes, 62 hours and approx. 6 months after mixing. Note that the 6 months sample was cured in a sealed container, then crushed into a powder and loaded into a polyimide capillary before the measurement.

The minor differences at higher Q values (1-10 $Å^{-1}$) are shown more clearly by the difference plot given in Figure 4.11. The broad diffuse peaks in this figure show that the changes occurring during reaction are attributed to an amorphous-amorphous phase transition. In general, the in-situ total scattering functions of all samples have a similar appearance (see Appendix B) as the reactions progress and are close to those of the fully cured samples of chapter 3.3.

A comparison of the in-situ total scattering data after 62 hours for Na-activated low-Ca IP with a sample of the same chemical composition that was fully cured (61 days in a closed bottle), milled and loaded in the capillary as a powder (> 6 months in age, the sample is the same as in chapter 3.3 and was remeasured on 11-ID-B in conjunction with the in-situ measurements) shows that after 6 months the SAS region decreases in intensity, Figure 4.12. This suggests that the porosity or layered features that emerge during the early stages of the reaction are disrupted after the extended curing period (including milling and exposure of the powder to air), indicating that (i) the layered features are associated with an intermediate reaction product, or (ii) the pore structure is significantly augmented during the later stages of reaction.

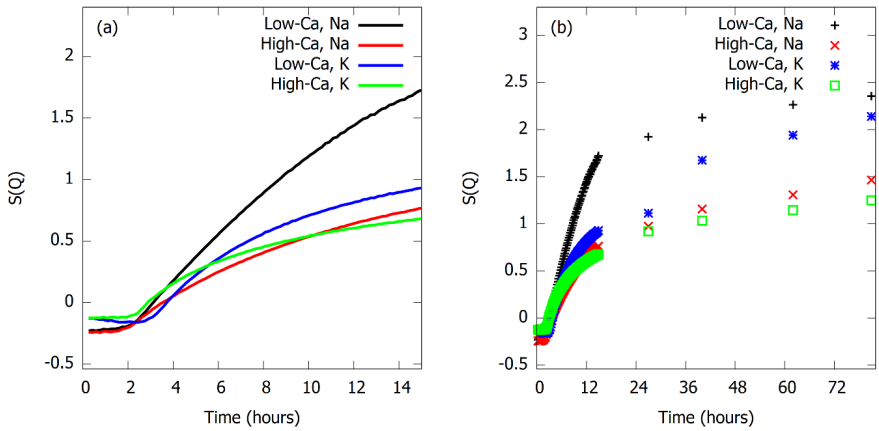

Figure 4.13: Evolution of the intensity of the small-angle region (maximum S(Q) within a Q range of 0.3-0.4 Å^{-1}) in the X-ray total scattering functions. (a) During the initial 15 hours of reaction and (b) up to 80 hours after initial mixing.

The intensity of the SAS peak as a function of time during the in-situ measurements is plotted for all samples in Figure 4.13. After an induction period of approximately 2 hours where the intensity does not change, the IP structure starts to form. As mentioned previously, without complementary experimental data on the evolution of the pore structure of Fe-rich IPs, it is difficult to assign these changes in the SAS intensity to a specific structural feature within the IP. However, Figure 4.13 indicates that the reactions are occurring faster for the low-Ca slag (steeper slope), which may be a direct reflection of faster reaction kinetics or the that the IP is forming (i) a more porous structure or (ii) a more ordered layered phase. Interestingly, setting of the Fe-rich slags occurs soon after the end of the induction period noted in Figure 4.13, typically ~ 3 hours after initial mixing.

In terms of the impact of the alkali (Na/K), there is a much stronger difference in the SAS region between sodium and potassium for the low-Ca systems compared with the high-Ca systems. While the Na-activated low-Ca sample is seen to initially react faster, which was also observed for metakaolin-based geopolymers [179], the reaction rate for the K-activated low-Ca sample seems to catch up with the Na-activated sample during the later stages of reaction, specifically between $\sim 27 - 40$ hours after mixing. According to Steins et al. [180], this behavior is associated with the higher amount of mesopores in the final structure of K-activated aluminosilicate IPs. In the present work, this is

difficult to confirm due to the decline in SAS intensity between 62 hours and $\sim$ 6 months, as seen in Figure 4.12.

Evolution in real space

The PDF data are presented in Figures 4.14 through 4.17 for the Na-activated low-Ca slag, Na-activated high-Ca slag, K-activated low-Ca slag and K-activated high-Ca slag, respectively. The atom-atom correlations corresponding to specific peaks in the PDF data are indicated based on chapter 3. The low-r correlations (Si-O, Fe-O, Ca-O and O-O) are denoted by vertical dashed lines whereas higher-r correlations have been highlighted using a finite width to indicate the variation of the center of the Fe-metal correlation with the oxidation state and coordination number of Fe. The center of the Fe-metal correlation can be located anywhere within this box, including the shoulders. To enable a better visual distinction between the Fe-Fe and Fe-Si boxes, different dash types are used. For Na-silicate activated samples, the nearest-neighbor Na-O correlation is positioned at $\sim$ 2.3-2.5 Å [199, 203] (also seen in chapter 3.3) which raises the intensity of the minimum between the Ca-O and O-O correlations, while the K-O correlation ($\sim$ 2.8-2.9 Å [11]) exerts a similar influence on the intensity between the O-O and Fe-Fe correlations.

Taking into account the X-ray absorption near edge spectroscopy and Mössbauer spectroscopy data on Fe-rich slags with similar chemical compositions of chapter 3.2, the position of the nearest-neighbor Fe-O correlation (Figures 4.14 through 4.17, see also chapter 3.3) 15 minutes after initial mixing is indicative of the precursor slag, and contains a combination of IV- and V-fold coordinated Fe species. Furthermore, with respect to the local bonding environment and speciation of Fe in the IPs, previous section (chapter 4.1) has shown that $^{VI}Fe^{2+}$ and $^{IV}Fe^{3+}$ species simultaneous emerge as the reaction continues. According to the Fe-O distances reported in literature, this behavior should lead to an increase in intensity on either side of the Fe-O correlation associated with the slag ($\sim$ 2.02 Å), specifically the high r ($\sim$ 2.14 Å) and low r ($\sim$ 1.86 Å) shoulder for $^{VI}Fe^{2+}$ and $^{IV}Fe^{3+}$, respectively [199, 212] (also seen in chapter 3.3). The inserts of Figures 4.14 and 4.16 show a shift of the Fe-O maximum intensity toward higher r values, confirming the emergence of $^{VI}Fe^{2+}$ species. However, the formation of $^{IV}Fe^{3+}$ is less evident. The isomer shifts from Mössbauer spectroscopy associated with this species were seen to be large, suggesting that the Fe-O bond lengths associated with this species will also be larger than commonly observed for a $^{IV}Fe^{3+}$ site [62, 24]. Hence, instead of seeing an intensity rise at 1.86 Å, the $^{IV}Fe^{3+}$-O is more likely to be positioned between 1.90 and 1.95 Å.

The evolution of the metal-metal correlations in the PDFs in Figures 4.14

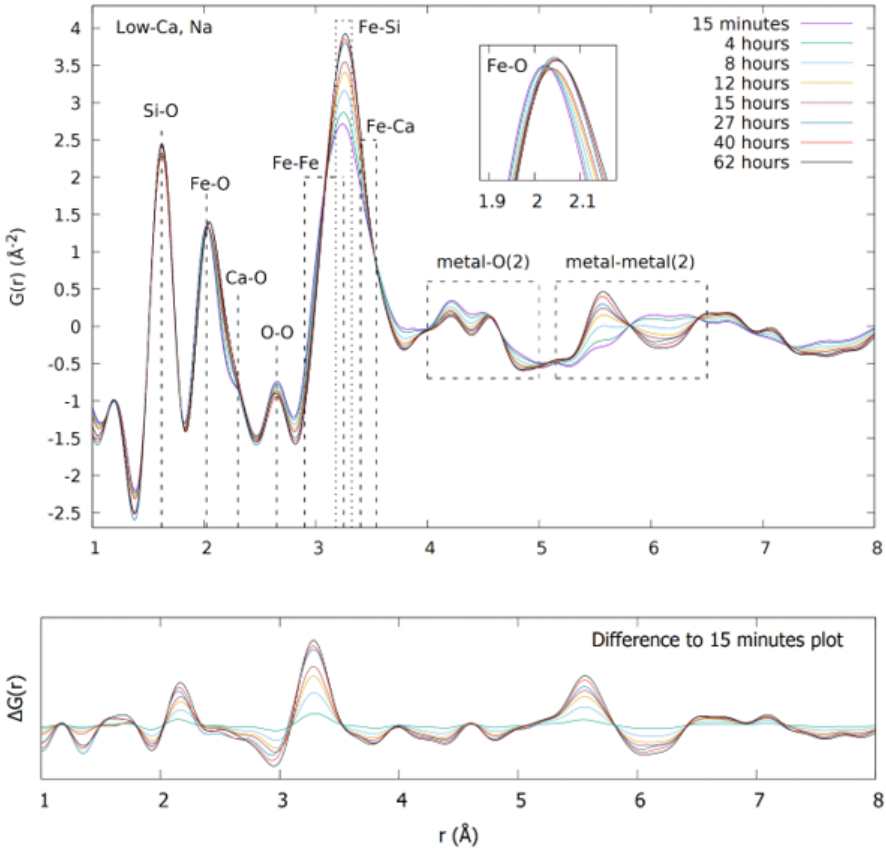

Figure 4.14: X-ray PDFs of the Na-silicate activated low-Ca IP during the initial 62 hours of reaction. Upper plot: Full PDFs and insert showing a zoom of the Fe-O correlation. Lower plot: Difference curves obtained by subtracting the initial data set (15 minutes) from those at later times.

through 4.17 is dominated by the rise in intensity of the main peak denoted as the Fe-Si correlation at $\sim$ 3.24 Å. However, the increase in distance between Fe and O upon formation of the $^{VI}Fe^{2+}$ should be considered, resulting in a potential Fe-Fe correlation at 3.25 Å [212]. The reason for this overall increase in the Fe-Si peak intensity and area as the reaction proceeds (Figures 4.14 through 4.17) has two possibilities. Firstly, an increase in sample density would lead to an increase in the atom-atom correlations, but since this should also affect the intensities of the nearest-neighbor bond lengths (such as Si-O), and the PDF curves do not reflect such a change, density is unlikely the cause of the

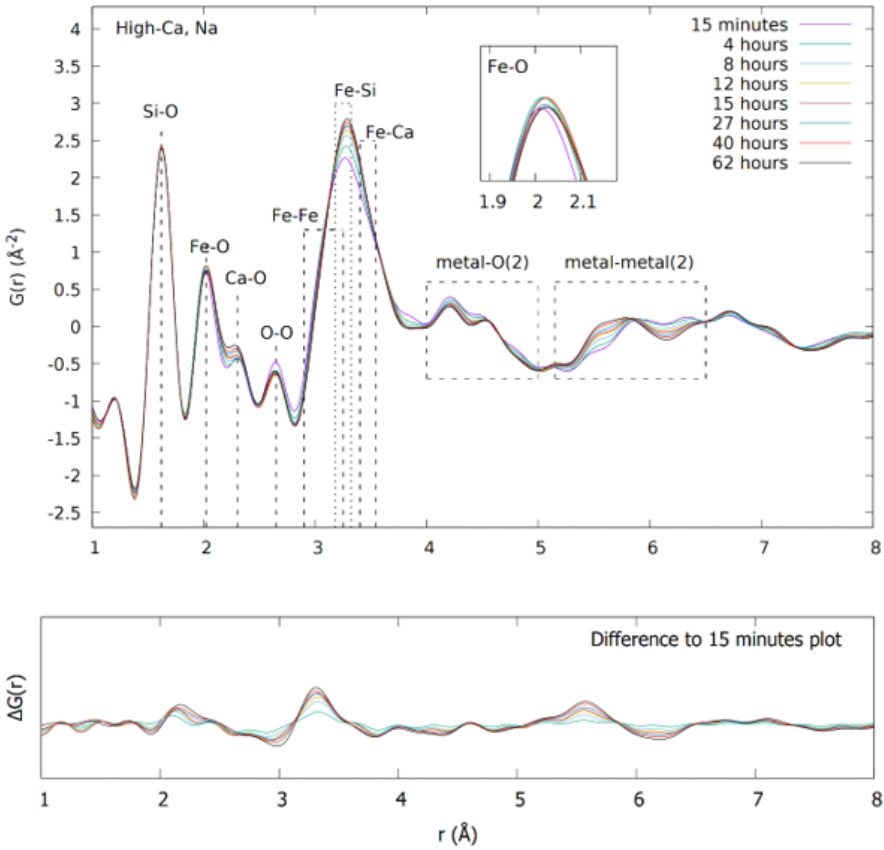

Figure 4.15: X-ray PDFs of the Na-silicate activated high-Ca IP during the initial 62 hours of reaction. Upper plot: Full PDFs and insert showing a zoom of the Fe-O correlation. Lower plot: Difference curves obtained by subtracting the initial data set (15 minutes) from those at later times.

increase in Fe-Si peak area. The second, and more probable explanation, is that the former Fe-Si correlation in the slag partially transitions toward a correlation containing an element with a larger scattering cross-section, such as Fe-Fe or Fe-Ca (see also chapter 3.3). Given that the Fe-Ca correlation is not usually observed around 3.25 Å [199, 212], the rise in intensity is attributed to a Fe-Fe correlation. The position of 3.25 Å for the Fe-Fe correlation directly results from the Fe-O distance of 2.14 Å and this rise in intensity of the metal-metal correlations should therefore be associated with the formation of a configuration with $^{VI}Fe^{2+}$. The elevated intensity of the Fe-Fe correlation suggests that this

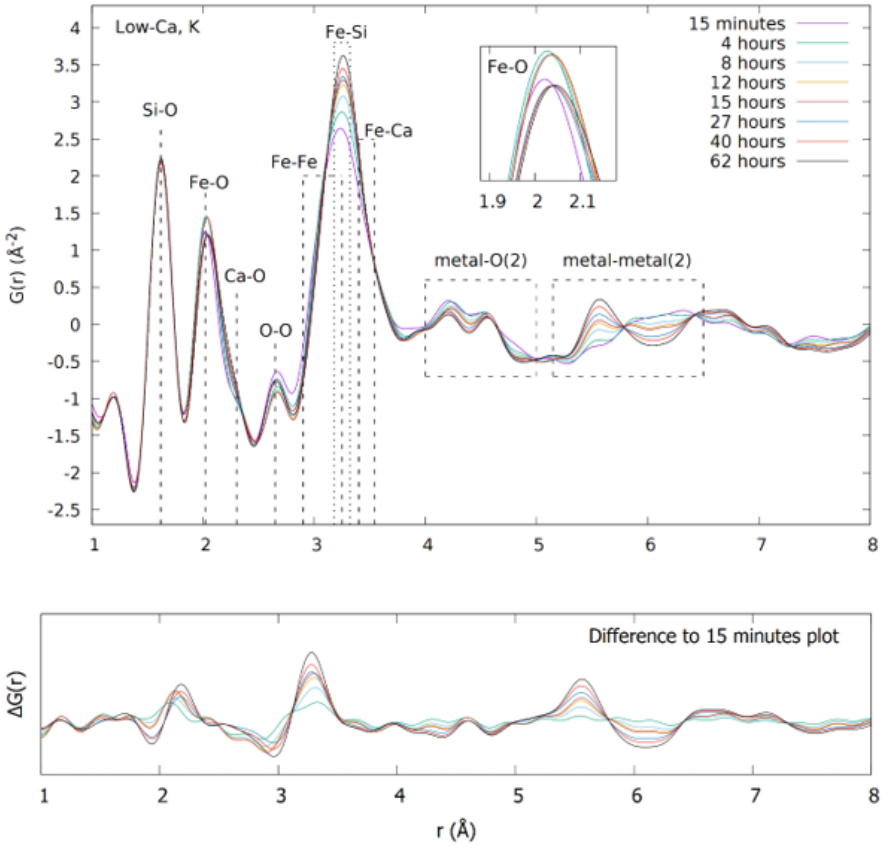

Figure 4.16: X-ray PDFs of the K-silicate activated low-Ca IP during the initial 62 hours of reaction. Upper plot: Full PDFs and insert showing a zoom of the Fe-O correlation. Lower plot: Difference curves obtained by subtracting the initial data set (15 minutes) from those at later times.

state contains an elevated amount of Fe-O-Fe linkages, and therefore $^{VI}Fe^{2+}$ is not homogeneously distributed throughout the silicate network, but instead shows a preferential aggregation. This phenomenon is clearly observed in the low-Ca systems (Figures 4.14 and 4.16) but is less pronounced when more Ca (and less Fe) is present (Figures 4.15 and 4.17). The intensity of the curves where the Fe-Ca, Ca-Si and Ca-Ca correlations would be present (3.4-4.0 Å [168, 202, 121, 50]) shows a drop as the reaction proceeds. This suggests that Ca does not take part in the formation of the binder during the early stages. Instead it may reside in the pore solution or be involved in a secondary phase (if present).

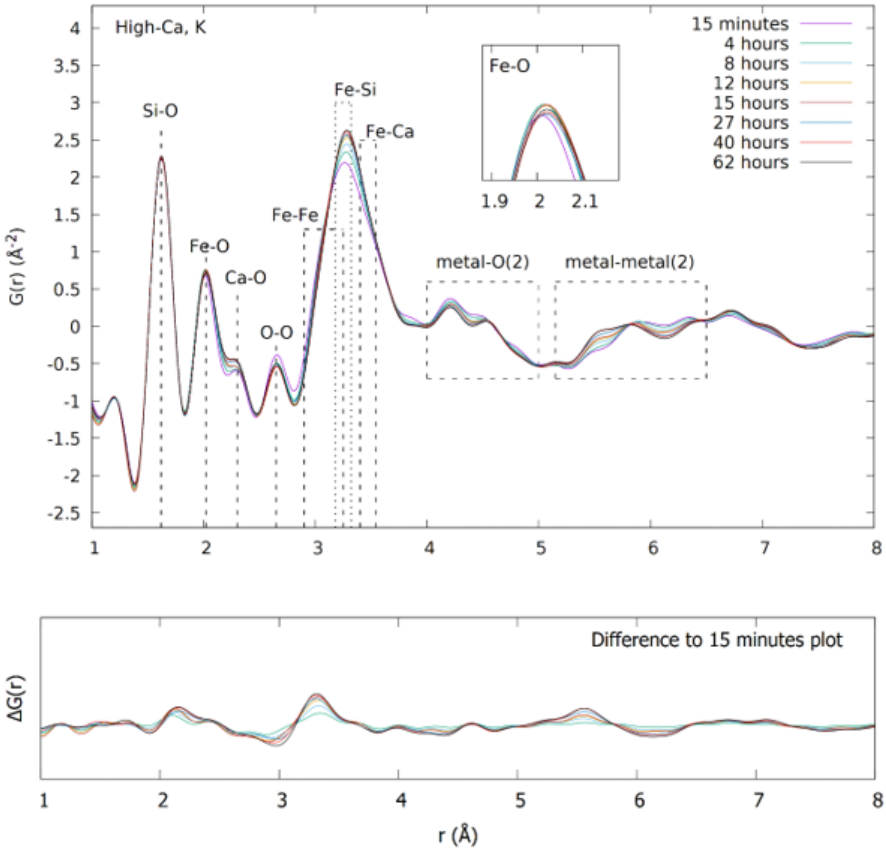

Figure 4.17: X-ray PDFs of the K-silicate activated high-Ca IP during the initial 62 hours of reaction. Upper plot: Full PDFs and insert showing a zoom of the Fe-O correlation. Lower plot: Difference curves obtained by subtracting the initial data set (15 minutes) from those at later times.

The extensive changes seen in the PDFs in Figures 4.14 through 4.17 during the in-situ test are also observed at higher r values ($\sim$ 8 - 20 Å, see Figures 4.18 and 4.19), especially for the Na-activated low-Ca slag system (Figure 4.18). For this sample, peaks emerge that are associated with the second ($\sim$ 5.6 Å) and third metal-metal correlations ($\sim$ 8.6 Å) (these positions were determined in chapter 3.3). Similar to the first metal-metal correlations (Figures 4.14 through 4.17), the changes as the reaction proceeds are less evident in the Na-activated high-Ca system in Figure 4.19.

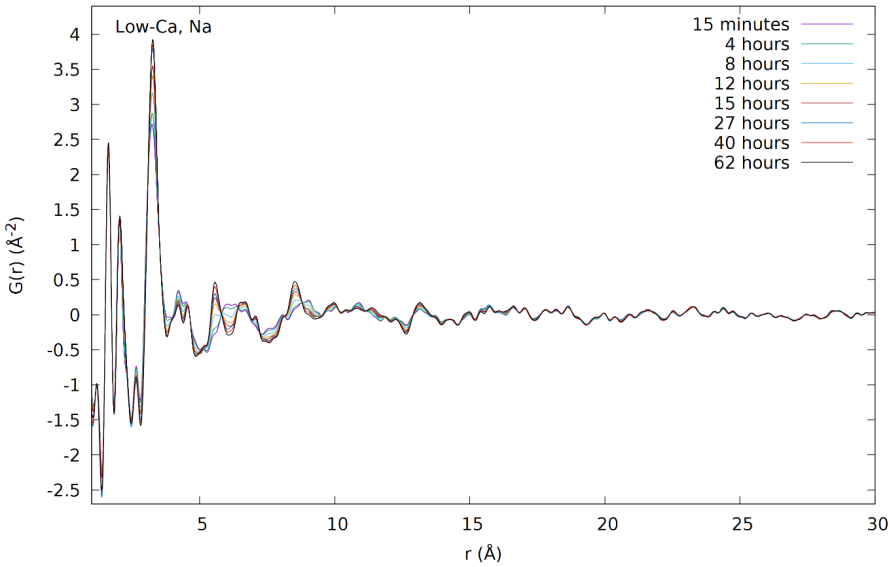

Figure 4.18: Long range X-ray PDFs of the Na-silicate activated low-Ca IP during the initial 62 hours of reaction.

Assignment of the peaks associated with the second and third metal-metal correlations has been carried out using the simulated X-ray PDFs of mineral phases that are similar to the chemical composition of the various IPs, as shown in Figure 4.20. The 15 minutes after mixing PDF for Na-activated low-Ca slag clearly aligns with the Fe-Fe(2) correlations in ferrosilite, the mineral phase closest in chemical composition ($FeSiO_3$) to the low-Ca slag. Therefore, this together with the fact that the first metal-metal peak is dominated by the Fe-Si correlation (as outlined above) implies that the bonding network for the low-Ca slag consists of Fe-O-Si-O-Fe linkages. Although it would be present in the slag, the Si-Si(2) is not observed in the PDF because of its relatively small scattering strength compared with Fe, and therefore has not been included in Figure 4.20.

During formation of the IP a clear rise in intensity is observed at 5.6 and 8.6 Å in the PDF data (Figure 4.20). The peak at 5.6 Å also corresponds well to goethite, FeO(OH), but the agreement of the other correlations with the experimental data are worse and the increase of the intensity should probably be associated with the observed increase of $^{VI}Fe^{2+}$-O-$^{VI}Fe^{2+}$ linkages, while goethite contains Fe^{3+}. Furthermore, there is a slight increase of the correlation at 6.5 Å, which distinguishes the trioctahedral layers from dioctahedral layers

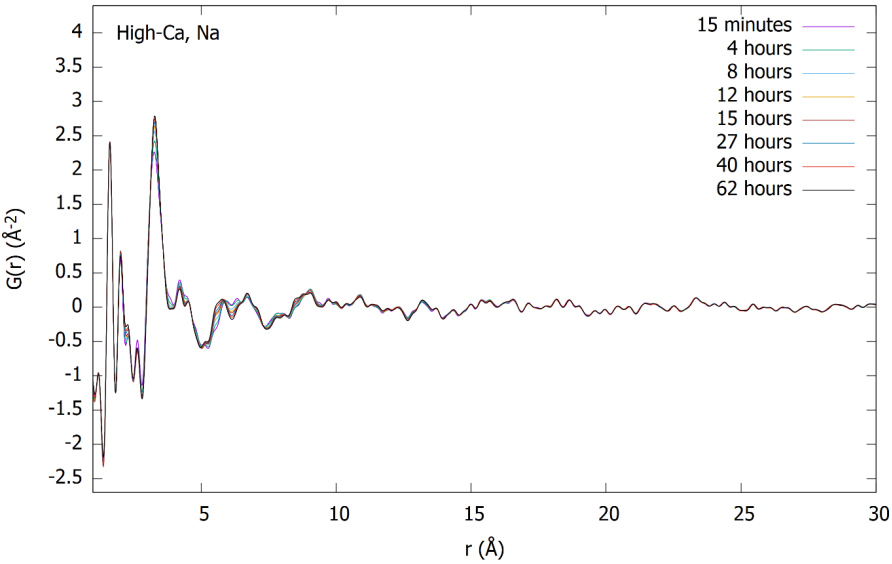

Figure 4.19: Long range X-ray PDFs of the Na-silicate activated high-Ca IP during the initial 62 hours of reaction.

[189, 49]. Importantly, for $Fe(OH)_2$ shown in Figure 4.20, the correlations positioned at 5.6 Å and 8.6 Å are valid for any material containing layers of ${}^{VI}Fe^{2+}$ in trioctahedral configuration (as shown in Figure 4.21), provided that there is a Fe-Fe distance of 3.25 Å. There are peaks associated with $Fe(OH)_2$ that do not appear in the experimental PDFs, specifically at 7.2 Å and 8.0 Å. These correlations correspond to out-of-plane distances in amakinite, and therefore the ${}^{VI}Fe^{2+}$-containing layers are not stacked as would be expected for such an $Fe(OH)_2$ phase. Instead, the PDF data indicate that the ${}^{VI}Fe^{2+}$-containing phase may consist of alternating layers of trioctahedral Fe(II)oxide and silicate. This proposed atomic arrangement is more closely related to mica or smectite clays, where trioctahedral layers of network modifiers (usually Mg, intermixed with Fe or Ca) are stacked with layers of network forming elements (Si, Al) [48, 164, 60]. There are also similarities between this stacking arrangement and that of calcium-silicate-hydrate (C-S-H) gel where calcium oxide sheets are sandwiched between layers consisting of silicate chains [183, 177]. Alkali-activated blast furnace slags give rise to a similar structure, with the Al from the slag in tetrahedral positions, making it a C-A-S-H gel [153, 202]. In cement nomenclature, the presented material might thus be referred to as F-F-S-H or F^2-S-H, as the Fe^{2+}-trioctahedral clusters have similarities to the calcium oxide sheets, while the Fe^{3+} might have the same role in the silicate network as Al^{3+}.

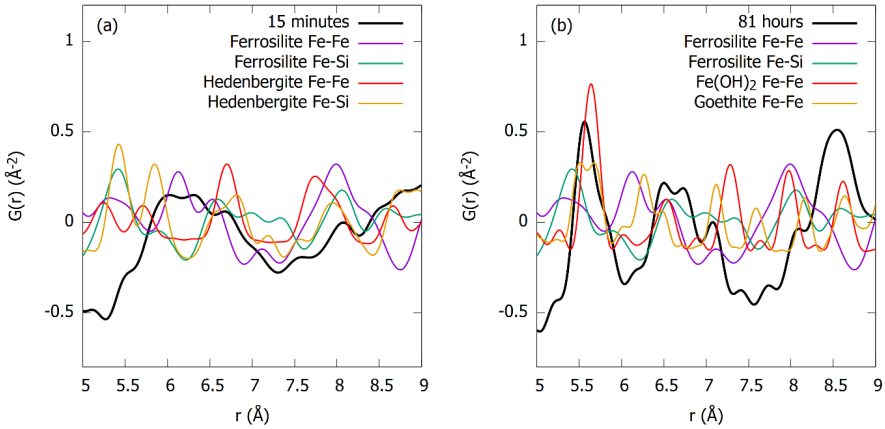

Figure 4.20: X-ray PDFs of (a) initial (15 minutes) and (b) final (81 hours) sample of the Na-activated low-Ca slag during the in-situ test, compared with ferrosilite ($Fe_2Si_2O_6$), hedenbergite ($CaFeSi_2O_6$), amakinite ($Fe(OH)_2$) and goethite ($FeO(OH)$).

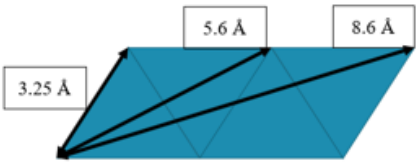

Figure 4.21: Calculation of the Fe-Fe distances in a trioctahedral Fe^{2+} layer. Fe atoms are located at the corners of the triangles.

However, no evidence of the layered nature of the silica was found in the PDF data and the presence of silicate hydrates cannot be confirmed from the present experiments. Future work, including for instance inelastic neutron scattering [**?**] should clarify the role of H, in the form of OH and/or H_2O, in the structure of the Fe-rich inorganic polymers.

With respect to the possibility of the formation of $Fe(OH)_2$, it is known that high pH conditions are necessary for the precipitation of Fe-hydroxides [181]. Hence, the IP activating solutions, where the pH is $\sim$ 13-14, are ideal conditions for the formation of $^{VI}Fe^{2+}$-containing trioctahedral layers. Furthermore, the presence of silicates in solution will influence the precipitated products. For instance, hydrothermal synthesis from Fe-silicate solutions results in the precipitation of Fe-based layered double hydroxides (LDHs) [149, 220, 219, 48, 164]. Smectite

or mica clays are additional examples of Fe-containing LDHs [48, 164, 60] incorporating trioctahedral $^{VI}Fe^{2+}$ layers. In the natural environment Fe atoms within the trioctahedral layers are extensively intermixed with Ca and/or Mg [48, 164, 60].

The high-Ca slag IP systems show less increase of the 5.6 Å and 8.6 Å peaks (associated with the Fe-Fe distances) compared with the low-Ca systems, even after taking into account the lower Fe content of the slag. This behavior indicates a lower extent of formation of the LDH-type phase in the high-Ca systems compared with low-Ca. There are two possible explanations for this behavior, the first being the intermixing of Ca atoms in the trioctahedral layers. Due to the larger ionic radius of Ca compared with Fe, this would lead to a distortion of the Fe-Fe distances associated with the LDH and therefore broaden the corresponding peaks in the PDFs. The second explanation involves the Ca atoms preventing the formation of the $^{VI}Fe^{2+}$-trioctahedral layers. Assessment of the peak widths in Figures 4.18 and 4.19 reveals that limited peak broadening occurs in the high-Ca sample, and therefore the Ca atoms are disrupting the overall formation of the $^{VI}Fe^{2+}$-trioctahedral layers.

Additional information on the LDH-type phase can be obtained from the SAS region in Figures 4.11-4.13. The LDH containing phase (e.g., $Fe(OH)_2$ or clays) should show a distinct peak in the SAS region representative of the basal spacing. As seen in Figure 4.13, the low-Ca systems undergo a more dramatic increase in SAS intensity compared with the high-Ca systems, which is correlated with the intensity increase of the 5.6 and 8.6 Å peaks in the PDF. Although it is impossible in the present study to definitively determine if the SAS intensity is due to a basal spacing arising from the $^{VI}Fe^{2+}$-containing phase or small pores, the longer-term decrease in SAS intensity (Figure 4.12) is directly linked with the same decrease in intensity of 5.6 and 8.6 Å PDF correlations (see Figure 4.22). The evolution of the intensity of the SAS and the peak at 5.6 Å in the PDF is quantitatively compared in Figure 4.23. The rise and fall of both intensities show the same relation across different samples, suggesting that this SAS region is directly related to the $^{VI}Fe^{2+}$-containing phase and shows that after extensive curing the $^{VI}Fe^{2+}$-containing phase has undergone significant alterations, as discussed in the next section.

As seen in Figure 4.18, the ordering of the $^{VI}Fe^{2+}$ trioctahedral layer only extends up to ~ 9 Å. Hence, this domain size for these ordered layers corresponds to approximately 20 FeO6 units. The formation of these $^{VI}Fe^{2+}$ domains can explain the results in chapter 3.1 from Fourier-transform infrared spectroscopy, where a shift of the Si-O stretching band to higher wavenumbers (from 850-900 to ~ 950 cm^{-1}) was observed as the slag dissolves and IP paste forms.The

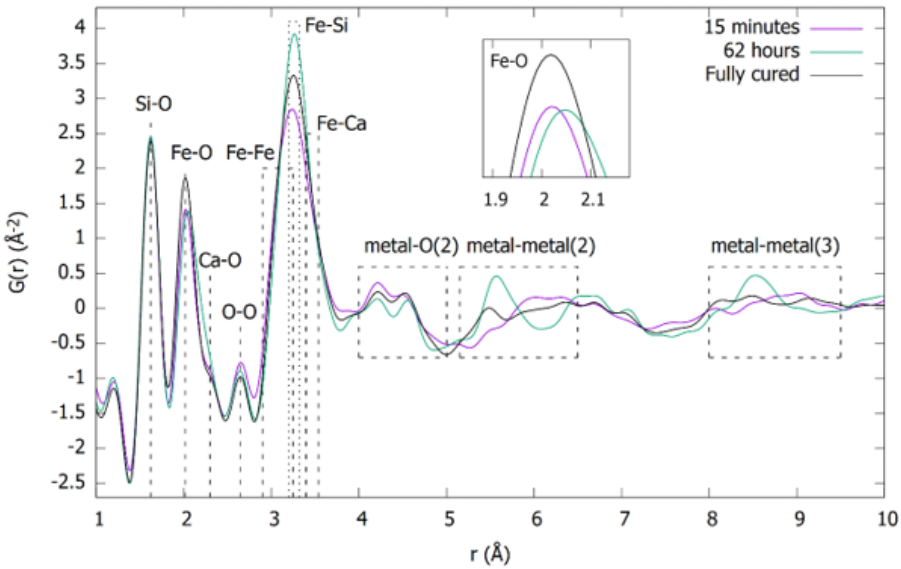

Figure 4.22: Comparison of the X-ray PDFs of the Na-activated low-Ca IP immediately after mixing (15 minutes), after 62 hours of reaction and fully cured/oxidized from chapter 3.3. The insert shows a zoom of the Fe-O correlation.

$^{VI}Fe^{2+}$ clustering and associated decrease in the Fe-Si correlation and increase in Fe-Fe causes an increase in the Si-Si correlation, when assuming that the connectivity of the Si units remains relatively unchanged. The amount of Si-O-Si bonds is thus increased (the amount of non-bridging oxygens is decreased) and the wavenumber of the Si-O stretching band increases. These Si-Si correlations are not clearly observed in the current PDF study because of the low scattering strength of Si with respect to Fe. In terms of nanoscale ordering of the IP paste, the main phase that contributes to an increase in ordering with respect to the initial slag is the $^{VI}Fe^{2+}$-containing trioctahedral structure, where the remainder of the material does not contribute to intermediate range ordering (Figures 4.18 and 4.19) and therefore the $^{IV}Fe^{3+}$-containing silicate network is amorphous.

The atomic rearrangements seen in Figures 4.14 through 4.17 for the in-situ reactions have been compared with the fully cured and milled pastes in previous work, where the same pastes as reported in chapter 3.3 were remeasured at $\sim$ 6 months after mixing. Figure 4.22 compares the in-situ Na-activated low-Ca sample after 62 hours of reaction with the fully cured version ($\sim$ 6 6 months), displaying a clear shift of the Fe-O correlation to a lower distance is observed.

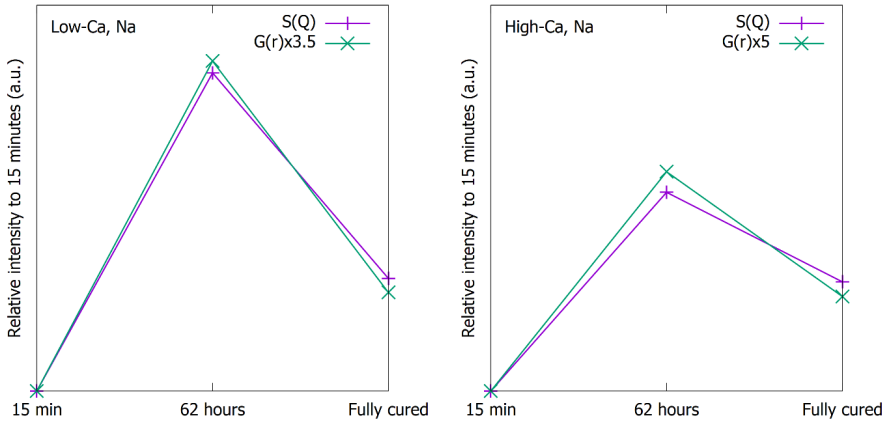

Figure 4.23: Comparison between the intensity of the SAS and peak at 5.6 Å in the PDF for the low-Ca (left) and high-Ca (right) system for the same times as presented in Figure 4.22.

This behavior is associated with the change in oxidation state of Fe, where the initially formed $^{VI}Fe^{2+}$-species in the layered trioctahedral configuration (also observed in chapter 4.1) transition to $^{IV}Fe^{3+}$. This transition is also noticeable in the metal-metal correlations via the decrease in intensity of the features associated to the trioctahedral layers. The intensity at 3.25 Å together with this peak's area are seen to decrease, indicating a transition from Fe-Fe linkages to Fe-Si. This transition is accompanied by a decrease in intensity of the peaks at 5.6 and 8.6 Å. Therefore, it can be concluded that the trioctahedral layers are converted when the Fe^{2+} species undergo oxidation during the later stages of reaction or during the milling procedure described in chapter 3.3. Future studies should concentrate on this later stage process(es) to determine the exact cause of the oxidation reaction and influence on macroscopic properties. Furthermore, as seen in Figure 4.22 for the fully cured sample (6 months), a peak is still observed at around 5.6 Å (also at 8.6 Å), indicating that a residue of the trioctahedral layers remains within the material.

The reaction kinetics have been evaluated using the atom-atom correlations showing the biggest change during the in-situ measurements, specifically the intensity 5.57 Å. As seen in Figure 4.24a, the intensity of the 5.57 Å correlation shows a similar trend as the SAS intensity in Figure 4.13. An induction period for the reactions that form the binder is observed at the beginning of the reaction (initial 2-3 hours), after which the reaction rate increases. This is contrary to the in-situ changes seen in metakaolin-based AAMs, where no induction

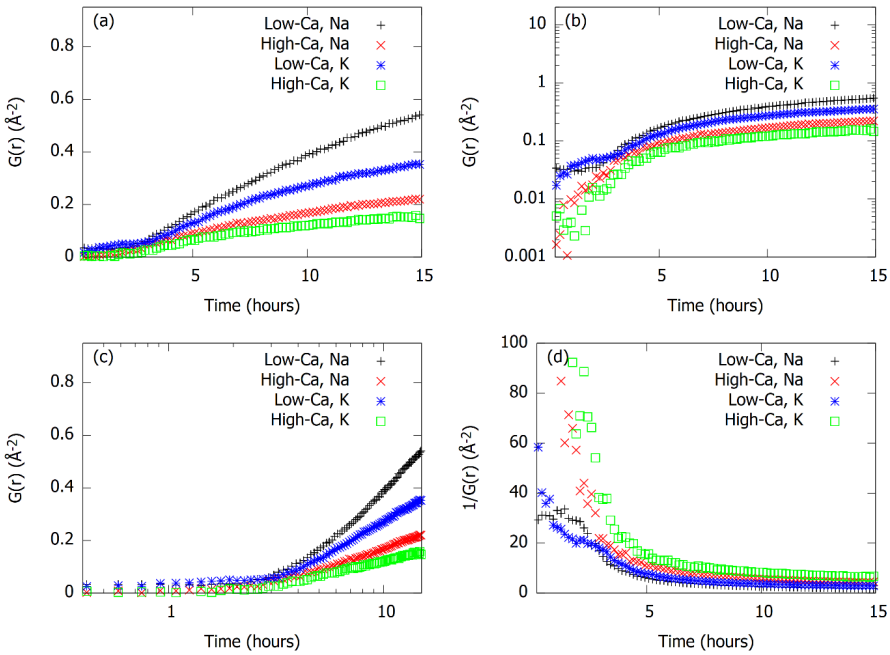

Figure 4.24: Evolution of the intensity of the 5.57 Å correlation in the X-ray PDFs on a (a) linear scale; G, (b) logarithmic y-axis; log time, (c) logarithmic x-axis; log G, (d) reciprocal y-axis; 1/G.

periods were identified [204]. To determine the rate law of the reactions, the data are plotted in Figure 4.24 on linear, logarithmic and reciprocal axes. Two straight lines are observed in Figure 4.24c and the overall formation reaction thus follows a logarithmic rate law indicative of two separate pseudo-single step first-order rate expressions, corresponding to the dissolution-dominated and polymerization-dominated stages.

The PDF curves during the dormant period are shown in Figure 4.25, for the K-activated and Na-activated low-Ca samples over an r range of $1.4 \leq r \leq 4.0$. While Mössbauer spectroscopy in chapter 4.1 showed that the oxidation state and coordination number of Fe stays constant during this period ($\sim$ 90% Fe^{2+}, combination of 4- and 5-fold coordinated species), it is also clear from Figure 4.25 that the Na-system only starts to show changes after $\sim$ 3 hours (also seen for this sample in Figure 4.14), whereas the K-system shows subtle changes to the local atomic structure immediately after mixing. In particular, the Fe-O correlation is seen to increase in intensity and distance, both of which

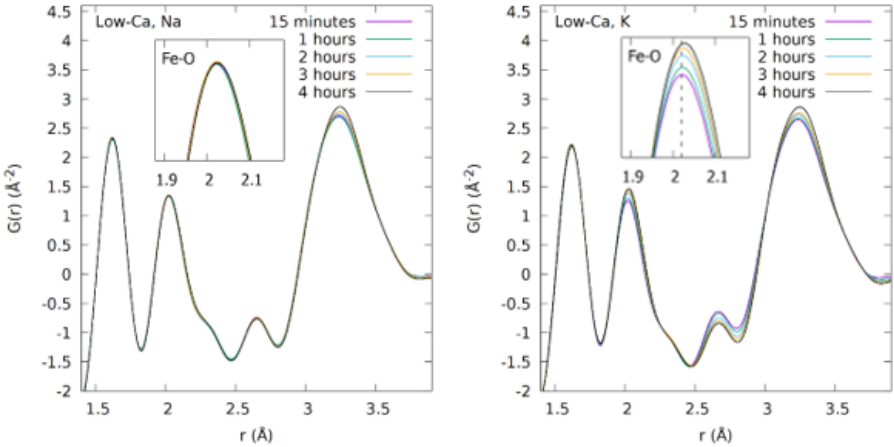

Figure 4.25: Low r region of the X-ray PDFs for the low-Ca IPs during the first 4 hours. The insert shows a zoom of the nearest neighbor Fe-O correlation.

indicate an increase in the average coordination number of Fe towards 5. More 5-fold coordinated Fe instead of a combination of 4- and 5-fold results in the increase in intensity of the Fe-O correlation since more Fe-O bonds are present in the system. In addition to the changes seen in the Fe-O correlation in Figure 4.25, the rearrangements are also seen as a rise in intensity at $\sim$ 3.25 Å and decline at $\sim$ 2.8 Å. These changes indicate a reconfiguration in the metal-metal correlations, as a consequence of the increased coordination number of Fe and can be influenced by a change in the K-O correlation, which should also be present at $\sim$ 2.8 Å. The lack of rearrangements in the Na-system before the polymerization reactions ($\sim$ 3 hours after mixing) indicates that the dissolution of the slag liberates Fe-silicate clusters, i.e., the slag is not dissolved to the ionic level, where the Fe atoms retain their original coordination environment found in the slag. In the K-system, the Fe coordination of these clusters in solution change as described above during the induction period. The kinetics of the changes of the Fe-O correlations are presented in Figure 4.26. After the rapid intensity increase of the Fe-O correlation for the K-system, the intensity of this correlation slowly declines again. This decline is also observed in the Na-system and can be explained by the formation of the $^{VI}Fe^{2+}$-trioctahedral clusters. The rise of the $^{VI}Fe^{2+}$ correlation at 2.14 Å at the expense of 4- and 5-fold coordinated Fe^{2+} (1.99-2.06 Å) results in a broadening of the Fe-O correlation.

Hence, the reaction mechanism of Fe-rich IPs can be summarized as follows:

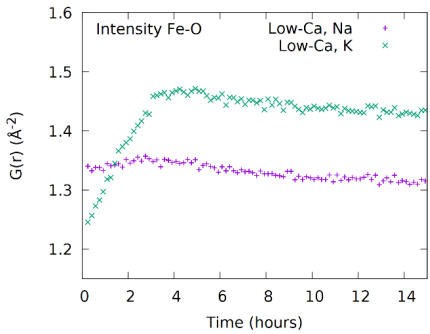

Figure 4.26: Evolution of the intensity for the nearest neighbor Fe-O correlation in the low-Ca systems.

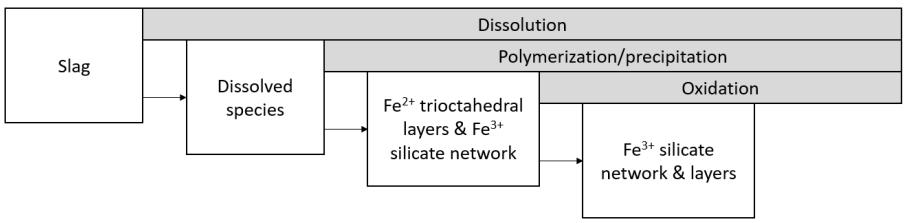

Figure 4.27: Schematic overview of the formation mechanism and different reaction stages of Fe-rich inorganic polymers.

1. Dissolution of precursor, liberating Fe-silicate species with the same atomic arrangement as the slag (for Na) or a similar atomic arrangement but an increased coordination number of Fe (for K).
2. After reaching a threshold value of Fe-silicate species in solution, the simultaneous formation of $^{VI}Fe^{2+}$ trioctahedral layers and a $^{IV}Fe^{3+}$ incorporating silicate binder phase with an increased degree of polymerization with respect to the precursor.
3. The oxidation of the $^{VI}Fe^{2+}$ trioctahedral layers towards more Fe^{3+} binder.

These reaction stages are schematically presented in Figure 4.27, which is an updated and more detailed version of Figure 4.9 in chapter 4.1.

This reaction mechanism and especially the unique last step (i.e., late stage oxidation) can have repercussions on the macroscopic behavior of the Fe-rich IPs. The oxidation reactions may lead to a volume reduction (i.e., shrinkage). To

accurately quantify this potential shrinkage, detailed atomistic representations or molar volumes would be required for the $^{VI}Fe^{2+}$ containing structure and the $^{IV}Fe^{3+}$-containing silicate binder phase since changes in coordination can result in geometrical shrinkage/expansion that cannot be determined solely using bond length changes. Moreover, it is unclear how fast this oxidation step would occur for non-milled samples, since exposure to an oxidizing environment for solid samples would depend on the diffusion rate of gas molecules through the partially-saturated pore network, which in turn would control the level of shrinkage attained during the life-time of the concrete. It is interesting to note that a decrease in the mechanical properties of the Fe-rich IPs has not been observed to date [92, 108]. Therefore, looking forward, future research concentrating on shrinkage data and pore structure information is needed for better prediction of the long-term performance of these novel Fe-rich binders.

4.2.4 Conclusions

The formation of low-CO_2 IPs starting from CaO-FeO_x-SiO_2 slag as the precursor was studied using in-situ X-ray total scattering and PDF analysis. Two slags with molar composition 0.83FeO-SiO_2-0.17CaO and 0.67FeO-SiO_2-0.33CaO were mixed with sodium and potassium silicate solutions. Three reaction stages were identified from the in-situ measurements; dissolution, polymerization and oxidation. During the initial few hours, the reactions are dominated by dissolution of the Fe-rich slag, the atomic rearrangements of the Fe-silicate species released into solution depend on the alkali cation. For sodium, the atomic correlations of the intermediate species in solution are found to be exactly the same as those in the precursor slag. On the other hand, potassium causes an increase in the coordination number of Fe once it is released into solution. The setting of the IP binder commences with the formation of two new phases with different Fe oxidation states (i.e., the polymerization stage). The Fe^{3+}-containing silicate network did not explicitly reveal details on its structure in the PDFs, apart from its glassy nature. On the other hand, the total scattering and PDF data reveal the emergence of $^{VI}Fe^{2+}$ trioctahedral layers, especially for the low-Ca slag IPs. The Fe-O distance associated with this phase is positioned at 2.14 Å, resulting in higher r Fe-Fe distances at 3.25, 5.6 and 8.6 Å. These $^{VI}Fe^{2+}$-containing layers are characteristic of layered double hydroxides (LDHs), observed in nature in clay minerals, e.g. in smectites or micas. The kinetics of formation of these layers follow a logarithmic rate law. A comparison with well-developed milled samples ($>$ 6 months) suggests that the Fe associated with the trioctahedral layers undergoes oxidation over the long term. Hence, this investigation has discovered the formation mechanism of Fe-rich IP binders, enabling future studies to focus on the processing and

performance of these materials by manipulating the fundamental formation behavior and the long-term performance of the material under the influence of the observed oxidation reaction.

4.3 The origin of oxidation and its influence on the final structure of Fe-rich inorganic polymers

This section is based on a paper in preparation:
A. Peys, A. P. Douvalis, C. Siakati, H. Rahier, B. Blanpain, Y. Pontikes, "The origin of oxidation and its influence on the final structure of Fe-rich inorganic polymers".

Contributions of the authors: In this paper, A. Peys made the experimental design, synthesis of samples and the experiment at the University of Ioannina together with A. P. Douvalis. The analysis of the experiments was performed in discussion with A. P. Douvalis. C. Siakati performed and helped in the analysis of the FTIR. All co-authors contributed to the discussion of the experiments and conclusions.

Abstract

Fe-rich inorganic polymers are rising in importance because of their low CO_2 emissions during production and their potential in upcycling metallurgical residues. Fundamental knowledge on the chemistry of the system is increasing, but some details on the structure and reaction mechanism remain unrevealed. Here, the oxidation reactions are investigated in more detail during the synthesis of inorganic polymers from a slag with approximate chemical composition 47 wt% FeO, 34 wt% SiO_2, 12 wt% CaO, 5 wt% Al_2O_3, 2 wt% MgO. Using ^{57}Fe Mössbauer spectroscopy after carefully designed curing schemes, it was shown that the oxidation at early stages is not influenced by (O_2 in the) air. The Fe^{2+}/Fe^{3+} ratio of the binder is thus inherent to the mixture itself. The Fe^{2+} state in the binder is not stable in air, as it was observed that during exposure to air as powder (crushed with mortar and pestle) for 28 days at room temperature or 1 hour at 200 °C, the Fe in the binder transforms completely to Fe^{3+}. This Fe^{3+} partially keeps the layered configuration of the former Fe^{2+} component of the binder. The total amount of Fe in the binder stays constant at 41 mol% during this transformation, showing that the slag dissolution is not continuing significantly. During heating of the inorganic polymer powder, the Mössbauer spectra remain stable until 400-500 °C. At this temperature the Fe^{2+} in the slag starts to be oxidized, increasing the absorption areas of the Fe^{3+} components. From 600 °C, a component with magnetic splitting appears, announcing the formation of Fe-oxides.

4.3.1 Introduction

Through the introduction of Fe-rich inorganic polymeric cementitious binders in concrete applications, a large reduction in CO_2 emissions can be achieved [145]. The environmental and economic benefit of this novel system can be extensive when also the transport distance can be decreased [145], i.e. in areas with no production of ordinary Portland cement and with an abundance of underutilized Fe-silicate resources – non-ferrous metallurgical slag (see the case of Belgium [145, 78, 137]), volcanic ashes (see the case of Cameroon [101, 102]), etc. The use of the non-ferrous metallurgical slags, which are momentarily not widely valorized, is also interesting from the perspective of circular economy and the limitation of excavating new natural resources. These slags thus have a major benefit with respect to metakaolin, fly ashes or blast furnace slag, as the latter are commonly already valorized in concrete applications in developed countries [59].

A drawback of the Fe-rich inorganic polymers with respect to the alumino-

or calcium silicates is the complexity of the system. This complexity and novelty of the use of Fe-rich precursors leaves numerous open fundamental questions. From a processing perspective, the system behaves similarly as the aluminosilicate inorganic polymers (geopolymers) [108, 92, 137, 155]. Powder is mixed with an alkaline solution, usually sodium silicate, the powder dissolves and forms a binder, resulting in a hardened monolith. The kinetics of this process seem to follow the same laws for Fe-rich IPs as aluminosilicates, increasing in speed with pH of the activating solution or fineness of the powder [92, 66]. The microstructure of the binder is dense, but with increasing alkalinity of the solution it can have a more globular outlook with particulates of a few nanometers (estimated from scanning electron microscopy) [136, 66].

The difficulty in understanding the system originates from the presence of Fe, for which the existence of multiple oxidation states (II, II) and coordination numbers (4, 5, 6) is plausible. Slags from the non-ferrous metallurgy have dominantly Fe in oxidation state II, with often a minor content of iron(III) [59, 148]. Coordination numbers are not so straightforward to deduce, as they mostly depend on the chemical composition and cooling conditions of the slag [126, 83, 5]. The IP binder was believed to only contain Fe^{3+}, based on the measurements in chapter 3.2, which were performed at late age and after storage of the samples as powder. The new Fe^{3+} state was in chapter 3.3 suggested to be in a silicate network with similar atomic arrangements as the precursor. Chapter 4.1 revealed the formation of an Fe^{2+} state. The in situ pair distribution function analysis in chapter 4.2 revealed the trioctahedral layered nature of this new Fe^{2+} containing clusters, which have in-plane similarities with $Fe(OH)_2$ or certain clays, but do not possess out of plane order. The reaction towards this new configuration happens simultaneously with the oxidation of another part of the Fe and concurrent polymerization of an Fe^{3+}-silicate binder. The counterreaction of this early age oxidation, as well as the mechanism for transcending from the mixed valence states during reaction towards the final Fe^{3+} binder are not yet defined and this will be the focus of this section.

The timing of the oxidation reactions, i.e. the formation of the Fe^{3+} silicate in the initial stage or the oxidation of the formed Fe^{2+} configuration, is a key to control the inorganic polymer reaction products. Cement science in general dictates that it is the molecular structure of the hydration/polymerization products that controls the properties of the material [191, 155, 29]. For aluminosilicate geopolymers it is for instance known that a fixed stoichiometry of $Na/Al = 1$ should be upheld in the binder product [159, 29], while for blast furnace slag based inorganic polymers it is also known that the Ca/Si ratio in the slag is directly linked to the connectivity of the network and the interlayer spacing [58, 117]. For the Fe-rich inorganic polymers, such rules have not been observed

and also the consequences of the oxidation reactions should be considered. Physical properties like density or color can be influenced by the oxidation state [25]. In glasses and minerals, the Fe-O distance is known to decrease upon oxidation from Fe^{2+} to Fe^{3+} [18, 126], which has also been observed for the inorganic polymers in previous section (chapter 4.2). This shortening of the Fe-O distance probably influences the chemical shrinkage of the material. When this happens after setting, the durability of the sample may be negatively influenced. It is therefore beneficial to time the main part of these reactions before setting, or to avoid them.

The work in this section reveals details on the state of the Fe throughout the reactions from slag to inorganic polymer. ^{57}Fe Mössbauer spectroscopy experiments are performed on a model (synthetic) slag – 47 wt% FeO, 34 wt% SiO_2, 12 wt% CaO, 5 wt% Al_2O_3, 2 wt% MgO – and its reaction products. Focus is placed on the importance of oxygen for the oxidation of Fe during the reactions. The synthesis of samples was also performed in inert atmosphere in a glove box to determine whether the oxidation in the early stage was due to air from the atmosphere or because of components in the initial mixture. Prolonged exposure of powdered samples to air at room temperature or in a furnace enabled the determination of the final state of the inorganic polymer and the sensitivity of the trioctahedral layers towards oxidation.

4.3.2 Materials and methods

The same slag was used as in chapter 4.1, its chemical composition is repeated in Table 4.4, measured with semi-quantitative X-ray fluorescence on a Philips PW 2400. The water quenched slag was crushed and milled to reach a Blaine

Table 4.4: Chemical composition of precursor slag in wt.% (estimated relative error 10%).

FeO	SiO_2	CaO	Al_2O_3	MgO
47	34	12	5	2

specific surface of 4000 ± 200 cm^2/g. The mineralogy was predominantly glassy (> 97 wt%), as observed using a Bruker D2-Phaser for X-ray diffraction (CuKα source, 30 kV and 10 mA, a slit size of 0.6 mm and an anti-scatter slit of 1 mm).

The synthesis of the inorganic polymer was initiated by adding 10 g of slag to 4.5 g of sodium silicate solution. This solution was made by blending commercial sodium silicate solution (Emsure, 7.5-8.5 wt% Na_2O, 25.5-28.5 wt% SiO_2) with sodium hydroxide pellets (Emsure, > 99.0 % purity) and demineralized water

in order to obtain a solution with molar ratios $SiO_2/Na_2O = 1.6$ and $H_2O/Na_2O = 20$. The mixing was performed by hand for 2 minutes before casting the paste in closed bottles. Curing was performed at 21 ± 1 °C. A glove box was used to study a selection of samples. In this case, all actions from adding the slag to the activating solution to loading the air-tight measuring cups was performed inside the N_2 atmosphere (including mixing and grinding with mortar and pestle). Samples prepared and sealed in N_2 atmosphere will be referred to as # DSI (**D**ays **S**ealed in **I**nert atmosphere), with # the amount of days since mixing, the samples sealed in air are named # DS. A study of the behavior of Fe after powdering of the paste was performed on samples cured for 7 days in a sealed bottle. The transformation at room temperature was investigated on one sample exposed as powder for 28 days: sample 7 DS 28. High temperature transformations were studied in detail using a tube furnace (Carbolite Furnaces, type TZF 12/65) for heating to 200, 300, 400, 500, 600 and 800 °C in air. The sample cured for 7 days in a closed bottle was powdered and 5 g was introduced in the furnace in an alumina crucible of approximately 10x0.5x0.5 cm^3. The dwell time at each temperature was 1 hour. These samples are abbreviated with 7 DS "T", with "T" the temperature to which the sample was exposed, e.g. 7 DS 400. All samples were prepared for ^{57}Fe Mössbauer spectroscopy measurements by powdering a piece of the sample with mortar and pestle.

^{57}Fe Mössbauer spectroscopy measurements were performed at a sample temperature of 77 K in a liquid N_2 cryostat (Oxford Instruments, Varios 760) using a constant acceleration spectrometer equipped with a ^{57}Co(Rh) source kept at room temperature. Calibration of the spectrometer was performed using metallic α-Fe at room temperature and all isomer shifts (IS) values of the components used to fit the spectra are given relative to this standard. Fitting the samples was performed with the IMSG software [34]. Attenuated total reflectance Fourier-transform infrared spectroscopy was performed on a Bruker Alpha-P with a diamond measuring crystal. The spectra are recorded with a resolution of 4 cm-1 and 32 scans per measurement. Each sample was measured twice and the average of the two measurements is presented in the text.

4.3.3 Results

The ^{57}Fe Mössbauer spectra are shown in Figure 4.28. The samples that have not been exposed to air in Figure 4.28a show as main feature a combination of doublets centered around 1 mm/s, suggesting a predominantly Fe^{2+} nature. The exception in Figure 4.28a is the sample that was 7 days sealed and 28 days open. A significant contribution from Fe^{3+} state(s) can be observed. The samples sealed in N_2 for one and three days seem very similar to those prepared

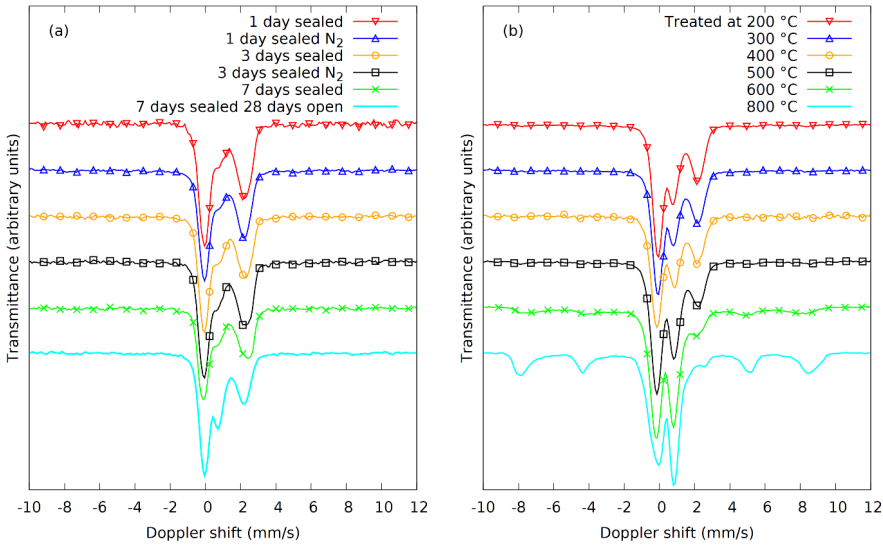

Figure 4.28: ^{57}Fe Mössbauer spectra of samples cured at room temperature (a) and treated in a furnace (b).

in air. For the samples heated up till 500 °C in Figure 4.28b the spectra look similar to the sample that was opened at room temperature, whereas at a temperature of 600 °C and 800 °C the features of a magnetic sextet are clearly revealed. The spectra were fitted following the same methodology as in chapter 4.1. The slag was fitted using 3 components: the isomer shift, quadrupole splitting, intensity and spread on the quadrupole split were determined by the least squares minimization procedure. The hyperfine parameters of these components are set constant throughout the reaction and the relative absorption areas are made dependent on each other. Similar to the study in chapter 4.1, the sealed samples were all fitted using the 3 slag components and 2 extra "IP" components, of which one considers an Fe^{2+} state and the other Fe^{3+}. These two IP components are refined. The samples that were exposed to air as a powder did not contain this extra Fe^{2+} IP component and could be fitted by just adding 1 Fe^{3+} state to the slag. For samples exposed to 600 °C and 800 °C, the spectra had changed too drastically and a different fitting approached was used. A combination of 1 Fe^{2+} doublet, 2 Fe^{3+} doublets and 1 magnetic Fe^{3+} component was necessary to fit the spectra. Example fits of samples 1DS, 7DS28 and 7DS800 are provided in Figure 4.29. The hyperfine parameters of the components in the samples are shown in Table 4.5 and 4.6.

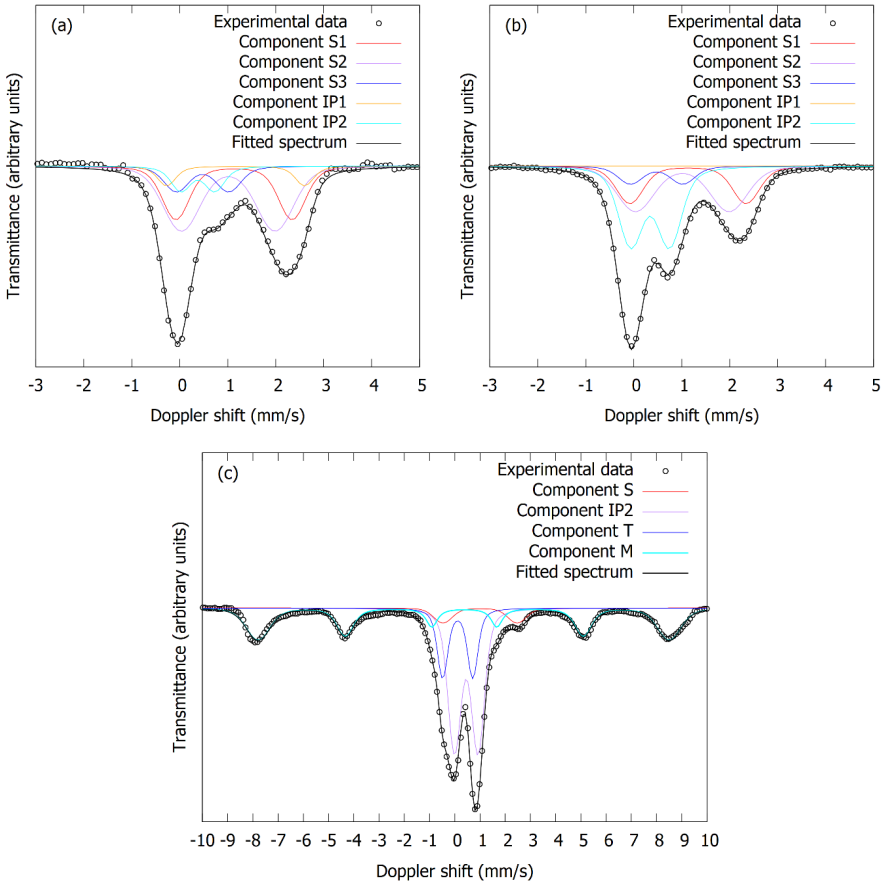

Figure 4.29: Fitted spectra of samples (a) 1DS, (b) 7DS28 and (c) 7DS800.

4.3.4 Discussion

The influence of the presence of air on the early age reactions can be derived from Figure 4.30, where the absorption area of the Fe^{3+} IP component is plotted in the first 3 days, comparing samples prepared in air and in a N_2 environment in a glove box. Oxidation, transformation of the slag to Fe^{3+} binder component, still happens in inert environment. The kinetics of oxidation are not influenced by the environment and external parameters thus do not play a role in the early age oxidation, i.e. external air does not participate in the early age oxidation reactions. Similarly, dissolved air in the silicate solution is not able to provide sufficient oxidative power to perform the observed conversion. Curing for three

Table 4.5: Resultant Mössbauer hyperfine parameters from fitting the spectra of Figure 4.28. IS is the isomer shift with respect to α-Fe at 300 K, QSc is the central value of the quadrupole splitting, $B_{hf}c$ is the central value of the hyperfine magnetic field, Δ QS and Δ B_{hf} are the spreading of the QS and B_{hf} respectively, AA is the relative absorption area of the components. Estimated errors on the parameters are $\pm$ 0.02 mm/s for IS and QSc, $\pm$ 0.3 T for B_{hf} and $\pm$ 5% for AA. The half line-width was kept constant at 0.14 mm/s to avoid interference as this parameter has the same influence on the spectra as Δ QS and Δ B_{hf}. **The table continues on the next page.*

Sample	IS (mm/s)	QS^c (mm/s)	Δ QS (mm/s)	AA (%)	Component
Slag	1.13	2.42	0.43	33	S1
	1.01	1.96	0.64	52	S2
	0.48	1.09	0.38	15	S3
1DS	1.13	2.42	0.43	28	S1
	1.01	1.96	0.64	43	S2
	0.48	1.09	0.38	12	S3
	1.15	2.87	0.26	7	IP1
	0.35	0.76	0.37	10	IP2
1DSI	1.13	2.42	0.43	29	S1
	1.01	1.96	0.64	45	S2
	0.48	1.09	0.38	13	S3
	1.15	2.86	0.28	3	IP1
	0.32	0.80	0.28	11	IP2
3DS	1.13	2.42	0.43	23	S1
	1.01	1.96	0.64	36	S2
	0.48	1.09	0.38	10	S3
	1.17	2.84	0.30	10	IP1
	0.35	0.82	0.38	20	IP2
3DSI	1.13	2.42	0.43	21	S1
	1.01	1.96	0.64	33	S2
	0.48	1.09	0.38	9	S3
	1.15	2.81	0.33	18	IP1
	0.35	0.74	0.37	19	IP2
7DS	1.13	2.42	0.43	22	S1
	1.01	1.96	0.64	34	S2
	0.48	1.09	0.38	10	S3
	1.16	2.95	0.28	18	IP1
	0.32	0.77	0.30	17	IP2
7DS 28	1.13	2.42	0.43	20	S1
	1.01	1.96	0.64	32	S2
	0.48	1.09	0.38	9	S3
	0.34	0.81	0.38	39	IP2

days delivers approximately 20 mol% of Fe^{3+} (the absorption area and mol% of the component are directly related with maximum 5% relative error [126]). Taking into account the dissociation of oxygen gas as other half-reaction: O_2 + 4 e^- => 2 O^{2-}, 1/4 mole of oxygen gas is needed to oxidize 1 mole (= 55.845 g) of Fe^{2+} to Fe^{3+} (Fe2+ + e- => Fe3+). The slag contains 47 wt% of FeO, thus 40 wt% of Fe. The oxidation reaction under investigation considers 20

Table 4.6: Continuation of Table 4.5: Hyperfine parameters of furnace samples

Sample	IS (mm/s)	QS^c (mm/s)	B^c_{hf} (kOe)	Δ QS (mm/s) or Δ B_{hf} (kOe)	AA (%)	Component
7DS 200	1.13	2.42	0	0.43	20	S1
	1.01	1.96	0	0.64	32	S2
	0.48	1.09	0	0.38	9	S3
	0.33	0.92	0	0.41	39	IP2
7DS 300	1.13	2.42	0	0.43	20	S1
	1.01	1.96	0	0.64	31	S2
	0.48	1.09	0	0.38	9	S3
	0.34	0.96	0	0.40	40	IP2
7DS 400	1.13	2.42	0	0.43	19	S1
	1.01	1.96	0	0.64	29	S2
	0.48	1.09	0	0.38	8	S3
	0.30	1.13	0	0.43	44	IP2
7DS 500	1.13	2.42	0	0.43	15	S1
	1.01	1.96	0	0.64	24	S2
	0.48	1.09	0	0.38	7	S3
	0.32	1.08	0	0.44	55	IP2
7DS 600	0.91	2.41	0	0.89	19	S
	0.38	1.00	0	0.43	49	IP2
	0.14	1.06	0	0.23	10	T
	0.38	-0.05	464	53	21	M
7DS 800	1.00	2.94	0	0.62	6	S
	0.46	0.93	0	0.39	42	IP2
	0.12	1.20	0	0.28	17	T
	0.37	-0.03	506	0.22	34	M

mol% of the total Fe, which is equal to 20 wt% of the Fe, because the molar weight of different oxidation and coordination states is the same. The mass of the slag that participates in the oxidation reaction is thus 8 wt%. This means that for 1 g of slag, 0.02 mole or 0.3 g of oxygen gas is needed, or 0.7 g per gram of activating solution. This drastically exceeds the solubility of oxygen gas in water [123]. An alternative oxidizer should be searched within the mixture in future work.

The oxidation of the Fe^{2+} binder component, observed in chapter 4.1 and 4.2, towards the final completely Fe^{3+} binder of chapter 3 is investigated in more detail by exposing the samples as powder to air. The samples were cured for 7 days like in chapter 4.1. After 7 days, the bottle is opened and the sample is milled. Figure 4.31 compares the absorption areas of the IP components in the samples from chapter 4.1 with these milled samples that were (1) exposed to air as powder for 28 days and (2) put in the furnace at 200 °C. In both cases the Fe^{2+} in the inorganic polymer binder was completely converted to Fe^{3+}. This

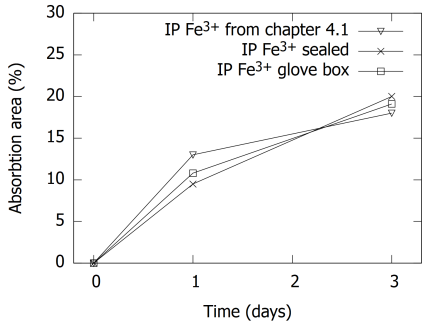

Figure 4.30: Absorption area of Fe^{3+} binder component for samples prepared in inert and atmospheric environments, compared with chapter 4.1. The error on the absorption area is estimated at approximately 3%.

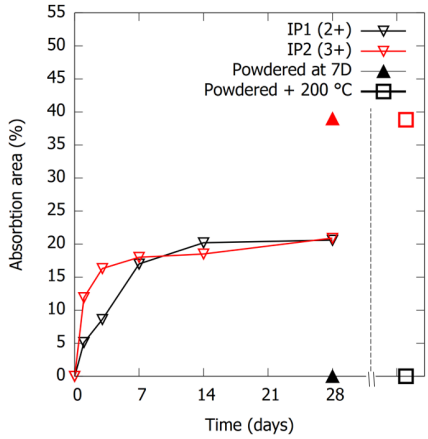

Figure 4.31: Evolution of the absorption area of the Fe^{2+} (black) and Fe^{3+} (red) components of the binder. After 7 days, part of the samples were milled and exposed to air at room temperature or 200 °C. The error on the absorption area is estimated at approximately 3%..

Fe^{3+} state only shows an absorption area of approximately 40%, because of the low conversion of the reaction, approximately 60% of unreacted slag remains in the investigated mixture. The exposure to air thus controls the kinetics of the transformation of the former Fe^{2+} state. The proposed trioctahedrally layered configuration of these FeO_6 units is in line with this observation. Literature on $Fe(OH)_2$ shows that hydroxide layers decompose and oxidize in air [181]. The observation that the Fe^{2+} binder state decomposes and oxidizes when the

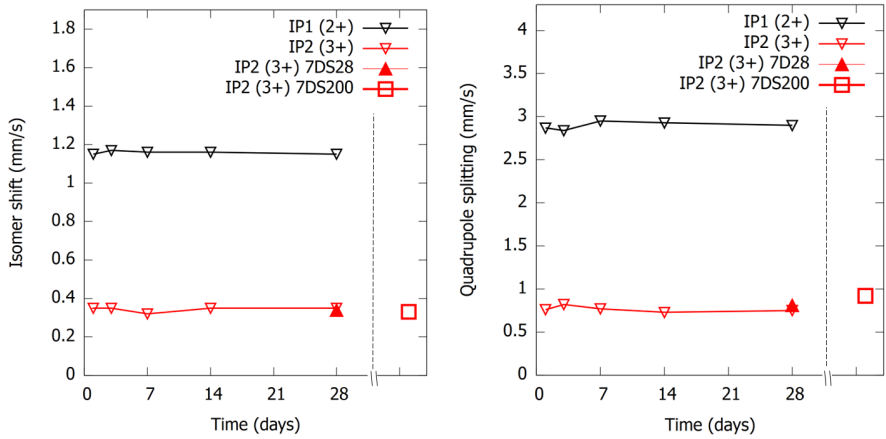

Figure 4.32: Evolution of the Mössbauer parameters of the Fe^{2+} and Fe^{3+} components of the binder. Left: isomer shift; right: quadrupole splitting.

powder is in contact with air can be used to streamline the conclusions from the previous sections. As chapter 4 considered measurements on samples that were not or not excessively exposed as powder before the measurement, the oxidation to Fe^{3+} only happened partially. Measurements in chapter 3 considered well developed binders (cured > 28 days), which were exposed as powder for > 28 days, resulting in a complete Fe^{3+} binder.

By comparing the fitting parameters of the Mössbauer spectra of the two states of Fe, structural changes are investigated. The isomer shift and quadrupole splitting of the samples discussed above are presented in Figure 4.32. The isomer shift is constant throughout the reaction. The quadrupole splitting of the Fe^{3+} state shows a slight increase after exposure to 200 °C. As discussed in chapter 4.1, the Fe^{2+} state shows isomer shift and quadrupole splitting values which correspond to an asymmetric octahedron, which turned out to be a configuration of ${}^{VI}Fe^{2+}$ trioctahedral layers (chapter 4.2). The parameters of the Fe^{3+} state were in chapter 4.1 suggested to correspond to tetrahedra and this ${}^{IV}Fe^{3+}$ is according to chapter 3.3 and 4.2 most likely situated in the silicate network. Fe is an amphoteric element and can as such not participate in the silicate framework without a charge balancing element [126]. The addition of Ca, Na or Fe with a different coordination/oxidation state is needed to achieve this charge balance. The occurrence of Fe in a different state should have been detected using Mössbauer spectroscopy. Chapter 4.1 showed a Na/Fe^{3+} ratio of approximately 1 after 28 days, rising the probability of Na to take up the role of charge balancer. In the results here however, because of the increased proportion of Fe^{3+} in the

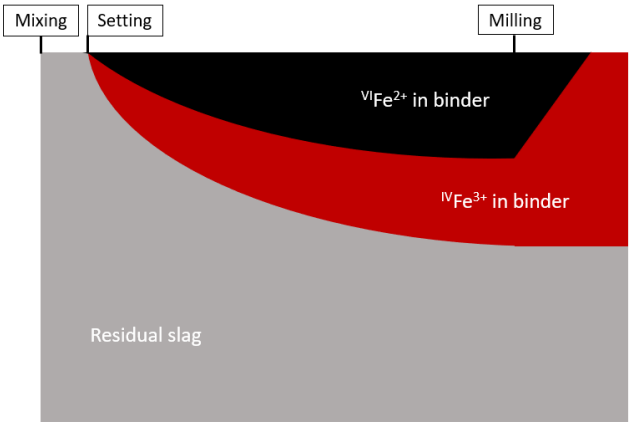

Figure 4.33: Schematic representation of the configuration of Fe throughout the reactions. The height of the boxes refers to the approximate amount of the configuration in the binder.

binder ($\sim$ 20% to $\sim$ 40%) after exposure of the powdered samples to air, this Na/Fe^{3+} ratio becomes 0.5 and it is thus impossible that Na is the only element providing the charge balance. In the present work, this role might be fulfilled by Ca. The oxidation of the $^{VI}Fe^{2+}$ by exposure of the powder to air seems to result in a reaction product with the same Mössbauer fitting parameters as the Fe^{3+} (IP2 component) that was formed before the milling. The parameters of this component are stable during exposure to air at room temperature, while at 200 °C the quadrupole splitting is increased, i.e. the electronic environment of Fe is slightly more distorted/asymmetric. The similarity of the Mössbauer parameters indicate that (1) the reaction product of this late age oxidation is the same as the earlier formed $^{IV}Fe^{3+}$ in the silicate network, or that (2) the reaction product has a similar environment as this earlier formed state. The comparison of final oxidized and in-situ samples in previous section (chapter 4.2) showed a remainder of the layered configuration in the final samples while the Fe was already completely in the Fe^{3+} state. It is thus likely that at least a part of the Fe does not go into the silicate network in the same configuration as the early oxidized part. The most probable explanation is that it is a combination of the two proposed mechanisms that contribute to the formation of the final configuration. The Mössbauer parameters suggest that the Fe^{3+} in the layers is also in tetrahedral configuration. The evolution of the Fe oxidation state during the different reaction stages is schematically presented in Figure 4.33. Chapter 4.2 did not show correspondence of the atomic correlations with known crystalline phases, but suggested that the final Fe^{3+} state at least partially considers an oxidized and distorted version of the trioctahedral Fe^{2+} layers. To

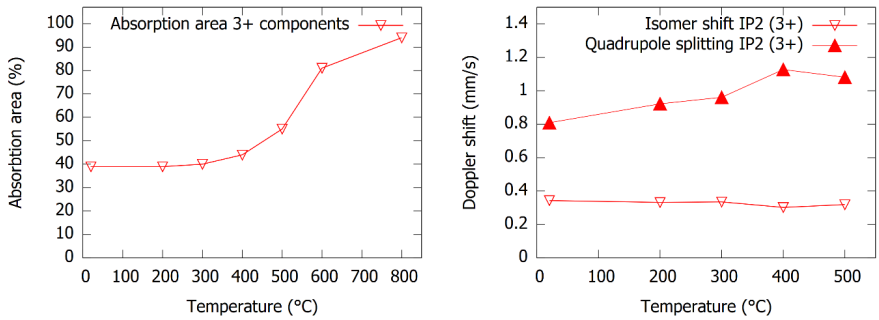

Figure 4.34: Evolution of Fe^{3+} component of the binder with temperature. Left: absorption area; right: Mössbauer parameters.

check the possibility of going from a trioctahedral ${}^{VI}Fe^{2+}$ layer to a ${}^{IV}Fe^{3+}$ layer directly, a potential chemical reaction is proposed. In going from ${}^{VI}Fe^{2+}$ to ${}^{IV}Fe^{3+}$ an extensive amount of non-bridging oxygens is transformed at the benefit of more bridging oxygens and OH-. This can go by the reaction:

$$ {}^{VI}Fe^{2+} + \tfrac{6}{2}O^{2-} + \tfrac{1}{4}O_2 \longrightarrow \quad {}^{IV}Fe^{3+} + \tfrac{4}{2}O^{2-} + 3OH^- $$

Herein, the O^{2-} refers to the oxygens that are coordinated around the Fe, H^+ counterbalances the non-bridging oxygens. As such, one dioxygen molecule can oxidize four Fe ions.

More information on the structure can be gained by studying its transformations at high temperature. The evolution of the absorption area (a) and isomer shift and quadrupole splitting (b) of the Fe3+ IP2 component are shown in Figure 4.34. Complimentary ATR-FTIR spectra are provided in Figure 4.35. The isomer shift and quadrupole splitting at 600 and 800 °C are not presented, as a completely different fitting model was used. The absorption area is still presented at these temperatures, but refers to the sum of the absorption areas of all 3+ states in the sample. As was already observed in Figure 4.31, the binder is completely oxidized from the lowest temperature. The next rise in absorption area can be observed starting from 400-500 °C: the slag starts to oxidize as well. Complete oxidation is not achieved (even at 800 °C 6% of Fe^{2+} remains). This is likely because of kinetics (the inside of the particles is probably not oxidized due to diffusion control). Considering the structural parameters in Figure 4.34b, the isomer shift seems to stay relatively stable, while the quadrupole splitting gradually increases up to 300 °C after which a jump is observed which should be attributed to a contribution of oxidation products of the slag, which include a different configuration of the Fe than what is observed in the oxidized binder.

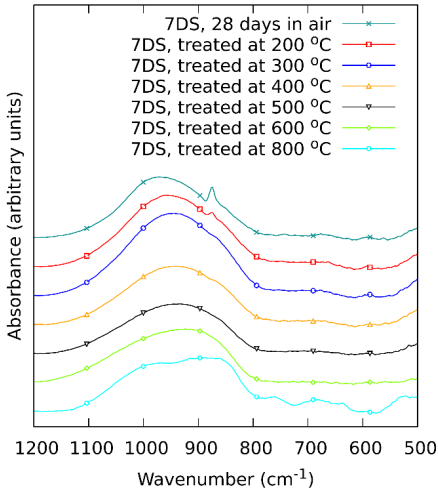

Figure 4.35: ATR-FTIR spectra of the samples as function of the temperature.

The gradual increase of the quadrupole splitting up to 300 °C is combined with a shift of the Si-O stretching band in FTIR ($\sim$ 950 cm^{-1}) to lower wavenumbers and the disappearing of a peak at $\sim$ 870 cm^{-1}. As discussed in chapter 4.1, the quadrupole splitting can be related to the amount of non-bridging oxygens around the Fe. Likewise, the shift of the Si-O stretching peak can indicate a change in the role of Fe in the silicate network (chapter 3.1). The band at 870 cm^{-1} is attributed to carbonates (chapter 3.1 and 3.3). The disappearance at 300 °C shows that it considers a sodium carbonate (chapter 3.3). From 600 °C the ^{57}Fe Mössbauer spectra in Figure 4.28 show drastic changes, among which the formation of Fe-oxides [61, 170, 107]. At 800 °C the FTIR spectrum is drastically changed, indicating now also here the formation of Fe-oxides. The structural changes with temperature increase should be taken into account when using the Fe-rich inorganic polymer at high temperature and when assessing the thermo-mechanical stability for instance for application as fire-proof materials.

4.3.5 Conclusions

The oxidation reactions during the first days after mixing are not driven by atmospheric air, as was shown by the similar kinetics when performing the preparation and curing procedures in a N_2 atmosphere. The mechanism of this oxidation, including the balancing half-reaction, remains unclear. The

transformation at later age from Fe^{2+} trioctahedral layers to Fe^{3+} was incited by O_2 in the air as the oxidizing agent. The Mössbauer parameters of the product of this oxidation were similar to those of the Fe^{3+} component of the binder that was initially formed. However, it was seen in chapter 4.2 that the layered nature was not completely lost and as such it is probable that the new configuration incorporates layers of tetrahedral Fe^{3+}, which should be charge balanced by Ca or Na. When elevating the temperature, the oxidation of Fe in the slag is observed from around 400-500 °C, as is seen by the increase of the absorption area of Fe^{3+} components beyond the amount of binder. The formation of Fe-oxides is observed from 600 °C.

Chapter 5

The internet of Fe-rich inorganic polymers

5.1 Software for database collection and support calculations

This section is based on the published proceeding paper:
A. Peys, E. Orfanakis, Y. Pontikes, "On a software development that aspires to make residue valorisation easier", *Proceedings of the 5th International Slag Valorisation Symposium* p317-320, April 2017, Leuven, Belgium.

Adaptations and additions are made in the text to include the progress after the publication of the proceeding and to clarify the role of A. Peys in the development of the software and its different modules. The software is online available at http://sreway.info/web/.

Contributions of the authors: Early versions of the software and the calculation tools were programmed by A. Peys. The paper was produced in collaboration with Y. Pontikes.

5.1.1 Introduction

Driven by environmental legislation and awareness, associated with increased processing and landfill costs, but also valorisation opportunities, an increasing interest exists for the valorisation of metallurgical slags, tailings, ashes and sludges. Efforts are certainly happening at bilateral projects and regional ones (e.g. European projects like MetGrow+ [118]), supported by policy and action plans [43] yet, a collective effort to streamline work on residues' valorisation seems absent for the time being. A bottom up movement based on voluntary involvement, might be able to contribute to this direction. Having this in mind, we try to develop an open access, free-to-use software. If successful, we believe the use of residues will become easier, and results ultimately predictable. As such the software becomes a tool for gaining market (and social) acceptance of residue-based binder materials.

5.1.2 A brief history

The origin of the software lies in an excel file. At the start of this PhD thesis, most researchers in the group calculated by hand their mixtures from grams to molar ratios and back. To boost efficiency and leave less room for errors, these calculations were cast in an excel file. With this excel file, it became easy to for instance calculate the Na/Fe ratio from the chemical composition of the slag and activating solution or calculate the SiO_2/Na_2O molar ratio of an activating solution with a certain amount of hydroxide pellets and waterglass. Not satisfied with the user friendliness of the excel interface, a more robust software was made using Visual Studio 2015 (later versions were made in Visual Studio 2017). The home page is shown in Figure 5.1. The module "CalRat" contains the above mentioned calculations. The "Eco-financial analysis" was added later and Figure 5.2 shows the interface of this module as a general example. This tool can be used to calculate the environmental impact of a mixture (to be defined by filling in the boxes), based on the LCA study in section 5.2. Additionally, a rough calculation of the price of a mixture can be performed.

Two other modules are observed in Figure 5.1, "Synthesis" and "Prop(erty) Estimator", corresponding (at least in idea) to later database modules. The synthesis module collects data, e.g. chemical composition, processing conditions and resulting properties of mortars, while providing a description on how to perform the experiments to ensure a consistent methodology. As such, a small database originated. When the compressive strength or setting time that the user would like to achieve is put in, together with a goal, for instance minimize cost, the "PropEstimator" can extract from this database the best mixture or

calculate a potential best mixture, interpolating the available data. Having only a small database, the accuracy was only reasonable in a small range of mixtures that were already tested in the research group. Really powerful estimations are only possible when collecting data worldwide. The need and ambition of taking the software online for everyone to use, made the development of the software grow out of the range of capabilities of the PhD candidate. The later versions are developed using professional help. The continuation of this section discusses the functionality of the current version of the software, "SReDat" in more detail.

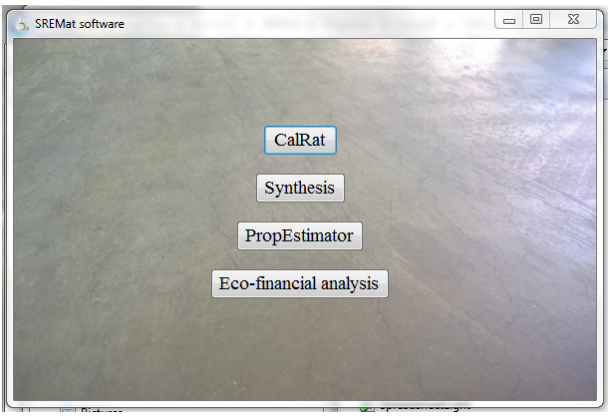

Figure 5.1: Home page of 1st SREMat software.

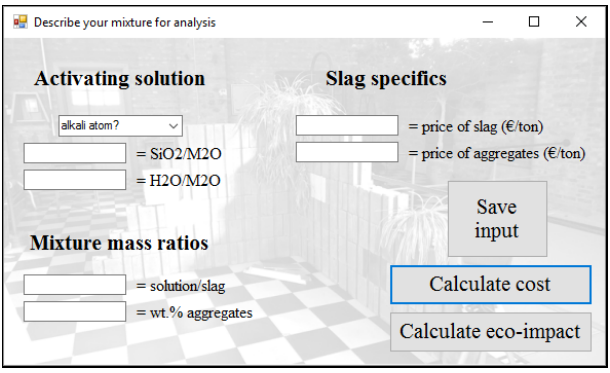

Figure 5.2: Interface of the Eco-financial analysis tool in the 1st SREMat software.

5.1.3 Software architecture

The structure of the SReDat software is around modules, schematically shown in Figure 5.3. These units can be stand-alone, or can interact and feed each other with data. The central module is the database. Conceptually, the database looks like the RRUFF database for minerals [95]. Instead of pure minerals, residues and treated residues can be found. The uploaded information contains for instance chemistry, location, industry of origin and the classification of the residue according to European legislation. Experimental data, like Fourier transform infrared spectra, Raman spectra, X-ray diffractograms or Mössbauer spectra, can be included. The input data will be stored online immediately if it comes from known users, e.g. researchers from the own research group or partner institutions. The data of unknown users has to be screened by a person knowledgeable in the topic and methods, e.g. the writer of this thesis. Users can be upgraded to be allowed to directly upload their data without check when a certain amount of good quality data submissions have been performed. An example residue (the "low-Ca slag" from section 3.3, 3.4 and 4.2) is shown in Figure 5.4. The database has been built by users, and the

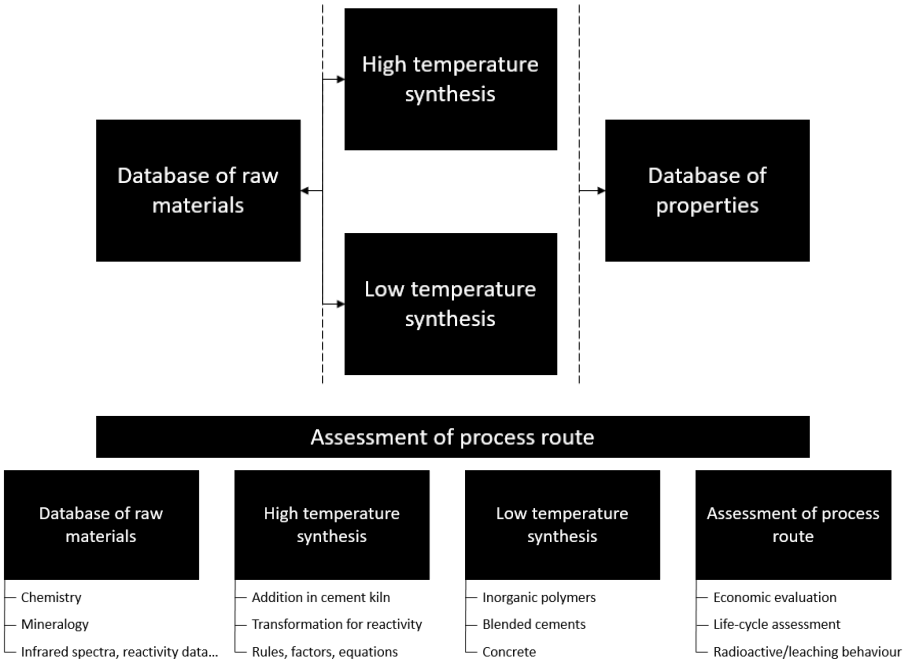

Figure 5.3: Overview of the software and its modules.

proper acknowledgment is given. Samples can be sent however also to the administrators, i.e. KU Leuven, and measurements are performed again, in order to verify the information listed. This creates a smaller database, the critically assessed one, within the bigger pool of data.

At a second stage, these residues (now raw materials) are introduced in existing or upcoming processes, and there are two separate modules for this task, i.e. that of high temperature and that of low temperature. The applications targeted can potentially incorporate substantial volumes in both cases, that is, cementitious and inorganic polymer binders for mortar and concrete development. The high temperature module is the first after the database module. From a processing perspective, there is a roasting process, a clinkering process and a melting process. The common denominator in all these processes is the high temperature and the formation of liquid phase, to small (roasting) or greater extent. Depending on the specifics, thermodynamic calculations can be incorporated by 3rd party software to predict the final outcome. The clinkering processes are well established when

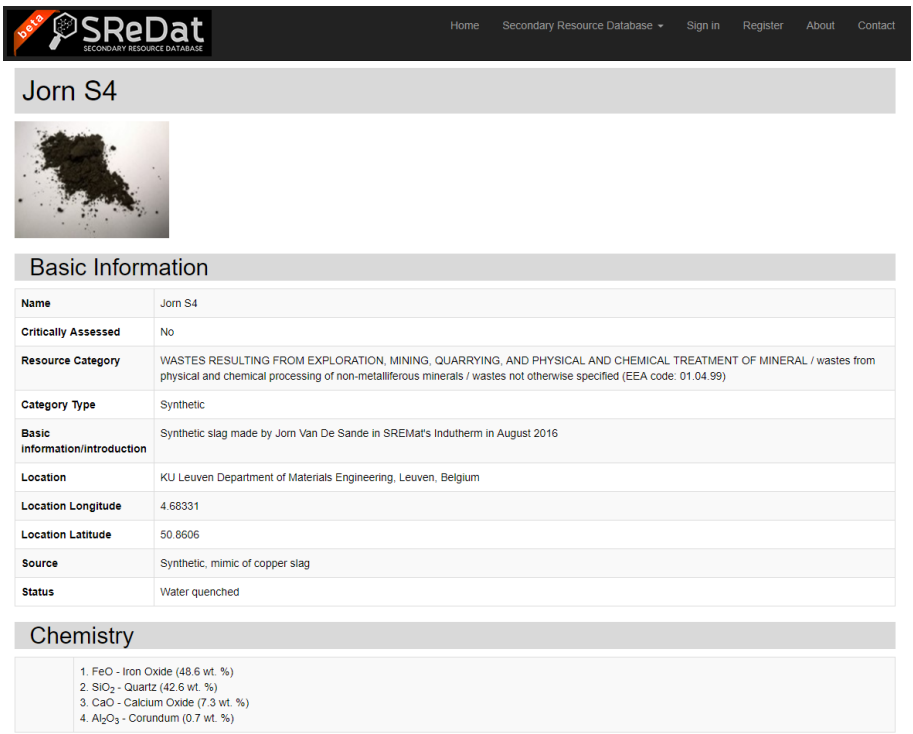

Figure 5.4: Example page of residue, showing its origin and chemical composition.

it comes to ordinary Portland cement (OPC), but emphasis is also placed in other clinkers, e.g. calcium-sulfoaluminate and calcium-sulfoferroaluminate cements. In the OPC case, the clinker is designed based on the silica ratio, alumina-iron ratio, lime saturation factor [72] and the results are qualitatively predicted by the well-established Boque equations (and the modified ones [184]). For the new clinkers, work is on-going, both for the raw materials' design of the clinker as well as for the prediction of the final mineralogical assemblage, for instance [188]. Apart from information on the quality of the clinker, data regarding the process itself are also generated, e.g. CO_2 emissions. The roasting and melting process coexist, and are treated (for now) as a mass balance exercise, where the final chemistry is calculated. The roasting process targets applications that require materials that need thermal activation in order to, for instance, enhance their pozzolanic performance and deliver blended cements or make them more suitable for the synthesis of inorganic polymers and geopolymers. A classic example for the latter would be the thermal treatment of kaolin to give metakaolin but other processes also emerge [70].

In the low temperature module raw materials in the database, either as produced or after high temperature processing (see paragraph above), are used to synthesize inorganic polymer binders, mortars and concrete. The work herein is borrowing ideas from a range of mix design software for concrete, e.g. the HIPERPAV® III software developed by the U.S. Federal Highway Administration (FHWA). The module "Process assessment" conducts calculations to support the choice of processing options and is thus based on the earlier developed "Eco-financial anlysis" tool described in section 5.1.2. Giving the mixture as input, an estimation of the cost (€/ton) and environmental impact (% in comparison with CEMI) is provided. The calculation of the environmental impact is based on the cradle-to-gate study presented in the next section and Peys et al. [145], with the difference that the mass is used as functional unit instead of load bearing capacity. This change makes the calculation independent of the transport distance and compressive strength of the samples, which complicates the online tool. The reader will note after reading the next section that transport distance and compressive strength are actually important parameters in calculating the environmental impact. The tool presented here thus only shows an estimation to quickly compare different recipes. A more detailed assessment should be performed afterwards. The performance with respect to radioactivity or leaching can also possibly be modelled and become an addition in future updates.

The last module is trying to propose options from the back-end, that is the application. Instead of selecting raw materials for certain processing and end-product requirements, in the "Target" module the user is provided with three options for a specific high temperature or low temperature product (see

respective modules to see what these are). The options are compressive strength, cost or environmental impact. Per criterion, a second level of options is given, that of “optimise”, “aim to max/min” (depending on the case) or “ignore”. The operation of this module is still suggestive, as the database with compressive strength, cost and environmental impact is under development.

Apart from the database and above mentioned calculations, the software also provides a toolbox with support calculations per module. These can involve complex calculations on the slag properties, e.g. the viscosity. This property is not only important for the high temperature process control, but also for the glass formation [190] and thus important for the reactivity of the slag in inorganic polymers or cementitious materials in general. The calculations are based on models that can be found in literature: Giordano et al. [53] and Zhang et al. [217]. While the model of Giordano et al. can also be used to calculate the glass transition temperature and fragility of the glass, the model of Zhang et al. provides more detailed attention to the interaction between different chemical elements and is therefore more suited for complex chemistries. The user of the software is able to select the preferred model. Future work will add the model of Liu et al. [105], including the influence of particles. Another example of support calculations is the "CalRat" module described in section 5.1.2. This tool should make the daily task of mixing even more easy for the researcher, as equations are implemented to transform reported parameters in literature, e.g. SiO_2/Na_2O molar ratio, to a recipe, e.g. mass of NaOH pellets to mix, and the other way around. These, what used to be annoying, calculations are programmed in such a way that the researcher can go to the lab without pre-calculating the recipe, open the smart-phone and quickly put in the parameters that were in mind and read what to mix.

5.1.4 Instead of conclusions

The residue database is now online at www.sredat.info/web. This beta version still contains bugs and user-unfriendly issues, but residues can be uploaded and searched. The support calculations and process assessment tools described in the above paragraph are all described in algorithms, ready to be implemented. The main action point and difficulty now is finding support for the idea and convincing people to put their data publicly available in the SReDat. This is tackled by presentations at conferences, sharing in social media and providing the links on our website(s). In the end, the final version of the software, including a well-filled database driving it, will increase the ease of formulating good recipes. This enables new-comers to the field, companies or researchers, to see the potential of their material, by showing the properties it can reach

and suggesting processing conditions to reach it. The software can thus be an important tool in the acceptance of residue-based binders with the general public and construction companies.

5.2 Simplifying the calculation of the environmental impact

This section is based on the published paper:
A. Peys, L. Arnout, B. Blanpain, H. Rahier, K. Van Acker, Y. Pontikes, "Mix-design parameters and real-life considerations in the pursuit of lower environmental impact inorganic polymers", *Waste and Biomass Valorization* 9 (6), 879-889.

Contributions of the authors: Samples were made together with L. Arnout. A. Peys performed the LCA studies and the analysis of the results under supervision of K. Van Acker. All co-authors helped in formulating the discussion and conclusions.

Abstract

The environmental impact of inorganic polymer mortars from non-ferrous slag was assessed and compared to ordinary Portland cement (OPC) mortar based on a load bearing capacity of 10 MN of bricks of 0.1 m high. Two strategies to minimize the environmental impact of inorganic polymers were pursued. Activating solutions with a lower alkali content (H_2O/Na_2O = 16, 24, 32, 40, 48; constant SiO_2/Na_2O = 1.6) were investigated while keeping the water/slag mass ratio of the inorganic polymer mortar mix constant. Another synthesis route considered the complete replacement of the activating solution by maize ashes. These were blended with the slag in different ash/slag mass ratios (0.2, 0.4, 0.6) before adding water, producing a so-called "one-part" inorganic polymer. A sensitivity analysis showed that the effect of compressive strength and transport distance is extensive. Because of this considerable transport distance dependence, several cities in Flanders were selected to perform a detailed LCA study. The optimal scores of the environmental impact were observed for Mol, the location of the sand supplier, and accounted for 23% with respect to OPC for the samples with the activating solution with a ratio of H_2O/Na_2O = 24 and 17% for an ash/slag ratio of 0.2.

5.2.1 Introduction

Inorganic polymers and geopolymers, in particular, have been proposed in the literature as good alternatives for ordinary Portland cement (OPC) in terms of CO_2 footprint [113, 115]. Despite this general consensus, a wide range of impact values can be found in literature, which are not only dependent on the mixture, but also on the way of reporting the environmental impact [28]. Mostly, carbon footprints or global warming potentials are reported, which are based on a weighted summation of all greenhouse gasses emitted during the processing. The inorganic polymers outperform OPC on that aspect because of the high processing temperature and CO_2 emitted during clinker production. It is however questionable if the inorganic polymer should be compared to a CEM1 OPC. Several precursors that are used for inorganic polymers can also be used in blended cements. To that extent, if the fate of a material is to be decided, it seems more proper to compare the inorganic polymer with the corresponding blended cement (e.g. with equivalent compressive strength), and not CEM1 OPC. This is not the case for the selected material in this study, as it is not being used commercially in blended cements. Considering other environmental impact categories than the CO_2 footprint (abiotic depletion, eutrophication, etc.), inorganic polymers are less performant than OPC [64]. However, the wide range of existing impact categories renders the analysis complex and a straightforward

conclusion, e.g. from the referred article of Habert and Ouellet-Plamondon [64], is not possible. Therefore, life cycle assessment (LCA) methodologies have been developed to combine all these impact categories and normalize them to a single score. Well-known examples are the ReCiPe methods, which provide weighting factors to transform the impacts of endpoint or midpoint categories to this single score [57].

Mix-design of inorganic polymers to optimize their environmental friendliness is not widely performed. Heath et al.[68] carried out a study of different formulations of clay-based inorganic polymers and observed a maximum of 30% reduction in global warming potential for bentonite based meta-clay geopolymers. Their results suggested an optimal SiO_2/Al_2O_3 molar ratio of 3.5–4.0. For metakaolin-based geopolymers, this range shows an optimum for compressive strength, as determined by Duxson et al.[38] and Lizcano et al.[106]. For iron-rich inorganic polymers from fayalitic (secondary copper) slag, investigated in the present section, the SiO_2/Al_2O_3 molar ratio is irrelevant. The SiO_2/M_2O (M = K or Na) molar ratio of the activating solution is in this case more appropriate. Depending on the reactivity of the precursor, this ratio is found optimal from between 1 and 2 [155] to above 3 [109].

In literature, several mix-design parameters and practical considerations that potentially lower the environmental impact of inorganic polymers are studied:

- Lower the activating solution/binder ratio [108]
- Lower the concentration of Na and/or Si in the activating solution [92]
- Use an alternative activator/alternative production route for the activating solution [115, 185, 120, 41, 55, 192, 146]
- Use local resources [113]

The activating solution is generally considered as the main contributor to the environmental impact [113, 115, 68]. Therefore, most strategies for lowering the impact focus on the activating solution: use less solution, a lower concentrated solution, or an alternative to the pure sodium silicate solution. The first option is not explored in the present section because this option also decreases the workability of the mixture [108]. This leads to complications in the comparison, as differences in processing have to occur. Lower concentrations of Na and Si in the activating solution have been used by Kriskova et al.[92] without a substantial loss of mechanical properties until an H_2O/Na_2O molar ratio of at least 30.8. Alternative activators can be used to replace the activating solution, at least partially. Rice husk ash, sugar cane ash, or waste glass has been used

to provide soluble silica for the activating solution [115, 185, 120]; a mixture of K_2CO_3 and $Ca(OH)_2$ has been used by Esaifan et al.[41] as an alternative route to produce a KOH solution. Sodium aluminate originating from a waste stream of chlorosilane production or from the Bayer-process has been used to activate a silica rich precursor [55, 192]. The use of biomass ashes from the cob of the maize plant as an activator to completely replace sodium/potassium silicate was proven to be successful in previous work using traditional silicate sources (metakaolin) [146]. Apart from the mix design parameters discussed above, some practical considerations are essential for lowering the environmental impact of inorganic polymers. The importance of transport in the environmental impact of inorganic polymers and, therefore, the importance of the use of local resources is mentioned qualitatively by Davidovits [28], and Provis and Bernal [152]. They have also mentioned the importance of advancing technology for the production of inorganic polymers as well as advances in enabling technologies like electricity production.

It is the aim of the present section to perform a mix-design to optimize the environmental impact of inorganic polymers. An iron-rich slag was selected, as this is currently not valorized in applications with added value. This kind of slag, which mainly consists of FeO and SiO_2 in an amorphous phase, was previously shown to successfully form inorganic polymers [137]. Starting from this iron-rich slag, two methodologies are followed: lowering the alkali content of the activating solution (using the same amount of water/slag, but different H_2O/Na_2O molar ratios) and using an alternative alkali source, i.e. biomass ashes. The production of these ashes is increasing in volume because of the increasing use of biomass combustion for electricity generation. A cradle-to-gate LCA quantifies the environmental impact using a ReCiPe normalization method and assesses the effectivity of the suggested routes. At the same time, the influence of location and technology on the environmental impact is quantified by performing several scenario analyses.

5.2.2 Experimental

Table 5.1 summarizes the compositions of the activating solutions and the mixtures investigated in this section. The first five mixtures considered the dilution of the activating solution, the other three used biomass ashes as an alternative activator. The same maize cob ash as in previous work [146] is investigated. This ash mainly consisted of amorphous potassium silicate, providing a suitable activator for the synthesis of inorganic polymers. In both systems, a non-ferrous slag presented earlier by Onisei et al.[137] was used as an iron-silicate precursor. This slag is not valorized in cementitious materials today,

although it has been demonstrated (depending on chemistry and mineralogy) that it can behave as a pozzolanic or latent hydraulic material [31]. The aggregate/(slag + ash) mass ratio was constant for all at 2.4. This way, the same volume of aggregates/binder as in the standards for OPC mortar testing was kept, where an aggregate/OPC mass ratio of three is proposed. Using the difference in bulk density between OPC and the slag powder, the mass ratio of 2.4 was obtained. Quartz sand with a particle size below 2 mm was used, according to the standard EN 196-1.

The SiO_2/Na_2O molar ratio was kept constant at 1.6 based on preliminary experiments. A sodium-based activating solution had been selected because environmental databases are more accurate for sodium hydroxide/silicate with respect to potassium hydroxide/silicate. The amount of ash was derived from previous work [146], recalculating for the density difference between the slag used here and the metakaolin used there. The water/solid ratio was higher in these samples with respect to that of the sodium silicate activated inorganic polymers. This was needed to keep the same workability.

Mortars for compressive testing were mixed using a Hobart mixer, after which a jolting table was used for enhancing the flow of the material inside the mold. Between demolding and testing, the samples were stored at 20 °C in airtight boxes, resulting in an environment of saturated humidity. The compressive strength was measured 28 days after synthesis on four samples of $4 \times 4 \times 4$ cm^3, using an Instron 5985 with a crosshead speed of 2 mm/min. For ordinary Portland cement, CEM I, a compressive strength of 52.5 MPa is assumed, which is the required strength after 28 days according to standards (EN 196). Densities of the mortars were measured geometrically. For OPC mortar, a value of 2200 kg/m^3 [196] was used.

Table 5.1: Investigated mixtures (SiO_2/Na_2O and H_2O/Na_2O only consider the activating solution; solid = ash + slag)

Sample name	SiO_2/Na_2O (molar)	H_2O/Na_2O (molar)	Ash/slag (mass)	Water/solid (mass)
$16H_2O$	1.6	16	0	0.26
$24H_2O$	1.6	24	0	0.26
$32H_2O$	1.6	32	0	0.26
$40H_2O$	1.6	40	0	0.26
$48H_2O$	1.6	48	0	0.26
0.2A	-	∞	0.2	0.28
0.4A	-	∞	0.4	0.28
0.6A	-	∞	0.6	0.28

To the ash-slag one-part mixes only water was added

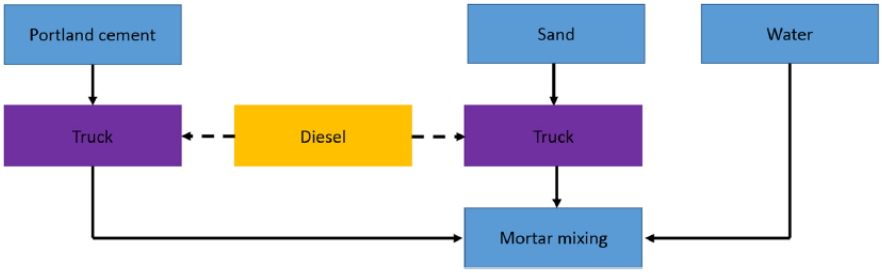

Figure 5.5: Overview of the ordinary Portland cement system

The above described experiments were designed to investigate the effect of the concentration of the activating solution and of the use of an alternative activator on the environmental impact of inorganic polymers. These impacts are compared with CEMI OPC as a reference.

5.2.3 Life Cycle Assessment

Goal and Scope

A comparative cradle-to-gate life cycle assessment (LCA) was performed on the mixtures in Table 5.1 along with a standard CEM I, based on the capacity to bear a vertical load of 10 MN. This force is translated into a material need by dividing it by the compressive strength after 28 days (MN/MPa = m^2). This results in a needed surface of material. To be able to compare the different mixtures, a constant height of the hypothetical bricks that are compared needs to be assumed, which results in the material volume needed to bear the load of 10 MN. A height of 0.1 m is chosen. The density of the mortars was used to transform the material need in volume to mass.

In the ordinary Portland cement mortar system (Fig. 5.5), the production of OPC powder was taken into account. Transport of the raw materials was performed by trucks. The transport of Portland cement was assumed to start at the cement distributor, which is not necessarily the same location as the production plant. The making of the mortar does not include energy for mixing or shaping; it only composes the mortar mixture in the right ratios.

Figure 5.6 illustrates the different sub-processes needed to obtain sodium silicate activated inorganic polymer mortars. The slag used as a binder is nowadays used in low-added value applications (e.g. sandblasting < €50/tonne), while

the end-product is of higher value (nonferrous metals > €1000/tonne). Using economic allocation [6], the impact of the production of the non-ferrous slag can be approximately fully attributed to the metal. More recent literature mentions a different approach for calculating the environmental impact of ironmaking slag [20]. There, the environmental impact difference of increasing the amount of produced slag in a certain ironmaking facility is assessed. This environmental impact is then extrapolated to the actual amount of slag produced. A thorough knowledge of the slag production process and its mass balances is needed to enable the implementation of this method, which is not the case here. Therefore, the reasoning of economic allocation is followed and the environmental impact of the production of slag is neglected. This reasoning would not be valid for the more frequently used by-products, e.g. blast furnace slag or fly ash. As they are used in a great extent in blended cements, they should be considered as a product and their production should be taken into account. The milling of the slag was included in the LCA to achieve a similar particle size distribution as cement.

An overview of the system of biomass ash activated inorganic polymers is provided in Fig. 5.7. Biomass ashes were also modelled as a waste, as it is not for the production of the ashes but for electricity generation that the biomass is burnt. A furnace treatment to decompose the carbonates and burn the remaining charcoal in the ashes is needed to increase the reactivity of the ashes.

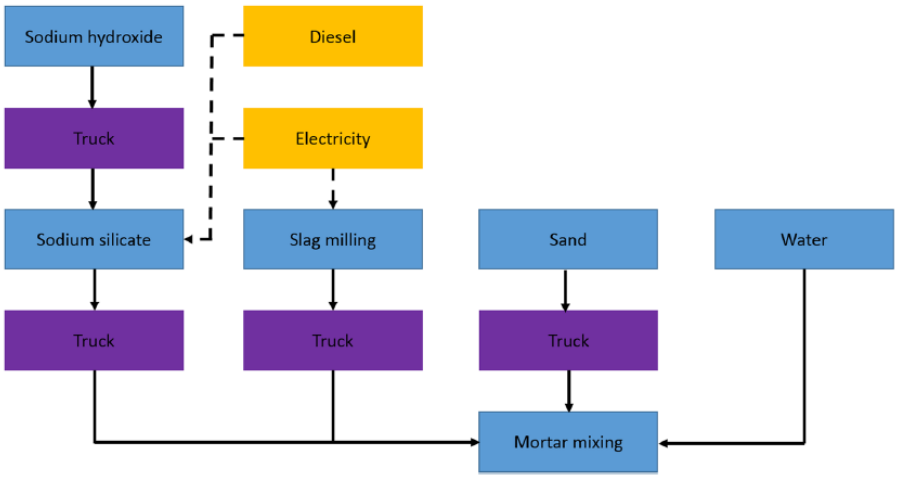

Figure 5.6: Overview of sodium silicate activated inorganic polymer system. (Diesel was also used for transport with trucks, but the arrows were not provided to avoid overloading of the figure)

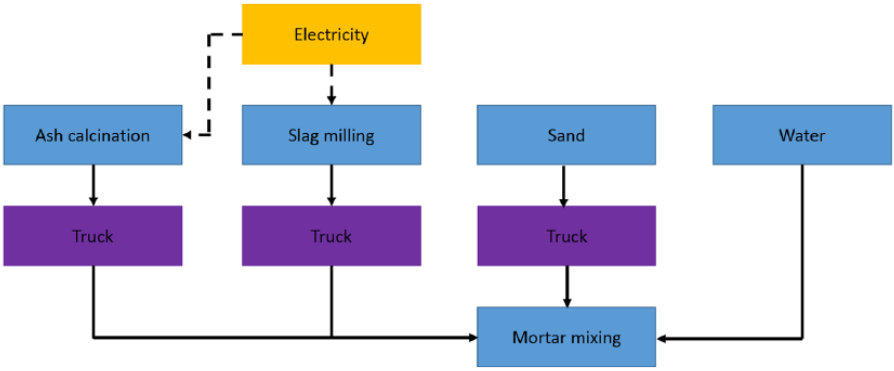

Figure 5.7: Overview of the biomass activated inorganic polymer system. (Diesel was also used for transport with trucks, but the arrows were not provided to avoid overloading of the figure)

Life Cycle Inventory

The inventory was gathered mainly from the GaBi database [187], with the addition of values from literature, experimental data, and theoretical calculations. The processes can all be found in Figs. 1, 2 and 3. The information was gathered preferably based on Belgian data (otherwise EU, neighboring country, or global data, in that order of preference). For transport, a diesel driven truck of category Euro 4 was selected. The foreground data that could not be gathered from the database or our own experiments was gathered from literature or calculations. These data refer to:

- Waterglass (sodium silicate solution)
- Slag milling
- Ash calcination

The inventory of sodium silicate solution was based on Fawer [45], as is done in the EcoInvent database v2.0 [215]. Two production methods exist: a high-temperature process (referred to as "furnace method" from now on), where sand is dissolved into molten soda, and a hydrothermal process, where the sand is dissolved in a concentrated sodium hydroxide solution in an autoclave. Based on experience [Peys A, unpublished results.], slag milling was assumed to be similar in energy consumption to cement milling, which consumes about 20 kWh/ton according to literature [8, 110, 75]. Infrastructure and tools were

neglected. The latter was not done for OPC. However, as milling infrastructure and tools did not provide a significant contribution to the impact, neglecting this for slag can still be defended. A calculation was performed to provide an estimation of the energy consumption during the calcination of the biomass ashes. Using a heat capacity of 1 J/(g K) of the ashes, 0.75 MJ of energy is needed to heat 1 kg of ash up to 750 °C. This heat, compared to the reaction heat gained from burning the remaining charcoal in the ashes ($C + O_2 = CO_2$, 33 MJ/kg C, calculated using HSC 6.1), is negligible. Therefore, as long as the ashes going to the furnace contain more than 2.3 wt% of C, the temperature of 750 °C can be sustained by the reactions themselves, with no need for extra energy sources. The ecological impact of infrastructure was neglected.

Impact Assessment

The systems were compared using ReCiPe midpoint categories for quantification of the impact starting from the inventory, excluding biogenic carbon in the climate change category. These categories are weighted using the Recipe Europe midpoint normalization looking from the hierarchist perspective to provide a common unit for comparison: person equivalents weighted (PEW). This unit refers to the environmental impact of an average person per year (for the ReCiPe Europe normalization, an average European citizen, based on data from 2010). The ReCiPe method conforms to ISO 14040 and 14044 standards [57].

The contributions to the total environmental impact of different sub-processes of the three studied systems (see Figs. 5.5, 5.6 and 5.7) are investigated to enable the use of a simple equation to calculate the environmental impact for different mixtures inside these systems (in PEW/10 MN). The transport distance will be assumed to be 100 km, a valid assumption in Flanders, for all raw materials in the first study. Therefore, this distance is phrased per 100 km in the equations. Afterwards, this will be varied to investigate its influence.

1. $EcoScore\ \ OPC = [wt\%\ \ OPC \times I_{OPC} + wt\%\ \ sand \times I_{sand} + (wt\%\ \ OPC \times d_{OPC}/100\ \ km + wt\%\ \ sand \times d_{sand}/100\ \ km) \times I_{transport}] \times \frac{\rho_{mortar} \times 0.1\ \ m}{52.5 MPa}$
2. $EcoScore\ \ IP = [wt\%\ \ slag \times I_{milling} + wt\%\ \ sand \times I_{sand} + wt\%\ \ solution \times (1 - wt\%\ \ water\ \ in\ \ solution) \times I_{solution} + (wt\%\ \ slag \times d_{slag}/100\ \ km + wt\%\ \ sand \times d_{sand}/100\ \ km + wt\%\ \ solution \times (1 - wt\%\ \ extra\ \ water\ \ added) \times d_{solution}/100\ \ km) \times I_{transport}] \times \frac{\rho_{mortar} \times 0.1\ \ m}{\sigma_{c,mortar}}$
3. $EcoScore\ \ biomass\ \ activated\ \ IP = [wt\%\ \ slag \times I_{milling} + wt\%\ \ sand \times I_{sand} + wt\%\ \ biomass\ \ ash \times I_{calcination} + (wt\%\ \ slag \times d_{slag}/100\ \ km +$

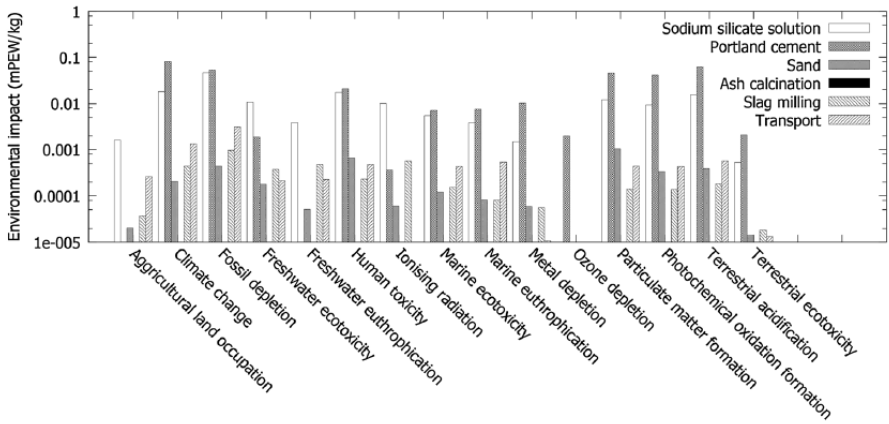

Figure 5.8: Environmental impact of the different sub-processes, subdivided into midpoint categories. The units are normalized to person equivalents weighted (PEW) to be able to compare the different categories. For the transport, 100 km was considered. A logarithmic scale for the y-axis was needed because of the large differences between the different sub-processes

$$wt\% \quad sand \times d_{sand}/100 \quad km + wt\% \quad biomass \quad ash \times d_{ash}/100 \quad km) \times I_{transport}] \times \frac{\rho_{mortar} \times 0.1 \quad m}{\sigma_{c,mortar}}$$

In these equations, I_x refers to the environmental impact of sub-process (PEW/kg), d_x refers to the distance to the supplier of substance (km), ρ_{mortar} the density of the mortar (kg/m^3), and $\sigma_{c,mortar}$ the compressive strength of the mortar (MPa).

5.2.4 Results and Discussion

Contribution Analyses - Factors for the Equations

The environmental impact of the different sub-processes defined in section 5.2.3 is shown in Fig. 5.8, providing all midpoint categories. The difference between the different activating solution processing routes was immediately noticeable; the furnace route has a 50% higher impact than the hydrothermal route. Therefore, the furnace route is not investigated further or discussed in the present work, and it is not presented in Fig. 5.8.

It is clear that especially on the aspect of climate change, the production of OPC exceeds all other sub-processes. The only impact categories that are

Table 5.2: Contributions of the raw materials and transport to the environmental impact (in mPEW/kg, factors I_x in equations 1–3) of the respective raw materials. Considering the sodium silicate solution, dry refers to the fact that the impact is rescaled to the dry content

Raw material	Climate change (mPEW/kg)	Fossil depletion (mPEW/kg)	Freshwater ecotoxicity (mPEW/kg)	Single score endpoint (mPEW/kg)
Ordinary Portland cement	0.0807	0.0530	0.0019	0.3355
Sodium silicate solution (SiO_2/Na_2O = 1.6, H_2O/Na_2O = 16, hydrothermal)	0.0181	0.0459	0.0106	0.1560
Sodium silicate solution, dry (SiO_2/Na_2O = 1.6, hydrothermal)	0.0512	0.1297	0.0300	0.4406
Ash (calcination)	0	0	0	0
Slag (milling)	0.0004	0.0010	0.0004	0.0039
Sand aggregates	0.0002	0.0004	0.0002	0.0037
Transport (by truck)	0.0013/100 km	0.0031/100 km	0.0002/100 km	0.0080/100 km

significantly in favor of OPC are freshwater ecotoxicity/eutrophication and ionizing radiation.

The values for a selection of midpoint categories as well as an aggregated single score are provided in Table 5.2. The aggregated single score is the sum of all impact categories displayed in Fig. 5.8. Other midpoint categories will not be discussed from this point onwards, but results of these are provided in the supplementary information. The impact of the sodium silicate solution is recalculated to its dry content. This enables the calculation of the impact for different H_2O/Na_2O molar ratios without the need of GaBi software.

Using the factors from Table 5.2 in the equations of section 5.2.3, the environmental impact of inorganic polymers can be calculated for all mixtures presented in section 5.2.2.

Environmental Impact and Sensitivity Analysis

The equations are used to calculate the impact per 10 MN load bearing capacity of the different mixtures of Table 5.1, assuming all the raw material suppliers are at 100 km from the mortar mixing plant. The results are shown in Table 5.3.

Table 5.3: Compressive strength and environmental impact of the inorganic polymer and Portland cement mortars

System	Compressive strength (MPa)	Equivalent mass (kg)	Climate change (mPEW/10 MN)	Fossil depletion (mPEW/10 MN)	Freshwater ecotoxicity (mPEW/10 MN)	Single score endpoint (% of OPC)
OPC	52.5	4.19	0.081	0.062	0.003	100
$16H_2O$	44.2 ± 0.8	5.80	0.019	0.046	0.008	43.8 ± 0.8
$24H_2O$	46.4 ± 0.7	5.51	0.014	0.035	0.006	32.9 ± 0.6
$32H_2O$	30.2 ± 0.4	8.47	0.018	0.045	0.008	41.6 ± 0.6
$40H_2O$	6.1 ± 0.5	41.90	0.082	0.203	0.033	187.8 ± 15.3
$48H_2O$	4.0 ± 0.2	64.00	0.122	0.295	0.047	272.5 ± 13.6
0.2A	15.9 ± 2.6	16.06	0.021	0.048	0.006	42.8 ± 7.1
0.4A	16.4 ± 0.6	15.63	0.020	0.047	0.006	42.2 ± 1.4
0.6A	11.9 ± 1.0	21.59	0.027	0.064	0.007	58.9 ± 5.1

The single scores are presented relative to OPC for easier comparison. The mass needed to provide the same load bearing capacity of 10 MN/10 cm is mentioned. The 90% confidence intervals extracted from the compressive strength tests are mentioned

A dramatic decrease in the impact on climate change can be observed when comparing OPC mortars to the inorganic polymers 16-24-32H_2O and to the ash activated inorganic polymers. Lower H_2O/ Na_2O ratios were ineffective because the compressive strength was lowered to a great extent, compensating for the lower use in alkalis. With respect to fossil depletion, the 16-24-32H_2O and 0.2–0.4 A samples are also the best performant. Only on the aspect of freshwater ecotoxicity the inorganic polymers performed poorly, which was expected from Fig. 5.8 and Table 5.2. However, the absolute values in this impact category are lower. Therefore, when calculating an aggregated single score, the inorganic polymers 16-24-32H_2O and biomass ash activated samples 0.2–0.4 A still have the lowest impact. Using an activating solution with an H_2O/ Na_2O molar ratio of 24 can lower the environmental impact to 32.9% of the impact of OPC. The use of biomass ashes as alternative activator reduced the impact to 42.2% (ash/slag = 0.4). It should be noted that the higher impact of biomass ash activated with respect to sodium silicate activated inorganic polymers originates from the lower strength. For non-load bearing applications, biomass ash activated inorganic polymers would be the option with the lower environmental impact.

The sensitivity of several input data is explored by varying these parameters by 10 and 20% (Fig. 5.9). This shows the possible error that can be made on the environmental impact by errors in the estimation or measurement of the input data. The sensitivity of the input values of the energy of the production of sodium silicate and the milling of the slag was low. Because of the direct relation of the compressive strength with the environmental impact,

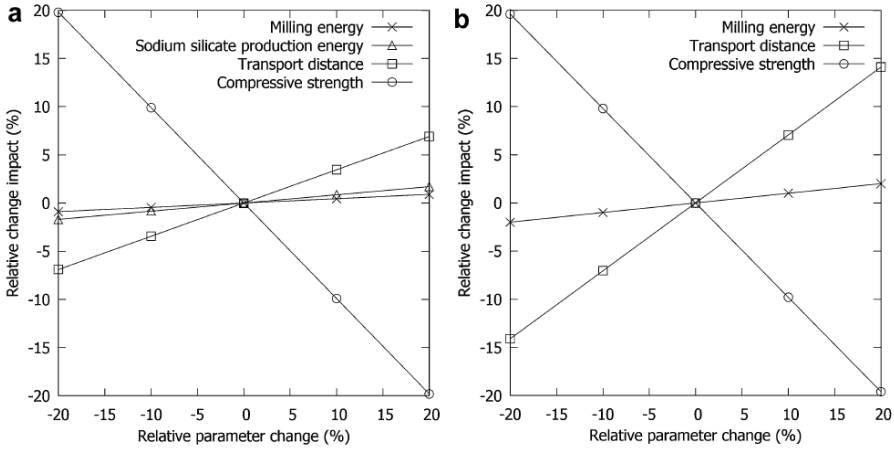

Figure 5.9: Sensitivity analysis of selected parameters for single scores of $24H_2O$ (a) and 0.4 A (b)

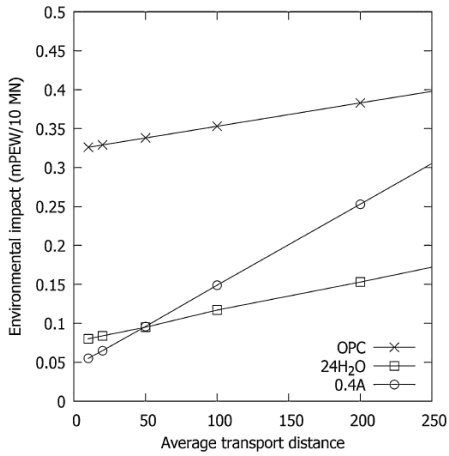

Figure 5.10: Influence of the average transport distance on the environmental impact of inorganic polymers and Portland cement mortar

changing the strength by X% will change the impact by the same X%. The 90% confidence intervals derived from strength measurements on four samples are, therefore, added in Table 5.3. This sensitivity on compressive strength shows the importance of further research to tune the mechanical properties of both systems.

Table 5.4: Single score environmental impact in % of OPC with an average transport distance of 100 km in four of Flanders' large cities (Ghent, Antwerp, Brussels, Hasselt) and the main raw material suppliers: non-ferrous slag (Beerse, Olen) and sand (Mol)

System	Ghent	Antwerp	Brussels	Hasselt	Beerse	Olen	Mol
OPC	100	97	100	95	96	95	93
$16H_2O$	45	38	42	36	34	33	32
$24H_2O$	35	28	32	26	25	24	23
$32H_2O$	44	35	40	32	29	29	27
0.2A	47	31	41	28	22	20	17
0.4A	44	29	39	28	22	20	17

The effect of the transport distance is also significant. This transport distance can vary drastically and is, therefore, investigated in more detail in Fig. 5.10, comparing the effect on the Portland cement mortar system and the optimal inorganic polymers ($H_2O/Na_2O = 24$ and ash/slag = 0.4). The impact of biomass activated inorganic polymers was more dependent on the transport distance in comparison with the impact of the sodium silicate inorganic polymers. Because of the lower compressive strength of the 0.4 A, more material is needed to provide the same load bearing capacity. More material needs to be transported, resulting in a higher absolute contribution of transport in the environmental analysis. Therefore, the transport distance is the important factor in the environmental impact of biomass activated inorganic polymers.

The differences in sensitivity and the large contribution of transport stress the need for the use of local raw materials for inorganic polymer synthesis and the importance of considering the transport distance in LCA analyses.

Location Specific Analyses

The section above showed that the analysis is very dependent on the location of the raw material producers and no generic conclusions can be drawn from the environmental analyses. Therefore, a set of cities in Flanders is chosen to investigate this dependence on location in detail (Fig. 5.11). Four major cities were selected, along with locations of the main raw material suppliers (sand/slag producers). The environmental impacts of the mixtures from Table 5.1, excluding those that did not prove to be promising from Table 5.3, are compared in Table 5.4.

It is clear that the inorganic polymer systems outperform OPC everywhere, showing 17–47% of the impact. Interestingly, the relative scores of $24H_2O$ and 0.4 A are dependent on the location because of the relative contributions of

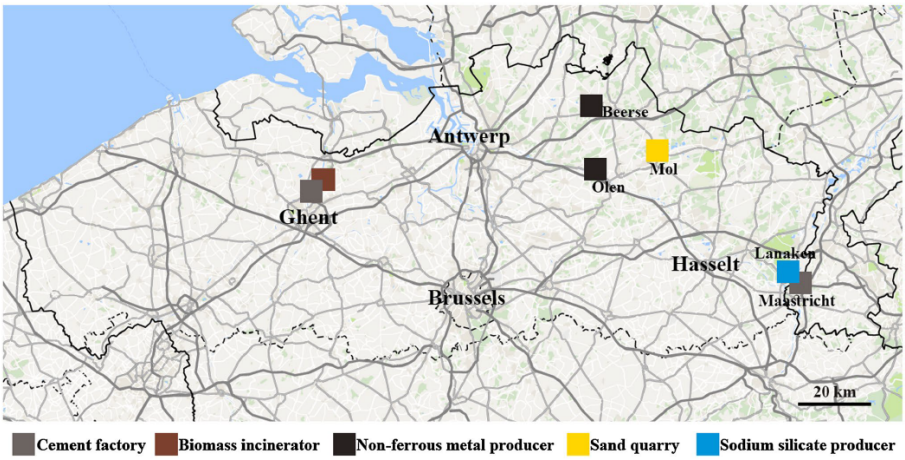

Figure 5.11: Adapted google maps view of Flanders with indications of cities selected for the analyses and locations of the raw materials suppliers

transport in the environmental analysis shown in Fig. 5.10 and discussed in the previous section. The lowest scores are found at the sand quarry (in Mol). Because sand represents the main mass of the mortar, this location represents the minimal amount of ton.km transport, resulting in the lowest environmental impact.

Scenario Analysis: Green Energy

The analyses in Tables 5.3 and 5.4 all considered historic data on the production of the activating solution, electricity, etc. This approach is criticized as technology advances [28]. Therefore, the following scenario analysis (see Fig. 5.12) investigates the use of a more green source of electricity for the production of the sodium hydroxide, implemented here as electricity from wind energy. This replaces the standard electricity production method used in the GaBi database for sodium hydroxide production: the average German production mix.

The use of wind energy has a huge effect on the environmental impact of sodium silicate activated inorganic polymers (Fig. 5.12), resulting in an impact of 8% of that of OPC (compare with 23% using current electricity production mix).

The impact of the activating solution in the hydrothermal processing route is mainly caused by the production of sodium hydroxide (82%), which on its turn mainly originates from the intensive electricity consumption in the chloralkali

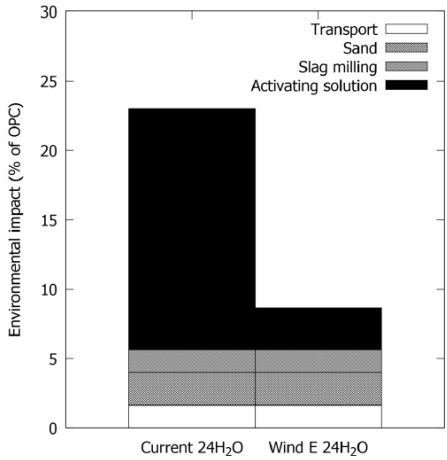

Figure 5.12: Future scenario analyses in Mol for $24H_2O$ comparing the current state of technology with a scenario using wind energy for the production of sodium hydroxide (Wind E). The results are shown relative to OPC

process [186], as is illustrated in Fig. 9. Therefore, the main contributor to the impact of sodium silicate activated inorganic polymers was electricity, which explains the effectiveness of using wind energy. Similar conclusions were drawn by Habert and Ouellet-Plamondon [64] on the effectiveness of changing the energy source for the calcination of metakaolin for lowering the environmental impact of geopolymers.

Following the results of the present section, suggestions can be formulated to minimize the environmental impact of inorganic polymers. In the production of the sodium silicate, it is beneficial to perform this via the hydrothermal route, as the furnace route shows a 50% higher impact. The large contribution of electricity in the production of the activating solution causes the environmental impact to be highly dependent on energy technology. A transition to green energy causes a significant drop of the impact. For the same reason, the environmental impact can be limited by the substitution of NaOH, eliminating the use of the electricity in the chloralkali process. Possible alternatives are the presented maize ashes, the $K_2CO_3/Ca(OH)_2$ mixture from Esaifan et al.[41], or the sodium aluminate from Gluth et al.[55] and van Riessen et al.[192]. The introduction of silicates in the NaOH for the production of the activating solution does not show a large contribution, thus substitution of sand for rice husk ash or sugarcane straw ash, as presented by Melado et al.[115], Tchacouté et al.[185], and Moraes et al.[120] does not provide a substantial reduction of

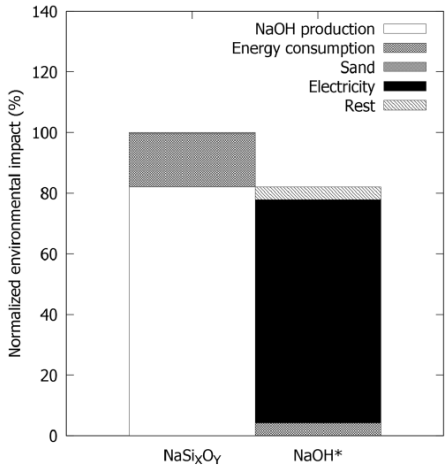

Figure 5.13: Contribution analysis of hydrothermally produced sodium silicate and sodium hydroxide (*estimation based on Thannimalay et al.[186]). The contributions in sodium hydroxide are normalized to 95% to fit the contribution of sodium hydroxide in sodium silicate. Therefore, the electricity contribution in sodium silicate is directly visualized

the environmental impact. Finally, lowering the concentration of the activating solution showed to be successful. However, care should be taken that the properties are maintained.

The limits of the calculations of the present section should be stressed to avoid faulty conclusions and wrong use of the presented data. The analyses do not include consequential LCA and are limited to the production of the mortars, no use or end-of-life phase in incorporated. Transport is only incorporated as road transport, while it would be interesting to see the influence of different methods of transport. The values presented in Table 5.4 are only valid for the Flemish situation sketched in Fig. 5.11. However, they can be extrapolated easily to other locations by using the proposed equations.

5.2.5 Conclusions

The environmental impact of inorganic polymers from non-ferrous slag was assessed and minimized. An equation, summarizing the different contributions, eased the calculations for different mixtures. Using sensitivity analyses, the impact was shown to be most dependent on compressive strength and transport

distance. The importance of transport distance shows the need for local analyses, which are performed for Flanders.

The optimal inorganic polymers had an H_2O/Na_2O molar ratio of 24 or an ash/slag mass ratio of 0.4. The environmental impact was the lowest for the city of Mol, 23 and 17% in comparison with OPC, respectively, as the total amount of ton.km transport was the lowest.

Scenario analyses revealed an even higher potential environmental impact drop when using a green source of electricity (wind) in the chloralkali process for the production of sodium hydroxide. An environmental impact of 8% with respect to OPC was observed when using wind energy for the generation of electricity (for the activating solution with a molar ratio H_2O/Na_2O of 24 and for Mol), compared to 23% with the current electricity production mix. A contribution analysis on the sodium silicate solution showed the large influence of sodium hydroxide (82%). Therefore, the environmental impact is much more dependent on the sodium than the silica content of the activating solution.

Chapter 6

Highlights

6.1 Inorganic polymer structure

- The final inorganic polymer binder contains Fe^{3+} after curing, milling and exposure to air as powder, although the precursor slags usually have Fe^{2+} as main oxidation state.
- The coordination state of the Fe in the final binder is 4-fold or a combination of 4 fold and higher coordinated species.
- The final molecular structure cannot be finetuned by the activating solution chemistry, but can be by the precursor slag chemistry.

6.2 Reaction mechanism

- Oxidation of Fe^{2+} to Fe^{3+} starts happening when the polymerization reactions start. This oxidation proceeds until a Na/Fe^{3+} ratio of approximately 1 is reached.
- Together with the oxidation, the formation of trioctahedral 2D clusters of Fe(II)-hydroxide is observed.
- The trioctahedral clusters are oxidized when the samples are exposed to air as a powder. The product contains Fe^{3+} in the same environment as the Fe oxidized in early stages.

Chapter 7

Conclusion

Inorganic polymers from CaO-FeO_x-SiO_2 slag are complex materials, whose characterization proved to be challenging. The results and conclusions in this work are considered to be directly applicable when using alkali-silicate activators and glassy precursor slags in the chemical range $Ca_{0-1}Fe_{1-2}Si_{1-2}O_{3-6}$, and might be relevant for other alkaline FeO_x-containing silicate systems. In terms of industrial sectors, the results are important for copper, lead, and ferronickel slags, and useful for plasmastone, basic oxygen furnace slag, or bauxite residue (these lists are not exhaustive).

The dissolution of the slag occurs through the dissolution of clusters. This was deduced from the lack of change in atomic arrangements before the polymerization/precipitation reactions seen in pair distribution function analysis and ^{57}Fe Mössbauer spectroscopy. Using sodium silicate activators, the dissolved clusters show identical arrangements to the atoms in the slag structure. A change in the local structure of the Fe was observed when activating with potassium silicate. The studied slag contained a combination of 4- and 5-fold coordinated Fe^{2+}, while the dissolved clusters had an increased amount of 5-fold coordinated species.

The reactions that lead to the setting of the material produce a structure in which Fe occurs in both Fe^{2+} and Fe^{3+} oxidation state. Whether these are two separate phases or if the two configurations co-exist in one phase is not clear from the presented results because of the lack of long and intermediate range ordering (no ordering > 9 Å). The Fe^{2+} is in an octahedral configuration and these octahedra are arranged in triangles, making trioctahedral layers, as present also in $Fe(OH)_2$ or Fe^{2+}-containing smectite/mica clays. Ordering

inside the layer is observed until 8.6 Å, so these layers are estimated to involve at least 20 octahedra. The Fe^{3+} resembles mostly tetrahedral Fe^{3+}, although with high isomer shift values, which is suggested to be present in the silicate network as network former, charge balanced by the alkali atom. A Na/Fe^{3+} molar ratio of 1 in the binder confirms this. The behavior of Fe^{3+} is thus seen to be similar to that of Al^{3+} in geopolymers. For the studied samples, the ratio between the Fe^{2+} and Fe^{3+} was 50:50. This ratio cannot be altered by changing the environment, i.e. the formation of Fe^{3+} was not lowered by conducting sample preparation in an N2 atmosphere. The Na/Fe^{3+} ratio of 1 suggests that the Na content might influence the oxidation, but future work on a more elaborate set of mixtures should clarify whether this ratio remains consistent when the composition of the mixture is adjusted. At this point in the development of the inorganic polymer, the binder consists of trioctahedral layers of Fe^{2+} and a glassy Fe^{3+}-silicate, where Na^{+} provides the charge balance.

When the inorganic polymer sample is exposed to air as powder, the oxidation of the Fe^{2+} trioctahedral layers occurs. The product of this oxidation remains at least partially in layered configuration, although some of the Fe might have rearranged and as such become part of the silicate network. The resulting Fe^{3+} shows similar Mössbauer parameters as the Fe^{3+} that was attributed to Fe in the silicate network during setting reactions, and therefore shows a similar symmetry to the electronegativity of the surrounding species. The final structure of the inorganic polymer binder thus contains Fe fully in the III oxidation state. For the studied samples, tetrahedral configuration was suggested, although the presence of higher coordinated species cannot be excluded.

To communicate the importance of residue-based binders to the general public and industry, the scope of the thesis expanded to involve the construction of an online, publicly accessible platform (SReDat). This is a database that centralizes knowledge with respect to residue valorization in cements. Starting as a collection of excel files compiled by the PhD student, the collective effort of the research group resulted in the development of the software in to a fully functional online database. It includes several tools to facilitate mix-design calculations or to perform environmental assessment of mix-design. The translation of a full life-cycle analysis in to easy-to-use formulas is also discussed in this thesis. The application of these formulas showed that a reduction of environmental impact of between 76% and 83% is possible when using Fe-rich inorganic polymers instead of OPC, making the system one of the most promising alternative cementitious materials in terms of environmental footprint.

Future work will tackle the role of Ca in the reactions and final structure of the inorganic polymer. A wider study on the variation of the oxidation state and coordination number Fe at different time stages will be performed. Thereby

the stoichiometry of the binder will be investigated and, more specifically, whether the ratio between Fe^{2+} and Fe^{3+} can be controlled. The oxidizing agent at early stages has not been identified and remains to be investigated. The influence of the presence of Al should also be investigated. The structures should also be verified from a theoretical perspective using computational techniques such as density functional theory and molecular dynamics. Research into the thermodynamics of the phases discovered in this thesis could be used to expand current databases, such as GEMS, to include Fe-rich systems. The influence of the activator formulation should be explored, in order to better understand the mechanisms entailed in hybrid cements (activation by Portland cement and alkalis) or the potential of using activators with lower alkalinity, e.g. sodium sulphate and sodium carbonate. The work on Fe-rich inorganic polymers should expand to investigate durability and resistance against chemical attack. The SReDat will be further developed and promoted as an easy tool to find engineering solutions for industrial residues.

Appendix A

Supplementary data chapter 3.3

A.1 X-ray and neutron weighting factors

The weighing factors for the possible atomic correlations in all samples are provided in Table A.1 and A.2, assuming a random distribution of all elements ($w = b_x b_y c_x c_y$, where b and c are respectively the scattering cross section and concentration of elements x and y). Also the relative weighting factors ($w_{X-ray}/w_{Neutron}$) are tabulated in Table A.3.

Table A.1: X-ray weighting factors of possible atomic correlations [1]. The factors are normalized to 100 for easier comparison.

	Low-Ca slag	High-Ca slag	Low-Ca IP	High-Ca IP
O-O	12.4	14.9	17.6	20.0
Si-O	6.4	7.8	8.0	9.2
Fe-O	21.5	19.8	22.8	20.3
Ca-O	2.4	5.8	2.6	6.1
Na-O	0.0	0.0	1.1	1.1
Fe-Si	11.1	10.4	10.3	9.4
Fe-Fe	37.4	26.4	29.4	20.6
Fe-Ca	4.2	7.8	3.4	6.2
Si-Si	3.3	4.1	3.6	4.3
Si-Ca	1.2	3.1	1.2	2.8

Table A.2: Neutron weighting factors of possible atomic correlations [2]. The factors are normalized to 100 for easier comparison.

	Low-Ca slag	High-Ca slag	Low-Ca IP	High-Ca IP
O-O	33.8	39.9	42.4	47.5
Si-O	5.5	6.7	6.1	6.9
Fe-O	28.5	25.7	26.5	23.3
Ca-O	1.3	3.1	1.3	2.9
Na-O	0.0	0.0	1.6	1.8
Fe-Si	4.7	4.3	3.8	3.4
Fe-Fe	23.9	16.6	16.6	11.4
Fe-Ca	1.1	2.0	0.8	1.4
Si-Si	0.9	1.1	0.9	1.0
Si-Ca	0.2	0.5	0.2	0.4

Table A.3: Ratio of X-ray weighting factor and neutron weighting factor ($\mathrm{w}_{X-ray}/\mathrm{w}_{Neutron}$).

	Low-Ca slag	High-Ca slag	Low-Ca IP	High-Ca IP
O-O	0.4	0.4	0.4	0.4
Si-O	1.2	1.2	1.3	1.3
Fe-O	0.8	0.8	0.9	0.9
Ca-O	1.8	1.9	2.1	2.1
Na-O	/	/	0.6	0.6
Fe-Si	2.4	2.4	2.7	2.7
Fe-Fe	1.6	1.6	1.8	1.8
Fe-Ca	3.8	3.8	4.3	4.4
Si-Si	3.6	3.7	4.1	4.2
Si-Ca	5.8	5.9	6.6	6.6

A.2 Calculation of coordination numbers

The coordination numbers (CNs) of Fe and Ca in the slags were calculated using the following formula to transform the PDF and integrate the relevant correlation (for theory see Keen [3]):

$$CN_i = \int_x^y (G(r) + 4\pi\rho_0 \times r) \times c_0 \times r \times \frac{\sum_{i=1}^{n} (c_i b_i)^2}{2 \times c_i b_i c_0 b_0}$$

Herein, b_i is the scattering length and ci is the fractional molar concentration of element i. A Si CN of 4 was used to normalize the data and decrease the dependence on estimated factors (i.e., number density ρ_0). The X-ray and neutron PDFs that were transformed using 3 Q_{max} values (20, 21.5, 28 Å^{-1}) were fitted using Fityk version 0.9.8. The fitting was performed in two ways: 1) without restriction of the fitting parameters and 2) restricting the full width half maximum (FWHM) of the Gaussian for the Ca-O correlation to the same width

as the Si-O correlation. Because of the probable presence of multiple species of Fe, the Fe-O FWHM was not restricted. The chemical composition (for calculating c_i) was extracted from Van De Sande et al. [4] using data from X-ray fluorescence (XRF) and electron probe micro-analysis (EPMA). The resulting CNs are presented in Table A.4 and A.5 (low-Ca, respectively from neutron and X-ray PDfs) and A.6 and A.7 (high-Ca, respectively from neutron and X-ray PDfs). Given that the X-ray data is more sensitive to the higher Z elements (i.e., Fe and Ca), CNs calculated from these data are discussed below. Furthermore, restricting the FWHM for Ca appears to give more sensible results, revealing an average CN of Fe is 3.4 for the low Ca slag and 4.2 for the high Ca. However, these values are low in comparison with literature [5-8], especially for the low Ca slag. Wright et al. [9] mention this issue of underestimation of the CN using X-ray PDFs and attribute this to the fact that the Fe-O correlation cannot be accurately represented using a single Gaussian and Fe with longer bond lengths does exist which is neglected in the Fe CN calculations (or, as is likely here, may have been inadvertently included as part of the Ca-O correlation). Furthermore, the simplification of the Fe-O correlation to 1 Gaussian instead of the more probable distribution of species can have a similar effect. Considering the above and previous experiments [10,11], the CN of both slags is most likely between 4 and 5. Similarly, the CN of Ca seems to be overestimated, specifically for the low-Ca slag, which is likely attributed to 1) the contributions from termination ripples, since these ripples will tend to dominate the low intensity atom-atom correlations, or 2) longer Fe-O bond lengths.

Table A.4: Coordination numbers of Fe and Ca in the low-Ca slag calculated from the neutron PDFs.

Q_{max} (Å^{-1})	Fitting method	Technique for composition	CN Fe	CN Ca
20	free	XRF	2.7	15.9
20	free	EPMA	2.9	18.1
20	fixed width	XRF	3.0	10.9
20	fixed width	EPMA	3.2	12.4
21.5	free	XRF	2.7	13.4
21.5	free	EPMA	2.9	15.3
21.5	fixed width	XRF	2.8	12.7
21.5	fixed width	EPMA	3.0	14.4
28	free	XRF	3.7	9.8
28	free	EPMA	3.9	11.1
28	fixed width	XRF	3.7	9.8
28	fixed width	EPMA	3.9	11.1

Table A.5: Coordination numbers of Fe and Ca in the low-Ca slag calculated from the X-ray PDFs.

Q_{max} (Å^{-1})	Fitting method	Technique for composition	CN Fe	CN Ca
20	free	XRF	3.1	16.6
20	free	EPMA	3.2	18.9
20	fixed width	XRF	3.5	9.7
20	fixed width	EPMA	3.7	11.0
21.5	free	XRF	2.8	16.6
21.5	free	EPMA	3.0	18.9
21.5	fixed width	XRF	3.2	11.8
21.5	fixed width	EPMA	3.4	13.4
28	free	XRF	2.6	18.5
28	free	EPMA	2.7	21.1
28	fixed width	XRF	3.2	10.7
28	fixed width	EPMA	3.4	12.2

Table A.6: Coordination numbers of Fe and Ca in the high-Ca slag calculated from the neutron PDFs.

Q_{max} (Å^{-1})	Fitting method	Technique for composition	CN Fe	CN Ca
20	free	XRF	2.9	9.0
20	free	EPMA	3.5	9.0
20	fixed width	XRF	3.3	6.2
20	fixed width	EPMA	4.0	6.2
21.5	free	XRF	2.6	9.5
21.5	free	EPMA	3.2	9.5
21.5	fixed width	XRF	2.9	7.6
21.5	fixed width	EPMA	3.5	7.5
28	free	XRF	4.1	8.0
28	free	EPMA	4.9	8.0
28	fixed width	XRF	4.1	8.0
28	fixed width	EPMA	4.9	8.0

A.3 Scattering functions

The X-ray and neutron scattering functions are shown in Figure A.1. The plots are stacked, grouped per precursor slag, i.e. the high-Ca system is not adapted, the low-Ca plots are shifted upwards (same shift for slag and IP).

A.4 Infrared spectroscopy

The attenuated total reflectance Fourier transformed infrared (ATR-FTIR) spectra of the inorganic polymers (IPs) are shown in Figure A.4. The contribution of D_2O vibrations is seen to be very low. Due to the milling

Table A.7: Coordination numbers of Fe and Ca in the high-Ca slag calculated from the X-ray PDFs.

Q_{max} (Å^{-1})	Fitting method	Technique for composition	CN Fe	CN Ca
20	free	XRF	3.6	8.0
20	free	EPMA	4.4	8.0
20	fixed width	XRF	3.8	6.4
20	fixed width	EPMA	4.6	6.4
21.5	free	XRF	3.2	8.4
21.5	free	EPMA	3.9	8.3
21.5	fixed width	XRF	3.8	7.1
21.5	fixed width	EPMA	4.6	7.0
28	free	XRF	3.1	8.8
28	free	EPMA	3.7	8.8
28	fixed width	XRF	3.9	6.5
28	fixed width	EPMA	4.7	6.5

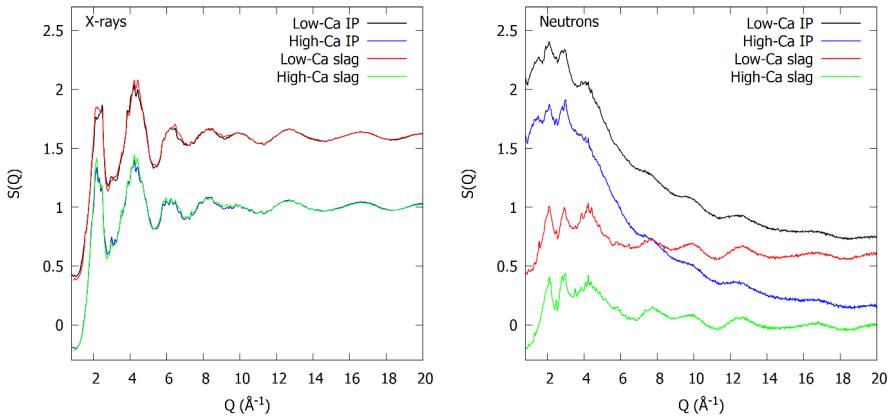

Figure A.1: X-ray (left) and neutron (right) scattering functions, comparing the slags and inorganic polymers.

procedure, drying of the sample occurred, with subsequent rehydration due to moisture in the air. An example temperature dependent plot of the absorbance at the wavenumber where CO_2 (2366 cm^{-1}) and water (1510 cm^{-1}) were best observed is provided in Figure A.3a, the simultaneously obtained thermogravimetric analysis is shown in Figure A.3b. From these results, a semi-quantitative estimation can be performed on the amount of water and carbonates. Taking the weight loss before 160 °C as water and between 160 °C and 700 °C as CO_2, the amount of water and carbonates is approximately 5.5 wt% and 2.7-2.9 wt% (depending on whether Na or Ca carbonates are present), respectively.

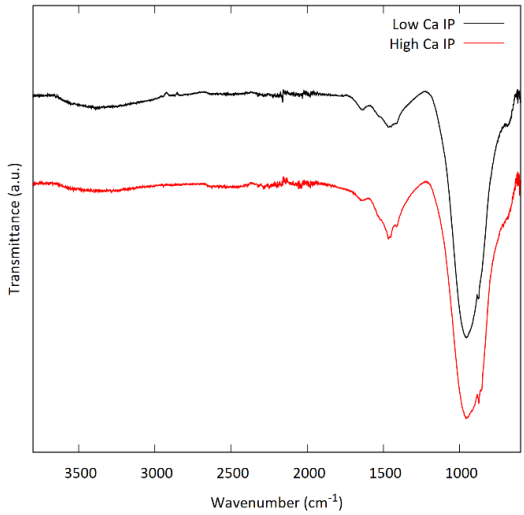

Figure A.2: Stacked plot of the ATR-FTIR spectra of the IPs. Carbonates are observed at $\sim$ 1400 and 870 cm^{-1}.

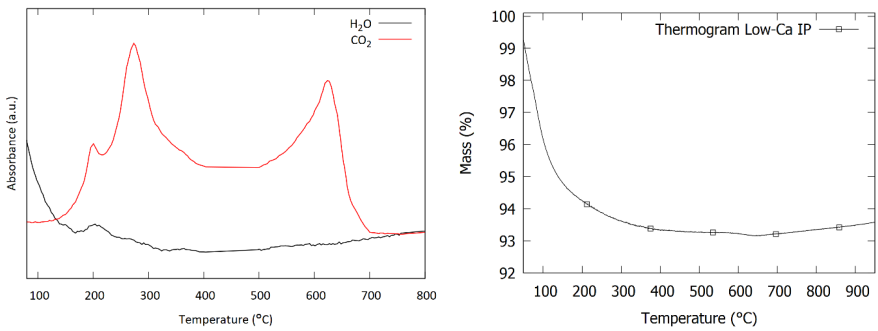

Figure A.3: Absorbance of the H_2O and CO_2 signal during TGA-FTIR (left) and the result from TGA analysis on the low-Ca IP (right).

A.5 Long-range PDF data

The long range PDF data (up to 25 Å) are presented in Figure **??** for the high-Ca system, revealing that both the slag and IP are amorphous.

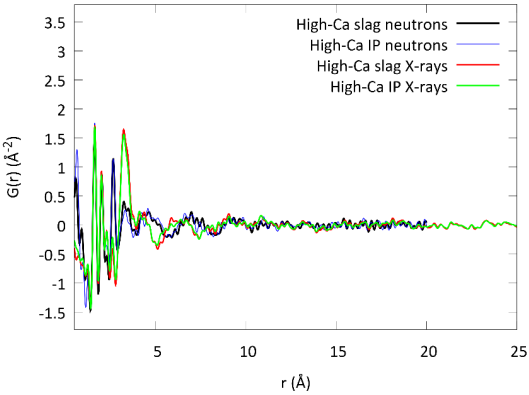

Figure A.4: Long-range PDFs of high-Ca slag and IP.

A.6 References

1. W. H. McMaster, N. Kerr Del Grande, J. H. Mallett, J. H. Hubbell (1969), Lawrence Livermore National Laboratory Report UCRL-50174 Section II Revision I, US Department of Commerce.
2. V. F. Sears, Neutron News, 1992, 3, 26.
3. D. A. Keen, Journal of Applied Crystallography, 2001, 34, 172.
4. J. Van De Sande, A. Peys, T. Hertel, S. Onisei, B. Blanpain, Y. Pontikes, presented at the 5th International Slag Valorisation Symposium, Leuven, Belgium, April 2017.
5. S. Rossano, A. Y. Ramos, J.-M. Delaye, Journal of Non-Crystalline, 2000, 273, 48.
6. O. L. G. Alderman, M. C. Wilding, A. Tamalonis, S. Sendelbach, S. M. Heald, C. J. Benmore, C. E. Johnson, J. A. Johnson, H.-Y. Hah, J. K. R. Weber, Chemical Geology, 2017, 453, 169.
7. W. E. Jackson, F. Farges, M. Yeager, P. A. Mabrouk, S. Rossano, G. A. Waychunas, E. I. Solomon, G. E. Brown Jr., Geochimica et Cosmochimica Acta, 2005, 69, 4315.
8. J. W. E. Drewitt, C. Sanloup, A. Bytchkov, S. Brassamin, L. Hennet, Physical Review B, 2013, 87, 224201.
9. A. C. Wright, S. J. Clarke, C. K. Howard, P. A. Bingham, S. D. Forder, D. Holland, D. Martlew, H. E. Fischer, Physical Chemistry of Glasses: European Journal of Glass Science and Technology B, 2014, 55, 243.
10. S. Onisei. A. P. Douvalis, A. Malfliet, A. Peys, Y. Pontikes, Journal of the American Ceramic Society, 2018, 101, 2245.
11. S. Simon, G. Gluth, A. Peys, S. Onisei, D. Banerjee, Y. Pontikes, Journal

of the American Ceramic Society, 2018, 101, 2107.

Appendix B

Supplementary data chapter 4.2

B.1 X-ray scattering functions

The scattering functions of all inorganic polymer (IP) samples discussed in chapter 4.2 are presented here. Figure B.1 through B.4 show the data of the sodium silicate activated low-Ca slag, sodium silicate activated high-Ca slag (the data presented in the manuscript), potassium silicate activated low-Ca slag and potassium silicate activated high-Ca slag, respectively.

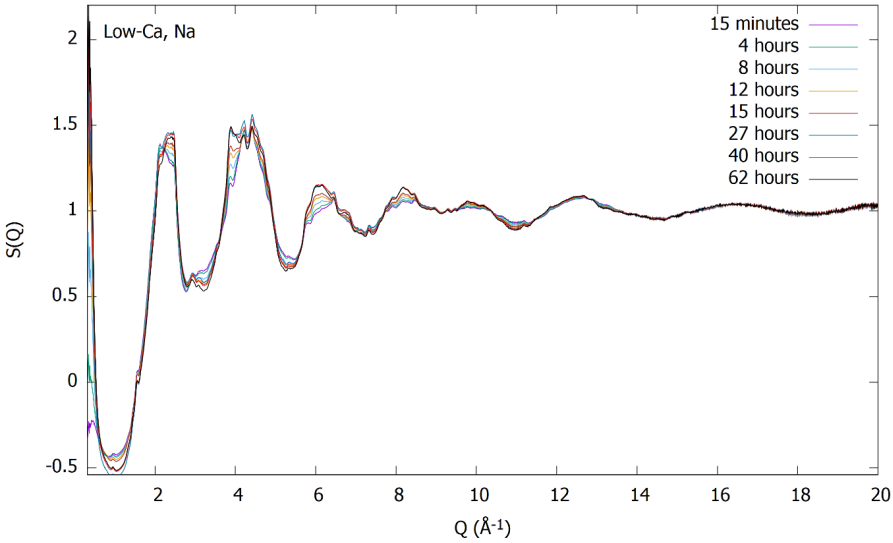

Figure B.1: X-ray total scattering functions of Na-silicate activated low-Ca IP during the initial 62 hours of reaction.

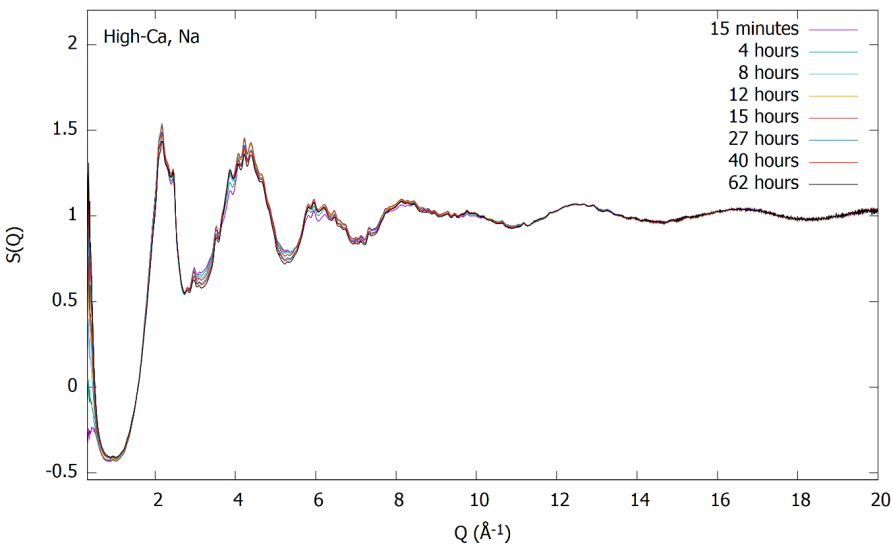

Figure B.2: X-ray total scattering functions of Na-silicate activated high-Ca IP during the initial 62 hours of reaction.

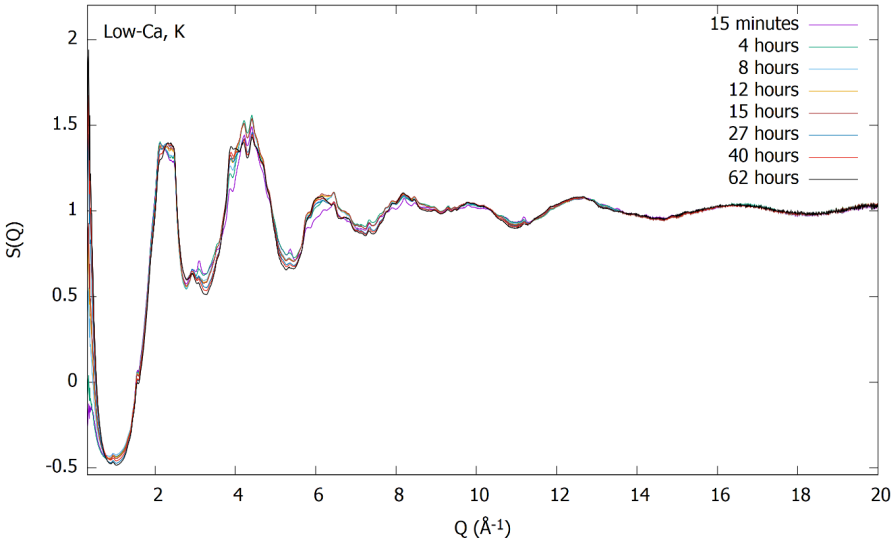

Figure B.3: X-ray total scattering functions of K-silicate activated low-Ca IP during the initial 62 hours of reaction.

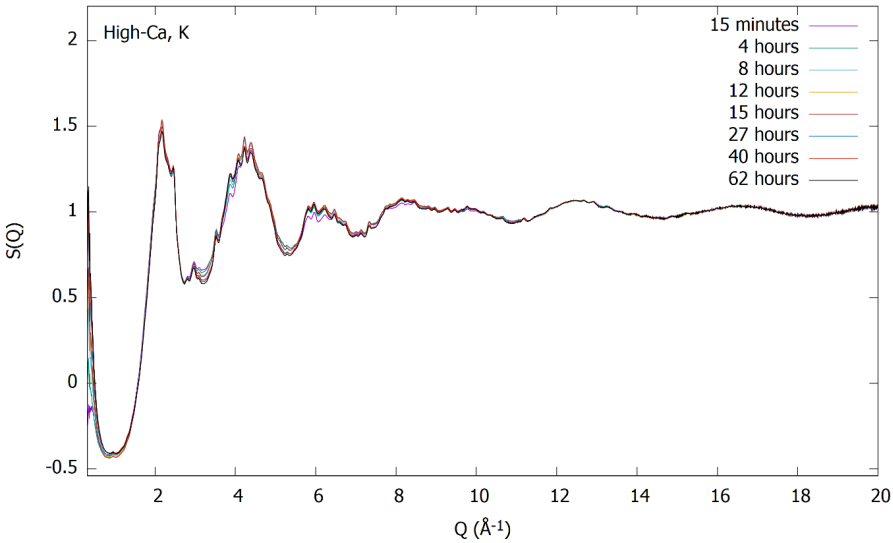

Figure B.4: X-ray total scattering functions of K-silicate activated high-Ca IP during the initial 62 hours of reaction.

Appendix C

On a lighter note...

Life is not all serious. This thesis would like to reflect that using this section. Let it tickle your readatory senses, clear your mind from painful memories and expand your time-occupation from the useful...

The Road to St. Corniche

On the road to Saint-Corniche,
you rarely see fish,
but if you look along the way,
you might see some lambs astray.

When you finally get there,
then you will see
the people that care
and feel love for thee.

It is not so abstract,
it is not very far,
as a matter of fact,
it's where you already are.

The Reminder Sonnet

When we fullfil our job with passion
we melt and quench our waste
or mix the slag into paste
and put in some love without transgression

When we stir it up ferociously
or smoothly with the Hobart
it warms up inside our heart
though it is just our duty

But when we go to civil engineering
to use the vicat, calorimeter
or any technique you find appealing

Then don't forget our neighbour
and fill in the sheet without simming
it is therefore, I send you this reminder

Lady Indutherm

So hot she gets when you supply her with power
so fastly she ramps, more than 1000 degrees/hour

She doesn't talk too much, no pointless chatter
and if she says E21, just provide her with water

But sometimes she nags in an annoying pitch
the E67 pops up and she's acting like a bitch

Just show some patience and treat her nice
and you give her the right feed
then she will melt down your ice
and provide the heat you need

The Grilled Pork

So soft is your texture,
While you melt in my mouth.
So strong is your flavour
I have to smother a shout.

Your taste is so pure
When treated on a grill.
You are the best cure,
For the loneliness I feel.

It really is the biggest shame,
That at home you don't taste the same.
I know I sound like a dork,
But I really love Greek pork.

't Sniejewt

1, 2, 3, 4, 5, 6, 7,
a lot is falling from the heaven.
It is not too dangerous though,
because the particles are only snow.

This beautiful blanket of white,
it makes the world shine bright
At least during the day,
because at night the sun is away.

This amount is too much to ascertain,
it makes you wonder what brought this doom,
this drastic change in the terrain.

But there is a reason I assume.
There is no other way to explain,
Jesus must have sneezed in the silica fume.

Inception Poetry

A poem that writes about itself
looks quite absurd to me
but anyway take it of the shelf
there is much more inside too see.

When you think about it closer
and ignore the childish rhyme
it hits you like a bulldozer
this shit fucks up space and time.

'cause when it's self referring
it refers to itself squared
the referrals keep on going
until infinity is declared.

Bibliography

[1] *EIT - Making innovation happen.* European Institute of Innovation and Technology, 2017.

[2] S. Ahmari, K. Parameswaran, and L. Zhang. Alkali Activation of Copper Mine Tailings and Low-Calcium Flash-Furnace Copper Smelter Slag. *Journal of Materials in Civil Engineering*, 27(6), 2015.

[3] C. Alba, L. E. Busse, D. J. List, and C. A. Angell. Thermodynamic aspects of the vitrification of toluene, and xylene isomers, and the fragility of liquid hydrocarbons. *The Journal of Chemical Physics*, 92(1):617–624, 1990.

[4] O. L. G. Alderman, L. Lazareva, M. C. Wilding, C. J. Benmore, S. M. Heald, C. E. Johnson, J. A. Johnson, H.-Y. Hah, S. Sendelbach, A. Tamalonis, J. B. Skinner, J. B. Parise, and J. K. R. Weber. Local structural variation with oxygen fugacity in Fe_2SiO_{4+x} fayalitic iron silicate melts. *Geochimica et Cosmochimica Acta*, 203:15–36, 2017.

[5] O. L. G. Alderman, M. C. Wilding, A. Tamalonis, S. Sendelbach, S. M. Heald, C. J. Benmore, C. E. Johnson, J. A. Johnson, H.-Y. Hah, and J. K. R. Weber. Iron K-edge X-ray absorption near-edge structure spectroscopy of aerodynamically levitated silicate melts and glasses. *Chemical Geology*, 453:169–185, 2017.

[6] F. Ardente and M. Cellura. Economic allocation in life cycle assessment: the state of the art and discussion of examples. *Journal of Industrial Ecology*, 16(3):387–398, 2012.

[7] L. Arnout, A. Peys, L. Machiels, P. T. Jones, S. Arnout, E. Nagels, B. Blanpain, and Y. Pontikes. The influence of the iron oxidation state in the synthesis of inorganic polymer. *In preparation.*

[8] N. A. Aydogan and H. Benzer. Comparison of the overall circuit performance in the cement industry: high compression milling vs. ball milling technology. *Minerals Engineering*, 24(3-4):211–215, 2011.

[9] V. F. F. Barbosa, K. J. D. MacKenzie, and C. Thaumaturgo. Synthesis and characterisation of materials based on inorganic polymers of alumina and silica: sodium polysialate polymers. *International Journal of Inorganic Materials*, 2(4):309–317, 2000.

[10] J. L. Bell and W. M. Kriven. Formation of an iron-based inorganic polymer (geopolymer). *Ceramic Engineering and Science Proceedings*, 30(2):301–312, 2010.

[11] J. L. Bell, P. Sarin, P. E. Driemeyer, R. P. Haggerty, P. J. Chupas, and W. M. Kriven. X-ray pair distribution function analysis of a metakaolin-based, $KAlSi_2O_6x5.5H_2O$ inorganic polymer (geopolymer). *Journal of Materials Chemistry*, 18(48):5974–5981, 2008.

[12] J. L. Bell, P. Sarin, J. L. Provis, R. P. Haggerty, P. E. Driemeyer, P. J. Chupas, J. S. J. van Deventer, and W. M. Kriven. Atomic Structure of a Cesium Aluminosilicate Geopolymer: A Pair Distribution Function Study. *Chemistry of Materials*, 20(14):4768–4776, 2008.

[13] M. Ben Haha, B. Lothenbach, G. Le Saout, and F. Winnefeld. Influence of slag chemistry on the hydration of alkali-activated blast-furnace slag — Part I: Effect of MgO. *Cement and Concrete Research*, 41(9):955–963, 2011.

[14] G. Berlier, G. Spoto, S. Bordiga, G. Ricchiardi, P. Fisciaro, A. Zecchina, I. Rossetti, E. Selli, L. Forni, E. Giamello, and C. Lamberti. Evolution of Extraframework Iron Species in Fe Silicalite: 1. Effect of Fe Content, Activation Temperature, and Interaction with Redox Agents. *Journal of Catalysis*, 208:64–82, 2002.

[15] S. A. Bernal, R. San Nicolas, J. S. J. van Deventer, and J. Provis. Alkali-activated slag cements produced with a blended sodium carbonate/sodium silicate activator. *Advances in Cement Research*, 28(4):262–273, 2016.

[16] A. Blyth, C. A. Eiben, G. W. Scherer, and C. E. White. Impact of activator chemistry on permeability of alkali-activated slags. *Journal of the American Ceramic Society*, 100(10):4848–4859, 2017.

[17] S. Bordiga, R. Buzzoni, F. Geobaldo, C. Lamberti, E. Giamello, A. Zecchina, G. Leofanti, G. Petrini, G. Tozzola, and G. Vlaic. Structure and Reactivity of Framework and Extraframework Iron in Fe-Silicalite as Investigated by Spectroscopic and Physicochemical Methods. *Journal of Catalysis*, 158:486–501, 1996.

[18] G. E. Brown Jr., F. Farges, and G. Calas. *Structure, Dynamics and Properties of Silicate Melts*, chapter X-Ray Scattering and X-ray Spectroscopy Studies of Silicate Melts. Mineralogical Society of America, 1995.

[19] R. G. Burns. Mineral Mössbauer spectroscopy: Correlations between chemical shift and quadrupole splitting parameters. *Hyperfine Interactions*, 91:739–745, 1994.

[20] K. Buttiens, J. Leroy, P. Negro, J. Thomas, K. Edwards, and Y. De Lassat. The carbon cost of slag production in the blast furnace: a scientific approach. *Journal of Sustainable Metallurgy*, 2(1):62–72, 2016.

[21] K. Chebli, J. M. Saiter, J. Grenet, A. Hamou, and G. Saffarini. Strong-fragile glass forming liquid concept applied to GeTe chalcogenide glasses. *Physica B: Condensed Matter*, 304(1-4):228–236, 2001.

[22] S. M. Chemtob, R. D. Nickerson, R. V. Morris, D. G. Agresti, and J. G. Catalano. Synthesis and structural characterization of ferrous trioctahedral smectites: Implications for clay mineral genesis and detectability on Mars. *Journal of Geophysical Research: Planets*, 120(6):1119–1140, 2015.

[23] Z. T. Chen, Y. Q. Liu, W. P. Zhu, and E. H. Yang. Incinerator bottom ash (IBA) aerated geopolymer. *Construction and Building Materials*, 112:1025–1031, 2016.

[24] J. M. D. Coey. *Mössbauer Spectroscopy Applied to Inorganic Chemistry*, chapter Mössbauer Spectroscopy of Silicate Minerals, pages 443–509. Springer, 1984.

[25] R. M. Cornell and U. Schwertmann, editors. *The Iron Oxides: Structure, Properties, Reactions, Occurences and Uses*. Wiley, 2003.

[26] A. Cuesta, R. U. Ichikawa, D. Londono-Zuluaga, A. G. De la Torre, I. Santacruz, X. Turrillas, and M. A. G. Aranda. Aluminum hydroxide gel characterization within a calcium aluminate cement paste by combined Pair Distribution Function and Rietveld analyses. *Cement and Concrete Research*, 96:1–12, 2017.

[27] J. Davidovits. Geopolymers: Inorganic Polymeric New Materials. *Journal of Thermal Analysis*, 37(8):1633–1656, 1991.

[28] J. Davidovits. Environmental implications of geopolymers. *Materials Today*, 2015.

[29] J. Davidovits. *Geopolymer Chemistry and Applications*. Geopolymer Institute, 2015.

[30] J. Davidovits. *Why Alkali-Activated Materials are NOT Geopolymers?* https://www.geopolymer.org/faq/alkali-activated-materials-geopolymers/, 2015.

[31] R. K. Dhir, J. de Brito, R. Mangabhai, and C. Q. Lye. *Sustainable Construction Materials: Copper Slag.* Woodhead Publishing, 2017.

[32] J. Dorschner, B. Begemann, T. Henning, C. Jäger, and H. Mutschke. Steps toward interstellar silicate mineralogy II. Study of Mg-Fe-silicate glasses of variable composition. *Astronomy and Astrophysics*, 300:503–520, 1995.

[33] K. T. Douglas, B. Howlin, and J. Silver. Solution Chemistry and Mössbauer Study of Iron(II) and Iron(III) Complexes from Gallocyanine. *Inorganica Chimica Acta*, 92:135–140, 1984.

[34] A. P. Douvalis, A. Polymeros, and T. Bakas. IMSG09: A ^{57}Fe ^{119}Sn Mössbauer spectra computer fitting program with novel interactive user interface. *Journal of Physics: Conference Series*, 217(1):012014, 2010.

[35] J. W. E. Drewitt, C. Sanloup, A. Bytchkov, S. Brassamin, and L. Hennet. Structure of $(Fe_xCa_{1-x}O)_y(SiO_2)_{1-y}$ liquids and glasses from high-energy X-ray diffraction: Implications for the structure of natural basaltic magmas. *Physical Review B*, 87:224201, 2013.

[36] P. Duxson, A. Fernandez-Jimenez, J. L. Provis, G. C. Lukey, A. Palomo, and J. S. J. van Deventer. Geopolymer technology: the current state of the art. *Journal of Materials Science*, 42(9):2917–2933, 2007.

[37] P. Duxson, S. W. Mallicoat, G. C. Lukey, W. M. Kriven, and J. S. J. van Deventer. The effect of alkali and Si/Al ratio on the development of mechanical properties of metakaolin-based geopolymers. *Colloids and Surfaces A*, 292(1):8–20, 2007.

[38] P. Duxson, S. W. Mallicoat, G. C. Lukey, W. M. Kriven, and J. S. J. van Deventer. The effect of alkali and Si/Al ratio on the development of mechanical properties of metakaolin based geopolymers. *Colloids and Surfaces A*, 292(1):8–20, 2007.

[39] T. Egami and S. J. L. Billinge. *Underneath the Bragg Peaks: Structural Analysis of Complex Materials.* Elsevier, 2012.

[40] G. Engelhardt, D. Hoebbel, M. Tarmak, A. Samoson, and E. Lippmaa. ^{29}Si-NMR-Untersuchungen zur Anionenstruktur von Kristallinen Tetramethylammonium-alumosilicaten und -alumosilicatlösungen. *Journal of Inorganic and General Chemistry - Zeitschrift für anorganische und algemeine Chemie*, 484(1):22–32, 1982.

[41] M. Esaifan, H. Khoury, I. Aldabsheh, H. Rahier, M. Hourani, and J. Wastiels. Hydrated lime/potassium carbonate as alkaline activating mixture to produce kaolinitic clay based inorganic polymer. *Applied Clay Science*, 126:278–286, 2016.

[42] European-Commision. *Paris Agreement*. https://ec.europa.eu/clima/policies/international/negotiations/paris_en/, 2017.

[43] European-Commission. *On the implementation of the Circular Economy Action Plan*. http://ec.europa.eu/environment/circular-economy/implementation_report.pdf, 2017.

[44] C. L. Farrow, P. Juhas, D. Bryndin, E. S. Bozin, J. Bloch, T. Proffen, and S. J. L. Billinge. PDFfit2 and PDFgui: computer programs for studying nanostructure in crystals. *Journal of Physics: Condensed Matter*, 19(33):335219, 2007.

[45] M. Fawer. Life cycle inventories of the production of sodium silicates. Technical report, Swiss Federal Laboratories for Materials Testing and Research, 1997.

[46] A. M. Ferretti, C. Oliva, L. Forni, G. Berlier, A. Zecchina, and C. Lamberti. Evolution of Extraframework Iron Species in Fe Silicalite: 2. Effect of Steaming. *Journal of Catalysis*, 208:83–88, 2002.

[47] E. Ferrow. Mössbauer effect and X-ray diffraction studies of synthetic iron bearing trioctahedral micas. *Physics and Chemistry of Minerals*, 14(3):276–280, 1987.

[48] E. Ferrow. Mössbauer Effect and X-ray Diffraction Studies of Synthetic Iron Bearing Trioctahedral Micas. *Physics and Chemistry of Minerals*, 14(3):276–280, 1987.

[49] M. D. Foster. Layer charge relations in dioctahedral and trioctahedral micas. *American Mineralogist*, 45(3-4):383–398, 1960.

[50] N. Garg and C. E. White. Mechanism of zinc oxide retardation in alkali-activated materials: an in situ X-ray pair distribution function investigation. *Journal of Materials Chemistry A*, 5(23):11794–11804, 2017.

[51] F. Gervais, A. Blin, D. Massiot, J. P. Coutures, M. H. Chopinet, and F. Naudin. Infrared reflectivity spectroscopy of silicate glasses. *Journal of Non-Crystalline Solids*, 89(3):384–401, 1987.

[52] A. Gharzouni, E. Joussein, B. Samet, S. Baklouti, and S. Rossignol. Effect of the reactivity of alkaline solution and metakaolin on geopolymer formation. *Journal of Non-Crystalline Solids*, 410:127–134, 2015.

[53] D. Giordano, J. K. Russel, and D. B. Dingwell. Viscosity of magmatic liquids: A model. *Earth and Planetary Science Letters*, 271:123–134, 2008.

[54] G. Giuli, G. Pratesi, C. Cipriani, and E. Paris. Iron local structure in tektites and impact glasses by extended X-ray absorption fine structure and high-resolution X-ray absorption near-edge structure spectroscopy. *Geochimica et Cosmochica Acta*, 66:4347–4353, 2002.

[55] G. J. G. Gluth, C. Lehmann, K. Rübner, and H. C. Kühne. Geopolymerization of a silica residue from waste treatment of chlorosilane production. *Materials and Structures*, 46(8):1291–1298, 2013.

[56] J.-M. R. Génin, A. A. Olowe, P. H. Refait, and L. Simon. On the stoichiometry and Pourbaix diagram of Fe(II)-Fe(III) hydroxyl-sulphate or sulphate-containing green rust 2: An electrochemical and Mössbauer spectroscopy study. *Corrosion Science*, 38(10):1751–1762, 1996.

[57] M. Goedkoop, R. Heijungs, M. Huijbregts, A. De Schryver, J. Struijs, and R. van Zelm. ReCiPe 2008: A life cycle impact assessment method which comprises harmonised category indicators at the midpoint and endpoint level. Technical report, Nederlands Ministerie van Volkshuisvesting, Ruimtelijke Ordening en Milieubeheer, 2013.

[58] K. Gong and C. E. White. Impact of chemical variability of ground granulated blast-furnace slag on the phase formation in alkali-activated slag pastes. *Cement and Concrete Research*, 89:310–319, 2016.

[59] B. Gorai, R. K. Jana, and Premchand. Characteristics and utilisation of copper slag – a review. *Resources, Conservation and Recyling*, 39(4):299–313, 2003.

[60] C. A. Gorski, L. Klüpfel, A. Voegelin, M. Sander, and T. B. Hofstetter. Redox Properties of Structural Fe in Clay Minerals. 2. Electrochemical and Spectroscopic Characterization of Electron Transfer Irreversibility in Ferruginous Smectite, SWa-1. *Environmental Science and Technology*, 46(17):9369–9377, 2012.

[61] A. T. Goulart, M. F. de Jesus Filho, J. D. Fabris, and J. M. D. Coey. Quantitative Mössbauer analysis of maghemite-hematite mixtures in external applied field. *Hyperfine interactions*, 83(1):451–455, 1994.

[62] N. N. Greenwood and T. C. Gibb. *Mössbauer Spectroscopy*. Chapman and Hall, 1971.

[63] S. Gunasekaran, G. Anbalagan, and S. Pandi. Raman and infrared spectra of carbonates of calcite structure. *Journal of Raman Spectroscopy*, 37(9):892–899, 2006.

[64] G. Habert and C. Ouellet-Plamondon. Recent update on the environmental impact of geopolymers. *RILEM Technical Letters*, 1:17–23, 2016.

[65] A. Hajimohammadi, J. L. Provis, and J. S. J. van Deventer. Effect of Alumina Release Rate on the Mechanism of Geopolymer Gel Formation. *Chemistry of Materials*, 22(18):5199–5208, 2010.

[66] V. Hallet, A. Peys, A. Katsiki, H. Rahier, S. Onisei, and Y. Pontikes. The influence of activating solution on the kinetics and compressive strength evolution of an Fe-rich slag paste. In *Proceedings of the 5th International Slag Valorisation Symposium*, pages 357–360, Leuven, Belgium, April 2017.

[67] V. Hallet, A. Peys, and Y. Pontikes. Influence of the activating solution on the kinetics and strength evolution of Fe-rich inorganic polymers. *in preparation*.

[68] A. Heath, K. Paine, and M. McManus. Minimising the global warming potential of clay based geopolymers. *Journal of Cleaner Production*, 78:75–83, 2014.

[69] C. M. B. Henderson and D. Taylor. Infrared spectra of aluminogermanate- and aluminate-sodalites and a re-examination of the relationship between T-O bond length, T-O-T angle and the position of the main i.r. absorption band for compounds with framework structures. *Spectrochimica Acta A*, 35(8):929–935, 1979.

[70] T. Hertel, B. Blanpain, and Y. Pontikes. A Proposal for a 100% Use of Bauxite Residue Towards Inorganic Polymer Mortar. *Journal of Sustainable Metallurgy*, 2(4):394–404, 2016.

[71] T. Hertel, C. R. Borra, B. Blanpain, and Y. Pontikes. Inorganic polymer mortars from bauxite residue and possibility to additionaly recover aluminium and sodium. In *Proceedings of the 5th International Conference on Industrial and Hazardous Waste Management*, pages 187–188, Chania, Crete, Greece, September 2016.

[72] P. C. Hewlett, editor. *Lea's Chemistry of Cement and Concrete*. Elsevier, 2004.

[73] K. Hirao, T. Komatsu, and N. Soga. Mössbauer studies on some glasses and crystals in the Na_2O-Fe_2O_3-SiO_2 system. *Journal of Non-Crystalline Solids*, 40:315–323, 1980.

[74] A. M. Hofmeister. Single-Crystal Absorption and Reflection Infrared Spectroscopy of Forsterite and Fayalite. *Physics and Chemistry of Minerals*, 14(6):499–513, 1987.

[75] C. Hosten and B. Fidan. An industrial comparative study of cement clinker grinding systems regarding the specific energy consumption and cement properties. *Powder Technology*, 221:183–188, 2011.

[76] C. K. Huang and P. F. Kerr. Infrared study of the carbonate minerals. *American Mineralogist*, 1960.

[77] C. K. Huang and P. F. Kerr. Infrared study of the carbonate minerals. *American Mineralogist*, 45:311–324, 1960.

[78] R. I. Iacobescu, V. Cappuyns, T. Geens, L. Kriskova, S. Onisei, P. T. Jones, and Y. Pontikes. The influence of curing conditions on the mechanical properties and leaching of inorganic polymers made of fayalitic slag. *Frontiers of Chemical Science and Engineering*, 11(3):317–327, 2017.

[79] W. E. Jackson, F. Farges, M. Yeager, P. A. Mabrouk, S. Rossano, G. A. Waychunas, and E. I. Solomon. Multi-spectroscopic study of Fe(II) in silicate glasses: Implications for the coordination environment of Fe(II) in silicate melts. *Geochimica et Cosmochimica Acta*, 60(17):4315–4332, 2005.

[80] A. A. Kamnev, R. L. Dykman, K. Kovacs, A. N. Pankratov, A. V. Tugarova, Z. Homonnav, and E. Kuzmann. Redox interactions between structurally different alkylresorcinols and iron(III) in aqueous media: frozen-solution ^{57}Fe Mössbauer spectroscopic studies, redox kinetics and quantum chemical evaluation of the alkylresorcinol reactivities. *Structural Chemistry*, 25(2):649–657, 2014.

[81] E. Kamseu, I. Lancellotti, V. M. Sglavo, L. Modolo, and C. Leonelli. Design of inorganic polymer mortar from ferricalsialic and calsialic slags for indoor humidity control. *Materials*, 9(6):410, 2016.

[82] E. Kamseu, C. Leonelli, D. S. Perera, U. Chinje Melo, and P. N. Lemougna. Investigation of volcanic ash based geopolymers as potential building materials. *InterCeram: International Ceramic Review*, 58(2-3):136–140, 2009.

[83] K. T. Karalis, D. Dellis, G. S. E. Antipas, and A. Xenidis. Bona-fide method for the determination of short range order and transport properties in a ferro-aluminosilicate slag. *Scientific Reports*, 6:30216, 2016.

[84] S. W. Karickhoff and G. W. Bailey. Optical absorption spectra of clay minerals. *Clays and clay minerals*, 21:59–70, 1973.

[85] R. C. Kaze, L. M. Beleuk à Moungam, M. L. Fonkwe Djouka, A. Nana, E. Kamseu, U. Chinje Melo, and C. Leonelli. The corrosion of kaolinite by iron minerals and the effects on geopolymerization. *Applied Clay Science*, 138:48–62, 2017.

[86] D. A. Keen. A comparison of various commonly used correlation functions for describing total scattering. *Journal of Applied Crystallography*, 34(2):172–177, 2001.

[87] H.-I. Kim, J. C. Sur, and S. K. Lee. Effect of iron content on the structure and disorder of iron-bearing sodium silicate glasses: A high-resolution ^{29}Si and ^{17}O solid-state NMR study. *Geochimica et Cosmochimica Acta*, 173:160–180, 2016.

[88] J. L. Knipping, H. Behrens, M. Wilke, J. Göttlicher, and P. Stabile. Effect of oxygen fugacity on the coordination and oxidation state of iron in alkali bearing silicate melts. *Chemical Geology*, 411:143–154, 2015.

[89] K. Komnitsas, D. Zaharaki, and V. Perdikatsis. Geopolymerisation of low Ca ferronickel slags. *Journal of Materials Science*, 42(9):3073–3082, 2007.

[90] K. Komnitsas, D. Zaharaki, and V. Perdikatsis. Effect of synthesis parameters on the compressive strength of low-calcium ferronickel slag inorganic polymers. *Journal of Hazardous Materials*, 161(2-3):760–768, 2008.

[91] C. Krebs, J. C. Price, J. Baldwin, L. Saleh, M. T. Green, and J. M. Bollinger Jr. Rapid Freeze-Quench ^{57}Fe Mössbauer Spectroscopy: Monitoring Changes of an Iron-Containing Active Site during a Biochemical Reaction. *Inorganic Chemistry*, 44:742–757, 2005.

[92] L. Kriskova, L. Machiels, and Y. Pontikes. Inorganic Polymers from a Plasma Convertor Slag: Effect of Activating Solution on Microstructure and Properties. *Journal of Sustainable Metallurgy*, 1(3):240–251, 2015.

[93] S. Kumar, R. Kumar, T. C. Alex, A. Bandopadhyay, and S. P. Mehrotra. Influence of reactivity of fly ash on geopolymerisation. *Advances in Applied Ceramics*, 106(3):120–127, 2007.

[94] J. Kuterasinska and A. Krol. Mechanical properties of alkali-acivated binders based on copper slag. *Architecture Civil Engineering Environment*, 8(3):61–67, 2015.

[95] B. Lafuente, R. T. Downs, H. Yang, and N. Stone. *Highlights in Mineralogical Crystallography*, chapter The power of databases: the RRUFF project. De Gruyter, 2015.

[96] I. Lancellotti, M. Cannio, F. Bollino, M. Catauro, L. Barbieri, and C. Leonelli. Geopolymers: An option for the valorization of incinerator bottom ash derived "end of waste". *Ceramics International*, 41(2):2116–2123, 2015.

[97] I. Lancellotti, E. Kamseu, M. Michelazzi, L. Barbieri, A. Corradi, and C. Leonelli. Chemical stability of geopolymers containing municipal solid waste incinerator fly ash. *Waste Management*, 30(4):673–679, 2010.

[98] P. N. Lemougna, U. Chinje Melo, M.-P. Delplancke, and H. Rahier. Influence of the activating solution composition on the stability and thermo-mechanical properties of inorganic polymers (geopolymers) from volcanic ash. *Construction and Building Materials*, 48:278–286, 2013.

[99] P. N. Lemougna, U. Chinje Melo, M.-P. Delplancke, and H. Rahier. Influence of the chemical and mineralogical composition on the reactivity of volcanic ashes during alkali activation. *Ceramics International*, 40(1A):811–820, 2014.

[100] P. N. Lemougna, U. Chinje Melo, E. Kamseu, and A. B. Tchamba. Laterite Based Stabilized Products for Sustainable Building Applications in Tropical Countries: Review and Prospects for the Case of Cameroon. *Sustainability*, 3(1):293–305, 2011.

[101] P. N. Lemougna, K. J. D. MacKenzie, and U. Chinje Melo. Synthesis and thermal properties of inorganic polymers (geopolymers) for structural and refractory applications from volcanic ash. *Ceramics International*, 37(8):3011–3018, 2011.

[102] P. N. Lemougna, K. J. D. MacKenzie, G. N. L. Jameson, H. Rahier, and U. F. Chinje Melo. The role of iron in the formation of inorganic polymers (geopolymers) from volcanic ash: a ^{57}Fe Mössbauer spectroscopy study. *Journal of Materials Science*, 48(15):5280–5286, 2013.

[103] P. N. Lemougna, K. Wang, Q. Tang, U. Chinje Melo, and X. Cui. Recent developments on inorganic polymers synthesis and applications. *Ceramics International*, 42(14):15142–15159, 2016.

[104] C. Leonelli, E. Kamseu, D. N. Boccaccini, U. Chinje Melo, A. Rizzuti, N. Billong, and P. Miselli. Volcanic ash as alternative raw materials for traditional vitrified ceramic products. *Architecture Civil Engineering Environment*, 106(3):135–141, 2007.

[105] Z. Liu, B. Blanpain, and M. Guo. Viscosity of Heterogeneous Silicate Melts: A Non-Newtonian Model. *Metallurgical and Materials Transactions B*, 48(6):3027–3037, 2017.

[106] M. Lizcano, H. S. Kim, S. Basu, and M. Radovic. Mechanical properties of sodium and potassium activated metakaolin-based geopolymers. *Journal of Materials Science*, 47(6):2607–2616, 2012.

[107] I. S. Lyubutin, C. R. Lin, Y. V. Korzhetskiy, T. V. Dmitrieva, and R. K. Chiang. Mössbauer spectroscopy and magnetic properties of hematite/magnetite nanocomposites. *Journal of Applied Physics*, 106(3):034311, 2009.

[108] L. Machiels, L. Arnout, P. T. Jones, B. Blanpain, and Y. Pontikes. Inorganic polymer cement from Fe-silicate glasses: varying the activating solution to glass ratio. *Waste and Biomass Valorization*, 5(3):411–428, 2014.

[109] K. J. D. MacKenzie and M. Welter. *Advances in Ceramic Matrix Composites*, chapter Geopolymer (aluminosilicate) composites: synthesis, properties and applications. Woodhead Publishing, 2014.

[110] N. A. Madlool, M. S. Saidur, R. Hossain, and N. A. Rahim. A critical review on energy use and savings in the cement industries. *Renewable and Sustainable Energy Reviews*, 15(4):2042–2060, 2011.

[111] C. F. Maitland, C. E. Buckley, B. H. O'Connor, P. D. Butler, and R. D. Hart. Characterization of the pore structure of metakaolin-derived geopolymers by neutron scattering and electron microscopy. *Journal of Applied Crystallography*, 44:697–707, 2011.

[112] I. Maragkos, I. Giannopoulou, and D. Panias. Synthesis of ferronickel slag-based geopolymers. *Minerals Engineering*, 22(2):196–203, 2009.

[113] B. C. McLellan, R. P. Williams, J. Lay, A. van Riessen, and G. D. Corder. Cost and carbon emissions for geopolymer pastes in comparison to ordinary Portland cement. *Journal of Cleaner Production*, 19(9-10):1080–1090, 2011.

[114] P. McMillan. Structural studies of silicate glasses and melts – applications and limitations of Raman spectroscopy. *American Mineralogist*, 69(7-8):622–644, 1984.

[115] A. Melado, C. Catalan, N. Bouzon, M. V. Borrachero, J. M. Monzo, and J. Paya. Carbon footprint of geopolymeric mortar: study of the contribution of the alkaline activating solution and assessment of an alternative route. *RSC Advances*, 4(45):23846–23852, 2014.

[116] J. Melar, G. Renaudin, F. Leroux, A. Hardy-Dessources, J.-M. Nedelec, C. Taviot-Gueho, E. Petit, P. Steins, A. Poulesquen, and F. Frizon. The

Porous Network and its Interface inside Geopolymers as a Function of Alkali Cation and Aging. *Journal of Physical Chemistry*, 119(31):17619–17632, 2015.

[117] C. Meral, C. J. Benmore, and P. J. M. Monteiro. The study of disorder and nanocrystallinity in C-S-H, supplementary cementitious materials and geopolymers using pair distribution function analysis. *Cement and Concrete Research*, 41(7):696–710, 2011.

[118] METGROW+. *Metal Recovery from Low Grade Ores and Wastes*. http://metgrowplus.eu/, accessed April 2017.

[119] P. J. M. Monteiro, S. A. Miller, and A. Horvath. Towards sustainable concrete. *Nature Materials*, 16:698–699, 2017.

[120] J. C. B. Moraes, M. M. Tashamima, J. L. Akasaki, J. L. P. Melges, J. Monzo, M. V. Borrachero, L. Soriano, and J. Paya. Increasing the sustainability of alkali-activated binders: the use of sugar cane straw ash (SCSA). *Construction and Building Materials*, 124:148–154, 2016.

[121] A. E. Morandeau and C. E. White. In situ X-ray pair distribution function analysis of accelerated carbonation of a synthetic calcium-silicate-hydrate gel. *Journal of Materials Chemistry A*, 3(16):8597–8605, 2015.

[122] A. E. Morandeau and C. E. White. Role of Magnesium-Stabilized Amorphous Calcium Carbonate in Mitigating the Extent of Carbonation in Alkali-Activated Slag. *Chemistry of Materials*, 27(19):6625–6634, 2015.

[123] C. N. Murray and J. P. Riley. The solubility of gases in distilled water and sea water – II. Oxygen. *Deep Sea Research and Oceanographic Abstracts*, 16(3):311–320, 1969.

[124] R. J. Myers, S. A. Bernal, and J. L. Provis. Phase diagrams for alkali-activated slag binders. *Cement and Concrete Research*, pages 30–38, 2017.

[125] B. O. Mysen. The structural behavior of ferric and ferrous iron in aluminosilicate glasses near meta-aluminosilicate joins. *Geochimica et Cosmochimica Acta*, 70:2337–2353, 2006.

[126] B. O. Mysen and P. Richet, editors. *Silicate glasses and melts: Properties and structure*. Elsevier, 2005.

[127] M. E. Natali, C. E. White, and M. C. Bignozzi. Elucidating the atomic structures of different sources of fly ash using X-ray and neutron PDF analysis. *Fuel*, 177:148–156, 2016.

[128] A. Nazari and J. G. Sanjayan, editors. *Handbook of Low-Carbon Concrete*. Elsevier, 2017.

[129] J. Neuefeind, M. Feygenson, J. Carruth, R. Hoffman, and K. K. Chipley. The Nanoscale Ordered Materials Diffractometer NOMAD at the Spallation Neutron Source SNS. *Nuclear Instruments and Methods in Physics Research B*, 287:68–75, 2012.

[130] K. L. Ngai, R. W. Rendell, L. D. Pye, W. C. LaCourse, and H. J. Stevens, editors. *The Physics of Non-Crystalline Solids*. Taylor and Francis, 1992.

[131] N. Nowack, I. Zebger, and F. Pfeifer. Structure of Liquid Slags and Ultraviolet/Visible Reflection Spectroscopy of Molten and Glassy Silicates (Fe_20_3-CaO-$Si0_2$). *Steel Research International*, 75(10):632–644, 2004.

[132] E. A. Obonyo, E. Kamseu, P. N. Lemougna, A. B. Tchamba, U. Chinje Melo, and C. Leonelli. A Sustainable Approach for the Geopolymerization of Natural Iron-Rich Aluminosilicate Materials. *Sustainability*, 6(9):5535–5553, 2014.

[133] Y. Ohashi, C. W. Burnham, and L. W. Finger. The Effect of Ca-Fe Substitution on the Clinopyroxene Crystal Structure. *American Mineralogist*, 60:423–434, 1975.

[134] J. G. J. Olivier, G. Janssens-Maenhout, M. Muntean, and J. A. H. W. Peters. Trends in global CO_2 emissions: 2016 Report. Technical report, Joint Research Centre of the European Commission, 2016.

[135] S. Onisei, W. Crijns, A. P. Douvalis, C. Siakati, A. Peys, and Y. Pontikes. The influence of Ca on the microstructure of Fe-rich slags for use as inorganic polymers. *In preparation*.

[136] S. Onisei, A. P. Douvalis, A. Malfliet, A. Peys, and Y. Pontikes. Inorganic polymers made of fayalite slag: On the microstructure and behavior of Fe. *Journal of the American Ceramic Society*, 101, 2018.

[137] S. Onisei, K. Lesage, B. Blanpain, and Y. Pontikes. Early Age Microstructural Transformations of and Inorganic Polymer Made of Fayalite Slag. *Journal of the American Ceramic Society*, 98(7):2269–2277, 2015.

[138] S. Onisei, Y. Pontikes, D. Apelian, and B. Blanpain. Synthesis of inorganic polymers from metallurgical residues. In *Proceedings of the 3rd International Slag Valorisation Symposium*, pages 355–358, Leuven, Belgium, April 2013.

[139] S. Onisei, Y. Pontikes, T. Van Gerven, G. N. Angelopoulos, T. Velea, V. Predica, and P. Moldovan. Synthesis of inorganic polymers using fly ash and primary lead slag. *Journal of Hazardous Materials*, 205-206:101–110, 2012.

[140] F. Pachego-Torgal, S. Jalali, J. Labrincha, and V. M. John, editors. *Eco-Efficient Concrete*. Woodhead Publishing, 2013.

[141] A. Palomo, A. Fernandez-Jimenez, G. Kovalchuk, L. M. Ordonez, and M. C. Naranjo. OPC-fly ash cementitious systems: study of gel binders produced during alkaline hydration. *Journal of Materials Science*, 42(9):2958–2966, 2007.

[142] D. Panias and I. Giannopoulou. The geopolymerization technology for the utilization of mining and metallurgical solid wastes. *Proceedings - European Metallurgical Conference*, 2:625–640, 2007.

[143] V. Petkov, S. J. L. Billinge, S. D. Shastri, and B. Himmel. Polyhedral Units and Network Connectivity in Calcium Aluminosilcate Glasses from High-Energy X-ray Diffraction. *Physical Review Letters*, 85(16):3436–3439, 2000.

[144] V. Petkov, T. Gerber, and B. Himmel. Atomic ordering in $Ca_{x/2}Al_xSi_{1-x}O_2$ glasses (x=0,0.34,0.5,0.68) by energy dispersive X-ray diffraction. *Physical Review B*, 58(18):11984–11988, 1998.

[145] A. Peys, L. Arnout, B. Blanpain, H. Rahier, K. Van Acker, and Y. Pontikes. Mix-design Parameters and Real-Life Considerations in the Pursuit of Decreasing the Environmental Impact of Inorganic Polymers. *Waste and Biomass Valorisation*, 9(6):879–889, 2017.

[146] A. Peys, H. Rahier, and Y. Pontikes. Potassium-rich biomass ashes as activators in metakaolin-based inorganic polymers. *Applied Clay Science*, 129(2):401–409, 2016.

[147] A. Peys, C. E. White, D. Olds, H. Rahier, B. Blanpain, and Y. Pontikes. Molecular structure of CaO-FeO_x-SiO_2 glassy slags and resultant inorganic polymers. *Journal of the American Ceramic Society*, doi: 10.1111/jace.15880, 2018.

[148] N. M. Piatak, M. B. Parsons, and R. R. Seal II. Characteristics and environmental aspects of slag: A review. *Applied Geochemistry*, 57:236–366, 2015.

[149] G. S. Pokrovski, J. Schott, F. Farges, and J.-L. Hazemann. Iron(III)-silica interactions in aqueous solution: Insights from X-ray absorption fine

structure spectroscopy. *Geochimica et Cosmochimica Acta*, 67(19):3559–3573, 2003.

[150] Y. Pontikes, L. Machiels, S. Onisei, L. Pandelaers, D. Geysen, P. T. Jones, and B. Blanpain. Slags with a high Al and Fe content as precursors for inorganic polymers. *Applied Clay Science*, 73:93–102, 2013.

[151] J. L. Provis. Alkali-activated materials. *Cement and Concrete Research*, doi: 10.1016/j.cemconres.2017.02.009, 2017.

[152] J. L. Provis and S. A. Bernal. Geopolymers and related alkali-activated materials. *Annual Review of Materials Research*, 44:299–327, 2014.

[153] J. L. Provis, A. Palomo, and C. Shi. Advances in understanding alkali-activated materials. *Cement and Concrete Research*, 78:110–125, 2015.

[154] J. L. Provis and J. S. J. van Deventer. Geopolymerisation kinetics. 2. Reaction kinetic modelling. *Chemical Engineering Science*, 62(9):2318–2329, 2007.

[155] J. L. Provis and J. S. J. van Deventer, editors. *Alkali Activated Materials: State-of-the-Art Report, RILEM TC 224-AAM*. Springer, 2014.

[156] X. Qiu, J. W. Thompson, and S. J. L. Billinge. PDFgetX2: a GUI-driven program to obtain the pair distribution function from X-ray powder diffraction data. *Journal of Applied Crystallography*, 37:678, 2004.

[157] H. Rahier, J. F. Denayer, and B. Van Mele. Low-temperature synthesized aluminosilicate glasses, Part IV: Modulated DSC study on the effect of particle size of metakaolinite on the production of inorganic polymer glasses. *Journal of Materials Science*, 38(4):3131–3136, 2003.

[158] H. Rahier, W. Simons, B. Van Mele, and M. Biesemans. Low-temperature synthesized aluminosilicate glasses, Part III: Influence of the composition of the silicate solution on production, structure and properties. *Journal of Materials Science*, 32(9):2237–2247, 1997.

[159] H. Rahier, B. Van Mele, M. Biesemans, J. Wastiels, and X. Wu. Low-temperature synthesized aluminosilicate glasses, Part I: Low-temperature reaction stoichiometry and structure of a model compound. *Journal of Materials Science*, 31(1):71–79, 1996.

[160] H. Rahier, B. Van Mele, and J. Wastiels. Low-temperature synthesized aluminosilicate glasses, Part II: Rheological transformations during low-temperature cure and high-temperature properties of a model compound. *Journal of Materials Science*, 31(1):80–85, 1996.

[161] H. Rahier, J. Wastiels, M. Biesemans, R. Willem, G. Van Assche, and B. Van Mele. Reaction mechanism, kinetics and high temperature transformations of geopolymers. *Journal of Materials Science*, 42(9):2982–2996, 2007.

[162] H. Rahier, B. Wullaert, and B. Van Mele. Influence of the Degree of Dehydroxylation of Kaolinite on the Properties of Aluminosilicate Glasses. *Journal of Thermal Analysis and Calorimetry*, 62:417–427, 2000.

[163] A. M. Rashad, Y. Bai, P. A. M. Basheer, N. C. Collier, and N. B. Milestone. Chemical and mechanical stability of sodium sulfate activated slag after exposure to elevated temperature. *Cement and Concrete Research*, 42(2):333–343, 2012.

[164] G. J. Redhammer. Characterisation of synthetic trioctahedral micas by Mössbauer spectroscopy. *Hyperfine Interactions*, 117(1-4):85–115, 1998.

[165] C. A. Rees. *Mechanisms and kinetics of gel formation in geopolymers*. PhD thesis, University of Melbourne, 2007.

[166] C. A. Rees, J. L. Provis, G. C. Lukey, and J. S. J. van Deventer. In situ ATR-FTIR study on the early ages of fly ash geopolymer gel formation. *Langmuir*, 23(17):9076–9082, 2007.

[167] J. P. Rino, I. Ebbsjö, R. K. Kalia, A. Nakano, and P. Vashita. Structure of rings in vitreous SiO_2. *Physical Review B*, 47(6):3053–3062, 1993.

[168] S. Rossano, A. Y. Ramos, and J.-M. Delaye. Environment of ferrous iron in $CaFeSi_2O_6$ glass; contributions of EXAFS and molecular dynamics. *Journal of Non-Crystalline Solids*, 273:48–52, 2000.

[169] J. Rouyer and A. Poulesquen. Evidence of a Fractal Percolating Network During Geopolymerization. *Journal of the American Ceramic Society*, 98(5):1580–1587, 2015.

[170] T. Ruskov, T. Tomov, and S. Georgiev. Mössbauer investigation of the Morin transition in hematite. *Physica Status Solidi (a)*, 37(1):295–302, 1976.

[171] S. M. K. S. Jewell. Minerals commodity summaries. Technical report, U.S. Department of the Interior and U.S. Department of Geological Survey, 2014.

[172] K. Sakkas, D. Panias, P. P. Nomikos, and A. I. Sofianos. Potassium based geopolymer for passive fire protection of concrete tunnels linings. *Tunneling and Underground Space Technology*, 43:148–156, 2014.

[173] K. Sankar and W. M. Kriven. Geopolymer reinforced with E-glass leno weaves. *Journal of the American Ceramic Society*, 100(6):2492–2501, 2017.

[174] F. Schorcht, I. Kourti, B. M. Scalet, S. Roudier, and L. D. Sancho. Best Available Techniques (BAT) Reference Document for the Production of Cement, Lime and Magnesium Oxide. Technical report, Joint Research Centre of the European Commission, 2013.

[175] J. Silver, I. E. G. Morrison, and L. V. C. Rees. A Mössbauer spectroscopic study of frozen solutions of $FeCl_3$ – phenols. *Inorganic Nuclear Chemistry Letters*, 15:433–436, 1979.

[176] S. Simon, G. J. G. Gluth, A. Peys, S. Onisei, D. Banerjee, and Y. Pontikes. The fate of iron during the alkali-activation of synthetic (CaO-)FeO_x-SiO_2 slags: An Fe K-edge XANES study. *Journal of the American Ceramic Society*, 2018.

[177] L. B. Skinner, S. R. Chae, B. C. J., H. R. Wenk, and P. J. M. Monteiro. Nanostructure of Calcium Silicate Hydrates in Cements. *Physical Review Letters*, 104:195502, 2010.

[178] S. Soyer-Uzun, S. R. Chae, C. J. Benmore, H.-R. Wenk, and P. J. M. Monteiro. Compositional evolution of calcium silicate hydrate (c-s-h) structures by total x-ray scattering. *Journal of the American Ceramic Society*, 95(2):793–798, 2012.

[179] P. Steins, A. Poulesquen, O. Diat, and F. Frizon. Structural Evolution during Geopolymerization from an Early Age to Consolidated Material. *Langmuir*, 28(22):8502–8510, 2012.

[180] P. Steins, A. Poulesquen, F. Frizon, O. Diat, J. Jestin, J. Causse, D. Lambertin, and S. Rossignol. Effect of aging and alkali activator on the porous structure of a geopolymer. *Journal of Applied Crystallography*, 47:316–324, 2014.

[181] W. Stumm and J. J. Morgan, editors. *Aquatic Chemistry: Chemical Equilibria and Rates in Natural Waters.* John Wiley and Sons, 1996.

[182] A. Tang Kai, H. Annersten, and T. Ericsson. Molecular Orbital (MSXα) Calculations of s-Electron Densities of Tetrahedrally Coordinated Ferric Iron: Comparison With Experimental Isomer Shifts. *Physics and Chemistry of Minerals*, 5(4):343–349, 1980.

[183] H. F. W. Taylor. Proposed structure for calcium silicate hydrate gel. *Journal of the American Ceramic Society*, 69(6):464–467, 1986.

[184] H. F. W. Taylor. Modification of the Bogue calculation. *Advances in Cement Research*, 2(6):73–77, 1989.

[185] H. K. Tchakouté, C. H. Rüscher, S. Kong, E. Kamseu, and C. Leonelli. Geopolymer binders from metakaolin using sodium waterglass from waste glass and rice husk ash as alternative activators: a comparative study. *Construction and Building Materials*, 114:276–289, 2016.

[186] L. Thannimalay, S. Yusoff, and N. Z. Zawawi. Life cycle assessment of sodium hydroxide. *Australian Journal of Basic and Applied Sciences*, 7(2):421–431, 2013.

[187] ThinkstepInternational. GaBi 6 Software-System and Databases for Life Cycle Engineering. *Leinfelden Echterdingen*, 2014.

[188] R. Thomas, D. Y. Tristana, R. Robert, and Z. Yongnin. Hybrid Cement Clinker and Cement Made from That Clinker. *Earth and Environmental Sciences Faculty Patents. Paper 1; also listed as US Patent 8,986,444 B2*, 2015.

[189] S. I. Tsipursky and V. A. Drits. The distribution of octahedral cations in the 2:1 layers of dioctahedral smectites studied by oblique texture electron diffraction. *Clay Minerals*, 19:177–193, 1984.

[190] J. Van De Sande, A. Peys, T. Hertel, S. Onisei, B. Blanpain, and Y. Pontikes. Glass forming ability of slags in the FeO_x-SiO_2-CaO system and properties of the inorganic polymers made theirof. In *Proceedings of the 5th International Slag Valorisation Symposium*, pages 397–400, Leuven, Belgium, April 2017.

[191] J. S. J. van Deventer. Valorisation of slag in construction: So much more than just technology. In *Proceedings of the 5th International Slag Valorisation Symposium*, pages 301–311, Leuven, Belgium, April 2017.

[192] A. van Riessen, E. Jamieson, C. S. Kealley, R. D. Hart, and R. P. Williams. Bayer-geopolymers: an exploration of synergy between the alumina and geopolymer industries. *Cement and Concrete Composites*, 41:29–33, 2013.

[193] A. Van Valkenburg Jr. and B. F. Buie. Octahedral cristobalite with quartz paramorphs from Ellora Caves, Hyderabad State, India. *American Mineralogist*, 30:526–535, 1945.

[194] R. E. Vandenberghe and E. De Grave. *Mössbauer Spectroscopy: Tutorial Book*, chapter Application of Mössbauer Spectroscopy in Earth Sciences, pages 91–185. Springer, 2013.

[195] T. A. Vilgis. Strong and fragile glasses: A powerful classification and its consequences. *Physical Review B*, 47(5):2882, 1993.

[196] R. Walker. *Mass, weight, density or specific gravity of bulk materials.* http://www.simetric.co.uk, 2011.

[197] S. Wang and K. L. Scrivener. Hydration products of alkali activated slag cement. *Cement and Concrete Research*, 25(3):561–571, 1995.

[198] B. E. Warren and J. Biscob. Fourier Analysis of X-ray Patterns of Soda Silica Glass. *Journal of the American Ceramic Society*, 21(7):259–265, 1938.

[199] C. Weigel, L. Cormier, G. Calas, L. Galoisy, and D. T. Bowron. Intermediate-range order in the silicate network glasses $NaFe_xAl_{1-x}Si_2O_6$ (x = 0, 0.5, 0.8,1): A neutron diffraction and empirical potential structure refinement modeling investigation. *Physical Review B*, 78(52-54):064202, 2008.

[200] C. Weigel, L. Cormier, G. Calas, L. Galoisy, and D. T. Bowron. Nature and distribution of iron sites in a sodium silicate glass investigated by neutron diffraction and EPSR simulation. *Journal of Non-Crystalline Solids*, 354(52-54):5378–5385, 2008.

[201] C. Weigel, L. Cormier, L. Galoisy, G. Calas, D. Bowron, and B. Beuneu. Determination of Fe^{3+} sites in a $NaFeSi_2O_6$ glass by neutron diffraction with isotopic substitution coupled with numerical simulation. *Applied Physics Letters*, 89(14):141911, 2006.

[202] C. E. White, L. L. Daemen, M. Hartl, and K. Page. Intrinsic differences in atomic ordering of calcium (alumino) silicate hydrates in conventional and alkali-activated cements. *Cement and Concrete Research*, 67:66–73, 2015.

[203] C. E. White, K. Page, N. J. Henson, and J. L. Provis. In situ synchrotron X-ray pair distribution function analysis of the early stages of gel formation in metakaolin-based geopolymers. *Applied Clay Science*, 73:17–25, 2013.

[204] C. E. White, J. L. Provis, B. Bloomer, N. J. Henson, and K. Page. In situ X-ray pair distribution function analysis of geopolymer gel nanostructure formation kinetics. *Physical Chemistry Chemical Physics*, 15(22):8573–8582, 2013.

[205] C. E. White, J. L. Provis, A. Llobet, T. Proffen, and J. S. J. van Deventer. Evolution of local structure in geopolymer gels: An in situ neutron pair distribution function. *Journal of the American Ceramic Society*, 94(10):3532–3539, 2011.

[206] C. E. White, J. L. Provis, T. Proffen, D. P. Riley, and J. S. J. van Deventer. Combining density functional theory (DFT) and pair distribution function (PDF) analysis to solve the structure of metastable materials: the case of metakaolin. *Physical Chemistry Chemical Physics*, 12(13):3239–3245, 2010.

[207] C. E. White, J. L. Provis, T. Proffen, and J. S. J. van Deventer. The Effects of Temperature on the Local Structure of Metakaolin-Based Geopolymer Binder: A Neutron Pair Distribution Function Investigation. *Journal of the American Ceramic Society*, 93(10):3486–3492, 2010.

[208] C. E. White, J. L. Provis, T. Proffen, and van Deventer J. S. J. Molecular Mechanisms Responsible for the Structural Changes Occuring During Geopolymerization: Multiscale Simulation. *AIChE Journal*, 58(7):2241–2253, 2012.

[209] M. Wilke, F. Farges, P.-E. Petit, G. E. Brown Jr., and F. Martin. Oxidation state and coordination of Fe in minerals: An Fe K-XANES spectroscopic study. *American Mineralogist*, 86(5-6):714–730, 2001.

[210] R. P. Williams and A. van Riessen. The first 20 hours of geopolymerization: An in situ WAXS study of fly ash-based geopolymers. *Materials*, 9(7):552–564, 2016.

[211] A. C. Wright. Neutron scattering from vitreous silica. V. The structure of vitreous silica: What have we learned from 60 years of diffraction studies? *Journal of Non-Crystalline Solids*, 179:84–115, 1994.

[212] A. C. Wright, S. J. Clarke, C. K. Howard, P. A. Bingham, S. D. Forder, D. Holland, D. Martlew, and H. E. Fischer. The environment of Fe^{2+}/Fe^{3+} cations in a soda-lime-silica glass. *Physics and Chemistry of Glasses - European Journal of Glass Science and Technology Part B*, 55(6):243–252, 2014.

[213] K. Yang and C. E. White. Modeling the Formation of Alkali Aluminosilicate Gels at the Mesoscale Using Coarse-Grained Monte Carlo. *Langmuir*, 32(44):11580–11590, 2016.

[214] K. Yang, V. O. Özçelik, N. Garg, K. Gong, and C. E. White. Drying-induced atomic structural rearrangements in sodium-based calcium-alumino-silicate-hydrate gel and the mitigating effects of ZrO_2 nanoparticles. *Physical Chemistry Chemical Physics*, 20(13):8593–8606, 2018.

[215] R. Zah and R. Hischier. Life cycle inventories of detergents; EcoInvent report no.12. Technical report, Swiss Centre for Life Cycle Inventories, 2007.

[216] O. V. Özçelik and C. E. White. Nanoscale Charge-Balancing Mechanism in Alkali-Substituted Calcium–Silicate–Hydrate Gels. *Journal of Physical Chemistry Letters*, 7(24):5266–5272, 2016.

[217] G. H. Zhang, K. C. Chou, and K. Mills. A Structurally Based Viscosity Model for Oxide Melts. *Metallurgical and Materials Transactions B*, 45(2):698–706, 2014.

[218] Z. Zhang, J. L. Provis, H. Wang, F. Bullen, and A. Reid. Quantitative kinetic and structural analysis of geopolymers. Part 2. Thermodynamics of sodium silicate activation of metakaolin. *Thermochimica Acta*, 565:163–171, 2013.

[219] S. Zhou, E. S. Howard, J. Liu, N. H. Bashian, K. Nolan, S. Krishnamoorthy, G. M. Rangel, M.-T. Sougrati, G. K. S. Prakash, K. Page, and B. C. Melot. Hydrothermal Preparation, Crystal Chemistry, and Redox Properties of Iron Muscovite Clay. *ACS Applied Materials and Interfaces*, 9(39):34024–34032, 2017.

[220] Y. Zhu and E. J. Elzinga. Formation of Layered Fe(II)-Hydroxides during Fe(II) Sorption onto Clay and Metal-Oxide Substrates. *Environmental Science and Technology*, 48(9):4937–4945, 2014.

[221] F. Zibouche, H. Kerdjoudj, J.-B. d'Espinose de Lacaillerie, and H. Van Damme. Geopolymers from Algerian metakaolin. Influence of secondary minerals. *Applied Clay Science*, 43(3-4):453–458, 2009.

Curriculum Vitae

Education

September 2012-July 2014: KU Leuven Master of Science in Materials Engineering
Magna cum laude

2009-2012: KU Leuven Bachelor of Science in Engineering
Cum laude

Research

October 2014-now: KU Leuven, PhD student in Engineering

January 2017, October 2017, July 2018: University of Ioannina, Visiting PhD student
Focused research stays on the determination of the behavior of Fe in the structure of slags and inorganic polymers by Mössbauer spectroscopy.

March 2017-August 2017: Princeton University, Visiting Student Research Collaborator
Focused research stay for analysis of the molecular structure of iron-rich inorganic polymers by pair distribution function analysis.

Responsibilities

Council memberships

October 2017-now: Bureau Arenberg Doctoral School
Commission guarding the quality of PhDs at KU Leuven Group Science and Technology: assesses applications for funding for summer schools and seminars, decides on requirements for PhDs.

October 2016-2018: Faculty Doctoral Commission
Commission guarding the quality of PhDs at KU Leuven Faculty of Engineering: assesses applications, progress, and submission of PhD.

December 2014-2018: Faculty council
Decision making in the KU Leuven Faculty of Engineering

Public relations

April 2019: Co-organizer 6th International Slag Valorisation Symposium
http://www.slag-valorisation-symposium.eu

April 2017: Co-organizer 5th International Slag Valorisation Symposium
http://www.slag-valorisation-symposium.eu

October 2016-now: Webmaster research group
https://www.mtm.kuleuven.be/Onderzoek/sremat

October 2016-now: Assistant editor of departmental newsletter
"MTM Stars"

Education

Coordination: Practical sessions Recycling and metallurgical company visits
Practical session of 1st master students on the recycling of industrial residues. A residues is assigned to the student for which they have to design and execute a flowsheet for their valorization.

Participation: Practicum microstructurele analyse, oefenzittingen mechanisch gedrag van materialen, PenO Reverse Engineering, PenO Chemische analyse

Other

2017-2018: Departmental trip
Organization of the yearly departmental trip.

2015-2018: Lunch and Learn meeting
Organization of bi-monthly lunch presentation sessions for PhDs and post-docs in the department of Materials Engineering.

2016-2018: SWEET^2 experienced teaching assistant
Sharing experience to new PhD students in teaching assistants training.

Skills

Language

Fluent: English, Dutch
Moderate: French
Basic understanding: German

Software

Co-developer "Sustainable metallurgy toolbox"
Advanced knowledge: Microsoft Office, gnuplot, Visual Studio (programming in C)
Intensive user: FactSage, PDFgetX2, PDFgui
Basic comprehension: MATLAB, TexMaker, Origin, EXAFS analysis software (Athena), JMP, Python

Sports

Triathlon and running: training for endurance sports gives you time to think and calm the mind, while in competition you learn determination and strengthen your mental force. Best marathon time 3:31:34 (Kasterlee 2017).

Awards

Cobaty 2014
For the contribution of the master thesis to sustainable development. For more information: http://www.cobaty.be/Prijs.html.

Oscar for Best Actor in a Supporting Role 2015-2016
(best teaching assistant 2015-2016) on movie-themed departmental dinner 2016, traditionally organized by 2nd master students. Chosen by department-wide election.

Gouden Krijtje 2017
For best assistant at the Department of Materials Engineering 2016-2017 (together with colleague Tobias Hertel). Organized by student organization (VTK), elected by students Faculty of Engineering Science.

Gouden Krijtje 2018
For best assistant at the Department of Materials Engineering 2017-2018. Organized by student organization (VTK), elected by students Faculty of Engineering Science.

Publication list

Journal papers

A. Peys, H. Rahier, Y. Pontikes (2016), "Potassium-rich biomass ashes as activators in metakaolin-based inorganic polymers", *Applied Clay Science* 119, 401-409.
A. Peys, L. Arnout, B. Blanpain, H. Rahier, K. Van Acker, Y. Pontikes (2018), "Mix-design Parameters and Real-Life Considerations in the Pursuit of Lower Environmental Impact Inorganic Polymers", *Waste and Biomass Valorization* 9, 879-889.
S. Simon, G. J. G. Gluth, **A. Peys**, S. Onisei, Y. Pontikes (2018), "The Fate of Iron During the Alkali-Activation of Synthetic FeO_x-SiO_2(-CaO) Slags: an Fe K-edge XANES Study", *Journal of the American Ceramic Society* 101, 2107-2118.
S. Onisei, A. P. Douvalis, A. Malfliet, **A. Peys**, Y. Pontikes (2018), "Inorganic polymers made of fayalite slag: on the microstructure and behavior of Fe", *Journal of the American Ceramic Society* 101, 2245-2257.
A. Peys, C. E. White, D. Olds, H. Rahier, B. Blanpain, Y. Pontikes (2018), "Molecular structure of CaO-FeO_x-SiO_2 glassy slags and resultant inorganic polymers", *Journal of the American Ceramic Society* 101, 5846-5857.
A. Peys, A. P. Douvalis, V. Hallet, H. Rahier, B. Blanpain, Y. Pontikes, "Inorganic polymers from CaO-FeO_x-SiO_2 slag: the start of oxidation of Fe and the formation of a mixed valence binder", *submitted*.
A. Peys, C. E. White, H. Rahier, B. Blanpain, Y. Pontikes, "CaO-FeO_x-SiO_2 inorganic polymers: Insights on the reaction mechanism from in situ X-ray pair distribution function analysis", *submitted*.

Conference proceedings

A. Peys, H. Rahier, Y. Pontikes (2015), "Biomass ash as alkaline activator in inorganic polymer synthesis", *Proceedings of the 4th International Slag Valorisation Symposium*, Leuven, Belgium.
T. Hertel, L. Arnout, A. Peys, L. Pandelaers, B. Blanpain, Y. Pontikes (2015), "A proposal for a 100% use of bauxite residue: The process, results on the novel Fe-rich binder and how this can take place within the alumina refinery", *Proceedings of the 1st Bauxite Residue Valorisation and Best Practices Conference*, Leuven, Belgium.
A. Mobili, A. Balo Madi, A. Peys, F. Tittarelli, N. Fagel, U. Chinje Melo, D. Njopwouo, H. Rahier (2016), "What if we use biomass ashes to activate one-part geopolymers?", *Proceedings of the National Young Researchers' Forum on Materials Science and Technology*, Ischia, Italy.
A. Peys, A. Mobili, L. Arnout, H. Rahier, B. Blanpain, Y. Pontikes (2016), "One-part inorganic polymers from residues only: Biomass ash activation of Fe-rich slag", *Proceedings of the 5th International Conference on Industrial and Hazardous Waste Management*, Chania, Greece.
L. Arnout, A. Peys, B. Blanpain, Y. Pontikes (2016), "Quartz glass cullet as pore forming precursor in the synthesis of inorganic materials", *Proceedings of the 5th International Conference on Industrial and Hazardous Waste Management*, Chania, Greece.
A. Peys, M. Peeters, A. Katsiki, L. Kriskova, H. Rahier, B. Blanpain, Y. Pontikes (2017), "Performance and durability of Fe-rich inorganic polymer composites with basalt fibers", *Proceedings of the 41st International Conference and Expo on Advanced Ceramics and Composites*, Daytona Beach, FL, USA.
A. Peys, L. Arnout, T. Hertel, R.I. Iacobescu, S. Onisei, L. Kriskova, H. Rahier, B. Blanpain, Y. Pontikes (2017), "The use of ATR-FTIR spectroscopy in the analysis of iron-silicate inorganic polymers", *Proceedings of the 5th International Slag Valorisation Symposium*, Leuven, Belgium.
A. Peys, E. Orfanakis, Y. Pontikes (2017), "On a software development that aspires to make residue valorisation easier", *Proceedings of the 5th International Slag Valorisation Symposium*, Leuven, Belgium.
V. Hallet, A. Peys, A. Katsiki, H. Rahier, S. Onisei, Y. Pontikes (2017), "The influence of activating solution on the kinetics and compressive strength of an iron-rich slag paste", *Proceedings of the 5th International Slag Valorisation Symposium*, Leuven, Belgium.
J. Van De Sande, A. Peys, T. Hertel, S. Onisei, B. Blanpain, Y. Pontikes (2017), "Glass forming ability of slags in the FeO_x-SiO_2-CaO system and properties of the inorganic polymers made thereof", *Proceedings of the 5th International Slag Valorisation Symposium*, Leuven, Belgium.
A. P. Douvalis, A. Peys, S. Onisei, Y. Pontikes (2017), "Investigating the

properties of iron in inorganic polymers with ^{57}Fe Mössbauer spectroscopy", *Proceedings of the 5th International Slag Valorisation Symposium*, Leuven, Belgium.
A. Katsiki, A. Peys, Y. Pontikes, H. Rahier (2017), "Activation of fayalite slag towards inorganic polymers", *Proceedings of the 5th International Slag Valorisation Symposium*, Leuven, Belgium.
P. Petrica, L. Kriskova, A. Peys, Y. Pontikes (2017), "Recycling of iron-rich inorganic polymers", *Proceedings of the 5th International Slag Valorisation Symposium*, Leuven, Belgium.

Conference contributions without proceeding paper

H. Rahier, A. Peys, B. Blanpain, Y. Pontikes (2015), "Plant ashes as activator for alkali activation", *Presented at the 39th International Conference and Expo on Advanced Ceramics and Composites*, Daytona Beach, FL, USA.
H. Rahier, A. Peys (shared first author), Y. Pontikes (2015), "Ashes from biomass incineration as alternative activator for inorganic polymers", *Presented at the 1st Geopolymer Conference*, Hernstein, Austria.
Y. Pontikes, S. Onisei, L. Machiels, R. I. Iacobescu, L. Kriskova, L. Arnout, A. Peys, P. T. Jones, B. Blanpain (2015), "Inorganic polymers from residues of high temperature processes: Going beyond the aluminosilicates", *Presented at the 1st Geopolymer Conference*, Hernstein, Austria.
A. Peys, A. Mobili, A. Katsiki, L. Arnout, H. Rahier, B. Blanpain, Y. Pontikes (2017), "Biomass ashes as activators in the synthesis of inorganic polymers: from a model system to a blend of industrial residues", *Presented at the 41st International Conference and Expo on Advanced Ceramics and Composites*, Daytona Beach, FL, USA.
A. Katsiki, A. Peys, T. Tysmans, J. Wastiels, H. Rahier (2017), "Development of novel aluminosilicate phosphate cement for structural applications", *Presented at the 41st International Conference and Expo on Advanced Ceramics and Composites*, Daytona Beach, FL, USA.
A. Katsiki, A. Peys, T. Tysmans, J. Wastiels, H. Rahier (2017), "Cementitious composites for structural applications based on metakaolinite phosphate cements", *Presented at the 41st International Conference and Expo on Advanced Ceramics and Composites*, Daytona Beach, FL, USA.
A. Peys, V. Hallet, J. Van De Sande, S. Onisei, H. Rahier, B. Blanpain, Y. Pontikes (2017), "Design of Fe-rich inorganic polymer pastes: Influence of the chemistry of the precursor slag and activating solution", *Presented at Euromat*, Thessaloniki, Greece.
K. Gong, A. Peys, Y. Pontikes, C. E. White (2018), "Alkali-activated Fe-rich Slag with Superior Resistance to $MgSO_4$ Attack", *Presented at the 9th Advances*

in Cement Based Materials (Cements 2018), State College, Pennsylvania, USA.
A. Peys, A. P. Douvalis, C. E. White, H. Rahier, B. Blanpain, Y. Pontikes (2018), "Inorganic polymerisation of FeO_x-rich slags: Unraveling the complex reactions of a simple system", *Presented at the 10th International Conference on the Environmental and Technical Implications of Construction Materials with Alternative Materials (WASCON)*, Tampere, Finland.
C. Siakati, A. Peys, Y. Pontikes (2018), "Inorganic polymers from FeO_x-CaO-SiO_2 slags: Influence of CaO on reactivity and strength development", *Presented at the Materials Science and Technology (MS & T) conference*, Columbus, Ohio, USA.

FACULTY OF ENGINEERING SCIENCE
DEPARTMENT OF MATERIALS ENGINEERING
SREMAT
Kasteelpark Arenberg 44
B-3001 Heverlee